THÈSE de DOCTORAT en COTUTELLE

de l'UNIVERSITÉ PARIS VII et de L'INSTITUT de PHYSIQUE

de l'ACADÉMIE des SCIENCES de LETTONIE

spécialité: Physique des Liquides

présentée par

Sandris LĀCIS

pour obtenir le grade DOCTEUR de l'UNIVERSITÉ PARIS VII et de L'INSTITUT de PHYSIQUE de l'ACADÉMIE des SCIENCES de LETTONIE

COMPORTEMENT D'UNE GOUTTE DE LIQUIDE MAGNETIQUE DANS UN CHAMP MAGNETIQUE VARIABLE: THÈORIE ET SIMULATION

MAGNĒTISKĀ ŠĶIDRUMA PILIENA DINAMIKA MAINĪGOS MAGNĒTISKOS LAUKOS: TEORIJA UN SKAITLISKĀ MODELĒŠANA

BEHAVIOUR OF A MAGNETIC FLUID DROP IN A TIME DEPENDENT MAGNETIC FIELD: THEORY AND SIMULATION

English version

soutenue le 15 février 1996 devant le jury composé de :

G.	BOSSIS	Rapporteur
A.	GAILITIS	Rapporteur
J.-C.	BACRI	
A.	CEBERS	
R.	GOLDSTEIN	

To my grandmother **Marta Plikause**

Acknowledgements

I am very much obliged to prof. Jaques Duran and prof. Alain Mauger for the warm hospitality and the stimulating conditions for scientific work in *Laboratoir d'Acoustique et Optique de la Matiére Condensée*, University Paris 6. I am very grateful to prof. Olģerts Lielausis for his support to my scientific work in Institute of Physics, Latvia.

I am very much obliged to both my thesis-directors, prof. Jean-Claude Bacri and prof. Andrejs Cēbers. I have had an opportunity to profit from the doubled experience of two directors as well as I have used non-ordinary chance to look on physical phenomena from two viewpoints, joining together the theoretical and experimental knowledge.

The thesis will never be possible without the assistance of prof. Regine Perzynski during both helpful discussions and everyday situations.

I would like to express my deepest gratitude to prof. George Bossis and prof. Agris Gailītis, who have agreed to be "rapporteurs" of my thesis and thus have made the enormous work in rather limited time.

I am also very thankful to prof. Raymond Goldstein who have found possible to take care of my work being a member of the thesis jury.

I feel it my pleasant duty to express my thankfulness to all the people of A.O.M.C. laboratory, who have stimulated my research. I would like especially to mention Umberto d'Ortona for his help during my first steps in UNIX enviroment.

The French version of the theses will never see the day-light without the excellent work of Jean-Christophe Dabadie translating it from English.

And last but not least, I would like to thank my Latvian colleges, who have helped me to keep connection to Latvia and to manage formalities in Latvia during my absence, especially I wish to thank assoc.prof. Leonīds Buligins and Ivars Driķis.

Contents

Introduction

The behaviour of a ferrofluid droplet in a rotating field is quite intricate including even transition to chaotic dynamics. If at present the behaviour of droplet in static field is quite well understood both theoretically and experimentally then in rotating field or even more in the field of more complicate character there are great variety of rather complex phenomena for which at present moment adequate theoretical understanding does not still exists. Existing theoretical approaches are based on simple assumptions of ellipsoidal shapes of droplets as in 3D and 2D. More complex shapes is possible to study enough thoroughly only by numerical means.

The goal of the present thesis work was to perform analytical and numerical studies of a 2D ferrofluid droplet in a rotating magnetic field including elaboration of the corresponding numerical tools. For that small perturbation theory is used in the case of simple geometry to find the growth rate of perturbations and boundary element method is used to solve the moving free boundary problem of droplet behaviour. In the last case the satellite problem of the creeping flow and the magnetic field have to be solved in the every time step.

In the first chapter the short overview about most important properties of magnetic fluids and especially about the concentrated phase of a magnetic fluid is given. The concentrated phase due to its abnormally high magnetic susceptibility and low surface tension on the interface between two phases, leading to high values of a magnetic Bond number, enables to observe many intrinsic phenomena, which are not to observe in experiments with conventional ferrofluids. In the rest of this chapter the low Reynolds number flow (called creeping flow) problem and the satellite problem of a magnetic field solution are defined for a 2D droplet using boundary integral equation formulation.

The second chapter contains approximation of boundary integral equations, given in the first chapter. The boundary element method (BEM) accuracy is tested using exact analytical solutions. The results of test display that BEM accuracy allows

to use it to simulate numerically unsteady motion of a 2D droplet in an external magnetic field. On the basis of given discrete algorithms the various computer codes are elaborated to perform BEM simulation in the case of the magnetic field problem at given geometry (chapter 3) and in the cases of coupled magnetic field and creeping flow problems (chapters 4 and 5).

In the case of a high-frequency rotating magnetic field time averaging of surface forces could be used if the rotation period is much smaller than characteristic relaxation time for a droplet. In the third chapter the equilibrium figures of a 2D droplet are studied from minimal energy viewpoint in high-frequency field. The favourite shape with a minimal energy is found from an *a priori* given set of shapes at a given magnetic field strength amplitude, using time-averaging for a magnetic energy. Such an approach allows to detect the magnetic field threshold at which the perturbation from the circular shape of a droplet appears, if a magnetic field strength is increased from the zero value. The decrease of a magnetic field strength displays the hysteresis effect, if magnetic permeability of the ferrofluid is high enough. The magnetic field is calculated by BEM, families of shapes are generated by the special technique described in this chapter.

The constraints of the droplet shape in the third chapter interfere in the obtaining transitions between shapes with different numbers of spikes. In the fourth chapter the solution of the whole free moving boundary problem of a 2D ferrofluid droplet by BEM in the case of time-averaged surface forces provides information about the evolution of shapes. It has been illustrated by direct numerical simulation that starting from random initial state transitions to configurations with two and three spikes are observed. The four spike shape appears to be unstable in 2D.

The fifth chapter contains results of a 2D droplet simulation in a low-frequency rotating magnetic field. It has been shown that two different scenarios for a behaviour of a droplet exist in dependence on the value of the magnetic Bond number. In the case of large magnetic Bond number values there is the critical frequency for a magnetic field rotation up to which droplet is able to follow the field rotation. Beyond this critical frequency droplet is no more phase locked to the magnetic field and exhibits rather intrinsic behaviour, peculiarities of which is analysed in more detail in

the case of the more general elliptic field polarisation in the next, namely sixth chapter. In the fifth chapter under the assumption of an elliptic shape of a droplet two sets of the equations of motion are derived and used to obtain the characteristics of a droplet behaviour in the fifth chapter. The comparison with the BEM shows fairly well agreement. The BEM simulations display that the role of the bending instability of a droplet increases, if the viscosity of a droplet is increased with respect to the one of a surrounding fluid.

The last, namely sixth chapter is devoted the behaviour of a droplet in an elliptical polarised rotating magnetic field. Elliptical polarisation of a field is the source of the second modulation frequency, interaction of which with the frequency of the droplet's rotation causes such effects as the mode-locking represented by the devil's staircase, overlapping of mode-locking intervals, period doubling and the transition to a chaos.

Throughout the present work the **cgs** system, and particularly the **electromagnetic cgs** system of units, centred on gauss unit for a magnetic field is used.

Chapter 1

Physical properties and models of magnetic liquids

1.1. Magnetic fluids and their properties

1.1.1. General properties

The studies of magnetic fluids started in the early 1960s. Most of applications of colloidal magnetic fluids (ferrofluids) were recognised slightly latter, when real ferrofluids become available, because they are pure artificial product: they are not found in nature. The name "ferrofluids" was proposed by R.E.Rosensweig [77], the name magnetic fluids was used in [99] by M.I.Shliomis. Perhaps the name "ferrohydrodynamics" (FHD) matches the topic of hydrodynamics of magnetic fluids at best, since the name "magnetohydrodynamics" (MHD) is mostly used for phenomena where the interaction between magnetic fields and electric currents in fluids takes place. Nevertheless, it should be noted that the term MHD is still used as more general, covering both topics, "classical" MHD and ferrohydrodynamics. Exhausting overviews about magnetic fluids and their most important physical and chemical properties are given in [22,25,91].

Ferrohydrodynamics studies the flow of magnetic fluid under the action of strong forces of magnetic polarisation. The main difference between MHD and FHD is that in MHD the body force acting on the fluid is the Lorentz force that arise when electric current flows at an angle to the direction of a magnetic field. In FHD usually there is no electric current flowing in the fluid. The body force in FHD is due to

polarisation force, which in turn requires material magnetisation in the presence of magnetic field gradients or discontinuities.

The uniqueness of ferrofluids is in giant magnetic response to magnetic field. As a result many surprising phenomena are exhibited by the magnetic fluids in response to magnetic fields:

- normal field instability (formation of a pattern of spikes on the fluid surface);
- the labyrinthine pattern formation in thin layers;
- the generation of body couple in rotary fields, which is manifested as antisymmetric stress;
- self levitation of an immersed magnet;
- enhanced convective cooling in ferrofluids having a temperature-dependent magnetic moment;
- and many others.

During the last thirty years since ferrofluids become available, great variety of applications of them in different branches are found. Actual commercial usage presently includes [25,87,91]:

- novel zero leakage rotary shaft seals, used in computer disk drives [15];
- vacuum feedthroughs for semiconductor manufacturing [76];
- pressure seals for compressors and blowers [90];
- liquid-cooled loudspeakers that employ a ferrofluid to conduct heat away from the speakers coils [23,56];
- piloting the path of a drop of ferrofluid in the body, to bring drugs to a target site [75];
- non-invasive circulatory measurements of the blood flow [78,84];
- artificial high specific gravity effect applied to separate mixtures of industrial scrap metals such as titanium, aluminium, and zinc [47,98];
- high-speed, inexpensive, silent printers. using magnetic fluid ink [72];

Here just more known applications are mentioned, in fact this list is still under growing.

Exist several types of magnetic fluids, but the principal type of them is "colloidal ferrofluid". A colloid is a suspension of finely divided particles in a continuous medium, including suspensions that settle out slowly. However, a true ferrofluid have not to settle out, even long exposure of a force field causes a slight concentration gradient. A good ferrofluid [95] have to be a concentrated, stable suspension of very small magnetic particles in a liquid. A surfactant normally provides the colloid stability. Therefore the traditional ferrofluids are composed of small (3-15 nm), solid, single-domain magnetic particles coated with a molecular layer of a dispersant and suspended in a liquid carrier. The difference of the ionic-ferrofluids [73] from the surfactant-stabilised ones is that they are stabilised due to the strongly screened electrostatic repulsion of ionic particles. Brownian motion keeps particles suspended, and the coatings prevent the particles from sticking to each other. Van der Waals attraction is one of the main problems to obtain colloidal particles that are stable with respect to mutual agglomeration. To prevent particles from approaching so close to one another that van der Waals attraction prevail, the steric repulsion mechanism is used. For that particle surface is coated by long chain molecules in such a way that the polar "heads" of chains are adsorbed by the particle but the "tail" creates "elastic bumper" layer. According to the simplest model of a stable magnetic fluid [22], a particle inside it is characterised by three dimensions, namely, magnetic core diameter d_m, solid diameter d_s, and coating diameter d_h. Quantities d_s and d_m are not the same because due to chemical interactions between stabiliser and the particles, the surface layer of the particles may lose magnetic properties.

A low evaporation rate, a low viscosity and chemical inertness are desirable properties fore the base liquid. A ferrofluid remains flowable in the presence of magnetic field even when magnetised to saturation. Nonetheless, the reology is affected by the presence of a field [25,100].

The stability of the magnetic liquid is ensured by the balance between the various interparticle interactions:

- magnetic dipole-dipole interaction,
- van der Waals interaction,
- dipole-magnetic field interaction,
- and
  - ♦ either steric repulsion via the solvent particles coated with a surfactant in the case of surfactant-stabilised ferrofluids when particles are coated with surfactant chains,
  - ♦ or strongly screened electrostatic repulsion for ionic particles in the case of ionic colloids when magnetic particles are made also macro-ions in order to create electrostatic repulsion.

Stability in a magnetic field gradient is the stability against settling of particles in a field gradient due to an external magnetic source. Thermal motion of particles should prevent the attraction of them to the higher intensity regions of a magnetic source. Stability against segregation is favoured by a high ratio of the thermal energy to the magnetic energy: $k_B T / MHV \geq 1$, here k_B: Boltzmann constant, T: temperature, M: magnetisation, H: magnetic field strength, V: volume of the particle. This relation forms an upper limit for particle size. The related topic is the stability against magnetic agglomeration. Due to collisions between particles, they could agglomerate rapidly if particles adhere together. Here again the thermal energy is responsible to separate the particles, i.e. to overcome dipole-dipole interaction, characterised by ratio of thermal and dipole-dipole contact energy. The requirement for stability in a gravitational field is usually lower than the requirements for stability in magnetic field.

There are two magnetic relaxation mechanisms in ferrofluids: relaxation by rotation if particle in the liquid and the relaxation due to rotation of the magnetic vector within the particle. Solidified ferrofluid has only the second mechanism. The particle rotation mechanism is characterised by a Brownian rotation diffusion time τ_B having hydrodynamical origin [25,50,91] and given by $\tau_B = 3V\eta_0 / kT$ where V is the particle volume and η_0 the viscosity of the carrier liquid. The second relaxation has so-called Néel relaxation time [25,50,91]

$$\tau_B = \frac{1}{f_0}\exp\left(\frac{KV}{kT}\right)$$

where KV is the height of energy barrier which separates the two possible magnetisation orientations inside the particle in absence of field for single-domain uniaxial ferromagnetic particle.

The two main magnetic fluid preparation kinds are sketched below.

Preparation by size reduction.

Size reduction by grinding can succeed in reducing bulk (micron-size) material to the order of 100Å in size. The method discovered by S.Papell [81], further developed by many researchers (see [91]). Preparation of ferrofluid consists from following steps 91:

- μm size magnetic powder is mixed with solvent and surfactant dispersing agent;
- size reduction in ball grind;
- centrifugation to separate oversize solids;
- correction of particle concentration.

Typical preparation time is about 1000h.

Preparation of ferrofluids by chemical precipitation

There are many chemical methods to prepare ferrofluids. Here just three more representative of them are mentioned according to [91]:

- magnetite precipitation with steric stabilisation;
- cobalt particles in an organic carrier;
- charge-stabilised magnetite.

The chemical methods are fast typical preparation time are few hours, they can be cheap, but they are restricted to a few particular compounds. Special fluids are produced mainly by size reduction. Additional stabilisation effect is achieved by steric repulsion mechanism due to the presence of long chain molecules absorbed onto the particle surface.

1.1.2. Concentrated phase

In the general purpose of technical applications require industrial products stable in time, proof against temperature variations and magnetic field action. Nevertheless in some particular cases it is possible to take advantage of the phase separation in magnetic liquids. The concentrated phase could be obtained due to failure of stability leading to a phase separation in two liquids of different particle concentrations: droplets of concentrated phase grow among the more dilute phase [31]. A phase separation could be induced by many factors, for example; temperature lowering, for sterically stabilised particles, some variations of free surfactant concentration; for electrostatically stabilised particles, an increase of ionic strength.

The concentrated phase causes interest due to its outstanding physical properties: it was found in [11] that susceptibility $\chi_{SI}=\mu-1\sim40$ (magnetic permeability $\mu\sim40$) and surface tension $\sigma\sim5\cdot10^{-7}$ J·m^{-2}=$5\cdot10^{-4}$ erg·cm^{-2} for an ionic ferrofluid and in [86] for a surfactant stabilised ferrofluid $\chi_{SI}=\mu-1\sim80$ ($\mu\sim80$) and $\sigma\sim3\cdot10^{-7}$ J·m^{-2}=$3\cdot10^{-4}$ erg·cm^{-2}.

These susceptibilities are about an order of magnitude higher than for usual magnetic fluids, what allows to observe some phenomena which appears only in the case of high susceptibility. Such extraordinary values of susceptibility are possible due to a high packing of particles in a concentrated phase, additional effect caused by a packing is large values of viscosity. In contrary, surface tension at the boundary of the two phases is very low. Magnetisation curve for concentrated phase exhibits [31]:

- a linear regime with very high initial susceptibility in low field, what means that the particles keep their rotational degrees of freedom,
- a very large saturation value (~ 90 kA/m=1130 Oe), what means a volume fraction of magnetic particles close to the maximum reasonable value (~24%) for a ferrosuspension retaining its fluidity [94].

Hence in order to obtain concentrated phase, repulsive interaction should be decreased. For ionic ferrofluids it is much simpler to realise since they are directly synthesised as micro-ions [73], but for by surfactant stabilised magnetic liquids it is very complicate to decrease repulsion.

In the concentrated phase, distance between particles are determined only by the solvate shells. The concentration of the concentrated phase is always the same and about equal to 25 % in volume. Every particle is surrounded by a shell of structural water of thickness 1 or 2 nm, so all the water shells mix into a single one in the whole phase. A liquid-gas like phase separation always causes that a concentrated phase appears as droplets inside a more diluted phase.

1.2. Ferrohydrodynamical surface instabilities

1.2.1. Free ferrofluid droplet in a static field

A deformation of a ferrofluid droplet in a static field is studied experimentally in [2,46] and theoretically under assumption of an ellipsoidal shape of a droplet [24,32] in zero gravity. Very interesting results are obtained in experiments with a concentrated phase [11,12,14]. In [11,14] under assumption of the prolate ellipsoidal shape of the ferrofluid droplet the equilibrium shapes are described from the balance between magnetic energy and interfacial tension energy. For magnetic permeability of the droplet μ=40 it is found that the droplet becomes unstable for a certain magnetic field threshold: it jumps from a slightly elongated shape to a much more elongated one. The ratio of semi-axes of the ellipsoidal shape changes from a/b~2 to a/b~13. At decrease of the field the droplet from the elongated shape a/b~7 reduces to a less elongated one a/b~1.5 at a smaller magnetic field threshold value. Such a transition takes place only if magnetic permeability is high enough, namely if μ>20.8 [89]. In [25,32] it is shown that the virial method and the energy approach gives equivalent results. The advantage of the virial method is that it could be used to study perturbations from the ellipsoidal shape. The virial method is already successfully used to calculate equilibrium shapes for selfgravitating rotating mass [42,41] and for rotating charged drops [40,88,89]. The similar results concerning the hysteresis phenomenon for the elongation of a droplet could be obtained both from virial and energy approach methods in 2D case. The critical value of a magnetic permeability for the hysteresis of the 2D droplet deformation in a static magnetic field is μ_{cr}=27. In some theoretical studies [68,97] it is reported about a conical tip formation for a ferrofluid droplet and the eventual breakup of it, if a magnetic permeability exceeds critical value μ=17.59 [68]. Nevertheless, such phenomena was never observed experimentally for a ferrofluid droplet even for the concentrated phase with μ=40 [11,12,14].

1.2.2. Sessile ferrofluid droplet in a static field

Equilibrium axisymmetric shapes of sessile drops of ferrofluid are studied in [19] experimentally. In [21] on the basis of the energy balance the elongation of the droplet is calculated as function of a magnetic Bond number under an assumption that the shape of a sessile droplet could be described as a half of an axisymmetric ellipsoid. In [96] the equilibrium state of partially and totally free ferrofluid droplet is studied by energy minimisation accounting for the gravity. It is found that the hysteresis phenomena take place if gravitational Bond number $Bg = \rho g(V)^{2/3}/\sigma$ is larger than critical value $Bg_{CR} \approx 8.5$, ρ being the density, g : gravity acceleration, V: volume of a drop, σ : surface tension. It means that for larger gravitational Bond number values there is some threshold value of magnetic Bond number Bm, beyond which drop elongates with jump. Decreasing a magnetic field, the jump back to the less elongated state takes place at smaller value of Bm. The influence of nonlinear magnetisation of the sessile drop is studied in [17,27,29]. The comparison with the linear magnetisation shows [27,29] that at low field values both results are very close, but increasing field above 140 gauss the difference increases and in particular case in [27] even at a magnetic field 160 gauss the difference in the drop height is about 1.6 times. It should be mentioned that agreement with experimental observations is within 2%, thus it is proved that the nonlinear behaviour of ferrofluids can significantly affect a drop shape at field strength as low as 140 gauss.

1.2.3. Free ferrofluid surface instability in vertical field

The ferrofluid surface instability in vertical field is one of the most studied problems of FHD. The first observation and predictions in the frame of the linear perturbation theory are given in [27]. By theoretical studies many phenomena were found out: subcritical character of hexagonal pattern structure [51,52,62], transition from hexagonal pattern to square one [52,62]. Most of predictions are proved experimentally [13,28]. In [13] the large hysteresis effect due to the high magnetic permeability $\mu \sim 40$ was observed. Interpretation of the hysteresis on the basis of a simple model is in reasonably good agreement with experimental data. Periodic pattern formation in normal field is observed in [19] for thin ferrofluid film. In [83]

for hexagonal ferrofluid bubble lattice at some field value abrupt increase of the magnetic field leads to the following: large initial ferrofluid bubbles droplets shrink and smaller bubbles appear, together forming inhomogeneous patterns.

1.2.4. Instabilities of ferrofluid in a narrow gap between two parallel plates

The thin gap between two parallel plates forms the quasi-two-dimensional domain. The fluid flow between plates could be described by Darcy equation. Presence of two fluid phases in the gap one of which is ferrofluid makes a system where many rather complicate phenomena are observed. In many cases instabilities lead to non-axisymmetric shapes. Presence of different instabilities in orthogonal with respect to a layer magnetic field:

- elliptic deformation instability for ferrofluid drops and bubbles in ferrofluid [36,38];
- bending instability [36,38];
- comblike instability in a vertical gap [37];

leads to the labyrinthine instability [38,92]. Instability of the vertex splitting has been numerically studied in [34]. The character of these instabilities depends on the magnetic field magnitude and on the conditions, how a field is applied. Dependence of the wave number of growing perturbations on ramp rate has been considered in [58]. Here also equivalence of approaches based on fictitious magnetic charges and current loops around magnetised body has been shown.

Instabilities of the flat layer are quite well studied by numerical simulation. The magnetic field problem is mostly treated accounting for demagnetising field in the first nonvanishing approximation (constant magnetisation approximation approach). Along the same lines the behaviour of the droplet in the field along the boundaries of the layer has been considered in [20,49]. Fluid flow is approximated by a Hele-Shaw flow and treated by the boundary integral technique for a flow potential [39]. In [67] the surface evolution is traced by the dissipative motion of closed 2D curves, conserving area. The formalism is derived from a general energy functional. The conformal mapping method for the simulation of the labyrinthine instabilities of

magnetic fluids has been considered in [58]. Computational limitations in most of cases restrict the studies to the simple patterns of labyrinth structure.

1.2.5. Instabilities of ferrofluid droplet in rotating field

For the first time the response of magnetic fluid microdrops to time dependent magnetic fields is tested in [10,4]. The concentrated phase of ferrofluid with relatively high magnetic permeability $\mu \approx 25$ is used. The first stage of shape deformation is an oblate ellipsoid, the plane of symmetry is one of field rotation. Increasing a magnetic field, oblate ellipsoid becomes unstable, leading to rather complicate shapes. In a high frequency rotating field a "starfish shape" for a droplets is observed. The droplet slowly rotates in the direction of a field, number of arms is proportional to the square of applied field strength. For lower field frequencies shapes could be more irregular, including loop-like and worm-like ones. Generally droplet tries to follow a field rotation, but additional bending effects take place due to friction forces acting from an external fluid. The ratio of the droplet viscosity versus the external fluid viscosity is about 100.

Similar results are observed in crossed field: $H_X = H_0 / \sqrt{2}$, $H_Y = H_0 \sin \omega t$ (static field crossed with linearly oscillating one) [10]. As in the case of a rotating field, the ultimate shape is a disk crowned with peaks. Difference is that there is no co-rotation of a "cog-wheel". Number of lateral peaks is still proportional to the square of the field.

By virial method [10,4,35] the symmetry destroying perturbation analysis is performed for oblate ellipsoid. The number of lateral peaks is explained by the most unstable perturbation mode, that is found by dispersion equation for surface waves of flat magnetic fluid surface and by lateral instability of a infinite ferrofluid cylinder.

Still unexplained is the behaviour of the microdroplet at finite surface perturbations, including slowly rotating distorted worms and reptating snakes, which behaviour strongly depends on frequency of the magnetic field.

1.3. Choice of the characteristical units

In order to obtain non-dimensional form for all equations, used to perform numerical calculations, some set of characteristical units should be chosen. As characteristic values are chosen: external field strength H_0, surface tension σ, external fluid viscosity η_{ex} and unperturbed droplet (i.e. circle) radius R. Thus all the processes are ruled by some non-dimensional numbers, characterising the balance between these forces. The acting forces in the present work are magnetic forces, surface tension and viscous stresses. Since surface tension is always present, it is chosen as reference force. The magnetic forces are characterised by the ratio between the magnetic forces and surface tension ones, called the **magnetic Bond number** is defined as $\mathrm{Bm} = H_0^2 R/\sigma$. It is sometimes convenient to incorporate in Bm some multiplier, containing magnetic permeability μ mostly because it better corresponds to the nature of magnetic forces. Here, in the present work it is avoided because usually it helps not completely to eliminate μ from all equations, governing the certain phenomenon. The other goal is that the same definition is kept for all the processes described in the present work.

In time dependent processes, the characteristic decay time for free surface perturbations $\tau=\eta_{ex}R/\sigma$ is introduced, in fact, this dimensional value characterises the ratio of viscous forces and surface tension ones. The viscosity of the surrounding fluid is chosen as the reference one, because the friction forces acting to the rotating droplet are governed mostly by it. The ratio of viscosities $\lambda=\eta_{in}/\eta_{ex}$ is used to characterise the system droplet-surrounding media.

These definitions lead to the following definitions of non-dimensional magnitudes:

- non-dimensional coordinates $x=x_{dim}/R$, $y=y_{dim}/R$,
- a non-dimensional velocity $v=v_{dim}\cdot\tau/R$,
- a non-dimensional magnetic field $H=H_{dim}/H_0$,
- a non-dimensional time $t=t_{dim}/\tau$,
- a non-dimensional angular frequency $\Omega=\Omega_{dim}\cdot\tau$,
- a non-dimensional surface force density $f_S=f_{S,dim}\cdot R/\sigma$.

1.4.Boundary integral equations

1.4.1. Stokes flow

In general case incompressible fluid motion is described by the momentum conservation law

$$\rho \frac{d v_i}{dt} = \sum_{j=1}^{3} \frac{\partial \sigma_{ij}}{\partial x_j} + F_i \ , \quad i = 1,2,3, \qquad (1.1)$$

and by the continuity equation

$$\mathrm{div}\, \mathbf{v} = 0. \qquad (1.2)$$

Here ρ denotes the density of the fluid, F_i are the components of the volume forces, acting in the fluid, and d/dt refers to the complete derivative, which is defined as $\partial/\partial t + \mathbf{v} \cdot \nabla$. The viscous stress tensor σ_{ij} has property of symmetry

$$\sigma_{ij} = \sigma_{ji} \ , \quad i = 1,2,3. \qquad (1.3)$$

The law for material properties of a media in the present case is **Stokes law** [54,55,66], which for a viscous fluid establishes a connection between stress tensor on the one hand and the pressure p and the rate-of-deformation tensor

$$\varepsilon_{ij} = \frac{1}{2}\left(\frac{\partial v_i}{\partial x_j} + \frac{\partial v_j}{\partial x_i} \right)$$

on the other. Stokes law is of the form

$$\sigma_{ij} = -p\delta_{ij} + \eta\left(\frac{\partial v_i}{\partial x_j} + \frac{\partial v_j}{\partial x_i} \right) \ , \quad i, j = 1,2,3, \qquad (1.4)$$

η being the coefficient of dynamic viscosity, connected with the coefficient of kinematic viscosity ν by relation $\eta = \rho\nu$. The substitution of (1.4) into the momentum conservation law (1.1) accounting for the continuity equation (1.2) gives the Navier-Stokes equation

$$\rho\left(\frac{\partial \mathbf{v}}{\partial t} + (\mathbf{v} \cdot \nabla)\mathbf{v} \right) = -\nabla p + \eta \Delta \mathbf{v} + \rho \mathbf{F} \qquad (1.5)$$

Dealing with slow viscous flows (so-called creeping flow [55], Reynolds number $\mathrm{Re} = vL\rho/\eta << 1$, L: the characteristic dimension of a flow, v: the characteristic velocity) Navier-Stokes equation could be linearized, that is, non-linear

term could be neglected since it is small compared with remaining terms. Other important simplification could be applied to Navier-Stokes equation when dealing with motions of a droplet of small size. In such a case inertial term $\rho\frac{\partial \mathbf{v}}{\partial t}$ could although be neglected. What results is the Stokes equations for creeping flow, describing the slow steady flow of a viscous fluid:

$$\begin{aligned} &-\nabla p + \eta\Delta\mathbf{v} + \rho\mathbf{F} = 0, \\ &\operatorname{div}\mathbf{v} = 0. \end{aligned} \qquad (1.6)$$

What have to be understood by the term "steady flow" in the dynamics of creeping flow for moving boundaries? Small shift of boundary causes velocity field in all the domain, but in the same instant this flow is slowed down due to the relatively large viscosity as a shift velocity is small. If volume forces are present, they are compensated by pressure and viscous stresses, influence of inertial terms is negligible as viscosity stresses dominate over inertia effects. The action of potential volume forces appears as additional pressure on surface. Every instant viscous flow stresses are compensated only by a pressure and volume forces. The known velocities of the fluid at boundaries of domains completely determine the flow inside the domains at given volume forces. Thus inside one fixed domain the problem of time dependent creeping flow at fixed time instant is equivalent to the steady flow inside the domain with given volume forces and given velocities at the boundary of this domain.

Since all the flow is driven by surface forces, the boundary integral equation technique turns out to be very powerful tool to solve the creeping flow problems with free moving boundaries.

1.4.2. Boundary conditions for a velocity field

The boundary conditions usually are split in kinematic ones and dynamic ones. The kinematic boundary conditions describes the velocity behaviour at the boundary, usually it is the continuity of a velocity field [66]:

$$\mathbf{v}^{in}\big|_{\Gamma} = \mathbf{v}^{ex}\big|_{\Gamma}. \qquad (1.7)$$

In particular cases velocity could have prescribed values at the boundary.

The dynamic boundary condition expresses the influence of surface forces $\Delta\mathbf{f}$ to the motion of the fluid [66]:

$$\tilde{\sigma}_{ij}^{ex} n_j\big|_{\Gamma} - \tilde{\sigma}_{ij}^{in} n_j\big|_{\Gamma} = \Delta f_i . \qquad (1.8)$$

Here stress tensor $\tilde{\sigma}_{ij} = -\delta_{ij} p^{\mathrm{mod}} + \sigma_{ij}$ consists from the pressure term and from viscous stresses. In general the discontinuity in the surface force $\Delta\mathbf{f}$ is dependent upon physical properties of fluids as well as upon the structure and thermodynamic properties of the interface. These thermodynamic properties could involve a number of physical constants [54,85], including the densities of the fluids, surface tension, surface elasticity, surface viscosity etc. An interface is called active one if $\Delta\mathbf{f} \neq 0$. In the present work the flow of fluids is caused by the surface tension and the magnetic forces acting to the interface between magnetic liquid droplet and the surrounding non-magnetic fluid. Thus the boundary condition (1.8) in absence of tangential surface forces could be written separately for tangent component of viscous stresses:

$$\sigma_{lm}^{in}\big|_{\Gamma} - \sigma_{lm}^{ex}\big|_{\Gamma} = 0 . \qquad (1.9)$$

and for normal ones:

$$-p^{in} + \sigma_{nn}^{in} = -p^{ex} + \sigma_{nn}^{ex} + 2\pi(\mathbf{Mn})^2 - \sigma/R_C . \qquad (1.10)$$

Here R_C stays for local curvature radius, which in 2D could be expressed in terms of a normal vector in the following way: $\sigma/R_C = \sigma\,\mathrm{div}\,\mathbf{n}$ [48].

1.4.3. Boundary integral formulation for a creeping flow

Stokes flow, governed by equations (1.6) has the following properties:

1. The reversibility of Stokes flow: reversing signs for velocity v and pressure p, reversed flow is mathematically acceptable and physically viable solution [55, 85]. It should be noted that the direction of the force and torque acting on any surface are also reversed.
2. Uniqueness of solution.
3. Stokes flow accumulates no kinetic energy since the fluid possesses no momentum and hence, no inertial mass.

4. Rate of viscous dissipation in Stokes flow is lower than that is in any other incompressible flow that has same boundary values of the velocity [55]

Beside that the "Stokes paradox" [55] should be avoided for 2D external flows. The essence of the Stokes paradox [64] is that a velocity solution of the homogeneous system (1.6) which is equal to 0 on boundary S and to given $\mathbf{v}^{\infty}$ at infinity generally does not exist. Thus, for 2D streaming motion perpendicular to the axis of a circular cylinder there exist no solution of the creeping motion equations vanishing on the cylinder that tends to infinity.

In order to write the boundary integral equations for some vector field, the corresponding fundamental solutions should be found at first. The fundamental solutions of a creeping flow were introduced in fact independently by Odqvist [79] and Lichtenstein [69]. They have constructed the corresponding hydrodynamical potentials and investigated their properties, and used them to solve the problems of a creeping flow. The general overviews of the fundamental solution of a creeping flow could be found in [64,85].

In the present work the boundary integral equations are used to describe the motion of the 2D magnetic fluid droplet under the action of the external magnetic field. The boundary integral equation formulation of a Stokes flow is based on 2D free space Green's functions. In 2D the free space Green's functions of the Stokes flow represents solutions of continuity equation $\nabla \mathbf{v} = 0$ and the singularity forced equation of Stokes flow [64,85]

$$-\nabla p + \eta \nabla^2 \mathbf{v} + \mathbf{g}\delta(\mathbf{r} - \mathbf{r}_0) = 0 \qquad (1.11)$$

where $\mathbf{g}$ is an arbitrary constant vector, $\mathbf{r}_0$ is an arbitrary point, and δ is the 2D delta-function, ∇^2 is 2D Laplacian operator. Introducing the free space Green's function $\mathbf{G}$ we wrote the solution for the velocity in the form

$$\mathrm{v}_i(\mathbf{r}) = \frac{1}{4\pi\eta} G_{ij}(\mathbf{r}, \mathbf{r}_0) g_j . \qquad (1.12)$$

Physically, formula (1.8) expresses the 2D flow due to a 2D point force $\mathbf{g}\delta(\mathbf{r} - \mathbf{r}_0)$. Let us introduce the fundamental solutions for the vorticity, pressure, and stress fields:

$$\omega_i(\mathbf{r}) = \frac{1}{4\pi\eta} \Omega_{ij}(\mathbf{r}, \mathbf{r}_0) g_j , \qquad (1.13)$$

$$p(\mathbf{r}) = \frac{1}{4\pi} P_j(\mathbf{r}, \mathbf{r}_0) g_j, \qquad (1.14)$$

$$\sigma_{ik}(\mathbf{r}) = \frac{1}{4\pi} T_{ijk}(\mathbf{r}, \mathbf{r}_0) g_j. \qquad (1.15)$$

Stress tensor T is defined by Stokes law [54,66]

$$T_{ijk}(\mathbf{r}, \mathbf{r}_0) = -\delta_{ik} p_j(\mathbf{r}, \mathbf{r}_0) + \frac{\partial G_{ij}(\mathbf{r}, \mathbf{r}_0)}{\partial x_k} + \frac{\partial G_{kj}(\mathbf{r}, \mathbf{r}_0)}{\partial x_i}. \qquad (1.16)$$

Pressure vector P and stress tensor T associated with a free space Green's function for infinite unbounded or bounded flow, constitute two fundamental solutions of Stokes flow.

The free-space Green's function for velocity or 2D Stokeslet [54,85] is

$$G_{ij} = -\delta_{ij} \ln r + \frac{\hat{x}_i \hat{x}_j}{r^2}, \quad r = |\hat{\mathbf{x}}|, \ \hat{\mathbf{x}} = \mathbf{r} - \mathbf{r}_0. \qquad (1.17)$$

The associated vorticity, pressure and stress fields are given by (1.13), (1.14), and (1.15) with

$$\Omega_{ij} = 2\varepsilon_{ijk} \frac{\hat{x}_k}{r^2}, \qquad (1.18)$$

$$P_i = 2\frac{\hat{x}_i}{r^2}, \qquad (1.19)$$

$$T_{ijk} = -4\frac{\hat{x}_i \hat{x}_j \hat{x}_k}{r^4}. \qquad (1.20)$$

For convenience potential volume forces could be incorporated into a modified pressure. For example, the magnetic volume force $\frac{1}{2}\nabla(\mathbf{MH})$, incorporated in a modified pressure under assumption of a constant magnetic permeability gives

$$p^{\text{mod}} = p - \frac{\mu - 1}{8\pi} \nabla(\mathrm{H}^2 \ . \qquad (1.21)$$

Thus the body-force-free Stokes equation written in terms of p^{mod} is to be considered:

$$-\nabla p^{\text{mod}} + \eta \nabla^2 \mathbf{v} = 0.$$

The use of (1.21) changes the boundary condition (1.10) to the following form [25]:

$$-p^{\text{mod},in} + \sigma_{nn}^{in} = -p^{\text{mod},ex} + \sigma_{nn}^{ex} + 2\pi(\mathbf{Mn})^2 + (\mathbf{MH})/2 - \sigma \operatorname{div} \mathbf{n}. \qquad (1.22)$$

Further in the text the superscript "mod" for a pressure is dropped, additional pressure due to a magnetic field appears in boundary conditions.

To describe such a motion, singularities (singular forces) of Green's functions should be placed on boundaries. So the motion inside the droplet at the point $\mathbf{r}_0$ is described by the boundary integral equation, which accounts for forces $\mathbf{f}^{in}$ acting to the droplet from the interface of it:

$$v_j^{in}(\mathbf{r}_0) = \frac{1}{4\pi\eta^{in}} \oint_L f_i^{in}(\mathbf{r}) G_{ij}(\mathbf{r},\mathbf{r}_0)\, dl(\mathbf{r}) - \frac{1}{4\pi} \oint_L v_i(\mathbf{r}) T_{ijk}(\mathbf{r},\mathbf{r}_0) n_k(\mathbf{r})\, dl(\mathbf{r}). \qquad (1.23)$$

Here $v_i(\mathbf{r})$ stays for the i-th velocity component on the boundary, η^{in}: the viscosity of the droplet. Due to the continuity of velocities on the boundary this value is the same from inside and outside of the droplet. It is convenient to derive another boundary integral equation from the Lorentz reciprocal identity [55,70], what arrives [85] at

$$\oint_L f_i^{ex}(\mathbf{r}) G_{ij}(\mathbf{r},\mathbf{r}_0)\, dl(\mathbf{r}) - \eta^{ex} \oint_L v_i(\mathbf{r}) T_{ijk}(\mathbf{r},\mathbf{r}_0) n_k(\mathbf{r})\, dl(\mathbf{r}) = 0. \qquad (1.24)$$

Here $\lambda=\eta^{in}/\eta^{ex}$, η^{ex}: the viscosity of a fluid outside the droplet, $\mathbf{f}^{ex}$ are the forces acting to the fluid outside the droplet from the interface of it. Now by combining (1.23) and (1.24) the boundary integral equation in terms of the surface force $\Delta\mathbf{f} = \mathbf{f}^{ex} - \mathbf{f}^{in}$ could be written:

$$\begin{aligned} v_j^{in}(\mathbf{r}_0) = &-\frac{1}{4\pi\eta^{in}} \oint_L \Delta f_i(\mathbf{r}) G_{ij}(\mathbf{r},\mathbf{r}_0)\, dl(\mathbf{r}) + \\ &\frac{1-\lambda}{4\pi\lambda} \oint_L v_i(\mathbf{r}) T_{ijk}(\mathbf{r},\mathbf{r}_0) n_k(\mathbf{r})\, dl(\mathbf{r}) \end{aligned} \qquad (1.25)$$

According to the (1.8) and (1.22) the surface force discontinuity for a linearly magnetizable ferrofluid droplet is

$$\Delta\mathbf{f} = \sigma \operatorname{div} \mathbf{n} - \frac{\mu-1}{8\pi}\left[(\mu-1)(\mathbf{Hn})^2 + \mathbf{H}^2\right]. \qquad (1.26)$$

In order to obtain the boundary integral equation for velocity on the boundary, the **principal value** (*PV*) of the second right hand side integral in (1.25) is derived as follows: if L is a Lyapunov line, i.e. it has a continuously varying normal vector, and the velocity **v** varies over L in a continuous manner,

$$\begin{aligned} &\lim_{\mathbf{r}_0 \to L} \overset{PV}{\oint_L} v_i(\mathbf{r}) T_{ijk}(\mathbf{r},\mathbf{r}_0) n_k(\mathbf{r})\, dl(\mathbf{r}) = \\ &\mp 2\pi\, v_j(\mathbf{r}) + \overset{PV}{\oint_L} v_i(\mathbf{r}) T_{ijk}(\mathbf{r},\mathbf{r}_L) n_k(\mathbf{r})\, dl(\mathbf{r}) \end{aligned} \qquad (1.27)$$

where minus sign applies when the point $\mathbf{r}_0$ approaches L from the internal side, and the plus sign otherwise. The normal vector is pointed outside from the droplet (see Fig.1.1). The point $\mathbf{r}_L$ lays on the boundary contour L and corresponds to the limit position of the point $\mathbf{r}_0$ when it tends to L. The superscript *PV* for a boundary integral here and further indicates the principal value of the double-layer potential, defined as the value of the improper double-layer integral corresponding to the case where the point $\mathbf{r}_0$ is located on L. Clearly, the double-layer potential undergoes a discontinuity $4\pi\mathbf{v}$ across L.

Thus use of (1.27) in (1.25) gives the necessary boundary integral equation to calculate the velocity $\mathbf{v}(\mathbf{r})$ on the boundary:

$$\mathrm{v}_j(\mathbf{r}_L) = -\frac{1}{2\pi\eta^{ex}(1+\lambda)}\int_L \Delta f_i(\mathbf{r})G_{ij}(\mathbf{r},\mathbf{r}_0)dl(\mathbf{r}) + \frac{1-\lambda}{2\pi(1+\lambda)}\oint_L^{PV} \mathrm{v}_i(\mathbf{r})T_{ijk}(\mathbf{r},\mathbf{r}_L)n_k(\mathbf{x})dl(\mathbf{r}) \qquad (1.28)$$

In (1.28) the only unknown is velocity values along the boundary (surface of a 2D droplet). It will be noted that when the viscosities of the two fluids are equal, i.e. λ=1, the coefficients of the double-layer integral on the right-hand side of (1.28) vanish, and the flow is expressed merely in terms of a single-layer potential with known density $\Delta\mathbf{f}$. Two other particular cases, namely λ=0 and λ=∞, requires special treatment, called the regularization of the double-layer potential. This treatment is discussed in details in [64,85], in the present work these cases are not to meet.

The analogue of the equation (1.25) for the velocities outside the droplet is

$$\mathrm{v}_j^{ex}(\mathbf{r}_0) = -\frac{1}{4\pi\eta^{ex}}\oint_L \Delta f_i(\mathbf{r})G_{ij}(\mathbf{r},\mathbf{r}_0)dl(\mathbf{r}) + \frac{1-\lambda}{4\pi}\oint_L \mathrm{v}_i(\mathbf{r})T_{ijk}(\mathbf{r},\mathbf{r}_0)n_k(\mathbf{r})dl(\mathbf{r}) \qquad (1.29)$$

The limit $\mathbf{r}_0 \to$ L arrives at the same equation (1.28).

So the equation (1.28) is used to obtain the velocity distribution along the droplet's boundary, once it is calculated, (1.25) and (1.29) could be used to obtain the velocity distribution in every point of internal and external domains.

1.4.4. Partial differential equations for a magnetic field

The equations for a magnetic field follow from the Maxwell's equations. A magnetic field satisfies the magnetic flux continuity equation

$$div\mathbf{B} = 0 \qquad (1.30)$$

and the second equation in the case when electric and displacement currents are absent is

$$rot\mathbf{H} = 0 \qquad (1.31)$$

Total magnetic field $\mathbf{H}$ is formed by given external magnetic field $\mathbf{H}_0$ which causes secondary field $\mathbf{H}_M$ due to magnetisation of magnetic fluid domain: $\mathbf{H} = \mathbf{H}_0 + \mathbf{H}_M$.

Throughout the present work a linear magnetisation of magnetic fluid is assumed:

$$\mathbf{M} = \chi\mathbf{H} \qquad (1.32)$$

where magnetic susceptibility χ and therefore magnetic permeability $\mu = 4\pi\chi + 1$ are constant. Thus from relation $\mathbf{B} = \mu\mathbf{H}$ it follows that in domains of a continuously constant magnetic permeability μ magnetic field intensity $\mathbf{H}$ satisfies equation

$$div\mathbf{H} = 0, \qquad (1.33)$$

what leads to Laplace equation for magnetostatic potential:

$$\Delta\Psi = 0 \qquad (1.34)$$

Thus magnetic field intensity has both solenoidal (1.33) and potential (1.31) character because it is created "from outside" by an external field, magnetisation of local ferrofluid domains is taken into account by appropriate boundary conditions. It is convenient according to Fig.1.1 denote a magnetostatic potential inside the droplet by ψ_1, but a potential outside the droplet denoted by ψ'_2 is split in a potential $\mathbf{H}_0\mathbf{r}$ of an external field and a potential ψ_2 due to a magnetisation of the droplet:

$$\psi'_2 = \mathbf{H}_0\mathbf{r} + \psi_2 \qquad (1.35)$$

1.4.5. Boundary conditions for a magnetic field

The boundary between a magnetic fluid (subscript "1") and a surrounding non-magnetic media (subscript "2") has not special magnetic surface properties, hence the boundary conditions are conventional, straight-forward following from (1.30), (1.31):

$$B_{n1} = B_{n2} \quad \text{or} \quad \mu H_{n1} = H_{n2} \qquad (1.36a)$$

$$H_{\tau 1} = H_{\tau 2}. \qquad (1.36b)$$

Boundary conditions for potentials on droplet surface are

$$\psi_1 = \mathbf{H}_0\mathbf{r} + \psi_2, \qquad (1.36c)$$

$$\mu \frac{\partial \psi_1}{\partial n} = \frac{\partial}{\partial n}(\mathbf{H}_0\mathbf{r} + \psi_2). \qquad (1.36d)$$

1.4.6. Derivation of boundary integral equations

Direct formulation of boundary integral equations

Since surface force formula for a viscous flow (1.22) requires to know tangential and normal components of a magnetic field, it is convenient to write boundary integral equations for H_n, H_t on the surface inside the ferrofluid droplet. The full derivation of equations is given in [33].

hird Green's identity in 2D [61]

$$\varphi(\mathbf{r}_L) = \frac{1}{\pi} \oint_L^{PV} \left[\ln \frac{1}{R(\mathbf{r}_L, \mathbf{r})} \frac{\partial \varphi(\mathbf{r})}{\partial n} - \varphi(\mathbf{r}) \frac{\partial}{\partial n} \left(\ln \frac{1}{R(\mathbf{r}_L, \mathbf{r})} \right) \right] dl - \frac{1}{\pi} \int_{S_L} \Delta\varphi(\mathbf{r}) \ln \frac{1}{R(\mathbf{r}_L, \mathbf{r})} dS \qquad (1.37)$$

$$R(\mathbf{r}_L, \mathbf{r}) = |\mathbf{r}_L - \mathbf{r}|$$

is a base on which expressions for the potentials ψ_1, ψ_2, $\mathbf{H}_0\mathbf{r}$ are obtained, taking into account direction of a normal and identity (1.34):

$$\psi_1(\mathbf{r}_L) = \frac{1}{\pi} \oint_L^{PV} \left[\ln \frac{1}{R(\mathbf{r}_L, \mathbf{r})} \frac{\partial \psi_1(\mathbf{r})}{\partial n} - \psi_1(\mathbf{r}) \frac{\partial}{\partial n} \left(\ln \frac{1}{R(\mathbf{r}_L, \mathbf{r})} \right) \right] dl, \qquad (1.38)$$

$$\psi_2(\mathbf{r}_L) = -\frac{1}{\pi} \overset{PV}{\oint_L} \left[\ln \frac{1}{R(\mathbf{r}_L, \mathbf{r})} \frac{\partial \psi_2(\mathbf{r})}{\partial n} - \psi_2(\mathbf{r}) \frac{\partial}{\partial n} \left(\ln \frac{1}{R(\mathbf{r}_L, \mathbf{r})} \right) \right] dl, \qquad (1.39)$$

$$(\mathbf{H}_0 \mathbf{r}_L) = \frac{1}{\pi} \overset{PV}{\oint_L} \left[\ln \frac{1}{R(\mathbf{r}_L, \mathbf{r})} \frac{\partial (\mathbf{H}_0 \mathbf{r})}{\partial n} - (\mathbf{H}_0 \mathbf{r}_L) \frac{\partial}{\partial n} \left(\ln \frac{1}{R(\mathbf{r}_L, \mathbf{r})} \right) \right] dl. \qquad (1.40)$$

Subscript "$_L$" is used to denote "observation point" on boundary contour L, for which equations are written, **r** without any subscript usually denotes integration coordinate. An application of the boundary conditions for magnetostatic potentials (1.36c), (1.36d) to the following combination of equations (1.38), (1.40):

$$\mu\psi_1(\mathbf{r}_L) + \psi_2(\mathbf{r}_L) - (\mathbf{H}_0 \mathbf{r}_L) =$$
$$\frac{1}{\pi} \overset{PV}{\oint_L} \ln \frac{1}{R(\mathbf{r}_L, \mathbf{r})} \left[\mu \frac{\partial \psi_1(\mathbf{r})}{\partial n} - \frac{\partial \psi_2(\mathbf{r}_L)}{\partial n} - \frac{\partial (\mathbf{H}_0 \mathbf{r}_L)}{\partial n} \right] dl -$$
$$\frac{1}{\pi} \overset{PV}{\oint_L} \left[\mu\psi_1(\mathbf{r}) - \psi_2(\mathbf{r}) - (\mathbf{H}_0 \mathbf{r}_L) \right] \frac{\partial}{\partial n} \left(\ln \frac{1}{R(\mathbf{r}_L, \mathbf{r})} \right) dl$$

allows to obtain after simplifications the boundary integral equation in terms of only one potential ψ_1:

$$\psi_1(\mathbf{r}_L) = \frac{2}{\mu + 1} (\mathbf{H}_0 \mathbf{r}_L) - \frac{1}{\pi} \frac{\mu - 1}{\mu + 1} \overset{PV}{\oint_L} \psi_1(\mathbf{r}) \frac{\partial}{\partial n} \left(\ln \frac{1}{R(\mathbf{r}_L, \mathbf{r})} \right) dl. \qquad (1.41)$$

Derivative along the boundary contour $\partial / \partial l_L$ gives a boundary integral equation for tangential field component H_t:

$$H_t(\mathbf{r}_L) = \frac{2}{\mu + 1} (\mathbf{H}_0 \mathbf{t}) + \frac{1}{\pi} \frac{\mu - 1}{\mu + 1} \overset{PV}{\oint_L} H_t(\mathbf{r}) \frac{\partial}{\partial n_L} \left(\ln \frac{1}{R(\mathbf{r}_L, \mathbf{r})} \right) dl. \qquad (1.42)$$

Here identity

$$\frac{\partial}{\partial l_L} \left[\frac{\partial}{\partial n} \left(\ln \frac{1}{R(\mathbf{r}_L, \mathbf{r})} \right) \right] = \frac{\partial}{\partial l} \left[\frac{\partial}{\partial n_L} \left(\ln \frac{1}{R(\mathbf{r}_L, \mathbf{r})} \right) \right]$$

and integration by parts are used. l_L denotes the observation point $\mathbf{r}_L$ coordinates, l : integration point **r, t** is a tangent unit vector.

The boundary integral equation for normal component [33]

$$H_n(\mathbf{r}_L) = \frac{2}{\mu + 1} (\mathbf{H}_0 \mathbf{n}) - \frac{1}{\pi} \frac{\mu - 1}{\mu + 1} \overset{PV}{\oint_L} H_n(\mathbf{r}) \frac{\partial}{\partial n_L} \left(\ln \frac{1}{R(\mathbf{r}_L, \mathbf{r})} \right) dl \qquad (1.43)$$

is derived in analogous way.

Indirect formulation of boundary integral equations

There are two indirect boundary integral equation formulations which use two different physical analogies: surface charge distribution and equivalent surface currents.

Surface charges

In this case imaginary magnetic surface charges are distributed by density $\kappa(\mathbf{r}_L)$ over boundary in such a way that the external field together with the field of charges satisfies the boundary conditions (1.36). Contour element dl(**r**) in 2D plane point $\mathbf{r}_0$ creates the field

$$d\mathbf{H}(\mathbf{r}_0) = \kappa(\mathbf{r})dl(\mathbf{r})\frac{\mathbf{r}_0 - \mathbf{r}}{|\mathbf{r}_0 - \mathbf{r}|^2}.$$

Hence total field for all points $\mathbf{r}_0$ which belong no to the boundary contour L is

$$\mathbf{H}(\mathbf{r}_0) = \mathbf{H}_0 + \int_L^{PV} \frac{\mathbf{r}_0 - \mathbf{r}}{|\mathbf{r}_0 - \mathbf{r}|^2}\kappa(\mathbf{r})dl(\mathbf{r}). \qquad (1.44)$$

Applying boundary conditions in the cases when $\mathbf{r}_0$ tends from inside and outside to the boundary point $\mathbf{r}_L$ the following boundary integral equation for surface charge density $\kappa(\mathbf{r}_L)$ is obtained:

$$\pi\frac{\mu+1}{\mu-1}\kappa(\mathbf{r}_L) = (\mathbf{H}_0\mathbf{n}(\mathbf{r}_L)) + \int_L^{PV} \kappa(\mathbf{r})\frac{\mathbf{n}(\mathbf{r}_L)(\mathbf{r}_L - \mathbf{r})}{|\mathbf{r}_L - \mathbf{r}|^2}dl. \qquad (1.45)$$

Corresponding equations for magnetic field normal and tangent components are

$$H_n(\mathbf{r}_L) = \frac{2\pi}{\mu-1}\kappa(\mathbf{r}_L), \qquad (1.46)$$

$$H_t(\mathbf{r}_L) = \mathbf{H}_0\mathbf{t}(\mathbf{r}_L) + \int_L^{PV} \kappa(\mathbf{r})\frac{\mathbf{t}(\mathbf{r}_L)(\mathbf{r}_L - \mathbf{r})}{|\mathbf{r}_L - \mathbf{r}|^2}dl. \qquad (1.47)$$

The equation (1.45) turns out to be equivalent to (1.43), so H_t could be calculated from known values of H_n

Equivalent currents

According to Biot and Savart's law in 2D [65], magnetic induction, created in point $\mathbf{r}_0$ by surface currents with density $\mathbf{j}(\mathbf{r})$ is

$$\mathbf{B}(\mathbf{r}_0) = \mathbf{B}_0 + \frac{2}{c}\oint_L \frac{\mathbf{j}(\mathbf{r}) \times (\mathbf{r}_0 - \mathbf{r})}{|\mathbf{r}_0 - \mathbf{r}|^2} dl(\mathbf{r}) \qquad (1.48)$$

Since $\mathbf{j}(\mathbf{r})$ has only z-component, it could be substituted by a modified scalar density $\nu(\mathbf{r})$ in such a way that $\mathbf{j}(\mathbf{r}) = \frac{c}{2}\nu(\mathbf{r})\mathbf{e}_z$. The corresponding boundary integral equation, which includes boundary conditions (1.36), is

$$\pi\frac{\mu+1}{\mu-1}\nu(\mathbf{r}_L) = -(\mathbf{H}_0\mathbf{t}(\mathbf{r}_L)) - \overset{PV}{\oint_L} \nu(\mathbf{r})\frac{\mathbf{n}(\mathbf{r}_L)(\mathbf{r}_L - \mathbf{r})}{|\mathbf{r}_L - \mathbf{r}|^2} dl. \qquad (1.49)$$

Equations for magnetic field are

$$H_n(\mathbf{r}_L) = \frac{1}{\mu}\left((\mathbf{H}_0\mathbf{n}(\mathbf{r}_L)) - \overset{PV}{\oint_L} \nu(\mathbf{r})\frac{\mathbf{t}(\mathbf{r}_L)(\mathbf{r}_L - \mathbf{r})}{|\mathbf{r}_L - \mathbf{r}|^2} dl\right), \qquad (1.50)$$

$$H_t(\mathbf{r}_L) = \frac{1}{\mu}\left((\mathbf{H}_0\mathbf{t}(\mathbf{r}_L)) + \overset{PV}{\oint_L} \nu(\mathbf{r})\frac{\mathbf{n}(\mathbf{r}_L)(\mathbf{r}_L - \mathbf{r})}{|\mathbf{r}_L - \mathbf{r}|^2} dl - \pi\nu(\mathbf{r}_L)\right). \qquad (1.51)$$

Application of (1.49) to eliminate integral term in (1.51) gives

$$H_t(\mathbf{r}_L) = -\frac{2\pi\nu(\mathbf{r}_L)}{\mu-1}. \qquad (1.52)$$

One can see, that (1.49) and (1.52) together gives (1.42).

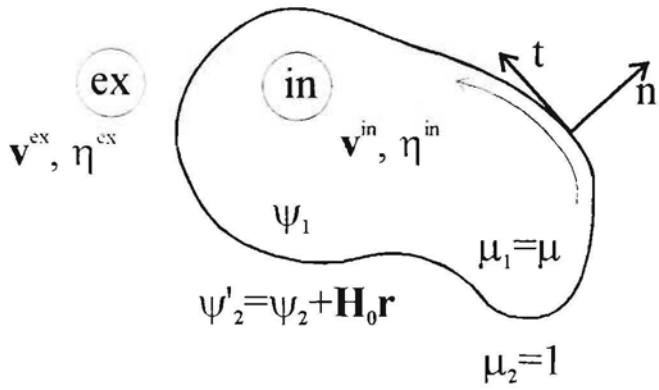

Figure 1.1. The sketch of the magnetic fluid droplet

Conclusions

The boundary integral equation technique allows to formulate the free moving boundary problem for a ferrofluid droplet in an external magnetic field in terms of surface values for both velocity and magnetic field. To solve obtained boundary integral equations, some approximation technique should be used, as well as the boundary contour itself should be described in a some approximation. The approximation technique and approximation errors are the subject of the next Chapter of the present work.

The essence of the direct magnetic field problem formulation, presented here, is to obtain both magnetic field components on the interface of a droplet by solving two corresponding boundary integral equations. Two kinds of the indirect formulation are derived here using either magnetic charges or equivalent currents on surface of the droplet. These two indirect formulations are mathematically completely equivalent to the direct formulation, but the numerical approximation of them, discussed in the next chapter, could give different levels of approximation errors. It is found that the normal field component is proportional up to constant factor to a surface charge density but the tangent component to a surface current density.

The principal difference of the indirect magnetic field problem formulation from the direct one is that the indirect formulation allows to obtain by a simple integration the one of two field components when another one is already found.

Chapter 2

Approximation of boundary integral equations

2.1. Interpolation of a planar boundary

The two-dimensional boundary may be represented by a planar line. To set up a boundary element representation, the planar line are traced by a set of marker points $\mathbf{r}_i$, i=1,...,N, numbered in the counter-clock wise direction according to Fig.2.1. In the numerical algorithm, a contour consists of its marker points and the interpolation functions between nodes. Cubic-spline interpolation is chosen to provide a smooth boundary with continuous first- and second-order derivatives [44]. At every time instant spline approximation is calculated in two steps [45]:

1. Calculation of boundary curve representation by two parametric cubic-spline functions: $x=f_x(p)$, $y=f_y(p)$. Initially the "perimeter" length p_i for N-sided polygon with marker points as vertexes are taken as the values of the parameter p at marker points, starting with vertex i=1 ($p_1=0$). Then cubic spline coefficients are calculated for a closed contour, accounting for the periodicity constrain. According to [71], a cubic-spline interpolation provides the unique curve, the shape of which is independent from the choice of p_i.

2. Calculation of natural curve parameter: the arc length for a curve is calculated using the integral $s(p) = \int_{p_1}^{p} \sqrt{x'^2(t) + y'^2(t)}dt$. Since the cubic-spline interpolation is unique, the natural parameter values $s_i=s(p_i)$ at corresponding i-th marker points are unique, too. After the integration the new cubic-spline functions $x=f_x(s)$, $y=f_y(s)$ in dependence on the natural parameter *s* are recalculated.

2.2. General remarks about discretization of boundary integral equations

Once the contour of integration is traced by marker points and cubic-spline interpolation, the approximation of the unknown boundary velocities and magnetic field components on the boundary inside the droplet could be performed. In the every element of the contour the local basis functions for unknowns is introduced and globally unknown values are described by global basis functions which are built from the local basis functions multiplied by coefficients and added together. The next step is the approximation of boundary integral equations for given set of boundary elements. The realisation of this step in so called **B**oundary **E**lement **M**ethod, widely known as **BEM**. The accuracy and the numerical stability of obtained numerical scheme depends on the choice of the approximation technique. Two governing approximation techniques applied to compute the coefficients of the local expansions are either the **collocation** method, or the method of **weighted residuals** [30,93,85]. The last of two methods are more general and in fact includes the first one as particular case. The main idea of the collocation method is the requirement to satisfy the boundary integral equation in N selected points, leading to the set of N linear algebraic equations. In the method of weighted residuals the integral equation is multiplied sequentially by every of N weighting functions in order to obtain the set of N linear algebraic equations after an integration along the boundary contour. For the method of weighted residuals different choices of the weighting functions lead to different schemes with varying degrees of complexity. Identifying the weighting functions with the global basis functions we obtain **Galerkin's method**, while identification of the weighting functions with delta functions having poles at selected points over the boundary contour gives the collocation method. In [85] the Galerkin's method is recommended only for problems with notable geometrical simplicity due to "increased computational requirements". In fact, obtained set of algebraic equations is harder to derive but once it is derived, calculations by computer can have the same level of complexity. In engineering boundary element methods almost all the codes are based on collocation methods. It is known that the right choice of the collocation points is significant for the stability and convergence of the approximation [30].

Preparing computer code for magnetic field calculations it was found that the collocation method gives the less accuracy than the Galerkin's method at the same CPU time consummation. Hence in the present work the Galerkin's method is used to derive sets of linear algebraic equations for the both magnetic field and creeping flow equations, using pyramidal functions (see Fig.2.2) [33] defined as

$$\varphi_i(s)=\begin{cases}0 & s \le s_{i-1},\\ (s-s_{i-1})/(s_i-s_{i-1}), & s_{i-1} < s \le s_i,\\ (s_{i+1}-s)/(s_{i+1}-s_i), & s_i < s \le s_{i+1},\\ 0 & s_{i-1} < s.\end{cases} \qquad (2.1)$$

where s is the natural boundary contour parameter and s_i are its values at marker points on the contour. For convenience substitutions of indexes like $s_{N+j}=s_j$, j=0, ±1, ±2 … are used in general formulae.

2.3. Equations for a magnetic field

The derivation of the set of linear algebraic equations for the integral equation for the tangential magnetic field component (see the equation 1.42 in Chapter 1)

$$H_t(s)=\frac{2}{\mu+1}(\mathbf{H}_0\mathbf{t})-\frac{1}{\pi}\frac{\mu-1}{\mu+1}\oint_L^{PV} H_t(s')\frac{y_s(x-x')-x_s(y-y')}{\left((x-x')^2+(y-y')^2\right)}ds' \qquad (2.2)$$

consists from the following steps [33]:

1) unknown function $H_t(s)$ is expressed in terms of pyramidal basis functions $\varphi_i(s)$ using values $H_{t,i}$ of the magnetic field tangent component at marker points as expansion coefficients:

$$H_t(s)=\sum_{i=1}^{N} H_{t,i}\,\varphi_i(s) \qquad (2.3)$$

2) the values of the ratio

$$R(s,s')=\frac{y_s(x-x')-x_s(y-y')}{\left((x-x')^2+(y-y')^2\right)\sqrt{x_s^2+y_s^2}} \qquad (2.4)$$

at marker points are taken as

$$R_{ki}=R(s_k,s_i)=\begin{cases}\dfrac{y_s(k)(x(k)-x(i))-x_s(k)(y(k)-y(i))}{\left[(x(k)-x(i))^2+(y(k)-y(i))^2\right]\sqrt{x_s^2(k)+y_s^2(k)}}, & i\neq k;\\ \dfrac{1}{2}\dfrac{y_{ss}(i)x_s(i)-x_{ss}(i)y_s(i)}{\left(x_s^2(i)+y_s^2(i)\right)^{\frac{3}{2}}}, & i=k.\end{cases} \qquad (2.5)$$

3) the integral equation (2.2) is multiplied by a basis function $\varphi_k(s)$ and integrated along the boundary contour:

$$\oint_L \varphi_k(s)\sum_{i=1}^{N} H_{t,i}\,\varphi_i(s)ds=\frac{2}{\mu+1}\oint_L \varphi_k(s)(\mathrm{H}_{0X}\,x_s+\mathrm{H}_{0Y}\,y_s)ds-$$
$$\frac{1}{\pi}\frac{\mu-1}{\mu+1}\oint_L \varphi_k(s)\left[\int_L^{PV}\sum_{i=1}^{N} H_{t,i}\,\varphi_i(s')\,\frac{y_s(x-x')-x_s(y-y')}{\left((x-x')^2+(y-y')^2\right)}ds'\right]ds \qquad (2.6)$$

Here and further it is taken into account that $\sqrt{x_s^2+y_s^2}\equiv 1$ for the natural parameter s.

The integration of the left-hand side of the equation (2.6) gives

$$\oint_L \varphi_k(s) \sum_{i=1}^{N} H_{t,i}\, \varphi_i(s)\, ds = \sum_{i=1}^{N} H_{t,i} \oint_L \varphi_k(s) \varphi_i(s) ds = \sum_{i=1}^{N} H_{t,i} \left(\Delta s_{i-1}\, \delta_{i,k+1} + \Delta s_i\, \delta_{i,k-1} + 2(\Delta s_{i-1} + \Delta s_i)\delta_{i,k}\right)/6 \qquad (2.7)$$

Here

$$\Delta s_i = s_{i+1} - s_i .$$

Use of the approximation inside the interval $[s_i, s_{i+1}]$

$$\mathbf{r}_s \approx \frac{\mathbf{r}(i+1) - \mathbf{r}(i)}{\Delta s_i} \qquad (2.8)$$

for an integration of the first term in the right-hand side of the equation (2.6) results in

$$\oint_L \varphi_k(s) \left(H_{0X}\, x_s + H_{0Y}\, y_s\right) ds = H_{0X} \frac{x_{k+1} - x_{k-1}}{2} + H_{0Y} \frac{y_{k+1} - y_{k-1}}{2} . \qquad (2.9)$$

To evaluate the second term $\oint_L \varphi_k(s) \left[PV \int_L \sum_{i=1}^{N} H_{t,i}\, \varphi_i(s') R(s,s') ds' \right] ds$ in the right-hand side of the equation (2.6) the integral in square brackets is evaluated by trapezoidal rule:

$$\oint_L \varphi_i(s') R(s,s') ds' \approx R(s, s_i) \frac{\Delta s_{i-1} + \Delta s_i}{2} , \qquad (2.10)$$

and the outer integral also evaluated by trapezoidal rule gives:

$$\oint_L \varphi_k(s) \left[PV \int_L \sum_{i=1}^{N} H_{t,i}\, \varphi_i(s') R(s,s') ds' \right] ds \approx R_{ki} \frac{\Delta s_{i-1} + \Delta s_i}{2} \frac{\Delta s_{k-1} + \Delta s_k}{2} . \qquad (2.11)$$

Thus the discrete analogue of the equation (2.2) is

$$\sum_{i=1}^{N} A_{ki}^{+} H_{t,i} = \frac{(x_{k+1} - x_{k-1}) H_{0X} + (y_{k+1} - y_{k-1}) H_{0Y}}{\mu + 1} , \quad k = 1, \ldots, N , \qquad (2.12)$$

where

$$A_{ki}^{\pm} = \frac{1}{\pi} \frac{\mu - 1}{\mu + 1} R_{ki} \frac{\Delta s_{i-1} + \Delta s_i}{2} \frac{\Delta s_{k-1} + \Delta s_k}{2} \pm I_{ki} , \qquad (2.13)$$

$$I_{ki} = \left(\Delta s_{i-1}\, \delta_{i,k+1} + \Delta s_i\, \delta_{i,k-1} + 2(\Delta s_{i-1} + \Delta s_i)\delta_{i,k}\right)/6 . \qquad (2.14)$$

In similar way the discrete equation for the normal component of a magnetic field (1.43) is derived arriving at

$$\sum_{i=1}^{N} A_{ki}^{-} H_{n,i} = \frac{(x_{k+1} - x_{k-1}) H_{0Y} - (y_{k+1} - y_{k-1}) H_{0X}}{\mu + 1} , \quad k = 1, \ldots, N , \qquad (2.15)$$

The definition of A_{ki}^{-} is already given in (2.13).

Separation of the external field components

Due to the linearity of the field equations, the solution of them could be split in two parts: two fields created separately by H_{0X} and H_{0Y}, which are described by variables α_x, α_y, β_x, β_y:

$$H_{n,i} = \alpha_{X,i}\, H_{0X} + \alpha_{Y,i}\, H_{0Y}, \qquad (2.16)$$

$$H_{t,i} = \beta_{X,i}\, H_{0X} + \beta_{Y,i}\, H_{0Y}. \qquad (2.17)$$

The corresponding equations are easy to obtain from (2.12),(2.15):

$$\sum_{i=1}^{N} A_{ki}^{-}\alpha_{x,i} = -\frac{y_{k+1} - y_{k-1}}{\mu + 1}, \quad k = 1,\ldots,N, \qquad (2.18)$$

$$\sum_{i=1}^{N} A_{ki}^{-}\alpha_{y,i} = \frac{x_{k+1} - x_{k-1}}{\mu + 1}, \quad k = 1,\ldots,N, \qquad (2.19)$$

$$\sum_{i=1}^{N} A_{ki}^{+}\beta_{x,i} = \frac{x_{k+1} - x_{k-1}}{\mu + 1}, \quad k = 1,\ldots,N, \qquad (2.20)$$

$$\sum_{i=1}^{N} A_{ki}^{-}\beta_{y,i} = \frac{y_{k+1} - y_{k-1}}{\mu + 1}, \quad k = 1,\ldots,N. \qquad (2.21)$$

This approach is used to obtain the time-averaged field term $\overline{H}_t^2 + \mu\,\overline{H}_n^2$ in the effective surface force in Chapters 3 and 4, where a 2D ferrofluid droplet in a high-frequency field is considered.

The shape periodicity of the droplet

In the case of the periodical shape with K periods, the angle occupied by the complete period is $\gamma_1 = 2\pi/K$. If the number of marker points per period is N_p then between the marker point i and the corresponding marker point $i+jN_p$ are j full periods. To derive transformation formulae, which bound together these two points, the magnetic field components $H_{0X'}$ and $H_{0Y'}$ in coordinates X',Y' rotated by the angle $\gamma_j = j\gamma_1$ with respect to X,Y coordinates, are introduced (see Fig.2.3):

$$H_{0X'} = H_{0X}\cos\gamma_j + H_{0Y}\sin\gamma_j, \qquad (2.22)$$

$$H_{0Y'} = H_{0Y}\cos\gamma_j - H_{0X}\sin\gamma_j. \qquad (2.23)$$

Due to the periodicity

$$H_{n,i+jN_p} = \alpha_{X,i}\, H_{0X'} + \alpha_{Y,i}\, H_{0Y'}. \qquad (2.24)$$

Collecting together (2.22)-(2.24) and accounting for (2.16) gives

$$\alpha_{X,i+jN_p} H_{0X} + \alpha_{Y,i+jN_p} H_{0Y} = \alpha_{X,i}\left(H_{OX}\cos\gamma_j + H_{OY}\sin\gamma_j\right) + \alpha_{Y,i}\left(H_{OY}\cos\gamma_j - H_{OX}\sin\gamma_j\right) \quad (2.25)$$

The separation of field components yields

$$\begin{cases} \alpha_{X,i+jN_p} = \alpha_{X,i}\cos\gamma_j - \alpha_{Y,i}\sin\gamma_j, \\ \alpha_{Y,i+jN_p} = \alpha_{X,i}\sin\gamma_j + \alpha_{Y,i}\cos\gamma_j. \end{cases} \quad (2.26)$$

In a similar way

$$\begin{cases} \beta_{X,i+jN_p} = \beta_{X,i}\cos\gamma_j - \beta_{Y,i}\sin\gamma_j, \\ \beta_{Y,i+jN_p} = \beta_{X,i}\sin\gamma_j + \beta_{Y,i}\cos\gamma_j. \end{cases} \quad (2.27)$$

Thus the account for the periodicity of the shape gives two sets of linear algebraic equations with matrices $2N_p \times 2N_p$, implemented in Chapter 3. The values of unknowns α_x, α_y, β_x, β_y depend only on the geometry of the problem and from μ. Thus these values are a useful tool to perform calculations for an arbitrary external field. Once calculated, they allow easy to obtain magnetic field on the boundary according to (2.16),(2.17).

The accuracy of the magnetic field calculations

The accuracy of the magnetic field calculation here is tested by few examples for the elliptic shape of the droplet. The exact field solution inside the ellipse is well known [65]:

$$H = H_{0X}\frac{a+b}{a+\mu b} + H_{0Y}\frac{a+b}{b+\mu a}. \quad (2.28)$$

Here the major semi-axis a is orientated in X-axis direction, b stays for minor semi-axis of the ellipse. To check the accuracy, both analytical and numerical values for the non-dimensional geometry-dependent magnetic field characteristics α_x, α_y, β_x, β_y (see formulae (2.16), (2.17)) are plotted versus the contour arc length s in Fig.2.4 and Fig.2.5, number of marker points N=200, magnetic permeability μ=15, a ratio of semi-axes a/b=16. The difference between Fig.2.4a and Fig.2.4b is that in Fig.2.4a the marker point distribution on the contour with equal arc lengths between them is used, but in Fig.2.4b the distribution is dependent on the local curvature: in the places with

large curvature the density of marker points is larger in such a way that the distances between marker points are proportional to the curvature radius. To prevent too high accumulation of marker points in some places causing absence of them in other locations the upper and lower limits of distances between marker points are introduced. Such a curvature-dependent distributions allows essentially improve the field calculation accuracy in the regions of a contour with large curvature (for example, the tips of a 2D droplet). The variable α_x and hence the normal magnetic field component on tips exhibit an impulse-like increase, which is a source for the saw-tooth type oscillations (see Fig.2.4). In Fig.2.4b the implementation of a curvature-dependent marker point distribution suppresses these oscillations, for β_x they are insignificant, but for α_x there is still presence of them in very tip of an ellipse. In fact, the saw-tooth type oscillations about the exact solution are eventual origins for breakup of the numerical algorithm: an artificially elevated field value causes the elevation of a surface force leading to the formation of a sharper tip and thus increasing again the elevation of calculated field. In Fig.2.5 the plot of variables α_y, β_y versus the contour arc length displays, that the field component which is perpendicular to the direction of a droplet elongation, plays less role for surface force. Other point is that the accuracy for these variables are higher but the comparison with equidistant distribution (not shown here) shows that there is no real improvement in the present case for α_y, β_y.

2.4. Equations for the motion of a free boundary

To make discretization of the boundary integral equation for velocities on the boundary (see the equation (1.28))

$$v_j(\mathbf{r}_0) - \frac{1-\lambda}{2\pi(1+\lambda)} \overset{Pr.Val.}{\int_L} v_i(\mathbf{x}) T_{ijk}(\mathbf{r},\mathbf{r}_0) n_k(\mathbf{r}) dl(\mathbf{r}) = -\frac{1}{2\pi\mu_1(1+\lambda)} \int_L \Delta f_i(\mathbf{r}) G_{ij}(\mathbf{r},\mathbf{r}_0) dl(\mathbf{r}) \qquad (2.29)$$

the collocation technique [30,9330] is applied, nevertheless this approach is similar to that of a magnetic field discussed above. The difference from magnetic field equations appears in treatment of singularities: both the logarithmic singularity of $G_{ij}(\mathbf{r},\mathbf{r}_0)$ and the singularity of $T_{ijk}(\mathbf{r},\mathbf{r}_0)$ require special treatment at the singularity point $\mathbf{r}=\mathbf{r}_0$. The equation (2.29), in fact, represents two coupled equations, because both components of the velocity vector, v_x and v_y are implemented in the right hand side of it. The discretization of this equation by N boundary elements (marker points) leads to the set of linear algebraic equations of order 2N×2N.

For the regular boundary element the conventional trapezoidal rule is used. To evaluate the term $v_i(\mathbf{r}) T_{ijk}(\mathbf{r},\mathbf{r}_0) n_k(\mathbf{r})$ at singularity $\mathbf{r}=\mathbf{r}_0$, the relations

$$\mathbf{x}(s) - \mathbf{x}(s_0) = \mathbf{x}_s(s_0)(s-s_0) + \mathbf{x}_{ss}(s_0)(s-s_0)^2/2 + O((s-s_0)^3 ,$$

$$n_x(s) = y_s(s) = y_s(s_0) + y_{ss}(s_0)(s-s_0) + O((s-s_0)^2 ,$$

$$n_y(s) = -x_s(s) = -x_s(s_0) - x_{ss}(s_0)(s-s_0) + O((s-s_0)^2$$

are used in infinitesimal neighbourhood of s_0 arriving at

$$v_i(\mathbf{r}) T_{ijk}(\mathbf{r},\mathbf{r}_0) n_k(\mathbf{r}) ds = -4\frac{\hat{x}_i \hat{x}_j \hat{x}_k}{r^4} v_i(\mathbf{r}) n_k(\mathbf{r}) ds = -4(x_s v_x + y_s v_y) ds\, x_{s,j} ds \times \frac{\left[(y_s + y_{ss} ds)(x_s ds + x_{ss} ds^2/2) - (x_s + x_{ss} ds)(y_s ds + y_{ss} ds^2/2)\right]}{ds^4} ds = -2x_{s,j}(x_s v_x + y_s v_y)(x_s y_{ss} - y_s x_{ss}) ds. \qquad (2.30)$$

Therefore the approximation of the integral in the left-hand side of the equation (2.30) gives

$$\int_L^{Pr.Val.} \mathrm{v}_i(\mathbf{r}) T_{ijk}(\mathbf{r}, \mathbf{r}(p)) n_k(\mathbf{r}) dl(\mathbf{r}) \approx -\mathrm{D}_{ij}^{*} v_j =$$

$$-2\sum_{\substack{m=1 \\ m\neq p}}^{N} \frac{x_j(m) - x_j(p)}{|\Delta\mathbf{r}(m,p)|^4} (\Delta\mathbf{r}(m,p)\mathbf{v}(m))(\Delta\mathbf{r}(m,p)\mathbf{n}(m))(\Delta s_{m-1} + \Delta s_m) - \qquad (2.31)$$

$$x_{s,j}(p)(\mathbf{r}_s(p)\mathbf{v}(p))(x_s y_{ss} - y_s x_{ss})(\Delta s_{p-1} + \Delta s_p)$$

$$\Delta\mathbf{r}(m,p) = \mathbf{x}(m) - \mathbf{x}(p), \qquad \Delta x_j(m,p) = x_j(m) - x_j(p).$$

Here $\mathbf{r}_0$ in (2.29) corresponds to the p-th marker point. For singular boundary element approximation both the result of the exact integral

$$\int_0^c (a + bx) \ln x \, dx = ac(\ln c - 1) + bc^2\left(\frac{\ln c}{2} - \frac{1}{4}\right) \qquad (2.32)$$

and the property that surface forces have only normal component are used. It leads to the following approximation formula:

$$\int_L \Delta f_i(\mathbf{r}) \left(-\delta_{ij} \ln r + \frac{\hat{x}_i \hat{x}_j}{r^2}\right) dl(\mathbf{r}) \approx \mathrm{F}_j^{*} =$$

$$\sum_{\substack{m=1 \\ m\neq p}}^{N} \left[\Delta f_i(m) \ln|\Delta r(m,p)| - \Delta x_j(m,p) \frac{\Delta f_k(m)\, \Delta x_k(m,p)}{|\Delta r(m,p)|^2}\right] \times \frac{(\Delta s_{m-1} + \Delta s_m)}{2} + \qquad (2.33)$$

$$\frac{1}{4}\Delta f_k(p)\left[\Delta s_p \ln|\Delta r(p+1,p)|^2 + \Delta s_{p-1} \ln|\Delta r(p,p-1)|^2 - 3(\Delta s_{p-1} + \Delta s_p)\right] -$$

$$\frac{\Delta s_{p-1}}{4} \Delta f_k(p-1) - \frac{\Delta s_p}{4} \Delta f_k(p+1)$$

Here

$$\Delta r(m,p) = \mathbf{x}(m) - \mathbf{x}(p), \qquad \Delta x_j(m,p) = x_j(m) - x_j(p).$$

Inserting (2.31), (2.33) in (2.29) we arrive at the set of linear algebraic equations

$$\sum_{i=1}^{2N} \mathrm{D}_{ij} \mathrm{V}_j = \mathrm{F}_i, \quad i = 1,2,\ldots,2N, \qquad (2.34)$$

where

$$\mathrm{V}_j = \mathrm{v}_x(j), \quad j = 1,2,\ldots,N,$$

$$\mathrm{V}_{j-N} = \mathrm{v}_y(j), \quad j = 1,2,\ldots,N,$$

$$\mathrm{D}_{ij} = \frac{1-\lambda}{2\pi(1+\lambda)} \mathrm{D}_{ij}^{*},$$

$$F_i = -\frac{1}{2\pi\mu_1(1+\lambda)} F_i^*.$$

After solution of the set (2.34) the shift of the i-th marker point during the time step Δt in normal to the contour direction is obtained by

$$\Delta \mathbf{r}(i) = \left(n_x(i)V(i) + n_y(i)V(i+N)\right)\Delta t\, \mathbf{n}(i) \qquad (2.35)$$

The accuracy of the boundary velocity calculations

The accuracy of the obtained boundary velocities was tested by the dynamical simulation of the droplet with small elliptical perturbation from circular shape: the test of droplet contraction due to surface tension. The decrement of the perturbation measured by non-dimensional major semi-axis of the ellipse is obtained in [33] from

$$\frac{a^2-1}{a} = \frac{a_0^2-1}{a_0}\exp\left(-\frac{t}{1+\lambda}\right) \qquad (2.36)$$

and is equal to $1/(1+\lambda)$. In Fig.2.6 the results of this test are shown for five different values of λ=0; 0.5; 1; 2; 5. The equidistant marker point distribution was used, number of marker points N=100, time step Δt=0.01. Solid lines represent results from the formula (2.36), by dotted lines results from numerical simulation are shown. Small shift between solid and dotted lines is caused mainly by initial values of perturbation, which is too large to obtain an almost identical fit by (2.36). Nevertheless the fit is rather good, and for t>2 solid and dotted lines have nearly the same inclination with respect to the time axis, thus showing excellent agreement for perturbation decrement between the analytical solution by small perturbation theory and the numerical simulation started from the initial state with slightly elliptic shape.

The conservation of fluid volume is implemented in boundary integral equations by use of appropriate Green's functions. The accuracy of the approximation of them is directly connected with volume conservation during the numerical simulations. Two simulation tests were carried out to check the numerical accuracy of volume conservation:

1. *Static field test:* static magnetic field, characterised by Bm=15, μ=15, number of marker points N=200 with curvature dependent distribution of them, default time step Δt=0.01. Transition motion of a droplet was simulated starting from

a circular shape. The volume conservation error was 0.25% during 990 time steps, time interval t_1-t_0=9.9.

2. *Rotating field test*: rotating magnetic field, characterised by Bm=105, μ=5, Ω_H=0.8, number of marker points N=200 with curvature dependent distribution of them, default time step Δt=0.01. Transition motion of a droplet was simulated starting from a steady state shape. The volume conservation errors were:

   2.1. 3.4% after 500 steps, time interval t_1-t_0=1.14;

   2.2. 7.2% after 1000 steps, time interval t_2-t_0=2.34;

   2.3. 20% after 2710 steps, time interval t_3-t_0=6.29.

These two tests shows that volume conservation was almost good. the overall performance is close to that of [97], where a ferrofluid droplet was considered in the static field, the errors were less than 0.1% over several hundred time steps. In the cases of rapid motion conservation was poor, with errors as 1% over 10 time steps [97], and the drop dimensions were rescaled in order to correct the volume. Throughout the present work forced volume conservation was used via rescaling of droplet dimensions after every time step, because the change of droplet dimensions leads to different effective time scaling unit and to different magnetic Bond number. thus changing the conditions of droplet behaviour. To improve the accuracy of numerical simulations, the time step was adjusted in every time iteration in such a way that for every marker point displacement during current time step was limited by 20% of distance to the nearest neighbour point.

The accuracy of the surface force approximation was tested by checking magnetic field threshold in high-frequency rotating magnetic field (see Chapters 3 and 4). To obtain it the inverse value of a decrement for elliptic shape perturbation is plotted versus magnetic Bond number Bm. The straight line plotted through the obtained points should intersect the zero-line at the threshold value of Bm. Results are shown in Fig.2.7a (μ=10) and Fig.2.7b (μ=25). The error is smaller than 0.5% in both cases. The equidistant marker point distribution was used. number of marker points N=200. time step Δt=0.01.

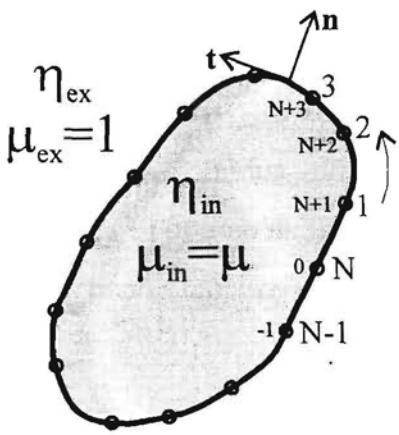

Figure 2.1. Approximation of a 2D droplet boundary by marker points

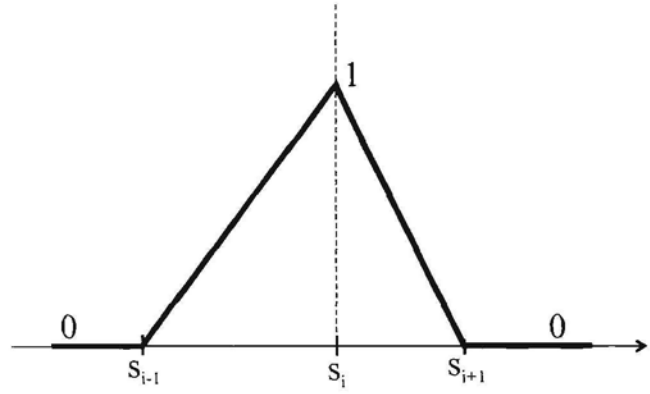

Figure 2.2. The definition of the pyramidal function

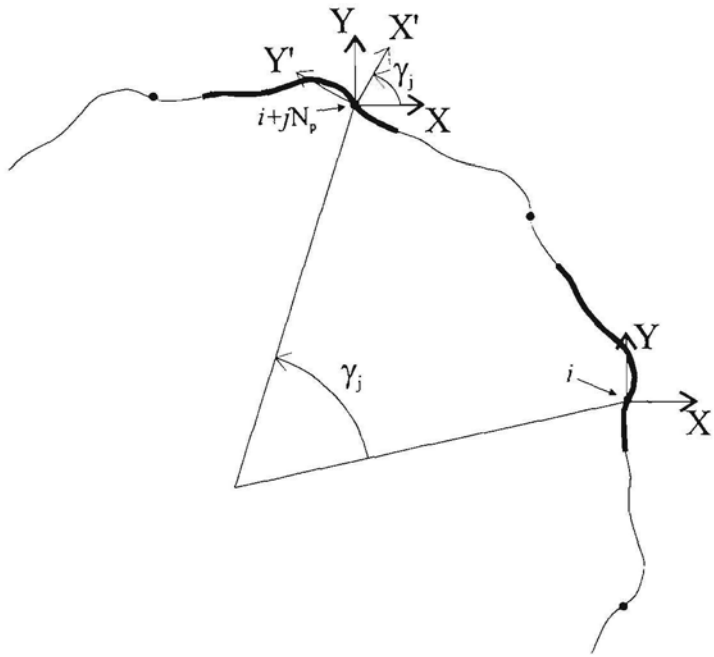

Figure 2.3. Periodic symmetry of a 2D droplet

(a)

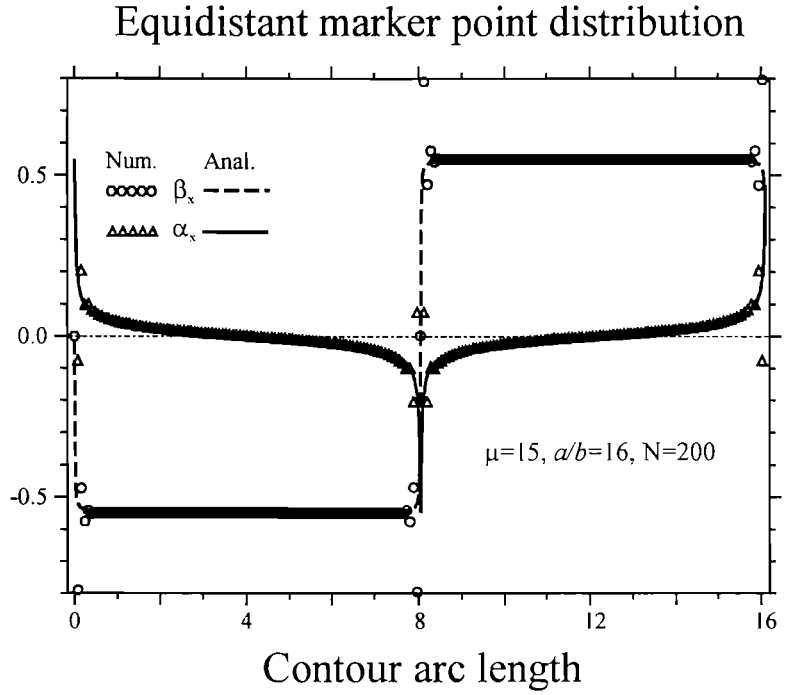

(b)

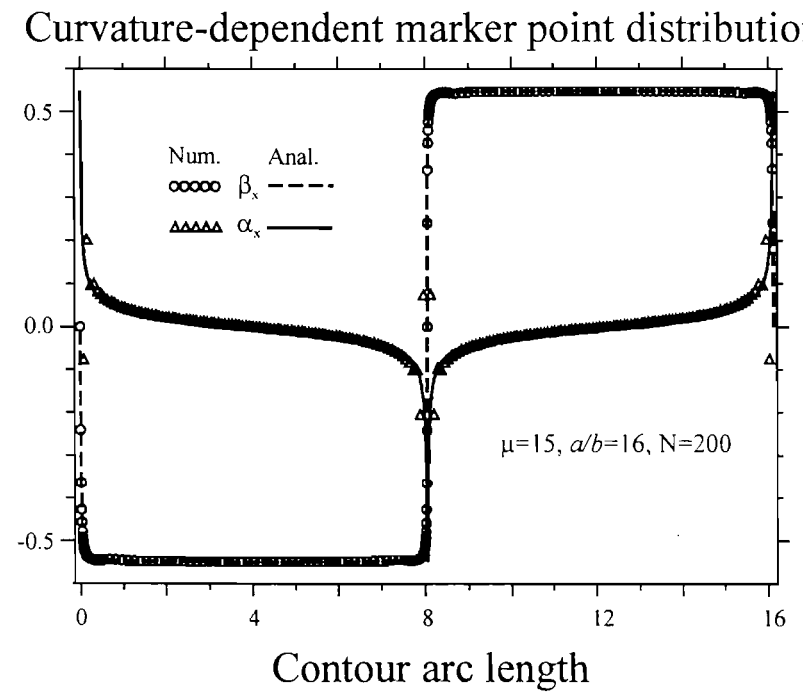

Figure 2.4. The magnetic field characteristics α_x, β_x versus the contour arc length;
(a): the equidistant marker point distribution,
(b): the curvature dependent marker point distribution.
Definitions of α_x, β_x: $H_n=\alpha_x H_{0X}+\alpha_y H_{0Y}$ $H_t=\beta_x H_{0X}+\beta_y H_{0Y}$

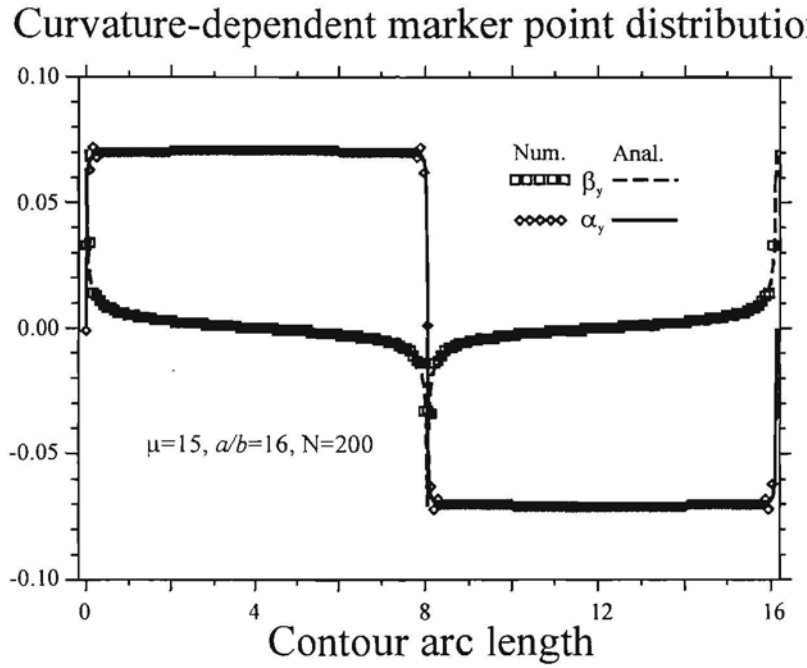

Figure 2.5. The magnetic field characteristics α_y, β_y versus the contour arc length, the curvature dependent marker point distribution. Definitions of α_y, β_y: $H_n=\alpha_x H_{0X}+\alpha_y H_{0Y}$, $H_t=\beta_x H_{0X}+\beta_y H_{0Y}$

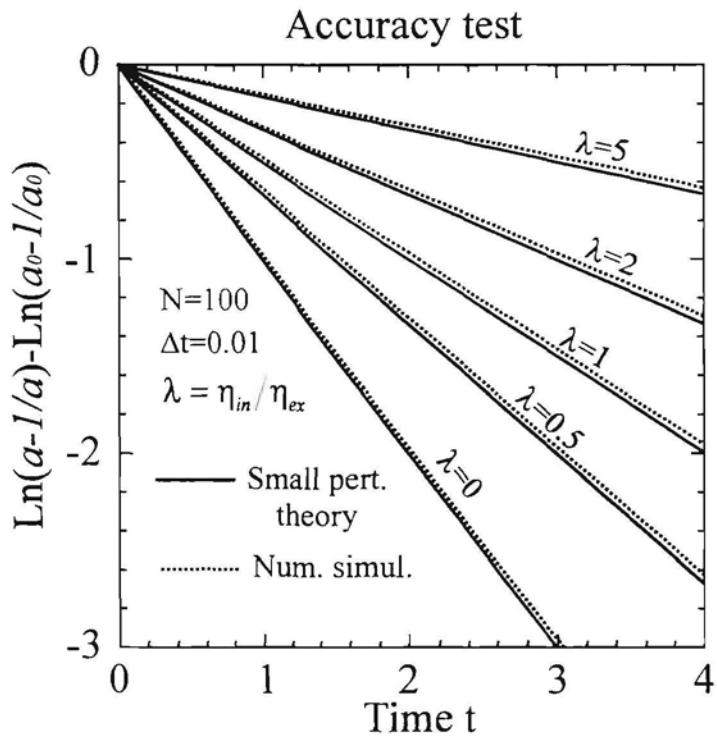

Figure 2.6. The small perturbation decrement test: the contraction of the droplet.

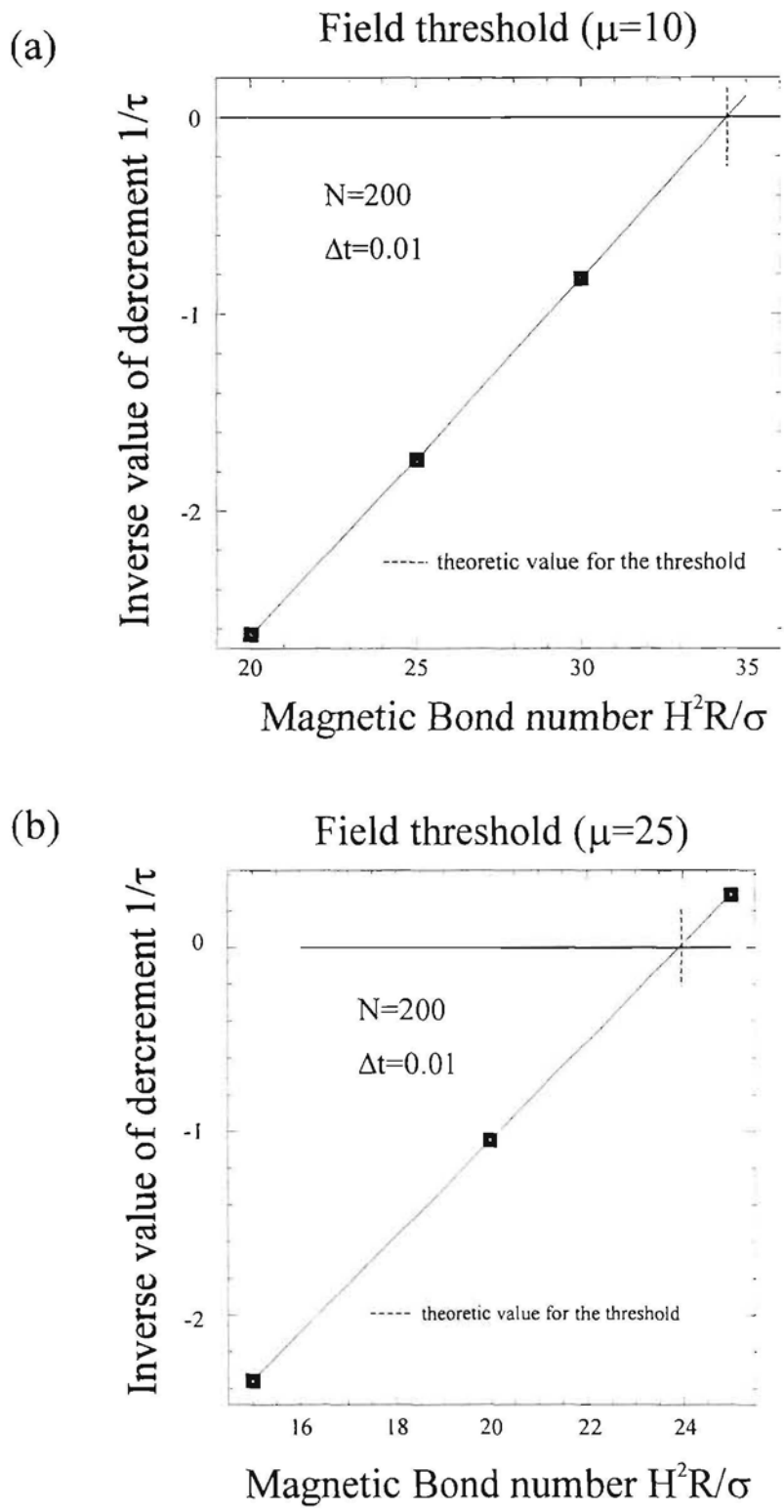

Figure 2.7. The magnetic Bond number threshold value test in high-frequency magnetic field.(a) μ=10, (b) μ=25.

Chapter 3

High-frequency rotating magnetic field: the energy approach.

3.1. Shape generation for energy calculations

The behaviour of a magnetic fluid droplet under the action of the high-frequency rotating magnetic field is considered under the assumption that the characteristic time of the droplet shape relaxation is much larger than the period of the rotating field and thus the time averaging with respect to the rotating field period is possible. The subject of studies is the calculation of the equilibrium shapes, characterised by an absence of flow if the eventual internal rotation of ferroparticles of a magnetic fluid is neglected. Under such assumptions the equilibrium shape corresponds to the minimum of the total energy of the droplet, formed by the sum of a magnetic energy and a surface energy. Further in this Chapter by magnetic field strength is understood the amplitude of a rotating field.

Thus the equilibrium shape at given magnetic field value, characterised by magnetic Bond number $Bm=H^2R/\sigma$, could be found from some initial shape, for example, by the variational technique, varying the shape of the droplet. In fact, such a minimisation of the total energy of the droplet changing its shape could be rather computer time consuming, since in every iteration the magnetic field have to be calculated for the new shape of a droplet. The variational technique is used, for example, in [27],[29] to calculate the equilibrium state of sessile ferrofluid drops in the case of non-linear magnetisation of a ferrofluid, applying the finite element method to calculate a magnetic field.

Concerning the time dependent magnetic field amplitude, the energy approach to shape calculation could be used only to calculate equilibrium shape at every time instant, if the inertia of the system plays no role in the current process. One of the processes without account for inertia is the creeping flow, considered here. The time history of the transition motion in the case of the time-dependent magnetic Bond number thus is substituted by "stroboscopic" shape series. Here it is proposed to detect these series of droplet's shapes in the external homogeneous magnetic field from the set of families of symmetric shapes, generated *a priori* for different numbers of spikes. The main point is how to generate the families of shapes. In the paper [7*] (included in the present Chapter) these families are obtained from the conformal map of the circle in the w plane with radius $r >$:

$$z = w + \frac{w^{-(n-1)}}{n-1}, \qquad (3.1)$$

transformed in order to obtain more elongated spikes and widen in such a way the families of shapes. The number of spikes is given by n. Two control parameters, δ and ε (see [7*] for more details), allow to control the curvature radius at the tip of every spike and the length of the spikes. The expression (3.1) gives the contour in z-plane described by the following parametric equations after the substitution $w = (1+\delta)\exp(i\varphi)$, i denotes the imaginary unit:

$$x = (1+\delta)\left(\cos\varphi + \frac{\cos(n-1)\varphi}{(n-1)(1+\delta)^n}\right),$$
$$y = (1+\delta)\left(\sin\varphi - \frac{\sin(n-1)\varphi}{(n-1)(1+\delta)^n}\right), \qquad (3.2)$$
$$\varphi \in [0, 2\pi]$$

In order to widen the families of shapes, the curves are at first transformed to the polar coordinates ($\rho = \rho(\delta,\varphi), \alpha = \alpha(\delta,\varphi)$) and then the shape is transformed again according to the following power:

$$\rho'(\alpha) = \rho_{min}\left(\frac{\rho(\alpha)}{\rho_{min}}\right)^{\varepsilon}. \qquad (3.3)$$

Here ρ_{min} is the minimal distance of the contour to the origin of the coordinates and $\varepsilon > 0$ is a control parameter by change of which arbitrary spike length could be obtained. After application of the rule (3.3) the droplet is rescaled back to the

"volume" of the circular droplet, characterised by the magnitude of the non-dimensional are $S_c=\pi$ enclosed by the boundary contour of the droplet.

At given magnetic Bond number control parameters are varied and the local minima are found. Thus, tracing the energy minima for some magnetic Bond number interval, the behaviour of the droplet in time-dependent magnetic field is detected without real account on transition phenomena. The shapes of droplet are found as the equilibrium shapes and so they correspond to the stationary state that establishes when transitions decay down at the constant magnetic field. In general this approach could be extended to the time-dependent magnetic Bond number, if the rate of the Bond number changes is small enough for the transition decay.

Some shapes, generated by transformation of (3.1) are juxtaposed in Fig.3.1 and Fig.3.2 with shapes from dynamical simulation from Chapter 4, regarded as almost "exact" ones, since there are no constraints made concerning the shape of a droplet. Fig.3.1 displays that the analytically generated shapes can not describe very well both the curvature radius at the tip and the shape of the "body" of the droplet where the "star-arms" come together. Thus the analytically generated droplet in comparison with the one from dynamical simulation has either too sharp tips or the "necking" in the places where arms join together. In fact, for Fig.3.1(b) this "necking" effect for shapes generated by formula (3.1) and the consequential shape transformation, may cause magnetic field defects leading to the essential change of the magnetic energy. Fig.3.2 displays that even small spikes could not be described very exact by the present shape generation technique. Nevertheless the present shape generation is still the best found one and allows to obtain important results, as it follows in [7*]. Improvement of the shape generation technique should lead to the more accurate results but not to some qualitatively new effect.

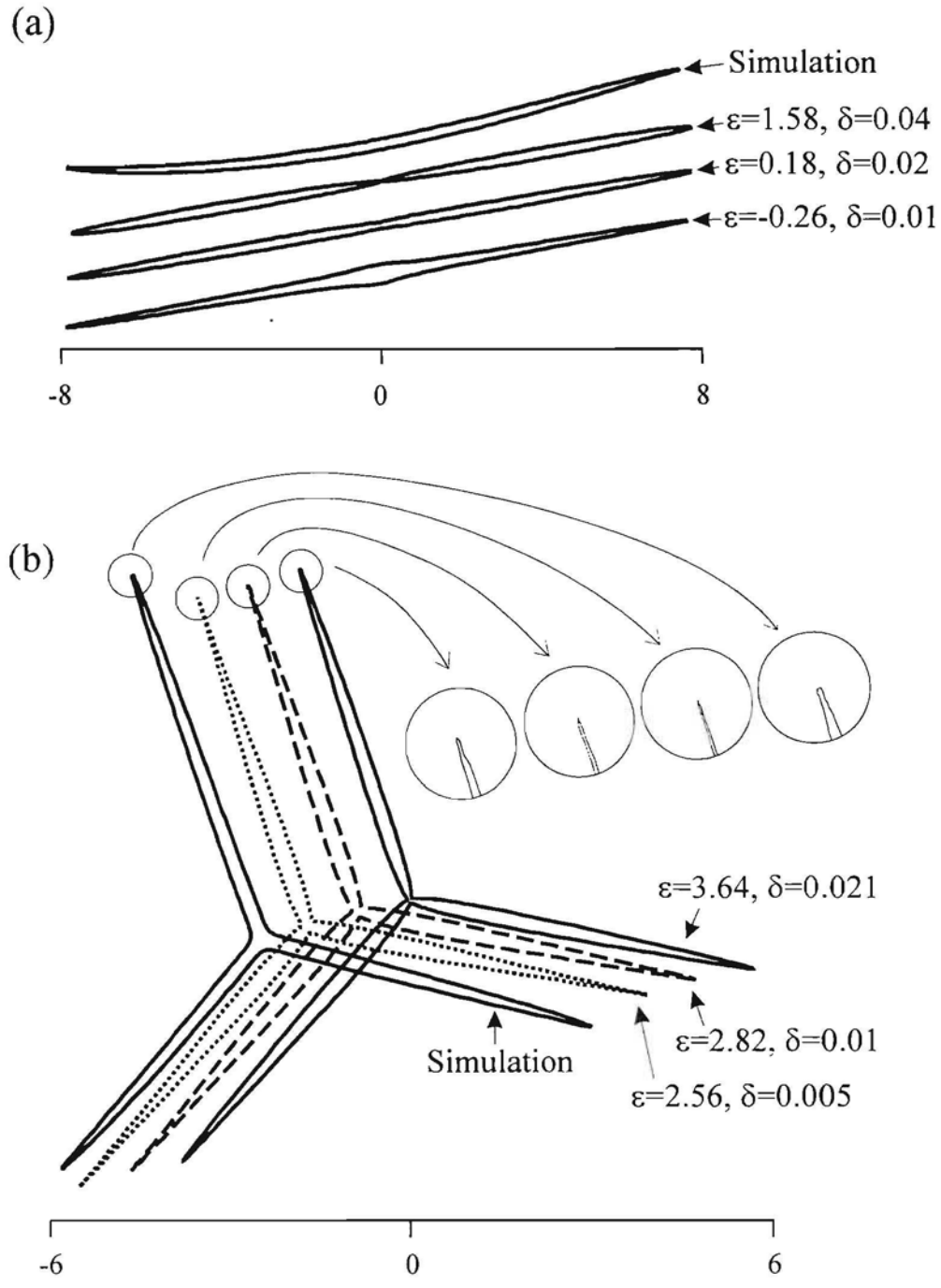

Figure.3.1: Analytically generated shapes juxtaposed with a dynamically simulated one: (a) 2-spike shapes, (b) 3-spike shapes.

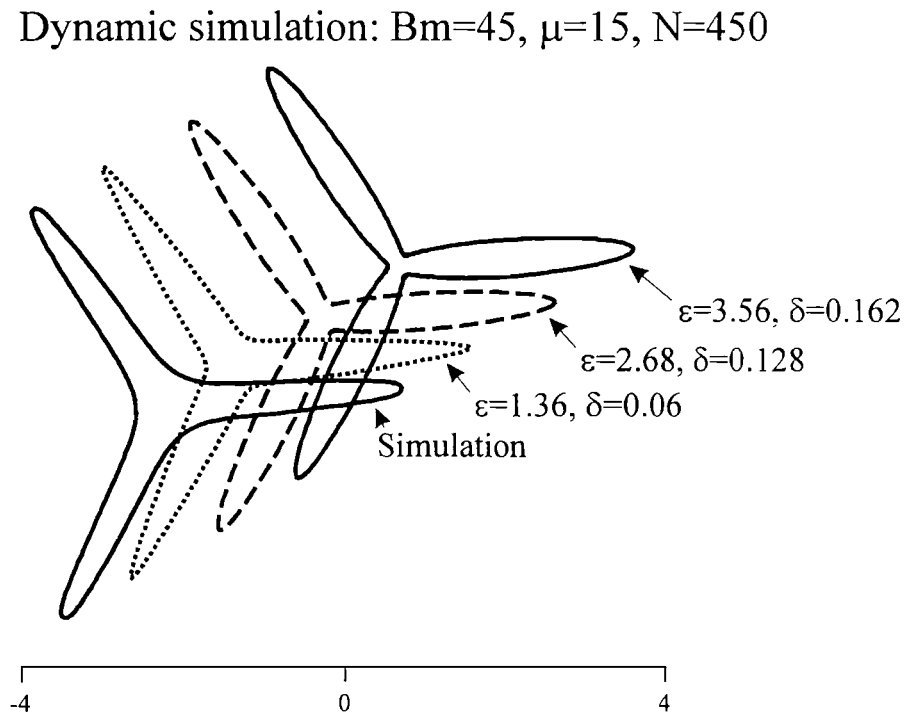

Figure.3.2: Analytically generated shapes juxtaposed with a dynamically simulated one.

Included paper:

J.-C. Bacri, A.Cēbers, S.Lācis, R.Perzynski

Shapes of 2D magnetic fluid droplets in a rotating magnetic field

Magnitnaya Gidrodinamika, 1995, N3 (accepted to publish)

Shapes of 2D Magnetic Fluid Droplets in a Rotating Magnetic Field

J.C.Bacri (*), A.Cēbers (**), S.Lācis(**),R.Perzynski(*)

(*) Université P.M.Curie, 4 place Jussieu, 75252 Paris, Cedex 05, France

(**) Latvian Academy of Sciences, Institute of Physics, Salaspils-1, LV-2169, Latvia

Abstract

The families of equilibrium figures of 2D magnetic fluid droplets in high-frequency rotating magnetic field are found numerically. The magnetic field energy is calculated by a boundary integral equation technique for nonlinear transformed and smoothed hypocycloidal curves. Comparison between families with different number of spikes shows that the lowest energy corresponds to the "two-spikes" shape. A minimum energy calculation shows that for a fixed number of spikes, these spikes arise at a given threshold in magnetic Bond number. Increasing magnetic Bond number, the spikes sharpens. Finally some conclusions concerning the discrepancy with the experimental results are pointed out.

1.Introduction

Droplets of magnetic fluid (MF) under the action of an external magnetic field show rather intricate behaviours [1-3]. Phenomena of particular interest are arising with MF droplets under the action of a rotating magnetic field [4]. Several different shape transformations are observed experimentally and explained theoretically by a linear stability analysis [4,5]. Among them, the sequence of shape transformations "oblate-prolate-oblate" is followed by the arising of the "star-fish" configurations. In [4,5] an analysis of the fastest growing mode of a 2D magnetizable liquid cylinder under the action of a transversal rotating

magnetic field is considered. A good agreement with the dependence of the number of the "star-fish" arms as function of the magnetic field strength is obtained. Nevertheless from a theoretical point of view the transitions between "star-fish" configurations with different number of arms, observed in the experiment [4], are remaining unexplained. In the frame of the 2D model mentioned above, we study the transitions between configurations with different numbers of arms through an analysis of the MF droplet energy in high-frequency rotating fields. We also look for the transitions between different possible configurations from an energetical point of view. An analysis, based on the choice of particular families of shapes reflecting the formation of sharp tips at the development of the MF instabilities [6,7], is undertaken in this paper. From the calculation of energy minima of shape families with different number of tips, we conclude that deepest minimum corresponds to the two-spikes shape of 2D MF droplet. It is in good accordance with the results of numerical simulations of the hydrodynamics of a 2D MF droplet [8] but not with the experimental observations of an increasing number of arms of the MF "star-fishes" with the field strength [4]. Thus the results of the present work show that, for the full understanding of the observed transitions between different "star-fish" configurations, the theoretical model must evidently account for 3D effects and possibly internal rotations and shear flows.

The numerical method of the present work is based on the boundary integral equation technique which has been used previously for the calculation of the elongation of the MF droplet in constant field [9] and the study of 2D droplet behaviour under the action of the magnetic field and shear flow [10].

2. Numerical algorithm

The approximate shape of a 2D droplet can be found from an energy minimum analysis, taking into account both magnetic and surface energies. In this case transient fluid motion and internal rotation effects are neglected. The method described below allows, to find the shape corresponding to a minimum of the total energy of droplet from a given family of shapes and at a given magnetic field strength:

$$\tilde{E}_c = \tilde{E}_s + \tilde{E}_m = \sigma L - \frac{1}{2}\int_S \vec{M}\vec{H}_0 dS. \qquad (1)$$

Here tilde denotes dimensional form of energy, σ is for surface tension, L is the perimeter of the droplet, $\vec{M}$ is the magnetization of MF inside the droplet, and $\vec{H}_0$ is the external magnetic field. The family of shapes is given a priori and the figures of equilibrium are obtained within some approximation, its accuracy depends on a successful choice of the family of shapes.

All along the paper, reduced quantities without dimension are used: non-dimensional energies are obtained with respect to the surface energy of a circular droplet $\tilde{E}_b = 2\pi\sigma R$, magnetic field with respect to external field H_0 and non-dimensional values of droplet size with respect to the radius R of an unperturbated droplet. As a result, the figures of equilibrium are constructed as a function of the magnetic Bond number $Bm = \frac{H_0^2 R}{\sigma}$.

Thus the non-dimensional surface energy is:

$$E_s = \frac{L}{2\pi R}. \qquad (2)$$

The non-dimensional magnetic energy for the linear part of the MF magnetization curve (magnetic permeability $\mu = const$) in a homogeneous external field is:

$$E_m = -\frac{\mu - 1}{16\pi^2} Bm \int_S \vec{H}\vec{H}_0 dS.$$

Last relation accounting for $div\vec{H} = 0$, can be rewritten as

$$E_m = -\frac{\mu - 1}{16\pi^2} Bm \oint_\Gamma (\vec{H}_0 \vec{r}) H_n dl. \qquad (3)$$

The boundary integral equation technique [10] is used to calculate the normal component of the magnetic field strength H_n on the droplet surface (the normal points outside of the droplet):

$$H_n\big|_\Gamma = \frac{2H_{0X}}{(\mu+1)}\frac{\partial x}{\partial n} + \frac{2H_{0Y}}{(\mu+1)}\frac{\partial y}{\partial n} + \frac{1}{\pi}\frac{(\mu-1)}{(\mu+1)}\oint_\Gamma H_n(l')\big|_\Gamma K(l,l')\frac{dl'}{\sqrt{x_l^2 + y_l^2}}, \qquad (4)$$

$$K(l,l') = \frac{x_l(y'-y) - y_l(x'-x)}{(y'-y)^2 + (x'-x)^2}$$

As it follows from relation (3), for energy calculations, the equation for the normal field component must only be solved.

For that, at first, the boundary contour is approximated by a finite number of marker points connected together by interpolating cubic spline functions. The arc length between marker points depends on the local curvature of the contour and the periodicity of the contour is taken into account. The boundary integral equation (4) is solved by an expansion of the normal component in pyramidal functions and using Galerkin's method. The pyramidal functions are defined as

$$\varphi_i = \begin{cases} \dfrac{l - l_{i-1}}{l_i - l_{i-1}}, & l_{i-1} \le l \le l_i; \\ \dfrac{l_{i+1} - l}{l_{i+1} - l_i}, & l_i < l \le l_{i+1}; \\ 0, & l < l_{i-1} \vee l > l_{i+1}. \end{cases} \qquad (5)$$

An approximation technique is described in [10] for the case of equal arcs lengths. In the present work this approximation technique is used for a non-uniform distribution of the marker points as described above. It leads to the following set of linear algebraic equations:

$$\sum_{k=1}^{N} f_k A_{ik} = \sum_{k=1}^{N} f_k \left[R_{ik} - I_{ik}\right] = \frac{H_{0Y}\left(x_{i+1} - x_{i-1}\right) - H_{0X}\left(y_{i+1} - y_{i-1}\right)}{\mu + 1}, \qquad (6)$$

$$H_n(l)\sqrt{x_l^2 + y_l^2} = f(l) = \sum_{i=1}^{N} f_i \varphi_i(l),$$

$$I_{ik} = \begin{cases} \dfrac{l_i - l_{i-1}}{6}, & i = k+1 \\ \dfrac{l_{i+1} - l_i}{6}, & i = k-1 \\ \dfrac{l_{i+1} - l_{i-1}}{3}, & i = k \\ 0, & i \ne k-1 \wedge i \ne k \wedge i \ne k+1 \end{cases},$$

$$R_{ik} = R_{ik}^{*} \frac{(\mu - 1)\left(l_{k+1} - l_{k-1}\right)\left(l_{i+1} - l_{i-1}\right)}{4\pi(\mu + 1)},$$

$$R_{ik}^{*} = \begin{cases} \dfrac{y_l(i)\left(x(i) - x(k)\right) - x_l(i)\left(y(i) - y(k)\right)}{\left(x_l(i) - x_l(k)\right)^2 + \left(y_l(i) - y_l(k)\right)^2}, & i \ne k \\ \dfrac{y_{ll}(i)x_l(i) - x_{ll}(i)y_l(i)}{2\left(x_l^2(i) + y_l^2(i)\right)}, & i = k \end{cases}.$$

Derivatives along the boundary contour are calculated by differentiating the interpolating cubic spline functions. Since the shapes observed in experiments [4] have an azimuthal periodicity, the numerical code can be made more efficient, accounting for that. In the case of

K periods and N_p markers per period, their coordinates for each period can be calculated according to:

$$x_i = x_k \cos\gamma_j - y_k \sin\gamma_j,$$
$$y_i = y_k \cos\gamma_j + x_k \sin\gamma_j, \qquad (7)$$
$$i = k + jN_p,\ k = 1,2,\ldots,N_p$$
$$\gamma_j = jT,\ j = 0,1,\ldots,K-\ ,$$

where $T = \frac{2\pi}{K}$ is the period of the pattern.

Equation (6) taking into account the periodicity can be rewritten as follows. Let us introduce the new field variables α_x^i, α_y^i:

$$f_i = \alpha_x^i H_{0X} + \alpha_y^i H_{0Y}. \qquad (8)$$

It is possible to obtain the variation of the variables α_x^i, α_y^i along the period of the contour from the conditions of periodicity and uniqueness of the solution. Solution f_i for marker point $i = k + jN_p$:

$$f_{k+jN_p} = \alpha_x^{k+jN_p} H_{0X} + \alpha_y^{k+jN_p} H_{0Y}$$

in the system of coordinates (x',y') rotated by the angle γ_j with respect to the system (x,y), can be rewritten as:

$$f_{k+jN_p} = f_k' = \alpha_x^k H_{0X'} + \alpha_y^k H_{0Y'} \qquad (9)$$

Expressing the field components in the system (x',y') by the relations:

$$H_{0X'} = H_{0X}\cos\gamma_j + H_{0Y}\sin\gamma_j$$

and

$$H_{0Y'} = -H_{0X}\sin\gamma_j + H_{0Y}\cos\gamma_j$$

from (9) due to the independence of H_{0x}, H_{0y} we obtain:

$$\alpha_x^{k+jN_p} = \alpha_x^k \cos\gamma_j - \alpha_y^k \sin\gamma_j\ ,$$
$$\alpha_y^{k+jN_p} = \alpha_y^k \cos\gamma_j + \alpha_x^k \sin\gamma_j\ . \qquad (10)$$

Inserting relations (8-10) into the equation (6) we have a new set of equations which can be separated in two sets of size N_p because of the independence of H_{0x} , H_{0y}. As a result we have:

$$\sum_{n=1}^{N_p}\sum_{j=0}^{K-1}\left(\alpha_x^n \cos\gamma_j - \alpha_y^n \sin\gamma_j\right)A_{i,n+jN_p} = -\frac{y_{i+1}-y_{i-1}}{\mu+1}, \quad i=1,2,\ldots,N_p\ , \qquad (11)$$

$$\sum_{n=1}^{N_p}\sum_{j=0}^{K-1}\left(\alpha_x^n \sin\gamma_j + \alpha_y^n \cos\gamma_j\right)A_{i,n+jN_p} = \frac{x_{i+1}-x_{i-1}}{\mu+1}, \quad i=1,2,\ldots,N_p\ . \qquad (12)$$

To solve the set of $2N_p$ equations (11,12) for $2N_p$ unknowns α_x^n, α_y^n a Gaussian elimination method is used (it is checked that iterative methods give worse accuracy). Found values of α_x^n, α_y^n allow to calculate magnetic energy (3). For that the integral in expression (3) is approximated by the trapezium approximation formula:

$$E_m = -\frac{\mu-1}{16\pi^2} Bm \times$$
$$\times\sum_{n=1}^{N_p}\sum_{j=0}^{K-1}\left[H_{0X}\left(x_n\cos\gamma_j - y_n\sin\gamma_j\right) + H_{0Y}\left(y_n\cos\gamma_j + x_n\sin\gamma_j\right)\right]\times$$
$$\times\left[H_{0X}\left(\alpha_x^n\cos\gamma_j - \alpha_y^n\sin\gamma_j\right) + H_{0Y}\left(\alpha_y^n\cos\gamma_j + \alpha_x^n\sin\gamma_j\right)\right]\times \qquad (13)$$
$$\times\frac{l_{n+1}-l_{n-1}}{2\sqrt{x_l^2(i)+y_l^2(i)}}$$

In the case of a high-frequency rotating field ($H_{0X}=\cos\omega t$, $H_{0Y}=\sin\omega t$), shape changes during a time period are negligible if $\omega >> 1/\tau$ for both characteristic times τ of shape changes due to - surface tension $\tau = \frac{\eta R}{\sigma}$ and - magnetic forces $\tau = \frac{\eta}{H_0^2}$, η is the MF viscosity. Then time averaging can be done. As a result for magnetic energy we have:

$$E_m = -\frac{\mu-1}{64\pi^2} Bm K \sum_{n=1}^{N_p}\left(x_n\alpha_x^n + y_n\alpha_y^n\right)\frac{l_{n+1}-l_{n-1}}{\sqrt{x_l^2(i)+y_l^2(i)}} \qquad (14)$$

3. Families of the figures of equilibrium

The family of shapes, taken for the energy minimization problem, are build up looking for the conformal map of the circle in the w plane with radius $r >$:

$$z = w + \frac{w^{-(n-1)}}{n-1}. \qquad (15)$$

It gives the contour in z plane described by the following parametric equations:

$$x = r\left(\cos\varphi + \frac{\cos(n-1)\varphi}{(n-1)r^n}\right)$$
$$y = r\left(\sin\varphi - \frac{\sin(n-1)\varphi}{(n-1)r^n}\right). \qquad (16)$$

For $r =$ the relations (16) gives hypocycloidal curves which have n singular points at $\cos n\varphi =$ (n=3 deltoid or Steiner curve, n=4 astroid) [13].

The choice of the value $r = 1+\delta$ in (16) allows to smooth out the singular points and for the curvature of the curve at tips ($\cos n\varphi =$) we now have a finite value which, at $\delta << 1$, can be taken as

$$K_c \approx \frac{1}{n\delta^2}.$$

The family of shapes corresponding to the n-spike "star-fish" configurations is constructed as follows. For the radius of the curvature at the tip $r_c = n\delta^2$ the value ζ^2/n ($\delta = \zeta/n$) is chosen. For definite values of $\zeta = n\delta = \sqrt{nr_c}$, curves corresponding to the parametric representation (16) are constructed. For each value of ζ, the curves with the equation in polar coordinates $\rho = \rho(\alpha)$ are transformed according to the following power:

$$\rho'(\alpha) = \rho_{\min}\left(\frac{\rho(\alpha)}{\rho_{\min}}\right)^{\varepsilon}. \qquad (17)$$

Here $\rho_{\min}$ is the minimal distance of the contour to the origin of the coordinates and ε a parameter which varies from 0 to some limiting value determined by the accuracy of calculations (elongated "star-fish" arms with sharp tips require too many marker points for a reasonable accuracy). After all these transformations the area enclosed by the contour is set back to πR^2 by a linear scaling. At first the area of transformed contour is calculated as

$$S_c = \frac{K}{2}\sum_{i=1}^{N_n}(x_i y_{i+1} - x_{i+1} y_i$$

and thus the scaling factor is obtained as

$$p_{sc} = \sqrt{\pi/S_c}.$$

The family of shapes constructed for n=3 and 6 at $\zeta = 0.1$ and $\zeta = 0.4$ are shown in Fig.1. One can see that tips at $\zeta = 0.1$ are much sharper.

The numerical calculations of energy minimization, according to the relations (11,12,14) for the more realistic "star-fish" configurations (17), are carried out for 4 fixed values of ζ (0.1;0.2;0.4;0.8). The values of the parameter ε, corresponding to the minima of the droplet energy (1,2,14), are thus found for different numbers of spikes. In Fig.2,4a,5,6,7 an energy

normalization is carried out to have a better representation: the total energy of circular droplet E_{c0} being subtracted from the energy of the droplet.

In Fig.2 the calculated energy minimum is presented as a function of the magnetic Bond number for $\zeta = 0.2$. Each curve in Fig.2 corresponds to a given number of spikes on the droplet surface. Small overshots above the energetical level of circular droplet are connected with hysteresis phenomena and are discussed in details below. From this picture several important conclusions can be drawn. As it can be seen from Fig.2 energy curves for different numbers of spikes do not cross each other. That means that it is difficult to expect from the energetical point of view in the framework of 2D model transitions between "star-fish" configurations with different number of spikes. One can mention that it is not the case, for example, for 2D polarized droplets in amphiphile monolayers [14], where an intersection between energetical curves corresponding to the configurations with different number of lobes, has been found, if the shape is given in polar coordinates as

$$\rho(\alpha) = \rho_n(\xi)(1+\xi\cos(n\alpha)), \quad \rho_n(\xi) = R/\sqrt{1+\xi^2/2}, \qquad (18)$$

where n denotes the number of lobes, and ξ is the relative amplitude of the undulation. This shape, for the present problem, gives worse results (larger energy) than smoothed hypocycloidal curves and therefore is not discussed.

Besides that, as one can see from Fig.2, the elliptic configuration has always a smaller energy than any configurations considered even including a "star-fish" configuration with two spikes $\zeta \geq 0.2$ (it is not exactly true in the case of $\zeta = 0.1$, see Fig.5).

It should be also pointed out that this conclusion is in agreement with the results of the direct numerical simulation [8] of the dynamics of the 2D magnetic fluid droplet in a rotating field. It shows that, starting from a randomly perturbated state and going through intermediate stages with a definite number of the spikes, the system ends up with the 2 spikes configuration. That means that the physical explanation of the observation in experiment [4] of transitions between configurations with different number of "star-fish" spikes, must be yet found. Another issue which should be mentioned concerning Fig.2, concerns the first order of the transition to "star-fish" configurations characterised by same hysteresis phenomena. These

a plateau and the droplet shape slides down along the energy curve to the state of smaller energy which corresponds to an elongated shape.

Decreasing the magnetic Bond number, the droplet conserves its elongated shape at subcritical conditions till the second critical value of Bm corresponding to the turning point in Fig.3. The energy minimum of an elongated shape disappears (Fig.4b) and the droplet restores its circular shape with a jump-like decrease of its energy (Fig.4a).

The influence of the spike shape on the energy minimization calculations is illustrated for a two-spikes "star-fish" in Fig.5; for a comparison, the energy of the elliptical droplet is also shown. The first kind transitions to "star-fish" configurations are shown by vertical lines. The threshold value is a function of the parameter ζ which controls the sharpness of the spike. It can be concluded that for almost all the magnetic Bond numbers the elliptical shape has the smallest energy in comparison with different two-spike configurations.

As one can see from Fig.6, the same conclusion can be drawn also with respect to the 4-spike "star-fish" configurations. It is interesting to note that the values of the magnetic Bond number, for the first-kind transition threshold to the "star-fish" configuration, decrease as the parameter ζ increases. Transitions between curves corresponding to the different values of the parameter ζ are also possible. So according to Fig.6, "star-fish" configuration arises at the threshold with rather rounded small tips which are growing sharper and sharper as the magnetic field strength increases.

The behaviour of the MF droplet described above for different numbers of spikes (n=2,4,6) is summarized in Fig.7 for $\zeta = 0.1, 0.2, 0.4, 0.8$. For each number of spikes, the curve corresponds to the minimal energy from the set $\zeta = 0.1, 0.2, 0.4, 0.8$ at each Bm. For n=4 this choice of the curve of minimal energy is illustrated by the path A-B-C-D-E-F-G in Fig.6 and Fig.7. Discontinuities for a given "star-fish" configuration correspond to a transition to a state of smaller energy, that is here to a lower value of the sharpness parameter ζ. In reality the curve obviously must be smooth due to the continuous variations of the parameter ζ. Fig.7 shows that despite of the free variations of the parameter ζ, it is only the two-spike configuration, or even the elliptic one, which have the smallest energy. That means that for a

pure 2D MF droplet, in the rotating magnetic field, a transition to a two-spike structure must take place. Numerical simulation results of the hydrodynamics of the MF droplet which will be published elsewhere [8] are in fair agreement with that conclusion. That means that physical mechanisms leading experimentally to the increase of the number of spikes with the increase of rotating field strength, includes 3D effects or viscous flow around the droplet: tip effects are more important at 3D than at 2D.

4.Conclusions

1. A 2D numerical analysis of MF droplets of different numbers of spikes shows that the equilibrium shape with two-spikes corresponds to the lowest energy.
2. Along the branch of equilibrium figures with a given number of spikes, a calculation of energy minimum shows that the spikes are sharpening as magnetic Bond number increases beyond a definite threshold.
3. The present calculation shows that 2D figures of equilibrium with a "star-fish" configuration can exist evidently only as transient states. A further confirmation of this point by a direct numerical simulation of the magnetic fluid droplet hydrodynamics is highly desirable.
4. Discrepancies between the present results and experimental observations are presumably connected with the fact that a 2D model is rather incomplete for the understanding the MF droplet behaviour in high-frequency rotating magnetic fields.

Acknowledgments

This work was supported by "Le Réseau Formation Recherche n°90R0933 du Ministère de l'Enseignement Superieur et de la Recherche" of France. Two of us (A.Cēbers, S.Lācis) are thankful to International Science Foundation for financial support of the research in terms of long-time grant LBG000.

References

1. Bacri J.C., Salin D. Instability of ferrofluid magnetic drops under magnetic field *J.Phys.Lett.*,1982, v.43, N17, pp L649-L654
2. Cēbers A., Maiorov M.M. Magnetostatic instabilities in plane layers of magnetic fluid *Magnitnaya.Gidrodinamika* (in Russ.), 1980, N1, pp.27-35
3. Langer S.A., Goldstein R.E., Jackson D.P. Dynamics of labyrinthine pattern formation in magnetic fluids. *Phys.Rev.A*, 1992,v.46,N8,pp 4894-4904
4. Bacri J.C., Cēbers A.O., Perzynski R. Behavior of a magnetic fluid microdrop in a rotating magnetic field *Phys.Rev.Lett.*, 1994, v.72, N17, pp 2705-2708
5. Cēbers A.O., Lācis S. Magnetic fluid free surface instabilities in high frequency rotating magnetic fields. *Brazilian Journal of Physics*, (to appear.)
6. R.E.Rosensweig. Ferrohydrodynamics. *Cambridge University Press*, 1985, 344p
7. Hao Li, Hasley T.C., Lobkovsky A., Singular shape of a fluid drop in an electric or magnetic field. *Europhys.Lett.*, 1994, v.27, N8, pp575-580
8. Bacri J.C., Cēbers A., Lācis S., Perzynski R. (to be published)
9. Sherwood J.D., Breakup of fluid droplets in electrical and magnetic fields *J.Fluid Mech.*, 1988, v.188, pp.133-146
10. Cēbers A. Numerical simulation of ferrofluid drop dynamics in static and rotating magnetic fields *Magnitnaya.Gidrodinamika* (in Russ), 1986, N4, pp.3-10 (Численное моделирование динамики капли намагничивающейся жидкости в постоянном и вращающемся магнитных полях)
11. Boudouvis A.G., Puchalla J.L., Scriven L.E. Magnetohydrostatic equilibria of ferrofluid drops in external magnetic fields. *Chem. Eng. Comm.* 1988, v.67, pp.129-144
12. Boudouvis A.G., Scriven L.E. Sensitivity analysis of hysteresis in deformation of ferrofluid drops. *J.Magn.Magn.Mater.* 1993, v.122, pp.254-258
13. Zwikker C. The advanced geometry of plane curves and their applications, *Dover Publication, Inc.*, New York, 1963, 299p

14. Vanderlick T.K., Möhwald H. Mode selection and shape transitions of phospholipid monolayer domains - *J.Phys.Chem.*, 1990, 94,pp.886-890

FIGURE CAPTIONS

FIGURE 1

Contours constructed for different values of spike number and parameters ε and ζ.

FIGURE 2

The total energy of the 2D droplet $E_c - E_{c0}$ versus the magnetic Bond number for ζ=0.2 (number of spikes n=2,...,6) and for ellipse, μ=25.

FIGURE 3

The large semi-axis $a = a_{\text{dim}} / R$ of the ellipse in the rotating magnetic field as a function of the magnetic Bond number.

FIGURE 4a

The total energy of the ellipse $E_c - E_{c0}$ in the rotating magnetic field as a function of the magnetic Bond number, μ=25.

FIGURE 4b

The total energy E_c curves of the ellipse in the rotating magnetic field versus its large semi-axis value $a = a_{\text{dim}} / R$, μ=25. Bm=23.97 corresponds to the threshold and Bm=20.7 to the turning point.

FIGURE 5

The total energy $E_c - E_{c0}$ as a function of the magnetic Bond number, for a 2-spike configuration: various curves correspond to the ellipse and to shapes with ζ=0.1, 0.2, 0.4, 0.8.

FIGURE 6

The total energy $E_c - E_{c0}$ as a function of magnetic Bond number, for a 4-spike configuration: various curves correspond to the ellipse and to shapes with ζ=0.1, 0.2, 0.4, 0.8.

FIGURE 7

The total energy $E_c - E_{c0}$ as a function of magnetic Bond number. The curves are the paths of minimal energy for ellipse and for the 2,4,6-spike "star-fish" configurations. Minimization is done for ζ=0.1, 0.2, 0.4, 0.8. Arrows show the direction of hysteresis curves.

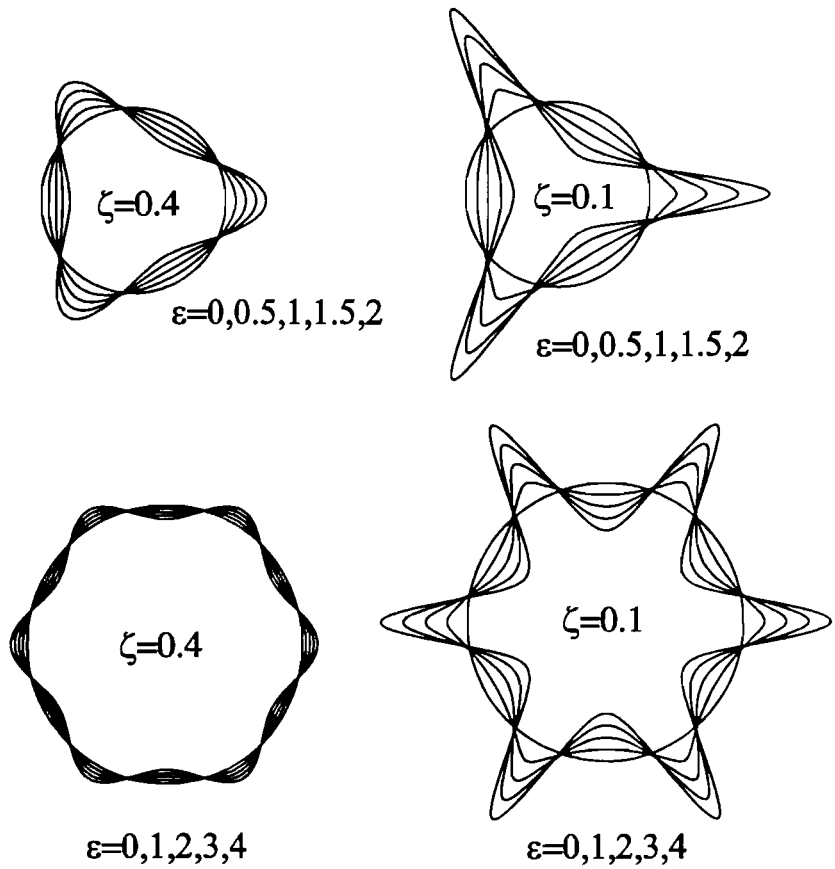

Fig. 1

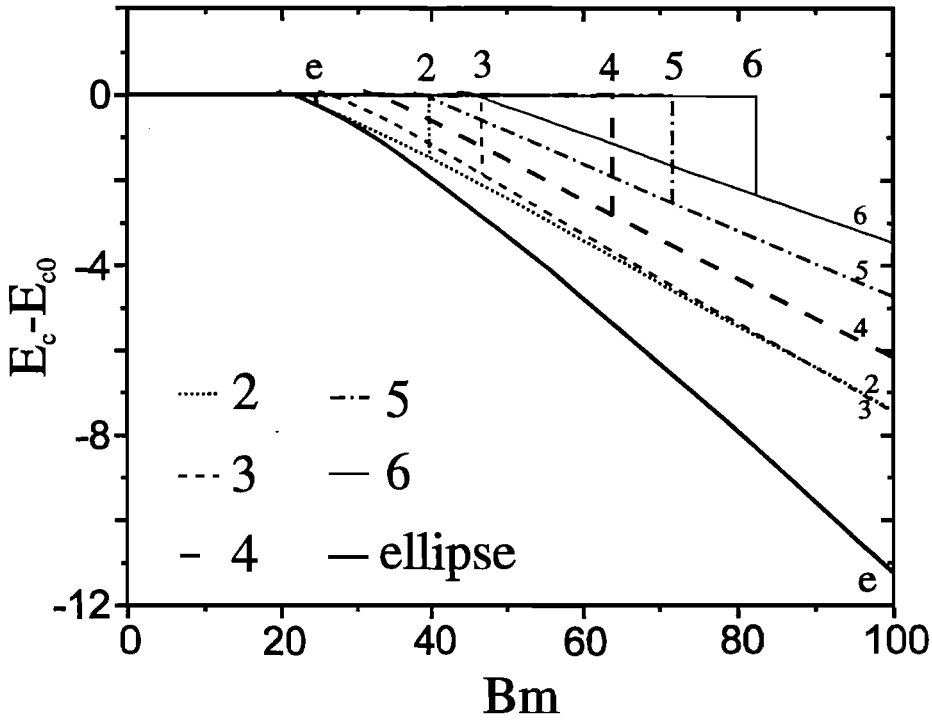
e
2
3
4
5
6
0
-4
-8
-12
E_c-E_{c0}
2
5
3
6
4
ellipse
0
20
40
60
80
100
Bm

Fig.2

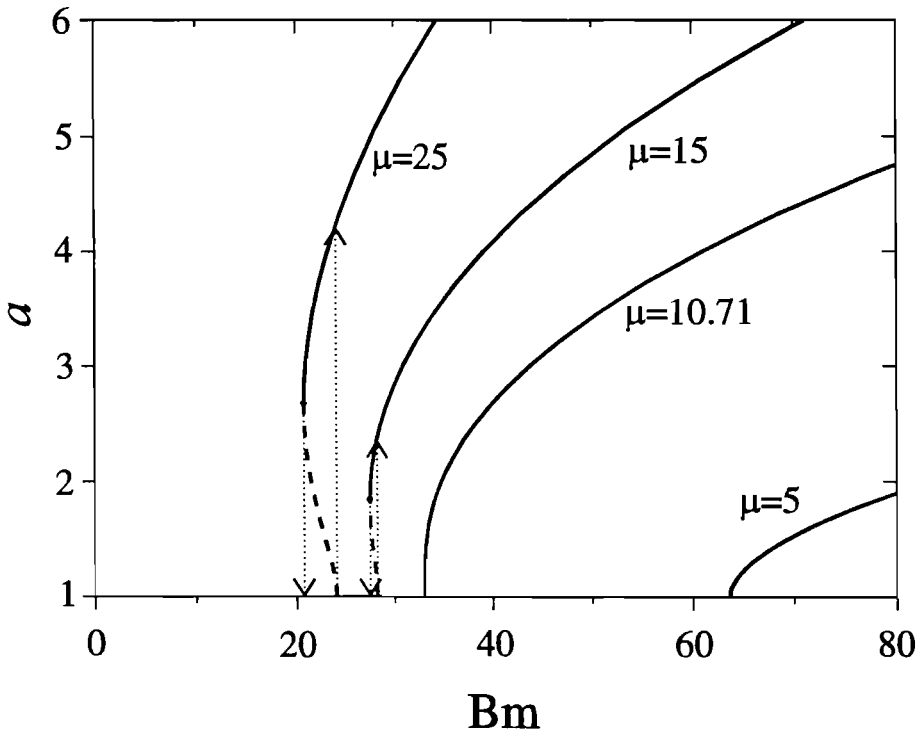
6
5
4
3
2
1
a
μ=25
μ=15
μ=10.71
μ=5
0
20
40
60
80
Bm

Fig.3

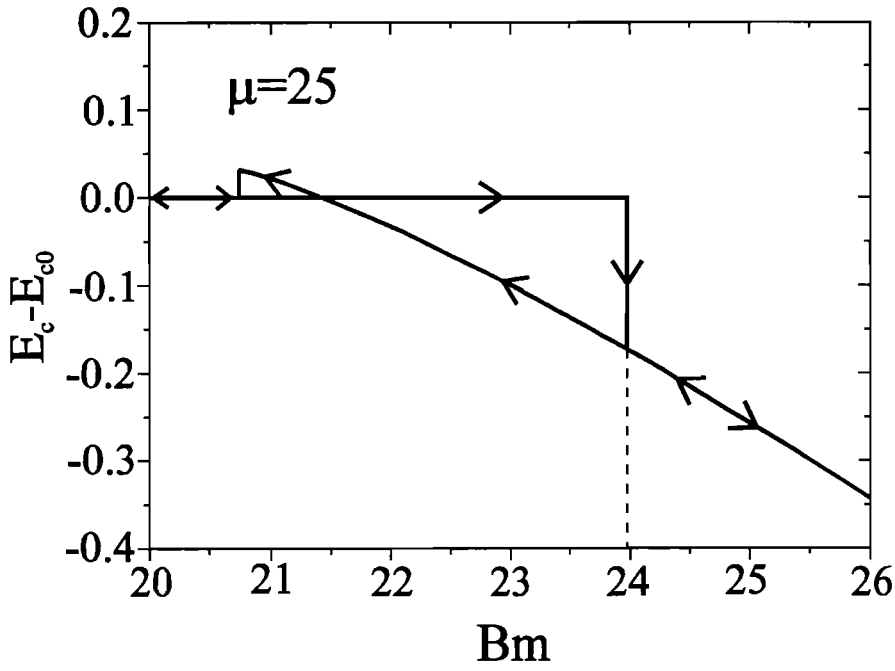
μ=25
E_c-E_{c0}
Bm
0.2
0.1
0.0
-0.1
-0.2
-0.3
-0.4
20
21
22
23
24
25
26

Fig.4a

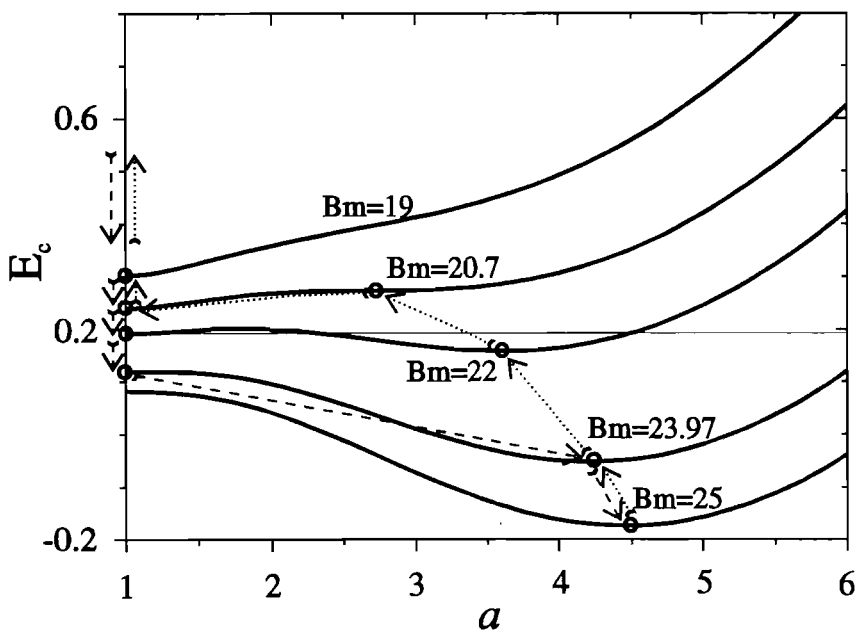
E_c
a
Bm=19
Bm=20.7
Bm=22
Bm=23.97
Bm=25
0.6
0.2
-0.2
1
2
3
4
5
6

Fig.4b

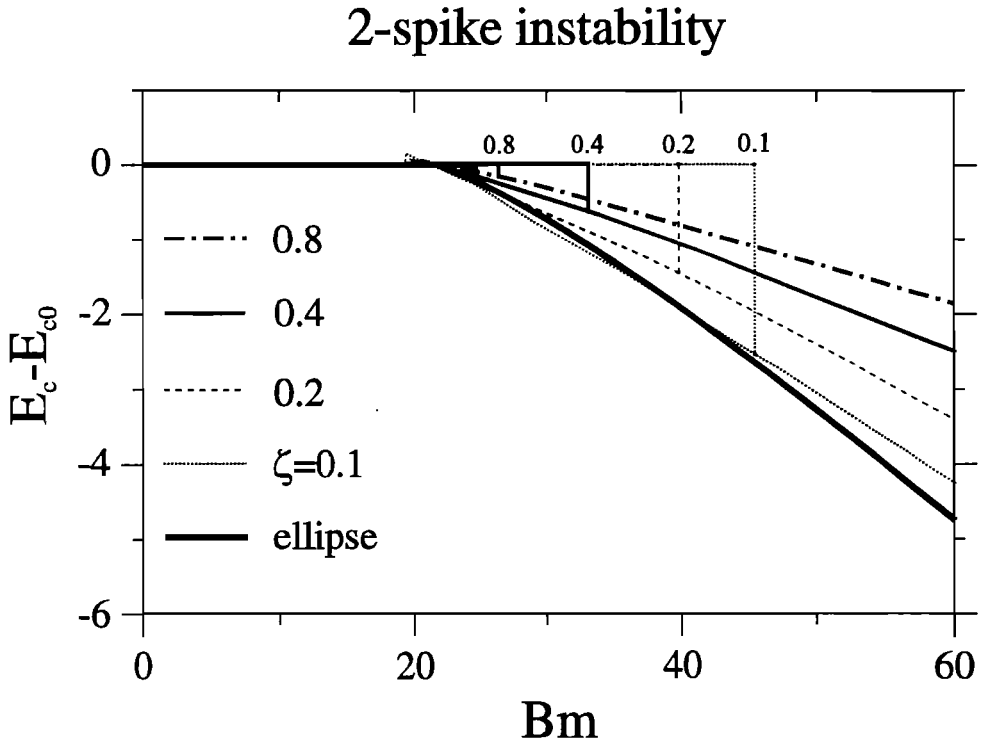
2-spike instability
0.8
0.4
0.2
0.1
0.8
0.4
0.2
ζ=0.1
ellipse
E_c-E_{c0}
0
-2
-4
-6
0
20
40
60
Bm

Fig.5

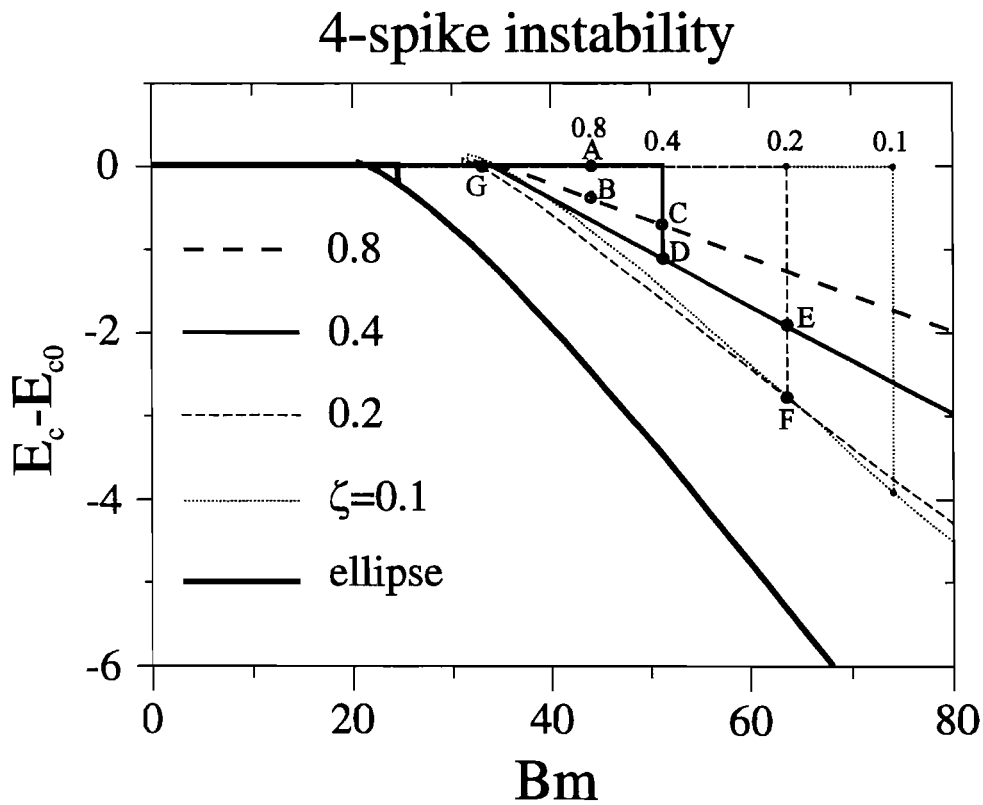
4-spike instability
0.8
0.4
0.2
0.1
A
B
C
D
E
F
G
0.8
0.4
0.2
ζ=0.1
ellipse
E_c-E_{c0}
0
-2
-4
-6
0
20
40
60
80
Bm

Fig.6

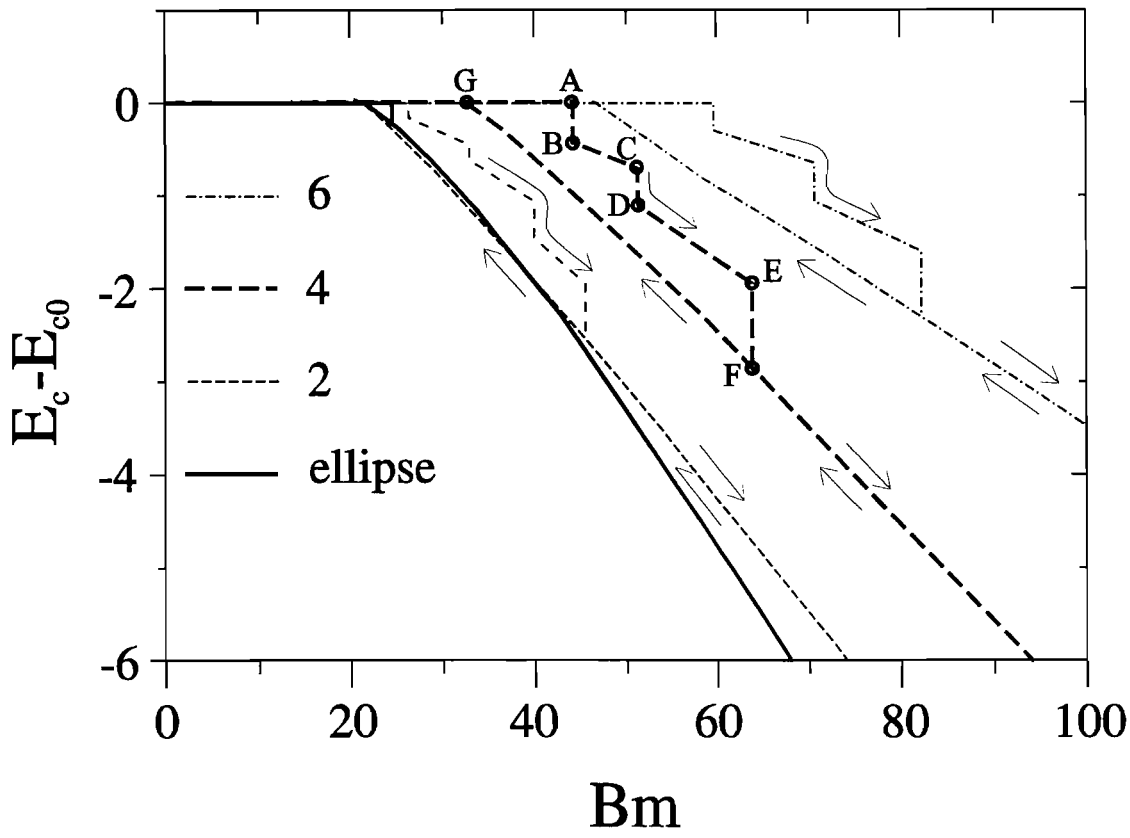

Fig.7

Conclusions

1. The results obtained from the energetical approach confirms existence of the magnetic field threshold in respect to any perturbation from circular shape in 2D in the high-frequency rotating magnetic field. Along the branch of the equilibrium figures with a given number of spikes, a calculation of energy minimum shows that the spikes are sharpening as magnetic Bond number increases beyond a definite threshold thus causing the concentration of the magnetic field in these spikes, specially if a magnetic permeability has as high value as $\mu \approx 25$ considering the concentrated phase.

2. A 2D numerical analysis of MF droplets with different numbers of spikes shows that the equilibrium shape with two-spikes corresponds to the lowest energy and thus the transition from 2-spike shape to the shape with larger amount of spikes does not take place.

3. The present calculation shows that 2D figures of equilibrium with a "star-fish" configuration can exist evidently only as transient states. A further confirmation of this point for number of spikes $n>3$ is given in Chapter 4 by a direct numerical simulation of the magnetic fluid droplet hydrodynamics.

4. Discrepancies between the present results and the experimental observations are presumably connected with the fact that a 2D model is rather incomplete for the understanding the MF droplet behaviour in high-frequency rotating magnetic fields. That means that physical mechanisms leading experimentally to the increase of the number of spikes with the increase of rotating field strength, includes 3D effects or even the viscous flow around the droplet.

Chapter 4

High-frequency rotating magnetic field: dynamic simulation.

In the previous chapter the equilibrium shapes were analysed from pure energetical approach. In such a way it is possible for the given magnetic Bond number to detect which shape from some *a priori* given set has the energy minimum. The advantage of this method is that for linear magnetisation it is necessary only once to calculate geometry and magnetic permeability dependent field variables α_x, α_y (see formulae (11),(12) in [7*]), and afterwards only simple calculations (see the formula (14) in [7*]) are needed to get the magnetic energy of a droplet. Thus by limited calculations the great variety of shapes could be analysed for the energy minimum for arbitrary values of Bond number. The drawback of the energy approach is that the shapes should be given a priory, thus limiting the possible shapes by that ones, generated in some fashion. Thus it is very hard to study the transitions, where non-symmetric shapes appear, because these non-symmetric shapes are almost impossible to predict *a priori*.

A direct dynamical simulation of the surface forced driven motion of the droplet in high-frequency rotating magnetic field is presented in this chapter. The dynamical simulation is in some aspect more computer time consuming method, but the power of it is stated by the absence of constraints on the shape of the droplet. The essence of the droplet behaviour is already described in the previous chapter, here the behaviour of the 2D droplet in the high-frequency rotating magnetic field is studied in more details using the dynamic simulation as an observation instrument, and, in particular, most of

attention is devoted to the transitional motion of a droplet. Transitions of a 2D droplet in the high-frequency rotating magnetic field could be classified as:

- transitions just beyond the magnetic Bond number threshold;
- transitions from the perturbed shape back to the circular one;
- transitions between shapes with different numbers of spikes.

4.1. Theoretical predictions

Transitions which appear at the magnetic Bond number threshold, where the shape of a 2D droplet is near to the circular one, could be studied using the small perturbation theory. The simplest case, the linear small perturbation theory, gives predictions about the critical magnetic Bond number and about the rate of the growth of perturbations.

In [35] the infinite cylindrical volume of magnetic fluid (2D droplet) is considered under the action of the rotating in a plane normal to its axis magnetic field. It is assumed the characteristical time of the droplet shape relaxation is much larger than the period of the rotating field and time averaging with respect to rotating field is possible. Under these assumptions the stability of the droplet's shape is considered with respect to n-lobe perturbation given in polar coordinates (r,ϕ) by

$$r(\phi) = R + a_n \cos(n\phi), \qquad (4.1)$$

where R is the radius of unperturbed 2D droplet. The differential equation for perturbation a_n development is obtained on the basis of the Cauchy-Lagrange integral [35,25], taking into account kinematic condition and the time averaged magnetic field strength, which is calculated in linear approximation of small perturbation theory:

$$\frac{d^2 a_n}{dt^2} + \frac{\sigma}{\rho R^3} \cdot n(n-1)\left((n+1) - \frac{\mathrm{Bm}}{2\pi}\frac{(\mu-1)^3}{(\mu+1)^3}\right)a_n = 0. \qquad (4.2)$$

The solution (4.2) defines an exponential dependence on time for perturbation $a=a_0\exp(\omega t)$, thus providing the dimensional growth increment of the surface perturbation ω:

$$\omega^2 = \frac{\sigma}{\rho R^3} \cdot n(n-1)\left(\frac{\mathrm{Bm}}{2\pi}\frac{(\mu-1)^3}{(\mu+1)^3} - (n+1)\right). \qquad (4.3)$$

From this expression the threshold value of magnetic Bond number with respect to n-lobe perturbation is found:

$$\mathrm{Bm}_{cr}^{(n)} = 2\pi(n+1)\frac{(\mu+1)^3}{(\mu-1)^3}. \qquad (4.4)$$

This value in the case of n=2 is in very good agreement with numerical simulation (see Chapter 2). According to (4), the perturbation with n lobes may appear only if magnetic Bond number exceeds the corresponding threshold value $\mathrm{Bm}_{cr}^{(n)}$. According to Fig.4.1(a), the dependence of the threshold value on the magnetic permeability is not particularly pronounced for $\mu>20$. Quite different is the situation in the case of small values of a magnetic permeability ($\mu<10$), decrease of the magnetic permeability, what physically can be caused by the dilution of the ferrofluid, leads to the drastic increase of the critical value of the magnetic Bond number (Fig.4.1(b)). More information about perturbation evolution could be obtained analysing the expression (4.3) with respect to "the most unstable mode", which has the greatest growth rate at given magnetic Bond number Bm. This "most unstable mode" is given by solution of the equation $\frac{\partial\omega^2}{\partial n}=0$:

$$(2n-1)\mathrm{Bm}^* - (3n^2-1) = 0, \qquad (4.5)$$

$$\mathrm{Bm}^* = \frac{\mathrm{Bm}}{2\pi}\frac{(\mu-1)^3}{(\mu+1)^3} = \frac{H_0^2 R}{2\pi\sigma}\frac{(\mu-1)^3}{(\mu+1)^3}, \qquad (4.6)$$

adding the condition that $\omega^2>0$ for the found value of n at given Bm. The largest root of the equation (4.5)

$$n_* = \frac{\mathrm{Bm}^* + \sqrt{\mathrm{Bm}^{*2} - 3\,\mathrm{Bm}^* + 3}}{3}, \qquad (4.7)$$

satisfies that condition for all $n_*>1$. The fairly good approximation of is given by

$$n_* \approx \frac{2\,\mathrm{Bm}^*}{3} - \frac{1}{2}, \qquad (4.8)$$

according to Fig.4.2, the absolute difference even at $n_*=2$ is only 0.06 (3%). According to (4.3) if Bm^* value is beyond the magnetic field threshold for mode n=2 ($\mathrm{Bm}^*>3$), then the set of competing modes from n=2 to n=Bm^*-1 co-exists, but the highest grows rate has mode n_*. It is illustrated in Fig.4.3 where a square of a

modified perturbation decrement $\omega^2\rho R^3/\sigma$ is plotted versus n at fixed value of modified Bond number Bm^*=16. Unstable modes are for $2\le n<14$, but the highest grows rate has mode n=10 (from formula (4.8) n_*=10.17).

4.2. n-lobe perturbation decrements in the case of creeping flow

In order to derive perturbation decrement in the case of a viscous 2D ferrofluid droplet placed in a surrounding non-magnetic viscous fluid in a presence of high-frequency rotating magnetic field, the problem of the creeping flow is solved at given perturbation rate $\xi_r = \dot{L}\cos(n\phi)$ on the surface of the circular boundary at the restriction that n≥2. The value n=1 corresponds to the pure translation motion v_x=const (check (4.14)-(4.17)), there is no change of nether magnetic nor surface energies, the rate of energy dissipation is zero. Solution of biharmonic equation

$$\Delta(\Delta\Phi) = 0, \qquad (4.9)$$

where Δ is Laplace operator and Φ is a stream function, is used to calculate velocity components in polar coordinates (r,ϕ):

$$v_r = \frac{1}{r}\frac{\partial\Phi}{\partial\phi}, \quad v_\phi = -\frac{\partial\Phi}{\partial r}. \qquad (4.10)$$

The unknown coefficients for the general solution of (4.9) are found from the following three constraints.

1. Continuity of velocity vector at boundary:

$$\mathbf{v}^{in}\big|_{r=R} = \mathbf{v}^{ex}\big|_{r=R}. \qquad (4.11)$$

2. Equality of tangent stresses on boundary:

$$\sigma_{nt}^{in}\big|_{r=R} = \sigma_{nt}^{ex}\big|_{r=R}. \qquad (4.12)$$

3. The constraint of the perturbation shape:

$$v_r\big|_{r=R} = \dot{\xi}_r\big|_{r=R} = \dot{L}\cos(n\phi\ . \qquad (4.13)$$

Since in the present case a velocity field is caused only by perturbation $\vec{\xi}$, the azimuthal component of perturbation ξ_ϕ, could be found from velocity field:

$$\dot{\xi}_\phi = v_\phi.$$

The general solution of (4.9) is found by substitution of Φ in (4.9) by the trigonometric series with respect to the azimuthal coordinate ϕ:

$$\Phi = \sum_n \left[f_n(r)\cos(n\phi) + g_n(r)\sin(n\phi) \right].$$

Application of constraints (4.11)-(4.13) gives the velocity field $\mathbf{v}^{in}$ inside the droplet and the velocity field $\mathbf{v}^{ex}$ outside the droplet:

$$v_r^{in} = \frac{\dot{L}}{2}\cos(n\phi)\left[(n+1)\left(\frac{r}{R}\right)^{n-1} - (n-1)\left(\frac{r}{R}\right)^{n+1} \right], \qquad (4.14)$$

$$v_\phi^{in} = \frac{\dot{L}}{2}\sin(n\phi)\left[-(n+1)\left(\frac{r}{R}\right)^{n-1} + \frac{(n-1)(n+2)}{n}\left(\frac{r}{R}\right)^{n+1} \right], \qquad (4.15)$$

$$v_r^{ex} = -\frac{\dot{L}}{2}\cos(n\phi)\left[(n-1)\left(\frac{R}{r}\right)^{n+1} - (n+1)\left(\frac{R}{r}\right)^{n-1} \right], \qquad (4.16)$$

$$v_\phi^{ex} = -\frac{\dot{L}}{2}\sin(n\phi)\left[(n-1)\left(\frac{R}{r}\right)^{n+1} - \frac{(n+1)(n-2)}{n}\left(\frac{R}{r}\right)^{n-1} \right]. \qquad (4.17)$$

The effective pressure $p^{eff} = p - \frac{\mu - 1}{8\pi} H^2$ is found from the Stokes equation $\nabla p = \eta \nabla^2 \mathbf{v}$:

$$p_{in}^{eff} = p_{0,in} - 2\eta_{in}\frac{\dot{L}}{R}\frac{n^2-1}{n}\left(\frac{r}{R}\right)^n \cos(n\phi), \qquad (4.18)$$

$$p_{ex}^{eff} = p_{0,ex} + 2\eta_{ex}\frac{\dot{L}}{R}\frac{n^2-1}{n}\left(\frac{R}{r}\right)^n \cos(n\phi). \qquad (4.19)$$

Thus the pressure difference on the surface of the circular droplet r=R is

$$\Delta p = p_{ex}^{eff} - p_{in}^{eff} = \Delta p_0 + 2(\eta_{ex} + \eta_{in})\frac{\dot{L}}{R}\frac{n^2-1}{n}\left(\frac{R}{r}\right)^n \cos(n\phi), \qquad (4.20)$$

where $\Delta p_0 = p_{0,ex} - p_{0,in}$.

The normal components of viscous stresses $\sigma_{rr} = 2\eta\frac{\partial v_r}{\partial r}$ on the surface r=R are zero according to the expressions

$$\sigma_{rr}^{in} = \frac{\dot{L}}{2R}(n^2-1)\cos(n\phi)\left[\left(\frac{r}{R}\right)^{n-2} - \left(\frac{r}{R}\right)^n \right], \qquad (4.21)$$

$$\sigma_{rr}^{ex} = \frac{\dot{L}}{2R}(n^2-1)\cos(n\phi)\left[\left(\frac{R}{r}\right)^{n+2} - \left(\frac{R}{r}\right)^n \right]. \qquad (4.22)$$

The dynamic boundary condition on the free boundary Γ is expressed in terms of normal forces:

$$\left(p_{ex}^{eff} - p_{in}^{eff}\right)_{\Gamma} = \left(\sigma_{nn}^{ex} - \sigma_{nn}^{in} + 2\pi(\mathbf{Mn})^2 + \frac{\mu-1}{8\pi}\mathrm{H}^2 - \sigma\,\mathrm{div}\,\mathbf{n}\right)_{\Gamma}. \qquad (4.23)$$

Without perturbations the boundary condition yields

$$\Delta p_0 = \frac{\mu-1}{8\pi}\left((\mu-1)(\mathbf{Hn})^2 + \mathrm{H}^2\right) - \frac{\sigma}{R}. \qquad (4.24)$$

Magnetic field solution for circular shape of a 2D droplet in polar coordinates is [35]:

$$\mathrm{H} = \frac{2\,\mathrm{H}_0}{\mu+1}\left(\cos(\Omega_H t - \phi)\mathbf{e}_r + \sin(\Omega_H t - \phi)\mathbf{e}_\phi\right). \qquad (4.25)$$

Here $\mathbf{e}_r$, $\mathbf{e}_\phi$ are unit vectors in radial, resp., azimuthal directions. Time averaging gives

$$\left\langle \mathrm{H}^2 \right\rangle = \frac{4\,\mathrm{H}_0^2}{(\mu+1)^2}, \qquad (4.26)$$

$$\left\langle (\mathbf{Hn})^2 \right\rangle = \frac{2\,\mathrm{H}_0^2}{(\mu+1)^2}. \qquad (4.27)$$

Inserting (4.26) and (4.27) in (4.25) gives pressure difference on the boundary of circular 2D droplet in high-frequency rotating field:

$$\Delta p_0 = \frac{\mu-1}{\mu+1}\frac{\mathrm{H}_0^2}{4\pi} - \frac{\sigma}{R}. \qquad (4.28)$$

In linear approximation small perturbation theory applied to (4.20) gives in addition to (4.28) the first-order terms containing L and $\dot{\mathrm{L}}$, thus enabling to obtain a non-dimensional perturbation decrement, denoted here by $\hat{\omega}$: $\dot{\mathrm{L}} = \hat{\omega}/\tau_0\,\mathrm{L}$, $\mathrm{L} \propto \exp(\hat{\omega}t/\tau_0$, $\tau_0=\eta_{ex}R/\sigma$: time scaling unit. To obtain additional terms of (4.23) in comparison with (4.24), (4.28), the perturbation of a magnetic field and a boundary contour curvature should be found. It is convenient to use Lagrange variation Δ_L (variation due to Lagrange displacement) technique [25,32,42,88] to derive the first variation of boundary conditions on shifted boundary, expressed by physical variables at unperturbed boundary placement r=R. Variation of an effective pressure and viscous stresses are already given by (4.20)-(4.22), since there is no flow in equilibrium state:

$$\Delta_L\left[\left(p_{ex}^{eff}-p_{in}^{eff}\right)-\left(\sigma_{nn}^{ex}-\sigma_{nn}^{in}\right)\right]_\Gamma =$$
$$\left(p_{ex}^{eff(1)}-p_{in}^{eff(1)}\right)_{r=R}-\left(\sigma_{rr}^{ex(1)}-\sigma_{rr}^{in(1)}\right)_{r=R} = \qquad (4.29)$$
$$2\left(\eta_{ex}+\eta_{in}\right)\frac{\dot{L}}{R}\frac{n^2-1}{n}\left(\frac{R}{r}\right)^n\cos(n\phi).$$

The magnetic field variation is found in [35], solving Laplace equation inside and outside the circular 2D droplet and applying first variations of boundary conditions for magnetostatic potential:

$$\left(\Psi_{in}^{(1)}-\Psi_{ex}^{(1)}\right)_{r=R}=(\mu-1)\left(\frac{\partial\Psi_{in}^{(0)}}{\partial r}\xi_r\right)\Bigg|_{r=R}, \qquad (4.30)$$

$$\left(\mu\frac{\partial\Psi_{in}^{(1)}}{\partial r}-\frac{\partial\Psi_{ex}^{(1)}}{\partial r}\right)\Bigg|_{r=R}=\frac{\mu-1}{R^2}\left(\frac{\partial}{\partial\phi}\left(\frac{\partial\Psi_{in}^{(0)}}{\partial\phi}\xi_r\right)\right)\Bigg|_{r=R}. \qquad (4.31)$$

Magnetostatic potential $\Psi_{in}^{(0)}$ of unperturbed droplet according to (4.25) is [35]:

$$\Psi_{in}^{(0)}=\frac{2H_0^2}{\mu+1}r\cos(\Omega_H t-\phi). \qquad (4.32)$$

First variation of magnetostatic potential inside the droplet $\Psi_{in}^{(1)}$ is found in [35] by technique described above, arriving at

$$\Psi_{in}^{(1)}=2LH_0\frac{\mu-1}{(\mu+1)^2}\left(\frac{r}{R}\right)^{n-1}\cos(\Omega_H t-\phi+n\phi). \qquad (4.33)$$

Magnetic field intensity components could be found from magnetostatic potential by the following derivatives:

$$H_r=\frac{\partial\Psi}{\partial r},\quad H_\phi=\frac{1}{r}\frac{\partial\Psi}{\partial\phi}. \qquad (4.34)$$

The Lagrange variation of magnetic field term in (4.23) due to Lagrange displacement is

$$\Delta_L\left[(\mu-1)(\mathbf{Hn})^2+H^2\right]_\Gamma =$$
$$\left[(\mu-1)2\left(\mathbf{H}^{(0)}\mathbf{n}^{(0)}\right)\left(\mathbf{H}^{(0)}\left(\Delta_L\mathbf{n}\right)+\mathbf{n}^{(0)}\left(\Delta_L\mathbf{H}\right)\right)+2\left(\mathbf{H}^{(0)}\left(\Delta_L\mathbf{H}\right)\right)\right]_\Gamma = \qquad (4.35)$$
$$\left[(\mu-1)2H_r\left(\mathbf{H}^{(0)}\left(\Delta_L\mathbf{n}\right)+\mathbf{e}_r\mathbf{H}^{(1)}\right)+2\left(\mathbf{H}^{(0)}\mathbf{H}^{(1)}\right)\right]_\Gamma.$$

A Lagrange variation of normal vector $\bar{n}$ and a variation of $\mathrm{div}\bar{n}$ in Cartesian coordinates are found according to formulae from [42] :

$$\Delta_L n_i = \left(n_j n_k \frac{\partial \xi_j}{\partial x_k} \right) n_i - n_k \frac{\partial \xi_k}{\partial x_i}, \qquad (4.36)$$

$$\Delta_L \left(\frac{\partial a_j}{\partial x_i} \right) = \frac{\partial}{\partial x_i} (\Delta_L a_i) - \frac{\partial a_i}{\partial x_k} \frac{\partial \xi_k}{\partial x_i}. \qquad (4.37)$$

In polar coordinates expressions (4.36) and (4.37) result in

$$\Delta_L n_r = 0, \quad \Delta_L n_\phi = \left(\frac{1}{r} \left(\xi_\phi - \frac{\partial \xi_r}{\partial \phi} \right) \right) \Bigg|_{r=R} = \frac{L(n^2-1)\sin(n\phi)}{nR}, \qquad (4.38)$$

$$\Delta_L (\operatorname{div} \mathbf{n}) = \left(\frac{1}{r^2} \left(\frac{\partial \xi_\phi}{\partial \phi} - \frac{\partial^2 \xi_r}{\partial \phi^2} \right) - \frac{1}{r^2} \left(\xi_r + \frac{\partial \xi_\phi}{\partial \phi} \right) \right) \Bigg|_{r=R} = -\left(\frac{1}{r^2} \left(\xi_r + \frac{\partial^2 \xi_r}{\partial \phi^2} \right) \right) \Bigg|_{r=R} = \frac{L(n^2-1)\cos(n\phi)}{R^2}. \qquad (4.39)$$

accounting for $\xi_\phi \big|_{r=R} = L \sin(n\phi)/n$.

Now expression (4.35) could be rewritten explicitly, inserting result of (4.38), what leads to

$$\Delta_L \left[(\mu - 1)(\mathbf{Hn})^2 + H^2 \right]_\Gamma = 2(\mu-1)\frac{2H_0}{\mu+1}\cos(\Omega_H t - \phi) \left(2\frac{LH_0}{R}\frac{\mu-1}{(\mu+1)^2}(n-1)\cos(\Omega_H t - \phi + n\phi) + \frac{2H_0}{\mu+1}\cos(\Omega_H t - \phi)\frac{L(n^2-1)\sin(n\phi)}{nR} \right) + 2\frac{2H_0}{\mu+1} 2\frac{LH_0}{R}\frac{\mu-1}{(\mu+1)^2} \times \left(\cos(\Omega_H t - \phi)\cos(\Omega_H t - \phi + n\phi) - \sin(\Omega_H t - \phi)\sin(\Omega_H t - \phi + n\phi) \right) \Big]_\Gamma \qquad (4.40)$$

Time averaging of (4.40) arrives at

$$\left\langle \Delta_L \left[(\mu - 1)(\mathbf{Hn})^2 + H^2 \right]_\Gamma \right\rangle = \frac{4LH_0^2}{R}\frac{(\mu-1)^3}{(\mu+1)^3}(n-1)\cos(n\phi \; . \qquad (4.41)$$

The time-averaged boundary conditions (4.23), accounting for (4.31), (4.39) and (4.41) results in equation

$$2(\eta_{ex} + \eta_{in})\frac{\dot{L}}{R}\frac{n^2-1}{n}\cos(n\phi) = \frac{LH_0^2}{2\pi R}\frac{(\mu-1)^3}{(\mu+1)^3}(n-1)\cos(n\phi) - L\sigma\frac{(n^2-1)\cos(n\phi)}{R^2}. \qquad (4.42)$$

Thus the non-dimensional perturbation decrement $\hat{\omega}$ is

$$\hat{\omega} = \frac{n\left(\mathrm{Bm}^{*} - (n+1)\right)}{2(1+\lambda)(n+1)}, \qquad (4.43)$$

where $\lambda=\eta_{in}/\eta_{ex}$ is a ration of viscosities but Bm* is already defined in (4.06). Magnetic field threshold with respect to n-lobe perturbation (4.13) is given by the same value of critical magnetic Bond number

$$\mathrm{Bm}_{cr}^{*(n)} = (n+1) \Rightarrow \mathrm{Bm}_{cr}^{(n)} = 2\pi(n+1)\frac{(\mu+1)^3}{(\mu-1)^3}. \qquad (4.44)$$

as in (4.4) for potential flow. Comparison of (4.43) with (4.3) displays the basic difference between these two models. The expression (4.3) corresponds to ideal flow, the system with inertia but without a friction, therefore there are only two choices with respect to n-lobe perturbation: either the exponential growth of perturbation ($\omega^2>0$, $a_n \propto \exp(\omega t)$) or the oscillations about the equilibrium state ($\omega^2<0$, $a_n \propto \exp(i\omega t)$). The expression (4.43), in contrary to (4.3), represents the highly damped system without inertia and oscillatory motion is damped in time interval that is much smaller than period of oscillations, thus only the perturbation due to the action of some force on the boundary could take place. Nevertheless, due to the same treatment of magnetic field and surface tension, in both cases magnetic field threshold has the same value. In the case of ideal fluid pure mathematically the lower limit of the perturbation growth spectrum is n=1 due to multiplier n-1 in (4.3) (see Fig.4.3) but in the case of creeping flow the lower limit for n always should be 2 due to the physical properties of the perturbation (4.13). The positive values of $\hat{\omega}$ in the formula (4.43) at n=1 if Bm* is large enough is the artefact since equation (4.42) at n=1 is always satisfied and thus have no roots. Beside that, as it is already mentioned above, "number of lobes" n=1 have no real physical sense.

The threshold value with respect to 2-lobe perturbation is the absolute threshold for any perturbations from circular equilibrium state, and thus determines the upper limit of the perturbation growth spectrum. The most unstable mode n_v^* in the case of viscous fluid is found considering equation $\frac{\partial\hat{\omega}}{\partial n} = 0$, where $\hat{\omega}$ is taken from expression (4.43):

$$n_v^* = \sqrt{Bm^*} - 1 = \sqrt{\frac{Bm}{2\pi}\frac{(\mu-1)^3}{(\mu+1)^3}} - 1. \qquad (4.45)$$

In Fig.4.4 the most unstable mode lobe numbers are plotted versus magnetic Bond number Bm for three values of magnetic permeability μ=5;15;25. These three curves display strong dependence of droplet behaviour on its magnetic properties, so the ratio of magnetic field strengths, needed to have the same most unstable mode two cases: μ=5 and μ=25, have the magnitude 1.63. The same ratio 1.63 stays for corresponding threshold values of μ=5 and μ=25. The increase of magnetic permeability causes increase of the number of lobes for the most unstable mode at the same magnetic Bond number, the limiting curve at μ=∞ is plotted in Fig.4.4 by the dashed curve. To illustrate the dependence of instability on magnetic permeability, in Fig.4.5 the characteristic multiplier $\sqrt{(\mu-1)^3/(\mu+1)^3}$ is plotted versus magnetic permeability μ.

Including characteristic multiplier $\sqrt{(\mu-1)^3/(\mu+1)^3}$ in the modified Bond number as it is defined by (4.6) allows to obtain general properties of the most unstable mode for an arbitrary value of μ. In Fig.4.6 the spectra of unstable modes are plotted in the case of the creeping flow according to the relation (4.43). In comparison with the potential flow (see Fig.4.3), the most unstable modes are shifted to the smaller values, for Bm*>10 even few different modes have about the same perturbation decrement, thus the initial state plays an important role to the formation of the dominant number of lobes.

The limiting curves plotted in Fig.4.7 represent the threshold of magnetic Bond number and n=2. The crossing of n=2 with the threshold curve at Bm*=3 gives the first limit: if Bm*<3, droplet stays circular; the crossing of n=2 with most unstable mode certifies that eventual transition to larger number of spikes than 2 can appear only if Bm*>9.

4.3. Dynamical simulation of the 2D droplet in the high-frequency rotating magnetic field

The dynamic simulation for 2D droplet is carried out for the time averaged surface forces. The averaging is done with respect to external field rotation, thus the droplet motion is still time-dependent as well as the amplitude of a magnetic field, expressed in terms of the magnetic Bond number Bm. The field threshold test with respect to the droplet perturbation from the circular shape is already shown in Fig.2.7. Here the test of the small perturbation growth according to the expression (4.43) is presented in Fig.4.8. All calculations were carried out for periodic perturbations with an amplitude a_n=0.01 (see expression (4.1)). Time step was taken Δt=0.01, number of marker points N=300, magnetic Bond number Bm=100 (Bm*=12.52) at magnetic permeability μ=25, the ratio of viscosities λ=1. The perturbation increment was calculated for the corresponding amplitude of the *n*–th harmonic in the Fourier spectrum for a radial perturbation of the shape. The calculated points, shown by circles in Fig.4.8, are in very good agreement with the theoretical curve, shown by the solid line. The small discrepancies are easy to explain by the competition of the most unstable modes with other ones.

In Fig.4.9 the perturbation growth and the corresponding Fourier spectra of perturbations are shown for three cases. Initial states were generated by random perturbation, realised in the following way: the circle in 60 equidistant points was shifted in the radial direction. The values of shift were taken as random number from 0.0 to 0.03·R, R being circle radius. The magnetic Bond number Bm=100 together with μ=25 corresponds to the limit of maximal allowed mode number n=12 (see Fig.4.8). Thus the n-lobe perturbations are allowed only for n=2..12. According to Fig.4.8, most unstable mode is n=3. Shape growth in Fig.4.9 displays, that modes n=2;3;4 already dominate. Since spikes are not situated symmetric and have the triangular shape, than in Fourier spectra appear higher harmonics and their growth rate is approximately the same as for most unstable mode.

The hysteresis phenomenon for 2D droplet in the rotating field is displayed in Fig.4.10. The solid curve represents the elongation of the elliptic droplet in time-

averaged rotating field (see [7*]), The pointed curve shows the behaviour of the 2D droplet obtained in the dynamical simulation without any shape constraint. This result is obtained by the piece-wise linearly time dependant magnetic Bond number. The value of it is at first kept constant (Bm=25, segment t=0..50), then Bm is linearly increased from Bm=25 to Bm=27 in next 20 time units (segment t=50..70). Discrepancies could be caused by the shape difference. Decrease of Bm to the value Bm=20 in segment t=70..120 causes a contraction of a droplet. The tendency to extend for a droplet at just after t=70, when the value of Bm already decreases, displays that the transient motion was not finished and at t=70 droplet was still not close enough to equilibrium state. Obviously the rate of Bm decrease was all along the curve too large, thus causing very different slope of the dotted curve in comparison to solid one. Without the constraint of the elliptic shape the behaviour of the droplet could be different from the one of elliptic droplet, but it seems that Bm=20 is already below the turning point (for ellipse it is about 20.7), since further decrease of the field causes smooth transition back to circular shape. The more exact "fit" to the transition curve of the elliptic droplet could be obtained by decreasing the rate of the change of Bm in sequential time intervals, but is should cause significant computer time increase.

The transient stages of the 2D magnetic fluid droplet are already described in [8*] (this paper is included in the present Chapter). In the addition to the paper, here in Fig.4.11 the energies E_m, E_s, E_t and the length r of the major spike are plotted in dependence on time t. The thick solid line represents the total energy $E_t=E_m+E_s$, the dotted line: the magnetic energy E_m, the dashed line: the surface energy E_s, the thin solid line: the length r of the major spike, measured from the mass centre of a droplet. These results correspond to the evolution of a droplet's shape in Fig.1a of [8*]. The curve of the length r of the major spike has an approximately constant inclination during the time interval $0<t<0.6$. The shapes of the droplet display that it is an initial time during which the droplet "finds the favourite growth direction". It means that strong competition between the spikes takes place, those ones who are larger and sharper can concentrate more magnetic field thus stimulating a further growth of themselves and suppressing the evolution of smaller spikes. Thus at t about 0.3 the

"weakest" spikes start to contract and non-reversible transitions to smaller number of spikes take place, since decreased value of the magnetic surface forces cannot balance the surface tension established by the curvature of a spike. Thus due to the lower local value of a magnetic Bond number the smallest spikes contract, causing further decrease of a magnetic field until these spikes are completely disappeared. So during the time interval $0.6<t<2.5$ the decrease of the smaller spikes and the accompanying concentration of a magnetic field in the larger spikes causes increase of the growth's rate of last ones. At $t\approx5$ the droplet has established elongated shape with a very small "side-spike", which start to disappear (see Fig.1a of [8*]). At this time moment the growth of the droplet elongation slows down, surface energy E_s has already reached the plateau, all changes of the total energy E_t are due to a change of the magnetic energy E_m. In the present graph E_m has noisy character, because the number of marker points N=350 is still not sufficient to have good accuracy for a magnetic field calculation at extremely sharp spikes. Nevertheless this approximation error could be regarded as some perturbation of the droplet shape which cause oscillations about the stable state, but do not produce the deviation of the mean value of the magnetic energy. Thus, in Fig.1b of [8*], the three-spike shape appears to be stable with respect to such a perturbation.

In [8*] the existence of the metastable three-spike shape at Bm=45, μ=15 is proved as well as the transition to the two-spike shape. This transition appears at the decrease of the magnetic Bond number Bm down to the value Bm=36 thus eliminating the energy barrier which have suppressed the 3-spike shape from transition to the 2-spike one at higher value of Bm. The corresponding energy curves are plotted in Fig.4.12 and Fig.4.13. The analysis of Fig.4.12 displays that the 3-spike metastable state is stable with respect to symmetric perturbation, the decay of this perturbation, given by initially over-elongated spikes, have exponential character. The juxtaposition of the horizontal guidelines with the corresponding energy curves in Fig.4.12 shows that final stage of the transition after t=20 has very small changes of energies in comparison with the initial stage at t<20. The decrease of the magnetic Bond number Bm below the magnetic field threshold with respect to 3-spike perturbation ($Bm_{cr}^{(3)} = 37.5$) causes the transition to 2-spike shape, illustrated in

Fig.4.13. The energy curves show that after initial decay of the transition to the smaller length of spikes ($0<t<25$) the transition to 2-spike shape occurs during the rather long time scale $25<t<90$, because it is caused by very fine interplay of magnetic and surface energies. Then, after $t=90$, during the short time, about 5 time units, the rest of the smallest spike is taken in by the droplet.

In Fig.4.14 the results of the numerical simulation of a droplet with the 4-spike initial shape are presented. Evidently the number of spikes, larger than 3 is critical with respect to the necking effect which takes place between two groups of spikes, since the number of spikes 4 is the smallest one for a formation of two groups of spikes, every of which have at least two spikes. The magnetic Bond number $Bm=60$ in Fig.4.14 is above the threshold value (4.4) with respect to a small 4-lobe perturbation: $Bm_{cr}^{(4)} = 46.9$ at $\mu=15$. The scenario is similar to the one of Fig.4.13. At the beginning the spikes elongate close to the equilibrium state for the symmetric 4-spike shape, afterwards the small perturbations, which are always present due to numerical truncation errors, causes the development of an asymmetric shape with a neck between two pairs of spikes (time interval from $t=8.74$ to $t=41.40$). After that this neck starts to elongate, simultaneously two opposite spikes decrease, other two increase (see a sketch inside the shape at $t=53.19$).

(a)

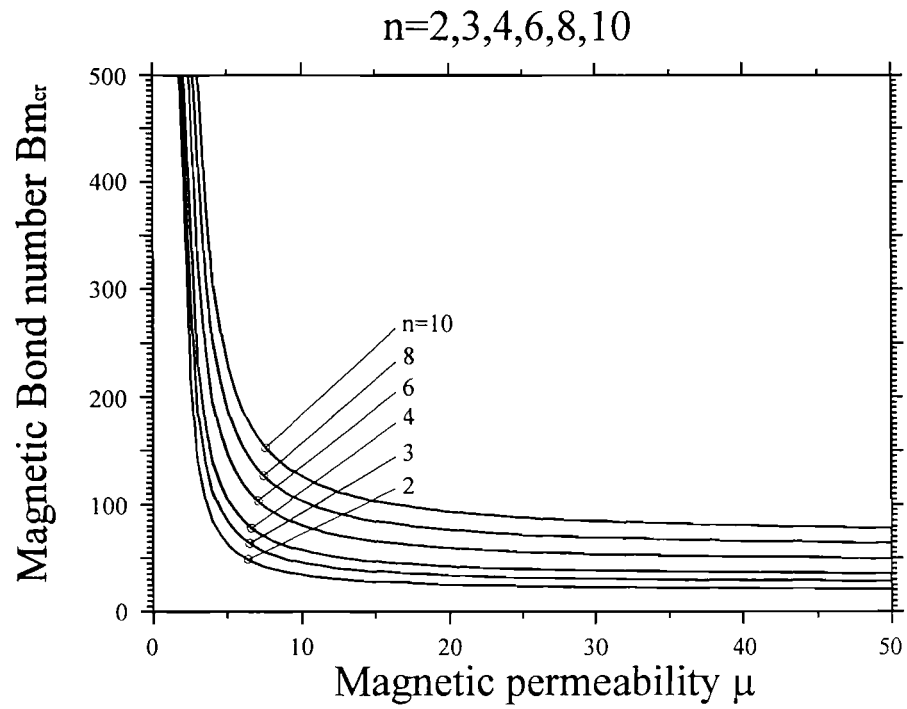

(b)

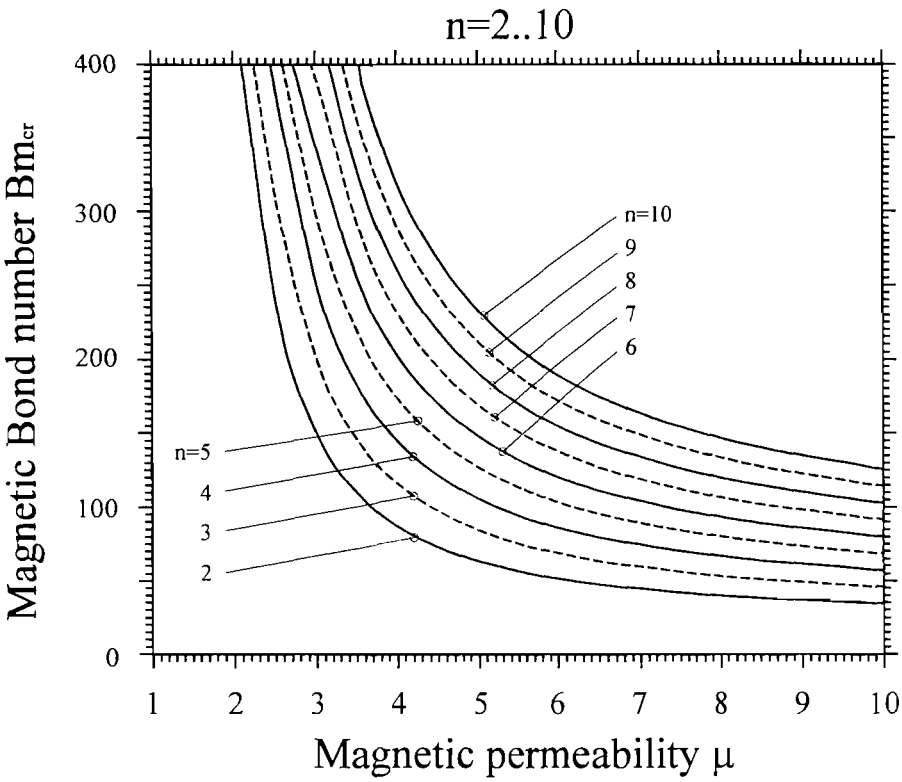

Figure 4.1. Dependence of magnetic Bond number on the value of magnetic permeability μ. (a): selected modes n=2,3,4,6,8,10 at $1<\mu<50$, (b): the behaviour of the critical Bond number at low values of μ.

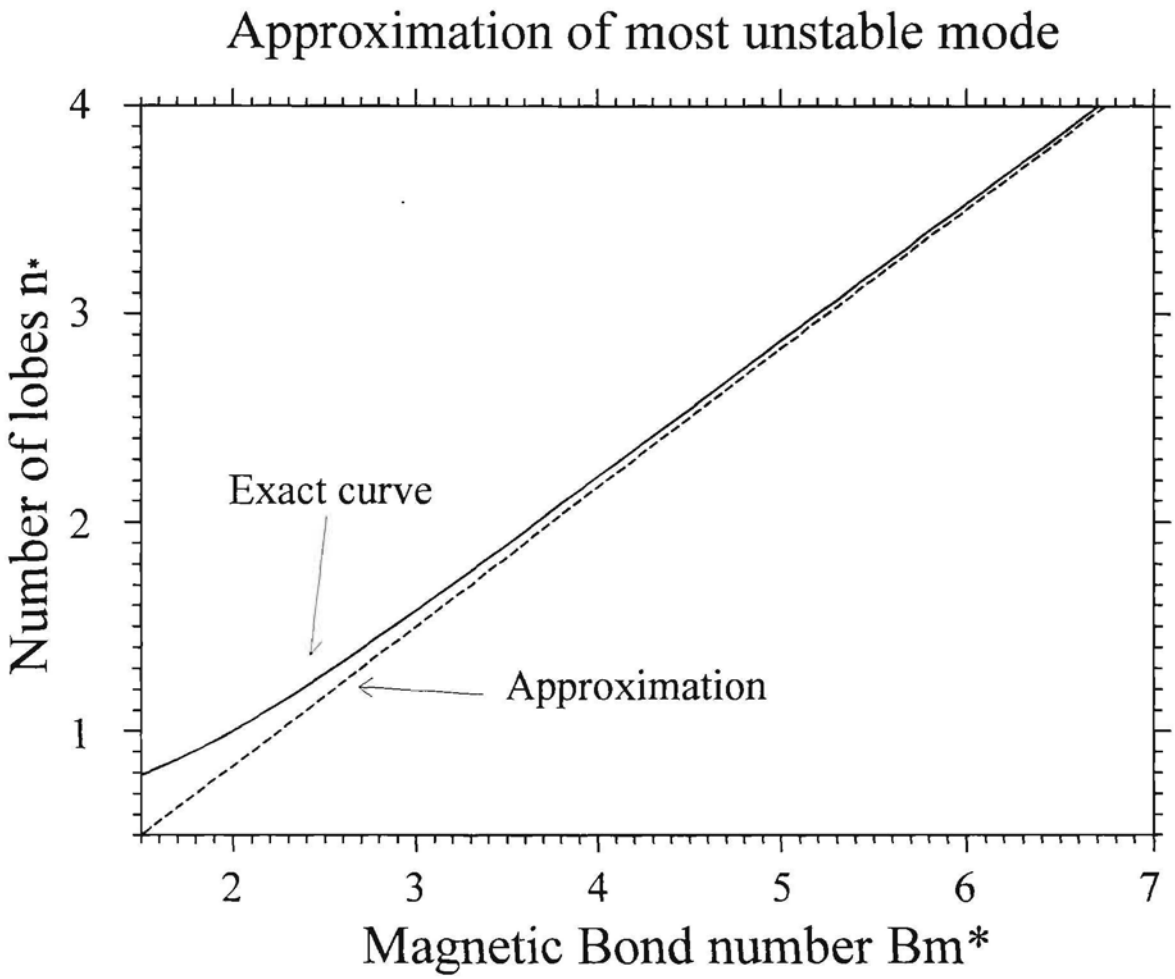

Figure 4.2. Approximation of the most unstable mode

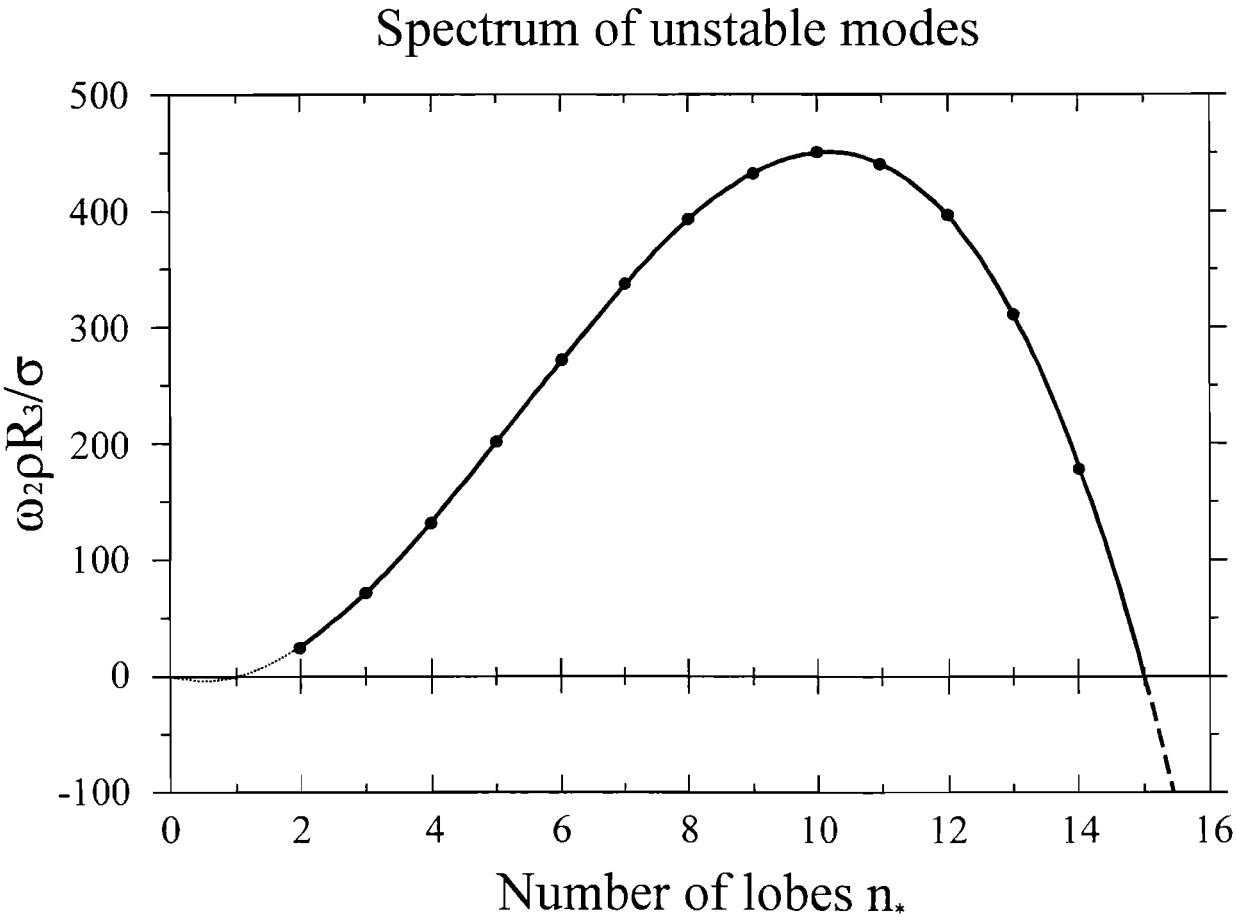

Figure 4.3. The spectrum of competing modes at Bm*=16 for a potential flow

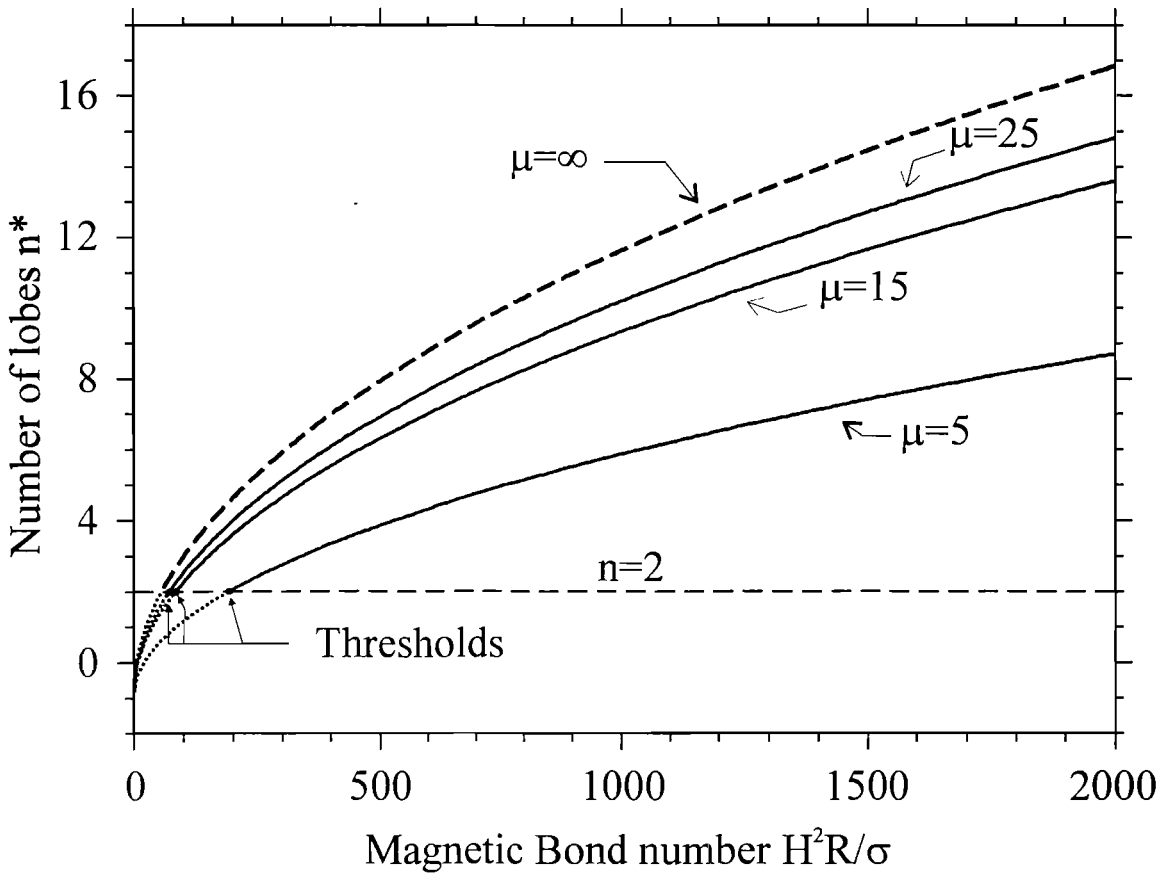

Figure 4.4. The most unstable n-lobe mode versus magnetic Bond number in the case of creeping flow

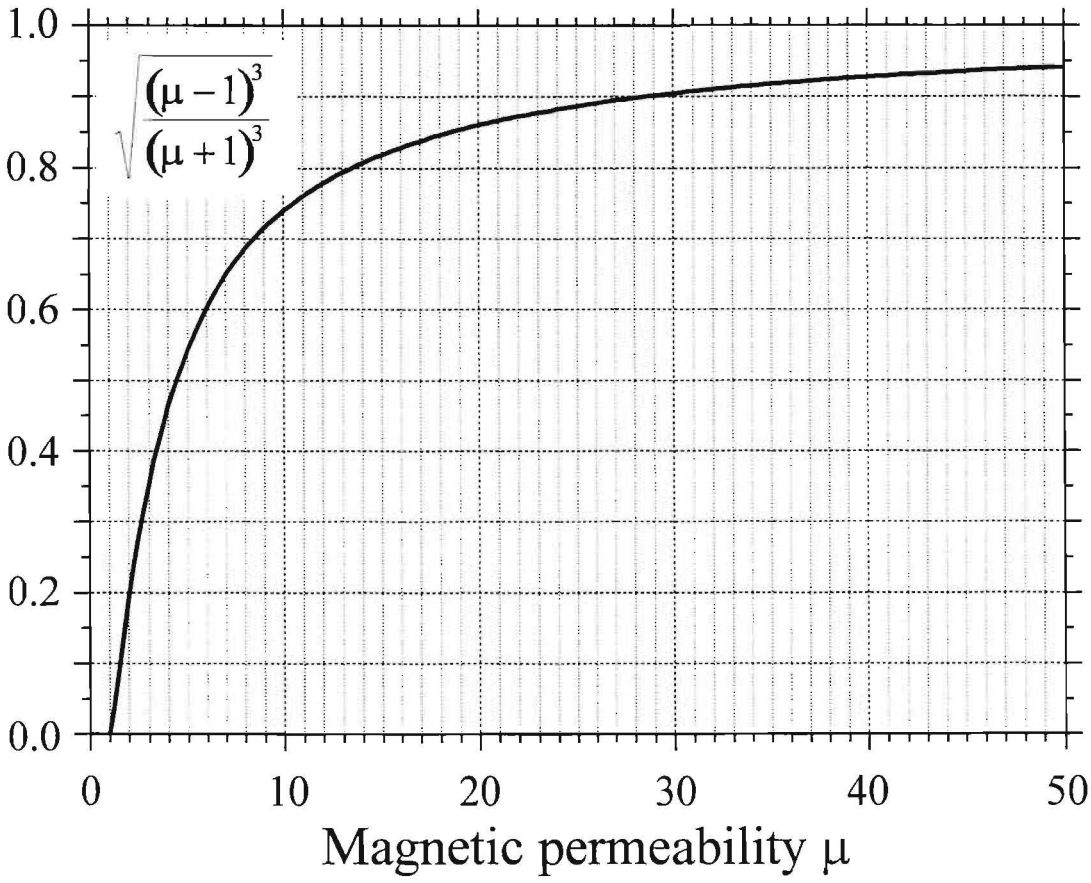

Figure 4.5. The influence of the magnetic permeability to the n-lobe mode formation: the multiplier $(((\mu-1)/(\mu+1))^3)^{0.5}$ versus the magnetic permeability μ.

Definitions:

$$\omega^* = 2\hat{\omega}(1+\lambda) \qquad Bm^* = \frac{H_0^2 R}{2\pi\sigma}\frac{(\mu-1)^3}{(\mu+1)^3}$$

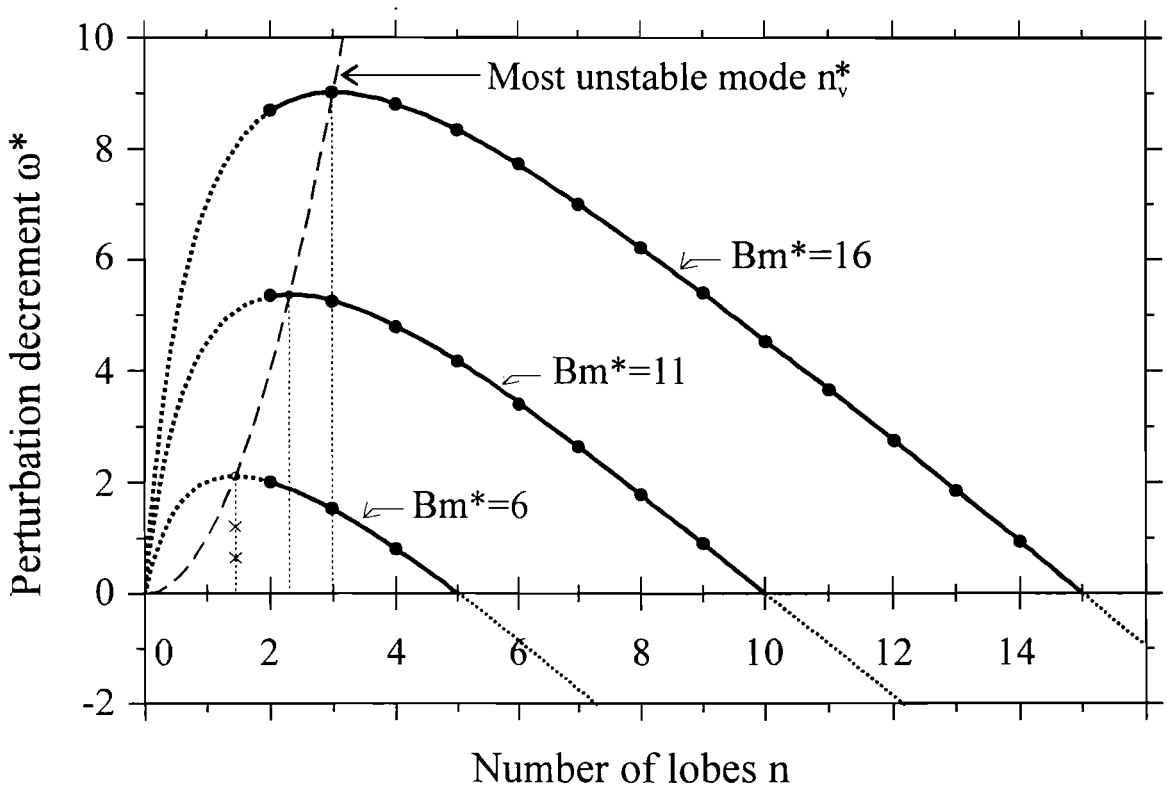

Figure 4.6. The spectrum of competing modes at Bm*=6; 11; 16 for a creeping flow

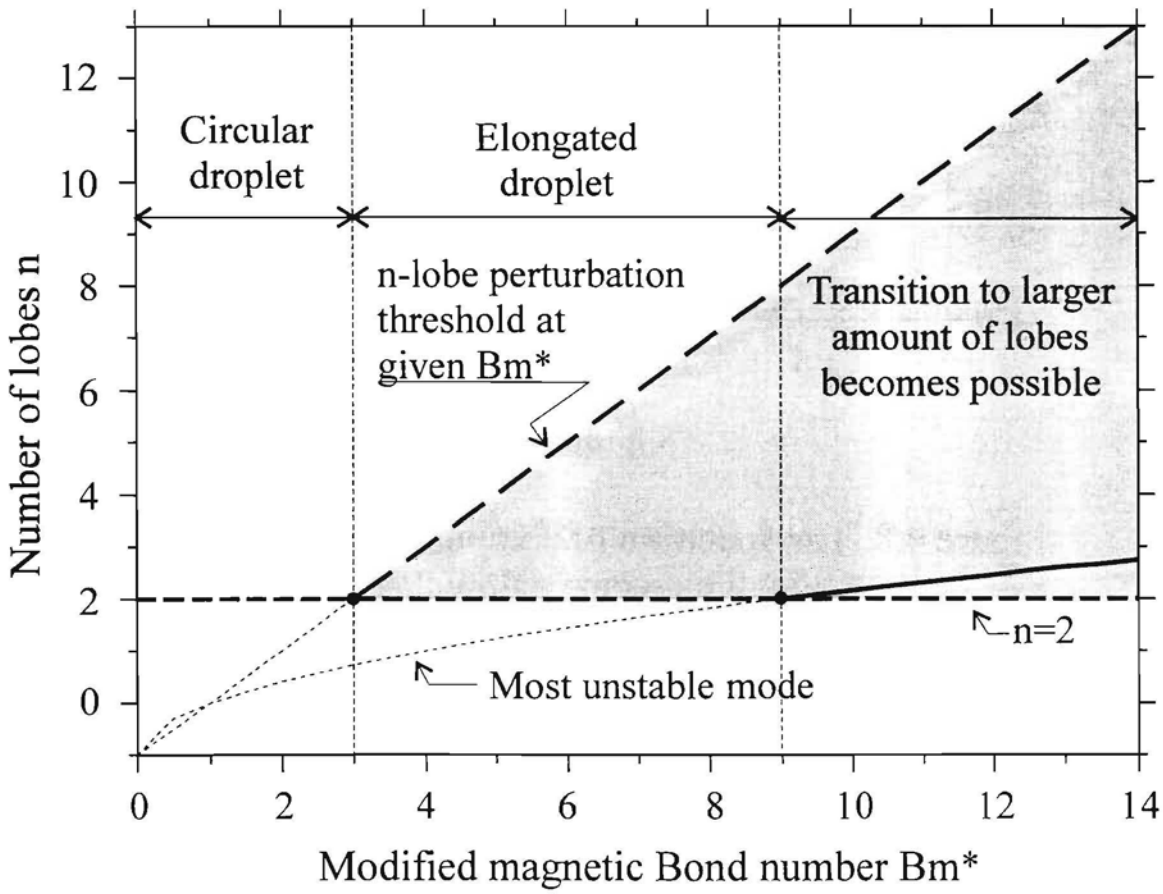

Figure 4.7. Transition diagram

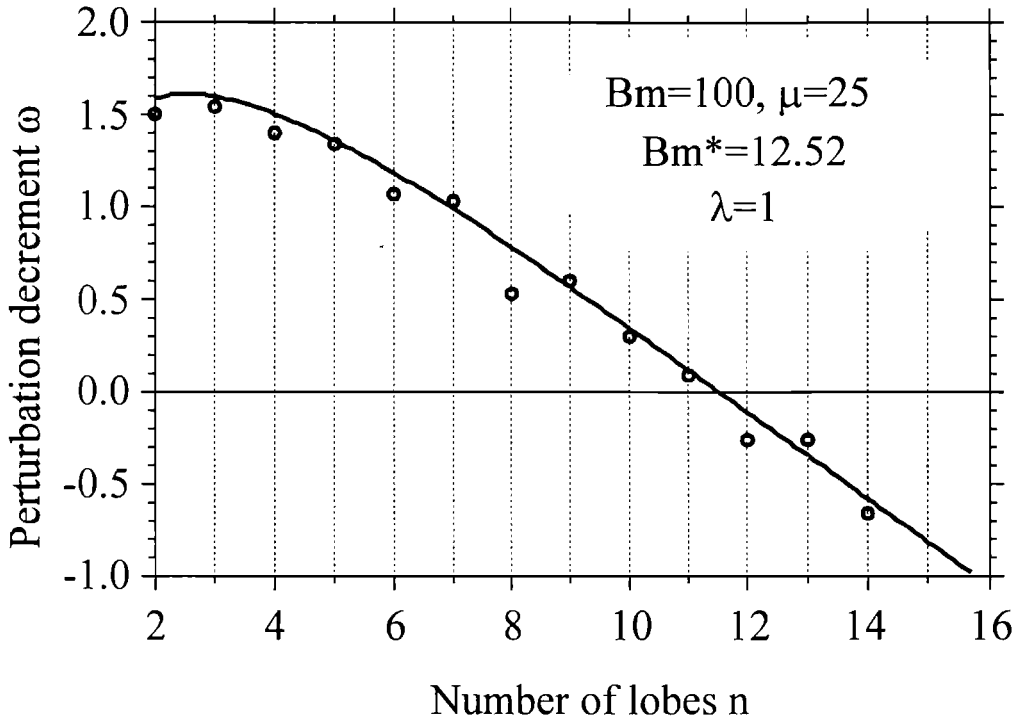

Figure 4.8. The spectrum of competing modes at Bm=100, λ=1, solid lide: the creeping flow theory, circles: BEM simulation

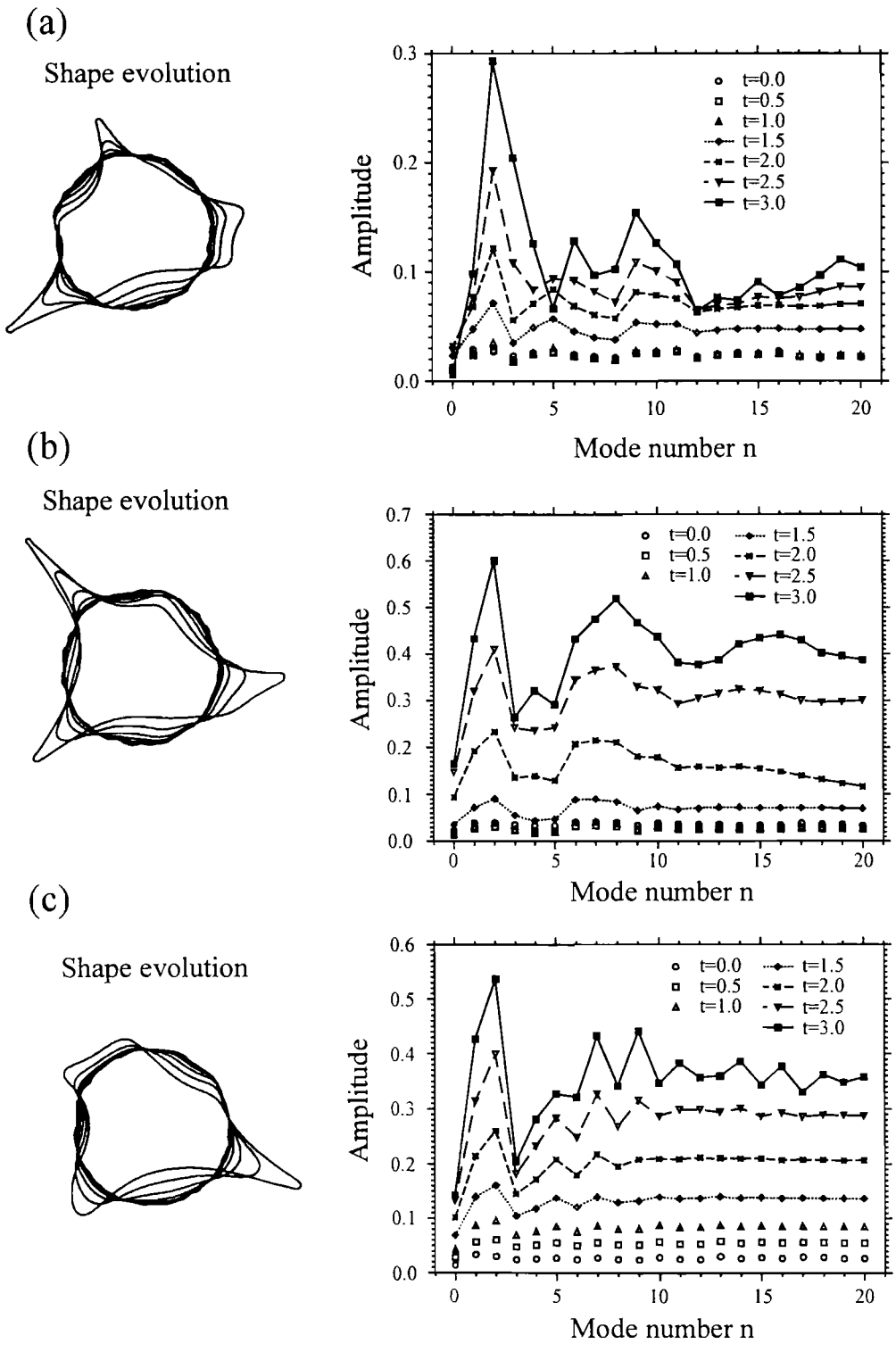

Figure 4.9(a)-(c). The amplitudes of modes versus a mode number n: the mode competition for a droplet with an initially perturbed surface. Bm=100, μ=25, Δt=0.01, N=200. The initial perturbation given by radial displacements from a circular shape in 60 equidistant points, generated randomly with the maximal value 0.03.

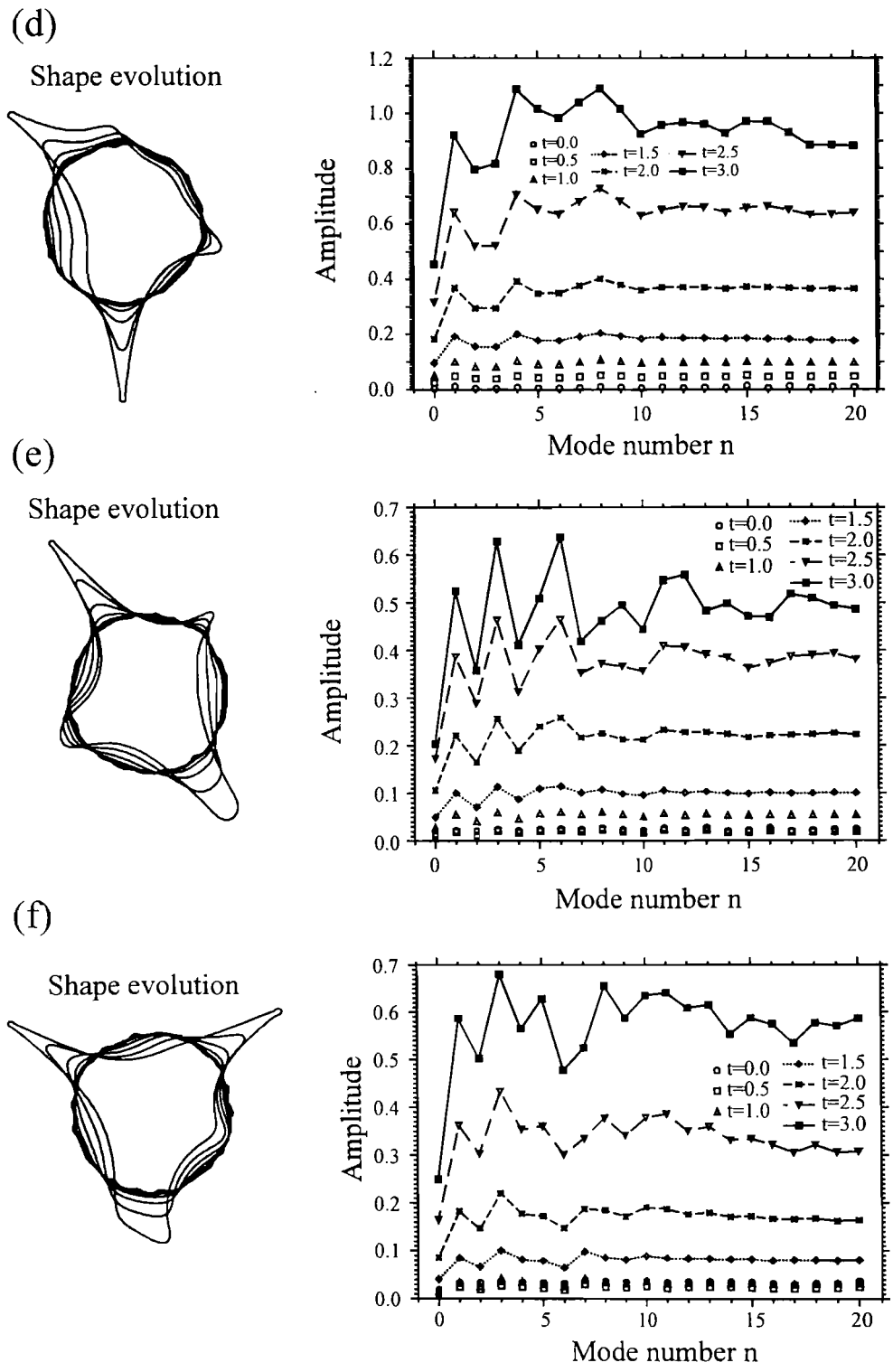

Figure 4.9(d)-(f). The amplitudes of modes versus a mode number n: the mode competition for a droplet with an initially perturbed surface. Bm=100, μ=25, Δt=0.01, N=200. The initial perturbation given by radial displacements from a circular shape in 60 equidistant points, generated randomly with the maximal value 0.03.

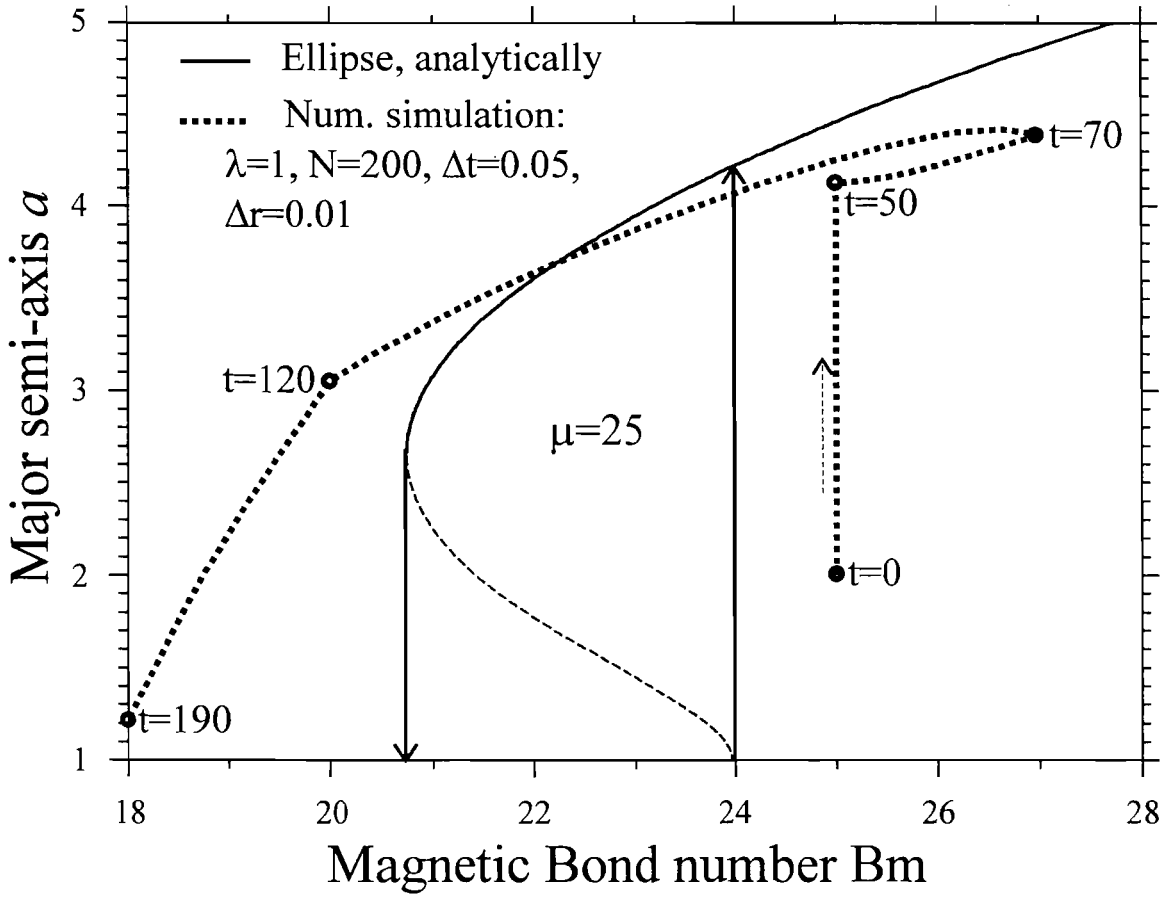

Figure 4.10. The elongation of the 2D droplet in a rotating magnetic field and the transition back to circular shape at the decrease of the magnetic Bond number below the turning point

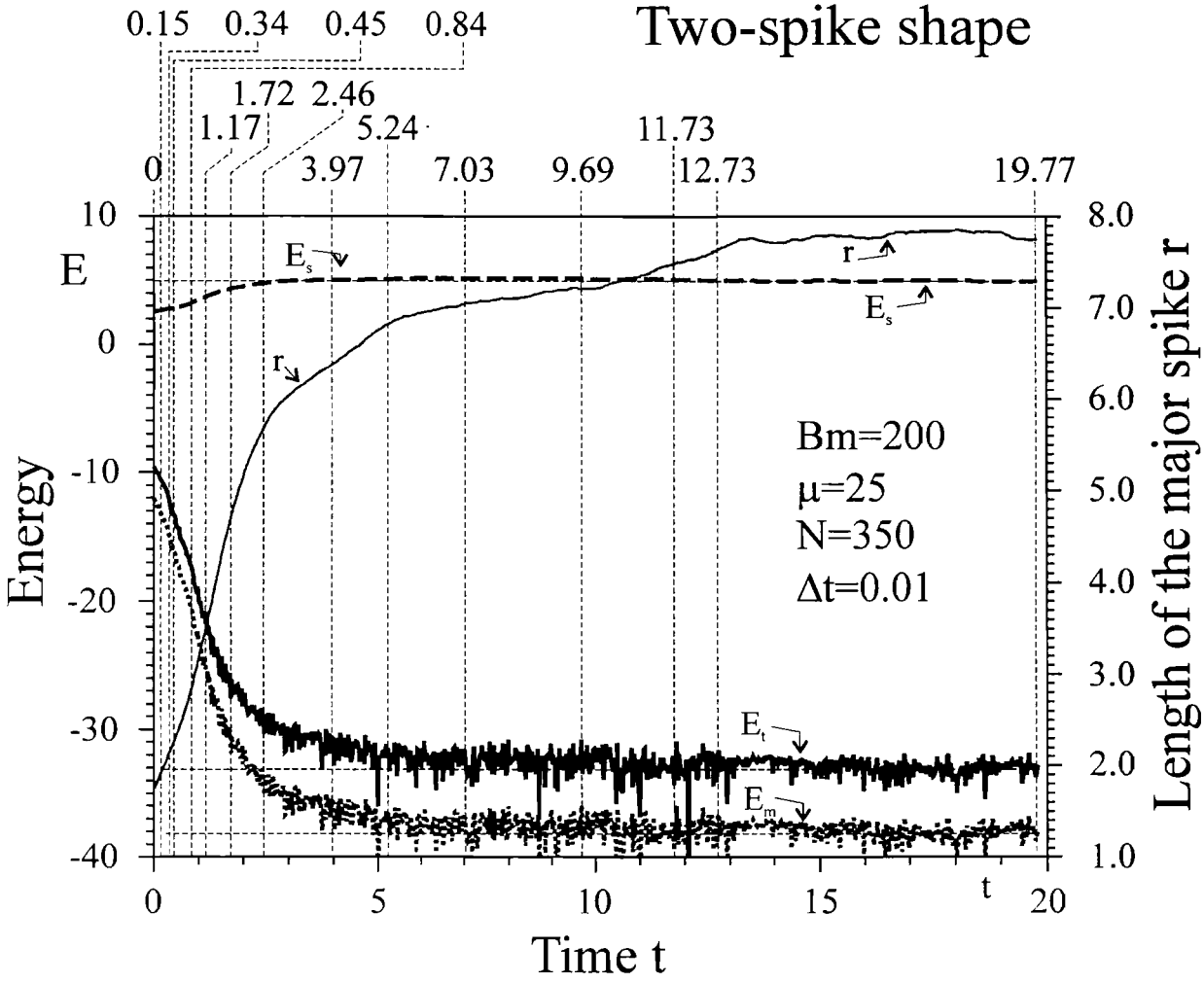

Figure 4.11. Surface, magnetic and total energies, and the length r of the major spike versus time t. The solid line: the total energy $E_t=E_m+E_s$, the dotted line: the magnetic energy E_m, the dashed line: the surface energy E_s, the thin solid line: the length *r* of the major spike, measured from the mass center of a droplet

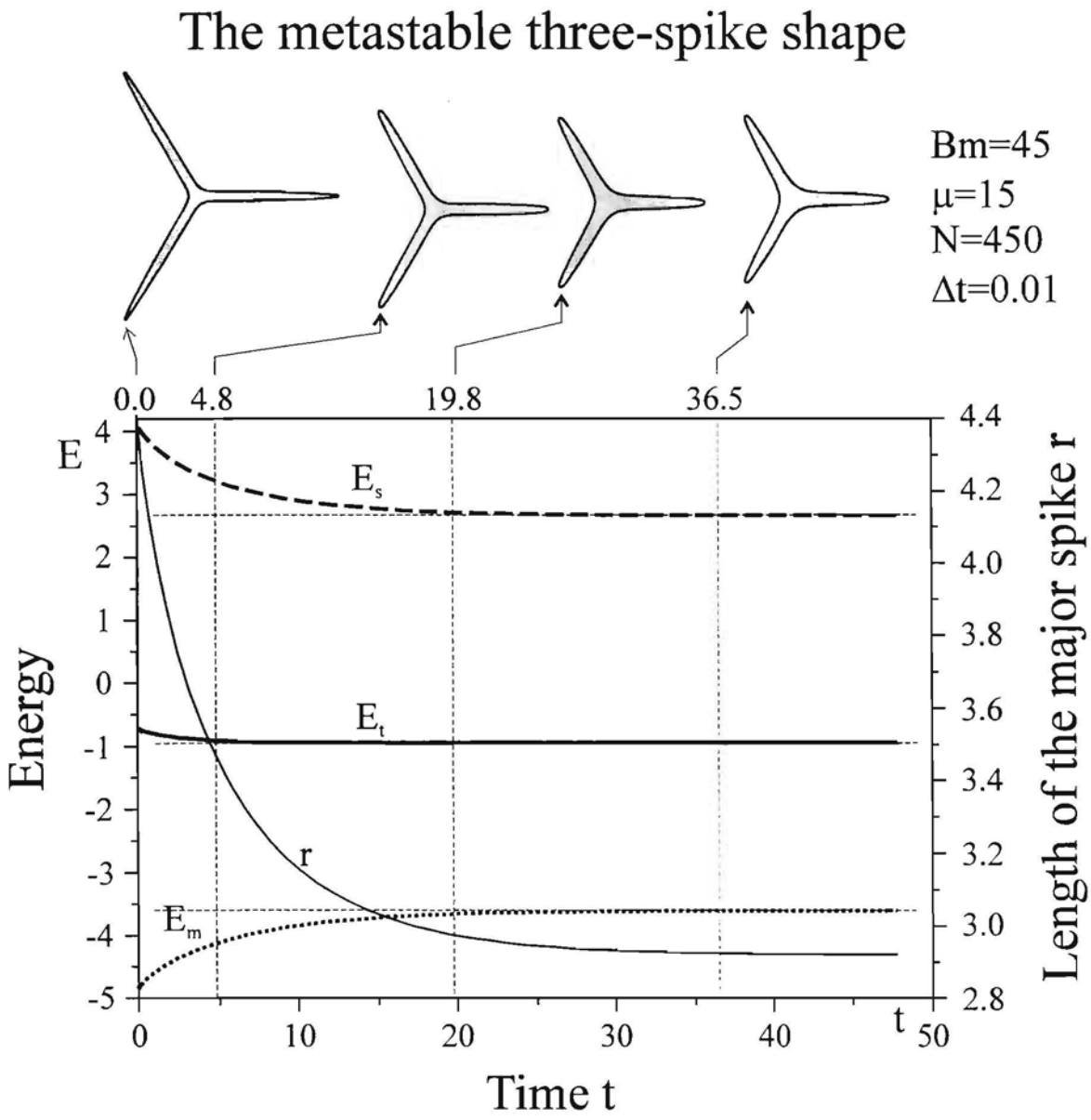

Figure 4.12. Surface, magnetic and total energies, and the length r of the major spike versus time t. The solid line: the total energy $E_t=E_m+E_s$, the dotted line: the magnetic energy E_m, the dashed line: the surface energy E_s, the thin solid line: the length *r* of the major spike, measured from the mass center of a droplet

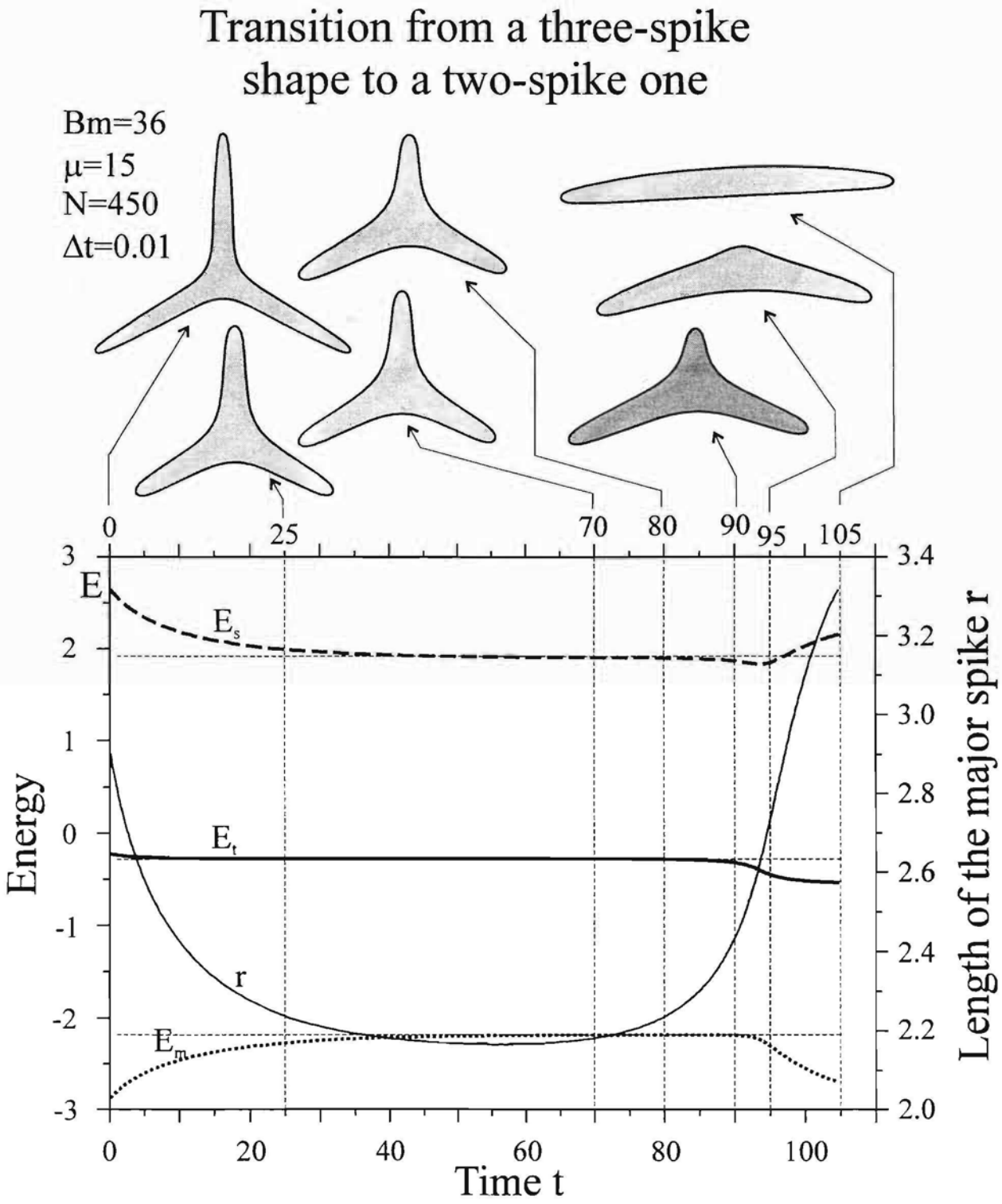

Figure 4.13. Surface, magnetic and total energies, and the length r of the major spike versus time t. The solid line: the total energy $E_t=E_m+E_s$, the dotted line: the magnetic energy E_m, the dashed line: the surface energy E_s, the thin solid line: the length *r* of the major spike, measured from the mass center of a droplet

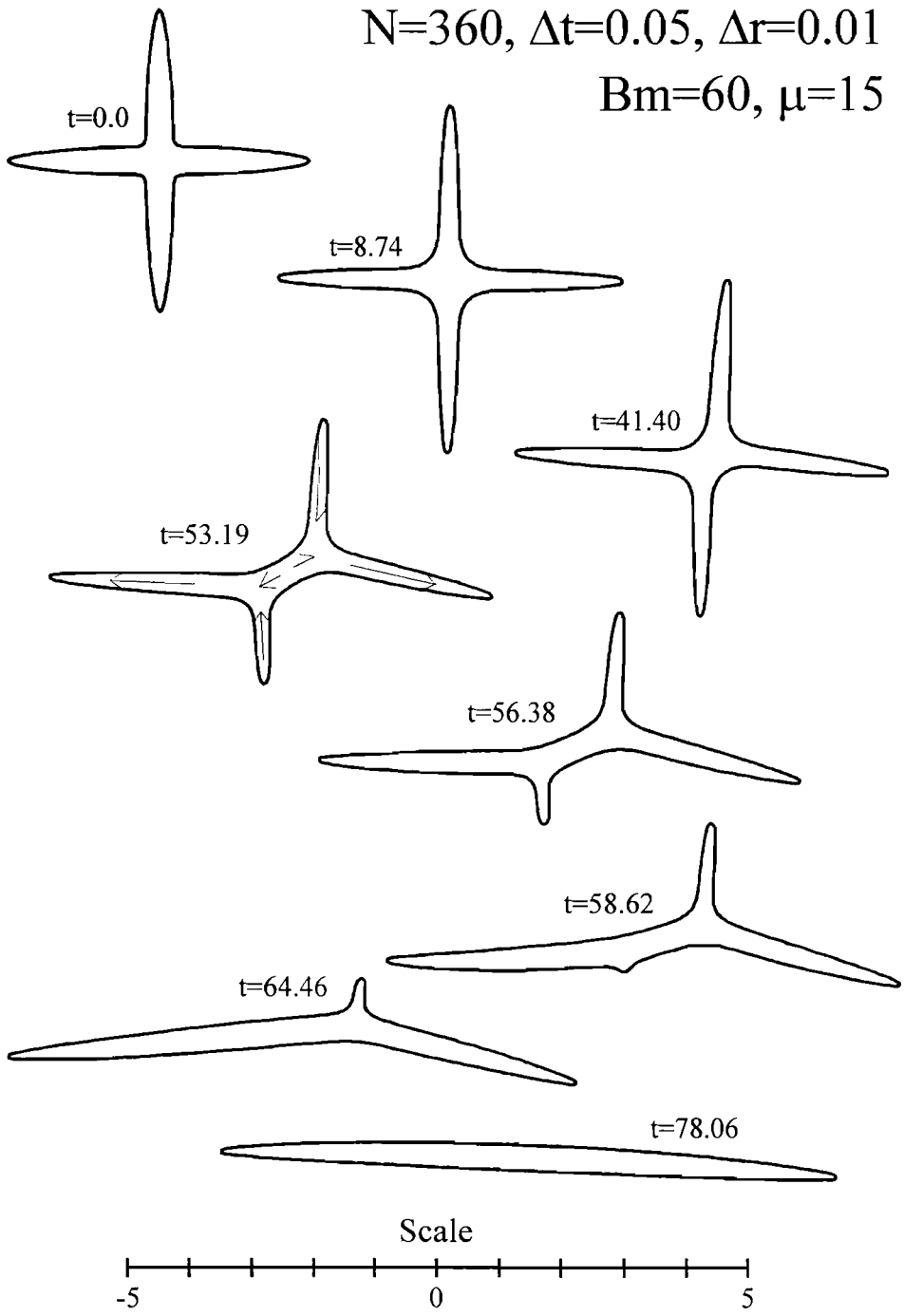

Figure 4.14. Transition from the four-spike shape to the two-spike one

Included paper:

Bacri J.C., Cēbers A., Lācis S., Perzynski R.

Numerical simulation of the transient stages of 2D magnetic fluid droplet in high-frequency rotating magnetic fields

Magnitnaya Gidrodinamika, 1996 (accepted to publish)

Numerical simulation of the transient stages of 2D magnetic fluid droplet in high-frequency rotating magnetic fields

J.C.Bacri (*), A.Cēbers (**), S.Lācis(**),R.Perzynski(*)

(*) Université P.M.Curie, 4 place Jussieu, 75252 Paris, Cedex 05, France
(**) Latvian Academy of Sciences, Institute of Physics, Salaspils-1, LV-2169, Latvia & Latvia University, Fac. Phys. Math., Raina boul. 19, Riga, LV-1586, Latvia

Abstract: It is found by numerical simulation that 2D magnetic fluid droplets in high-frequency rotating form shapes with 2 or 3 spikes. Number of spikes depends on both an initial shape of the droplet and a magnetic field strength. It is found that 3-spike shape of the droplet exists as metastable state and an energy barrier suppresses the transition to 2-spike shape which corresponds to the energy minimum. Results obtained dynamical simulation are in good agreement with the energy minimum calculations carried out previously. In the case of the initial shape with some perturbations, development of spikes and transition to smaller amount of them are observed. At increase of magnetic Bond number the spikes sharpens. Finally some conclusions concerning the comparison of the results of numerical simulation with the experimental observations are pointed out.

An experimental study of a magnetic fluid (MF) microdrop in a rotating magnetic field shows a wide variety of complex phenomena [1]. The complete theoretical description of all features of corresponding phenomena is yet absent. A linear small perturbation analysis gives us magnetic field threshold values with respect to n-lobe perturbations [1,2]. It is important to know if n-lobe shapes exist as stable or metastable configurations. In order to investigate that, we simulate numerically the behaviour of a MF droplet in 2D. Neglecting inertia terms in the Navier-Stokes equation one can use boundary integral equations [3] to describe creeping flow with a free boundary. A high frequency range of rotating magnetic field is considered, allowing to make time-averaging of forces. Thus here a small oscillatory motion of a surface of a droplet caused by field rotation is neglected.

Governing equations for fluid flow both inside and outside the droplet are

$$-\nabla p + \eta\nabla^2 \mathrm{v} + (\mathrm{M}\nabla)\mathrm{H} = 0, \qquad (1)$$

$$\mathrm{div}\,\mathrm{v} = 0. \qquad (2)$$

Here p is pressure, η : viscosity, **v** : fluid velocity, **H** : intensity of magnetic field, **M** : magnetisation of magnetic fluid. Outside the droplet fluid is non-magnetic, hence magnetisation M=0 and third term in left side of (1) is absent. Corresponding boundary conditions are

$$\mathrm{v}^{in} = \mathrm{v}^{ex}, \quad \sigma^{in}_{\tau n} = \sigma^{ex}_{\tau n},$$

$$-p^{in} + \sigma^{in}_{nn} = -p^{ex} + \sigma^{ex}_{nn} + 2\pi(\mathrm{Mn})^2 - \sigma/R_C. \qquad (3)$$

Here σ stays for surface tension but R_C represents local curvature of the boundary contour of 2D droplet, **n** : external normal, subscript 'in' denotes region occupied by MF droplet and 'ex' surrounding fluid.

Further in a paper a non-dimensional form for physical parameters and geometric dimensions of droplet is used. As characteristic values are chosen: external field strength H_0, surface tension σ, external fluid viscosity η_{ex} and unperturbed droplet (i.e. circle) radius R. Physical processes are characterised by magnetic Bond number $\mathrm{Bm} = \frac{H_0^2 R}{\sigma}$, characteristic decay time for free surface perturbations $\tau = \frac{\eta_{ex} R}{\sigma}$ and ratio of viscosities $\lambda = \frac{\eta_{in}}{\eta_{ex}}$. So we have non-dimensional coordinates $\tilde{x} = x/R$, $\tilde{y} = y/R$, a non-dimensional velocity $\tilde{\mathrm{v}} = \frac{\mathrm{v}}{R/\tau}$, a non-dimensional magnetic field $\tilde{\mathrm{H}} = \mathrm{H}/H_0$ and a non-dimensional time $\tilde{t} = t/\tau$. For simplicity further tildes are omitted.

Motion of MF droplet under the action of magnetic field is driven by effective surface forces assuming that magnetic volume force $(\mathbf{M}\nabla)\mathbf{H}$ is potential. Action of the gravity forces is neglected. Hence the effective time-averaged surface forces have only the normal component [3,4] which can be written in non-dimensional form as follows:

$$f_s^n = \frac{1}{R_L} - \frac{\mu - 1}{8\pi}\mathrm{Bm}\left(\mu\left\langle H_n^2\right\rangle + \left\langle H_t^2\right\rangle\right). \qquad (4)$$

Here μ is magnetic permeability of MF. One can see that magnetic field strength values on the boundary are needed to calculate surface forces. Both normal and tangential magnetic field strength components $\mathrm{H_n}$, $\mathrm{H_t}$ on the boundary are found as solutions of the corresponding boundary integral equations [4,5]:

$$H_n\big|_\Gamma = \frac{2H_{0X}}{(\mu+1)}\frac{\partial x}{\partial n} + \frac{2H_{0Y}}{(\mu+1)}\frac{\partial y}{\partial n} + \frac{1}{\pi}\frac{(\mu-1)}{(\mu+1)}\oint_L H_n(l')\big|_\Gamma K(\bar{r},\bar{r}')\frac{dl'}{\sqrt{x_l'^2 + y_l'^2}}, \qquad (5)$$

$$H_t\big|_\Gamma = \frac{2H_{0X}}{(\mu+1)}\frac{\partial x}{\partial l} + \frac{2H_{0Y}}{(\mu+1)}\frac{\partial y}{\partial l} - \frac{1}{\pi}\frac{(\mu-1)}{(\mu+1)}\oint_L H_t(l')\big|_\Gamma K(\bar{r},\bar{r}')\frac{dl'}{\sqrt{x_l'^2 + y_l'^2}}, \qquad (6)$$

$$K(\bar{r},\bar{r}') = \frac{x_l'(y'-y) - y_l'(x'-x)}{(y'-y)^2 + (x'-x)^2}.$$

Here l is a natural parameter: contour arc length.

Approximation technique, applied to the equations (5),(6), is described in details in [3,4,5,6]. Magnetic field strength is calculated at discrete marker points $\mathbf{r}_i$. To carry out time averaging, $\mathrm{H_n}$, $\mathrm{H_t}$ are expressed by $\mathrm{H_{0X}}$, $\mathrm{H_{0Y}}$ in every k-th marker point:

$$H_n(\mathrm{r}_k) = \left(\alpha_{Xk}^n H_{OX} + \alpha_{Yk}^n H_{OY}\right)\Big/\sqrt{x_l'^2(k) + y_l'^2(k)},$$

$$H_t(\mathrm{r}_k) = \left(\alpha_{Xk}' H_{OX} + \alpha_{Yk}' H_{OY}\right)\Big/\sqrt{x_l'^2(k) + y_l'^2(k)}.$$

Expanding the unknowns $\alpha_{X,Yk}^{n,t}$ by the series of pyramidal functions similarly to [5], obtained equations are

$$\sum_{k=1}^{N}\begin{pmatrix}\alpha'_{Xk}\\ \alpha'_{Yk}\end{pmatrix}A_{ik}^{+}=\sum_{k=1}^{N}\begin{pmatrix}\alpha'_{Xk}\\ \alpha'_{Yk}\end{pmatrix}\left[R_{ik}+I_{ik}\right]=\frac{1}{\mu+1}\begin{pmatrix}x_{i+1}-x_{i-1}\\ y_{i+1}-y_{i-1}\end{pmatrix}, \qquad (7)$$

$$\sum_{k=1}^{N}\begin{pmatrix}\alpha''_{Xk}\\ \alpha''_{Yk}\end{pmatrix}A_{ik}^{-}=\sum_{k=1}^{N}\begin{pmatrix}\alpha''_{Xk}\\ \alpha''_{Yk}\end{pmatrix}\left[R_{ik}-I_{ik}\right]=\frac{1}{\mu+1}\begin{pmatrix}-(y_{i+1}-y_{i-1})\\ x_{i+1}-x_{i-1}\end{pmatrix}, \qquad (8)$$

$$I_{ik}=\begin{cases}\dfrac{l_i-l_{i-1}}{6}, & i=k+1\\ \dfrac{l_{i+1}-l_i}{6}, & i=k-1\\ \dfrac{l_{i+1}-l_{i-1}}{3}, & i=k\\ 0, & i\neq k-1\wedge i\neq k-1\wedge i\neq k-1\end{cases},$$

$$R_{ik}=R_{ik}^{*}\frac{(\mu-1)(l_{k+1}-l_{k-1})(l_{i+1}-l_{i-1})}{4\pi(\mu+1)},$$

$$R_{ik}^{*}=\begin{cases}\dfrac{y_I(i)(x(i)-x(k))-x_I(i)(y(i)-y(k))}{(x_I(i)-x_I(k))^2+(y_I(i)-y_I(k))^2}, & i\neq k\\ \dfrac{y_{II}(i)x_I(i)-x_{II}(i)y_I(i)}{2(x_I^2(i)+y_I^2(i))}, & i=k\end{cases}.$$

The contour is approximated by interpolating with cubic spline functions coordinates of the finite number of marker points. First and second derivatives along the boundary contour (x_I, x_{II}, y_I, y_{II}) are calculated by differentiating the interpolating cubic spline functions for both coordinates. For better accuracy of the numerical treatment of the tips of the droplet, which have large curvature, special non-equidistant distribution of the marker points is used: the arc lengths between them depend on the local curvature of the contour.

For rotating field we have $H_{0X}=\cos t\Omega$, $H_{0Y}=\sin t\Omega$ what lead to

$$\left(\mu\left\langle H_n^2\right\rangle+\left\langle H_t^2\right\rangle\right)_{r=r_k}=\frac{1}{2}\frac{\mu\left(\alpha''^{\,2}_{Xk}+\alpha''^{\,2}_{Yk}\right)+\left(\alpha'^{\,2}_{Xk}+\alpha'^{\,2}_{Yk}\right)}{x_I^2(k)+y_I^2(k)}. \qquad (9)$$

Surface motion is calculated using the potential theory of viscous (creeping) flow, described in [6,7]. The corresponding boundary integral equation for 2D is

$$v_i(\vec{x})=-\frac{1}{2\pi(1+\lambda)}\oint_L n_j f_s'' G_{ij}(\vec{x},\vec{x}')dl'+\frac{1-\lambda}{4\pi(1+\lambda)}\oint_L v_j(\vec{x}')n_k(\vec{x}')f_s'' T_{ijk}(\vec{x},\vec{x}')dl', \qquad (10)$$

where

$$G_{ij}(\vec{x},\vec{x}')=-\delta_{li}\ln|\vec{x}'-\vec{x}|+\frac{(x_i'-x_i)(x_l'-x_l)}{|\vec{x}'-\vec{x}|^2},$$

$$T_{ijk}(\vec{x},\vec{x}')=-4\frac{(x_i'-x_i)(x_j'-x_j)(x_k'-x_k)}{|\vec{x}'-\vec{x}|^4}.$$

Boundary integral equation (10) approximation is similar to [3]:

$$\sum_{j=1}^{N} v_m(j)\left[\delta_j^i + P_{m,ij}\right] = Q_{m,i}; \quad m = x, y; \quad i = 1,2,\ldots,N, \qquad (11)$$

$$P_{m,ij} = \begin{cases} 0, & i = j \\ \dfrac{1}{\pi}\dfrac{1-\lambda}{1+\lambda}\left[v_k(j)(x_k(j)-x_k(i))\right]\left[n_s(j)(x_s(j)-x_s(i))\right]\times, & \\ \qquad \dfrac{(x_m(j)-x_m(i))(l_{j+1}-l_{j-1})}{2\left|\vec{x}(j)-\vec{x}(i)\right|^4}, & i \neq j \end{cases}$$

$$Q_{m,i} = \frac{1}{2\pi(1+\lambda)}\sum_{j=1}^{N}\left(\delta_j^k \ln\left|\vec{x}(j)-\vec{x}(i)\right| - \frac{(x_j(j)-x_j(i))(x_k(j)-x_k(i))}{\left|\vec{x}(j)-\vec{x}(i)\right|^2}\right) \times$$

$$f_s^n(j)n_k(j)\frac{l_{j+1}-l_{j-1}}{2} -$$

$$\frac{1}{4}\left[\Delta l_i G_m(i+1) + \Delta l_{i-1} G_m(i-1) + 3(\Delta l_i + \Delta l_{i-1})G_m(i)\right] +$$

$$\frac{G_m(i)}{2}\left[\Delta l_i \ln\left|\vec{x}(i+1)-\vec{x}(i)\right| + \Delta l_{i-1}\ln\left|\vec{x}(i)-\vec{x}(i-1)\right|\right]$$

$$f_s^n(i) = \left(\frac{y_{II}(i)x_I(i) - x_{II}(i)y_I(i)}{\sqrt{x_I^2(i)+y_I^2(i)}} - \frac{\mu-1}{16\pi}Bm\left(\mu\left(\alpha_{xk}^{n\,2} + \alpha_{yk}^{n\,2}\right) + \left(\alpha_{xk}^{t\,2} + \alpha_{yk}^{t\,2}\right)\right)\right) \Big/ \left(x_I^2(i) + y_I^2(i)\right)$$

$$\Delta l_j = l_{j+1} - l_j.$$

As one can see, for $\lambda=1$ ($\eta_{in}=\eta_{ex}$) term $P_{m,ij}$ in (11) disappears and we have explicit expression for velocity v:

$$v_m(i) = Q_{m,i}\ ; \quad m = x, y; \quad i = 1,2,\ldots,N \qquad (12)$$

If $\lambda \neq 1$ $(\eta_{in} \neq \eta_{ex}$, then the set of linear algebraic equations (11) must be solved, what increases computational time considerably.

Two numerical simulations, shown in Fig.1a,b, represent dynamical developments of the droplet shape from two different arbitrary initial shapes. These shapes are generated artificially, by randomly distributed perturbations in selected points joined by lines. As one can see, random initial perturbations can lead to very different states. Final shapes show that both 2-spike and 3-spike configurations can exist in time intervals, which are longer than the characteristic transition time. In both cases N=350 marker points for boundary discretisation are taken, μ=25 and magnetic Bond number Bm=200. These simulations are extremely CPU-time expensive since require sufficient refinement of a discrete representation of the boundary. Numerical simulations clearly show that in 2D after maybe quite long evolution to final state the 2-spike configuration is realised in high-frequency rotating field. This conclusion from the results of a numerical simulation is in correspondence with the conclusions drawn in [4] on a basis of purely energetical grounds: whatever is the magnetic Bond number 2-spike configuration always corresponds to the lowest energy. From our simulation results it follows that 3-spike configurations can be observed as quite long-living

transient states (see Fig.1b). In that connection the question arises are 3 and more spike configurations existing as possible 2D equilibrium figures in high-frequency rotating fields. To check it numerically we have done numerical simulations from symmetric initial states. In that case we can hope to obtain the metastables states with higher number of spikes than 2. The results of numerical simulations shown on Fig.2 indeed confirm the existence of metastable three spike-configuration. On Fig.2a starting from symmetric 3-spike shape at $Bm=45>Bm_c^{(3)}$ [2,4] the establishment of the figure of equilibriums with 3-spikes is observed. The decrease of Bm below $Bm_c^{(3)}=37.5$ causes slow evolution to 2-spike shape (Fig. 2b). Thus as it has been already concluded from the energetical calculations the numerical simulation of the dynamics of the droplet in high-frequency field show that the ground state corresponds to 2-spike configuration. Configurations with higher number of spikes can be obtained from very symmetric initial conditions. We must recognise that this behaviour is quite distinct from 3D droplets [1], where observed number of spikes grows proportionally to the square of the magnetic field strength. A 2D model can not describe the behaviour of the droplet as observed in experiment and at present moment we believe that it is caused by pure 2D properties of it. Main conclusion is that 3-spike shape of 2D droplet is stable in high frequency magnetic field, because transition to 2-spike shape is suppressed by the presence of an energy barrier. These results are in good agreement with the energy minimum calculations, carried out in [4].

Concerning the behaviour of 2D droplets it seems quite interesting to study the transitions with different number of spikes at decrease of the frequency of rotating field. In the case arising oscillations can be large enough to cause the transition over energy barrier from, for example, 3-spike configuration to 2-spike configuration. We presume to study this interesting problem in future.

This work was supported by "Le Réseau Formation Recherche n°90R0933 du Ministère de l'Enseignement Superieur et de la Recherche" of France. Two of us (A.Cēbers, S.Lācis) are thankful to International Science Foundation for financial support of the research in terms of long-time grants LBG000 and LJQ100.

References

[1] *Bacri J.C., Cebers A.O., Perzynski R.* Behaviour of a magnetic fluid microdrop in a rotating magnetic field // Phys.Rev.Lett. - 1994. - Vol.72, N17 - PP.2705-2708

[2] *Cēbers A.O., Lācis S.* Magnetic fluid free surface instabilities in high frequency rotating magnetic fields // Brazilian Journal of Physics - 1995. - Vol.25, N2 - PP.101-111

[3] *Cebers A.* // Magnitnaya Gidrodinamika (in Russ), 1986, N4, pp.3-10

[4] *Bacri J.C., Cēbers A., Lācis S., Perzynski R.* Shapes of 2D magnetic fluid droplets in a rotating magnetic field // Magnitnaya Gidrodinamika (to appear)

[5] *Bacri J.C., Cēbers A., Lācis S., Perzynski R.* Dynamics of the magnetic fluid droplet in rotating field // J. Magn. Magn. Mater. (to appear)

[6] *Pozrikidis C.* Boundary Integrals and Singularity Methods for Linearized Viscous Flow - Cembridge University Press - 1992. - P.260

[7] *Ladyzhenskaya O.A.* The Mathematical Theory of Viscous Incompressible Flow - Gordon & Breach - 1969.

Captions

Fig.1. Numerical simulation started from perturbed state, leading to 2-spike and 3-spike shapes.

Fig.2. Numerical simulation started from symmetric 3-spike shape.
a) stable 3-spike state ($Bm>Bm_c^{(3)}$),
b) transition of 3-spike shape to 2-spike shape ($Bm<Bm_c^{(3)}$),.

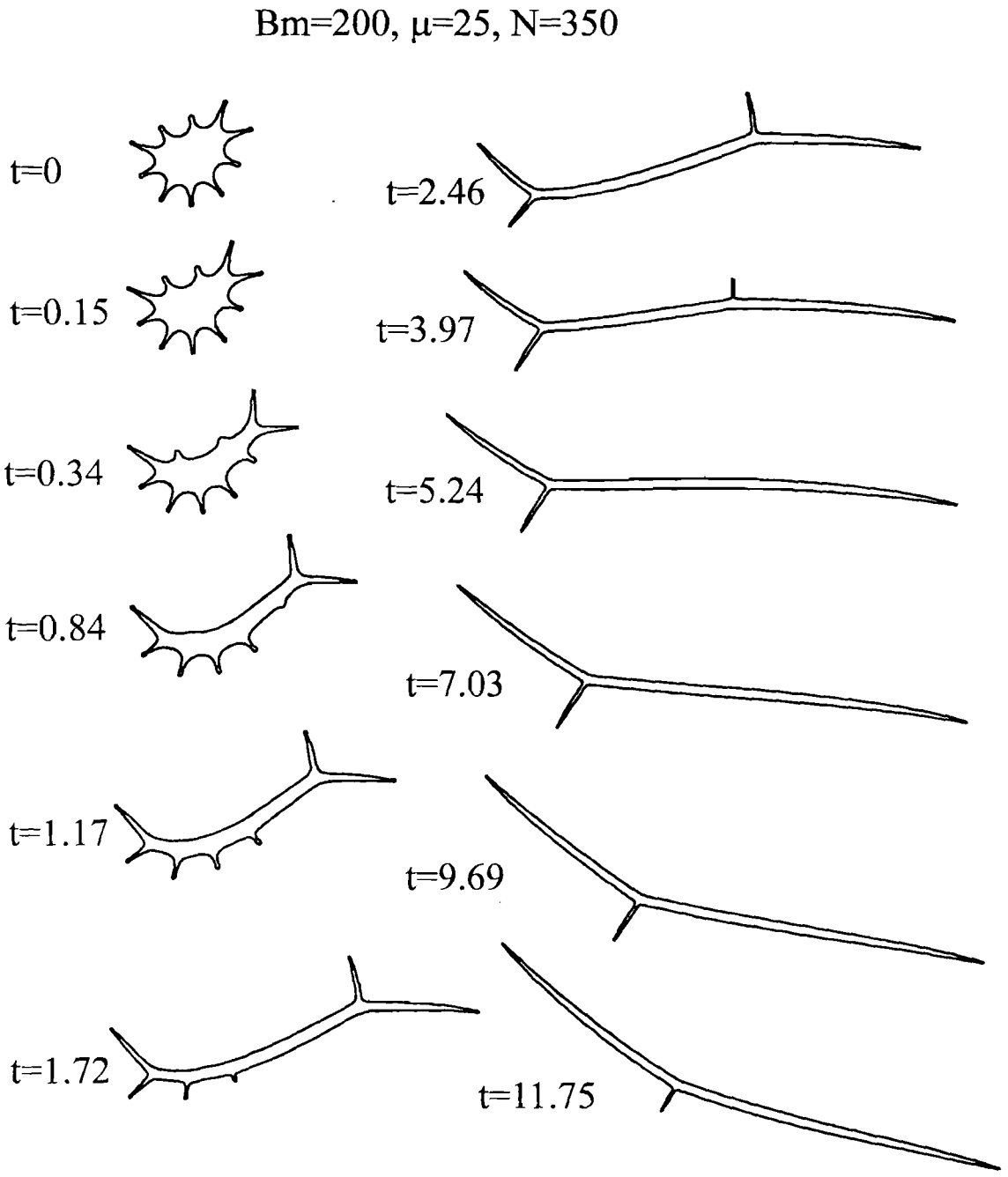
Bm=200, μ=25, N=350
t=0
t=0.15
t=0.34
t=0.84
t=1.17
t=1.72
t=2.46
t=3.97
t=5.24
t=7.03
t=9.69
t=11.75

Figure 1a

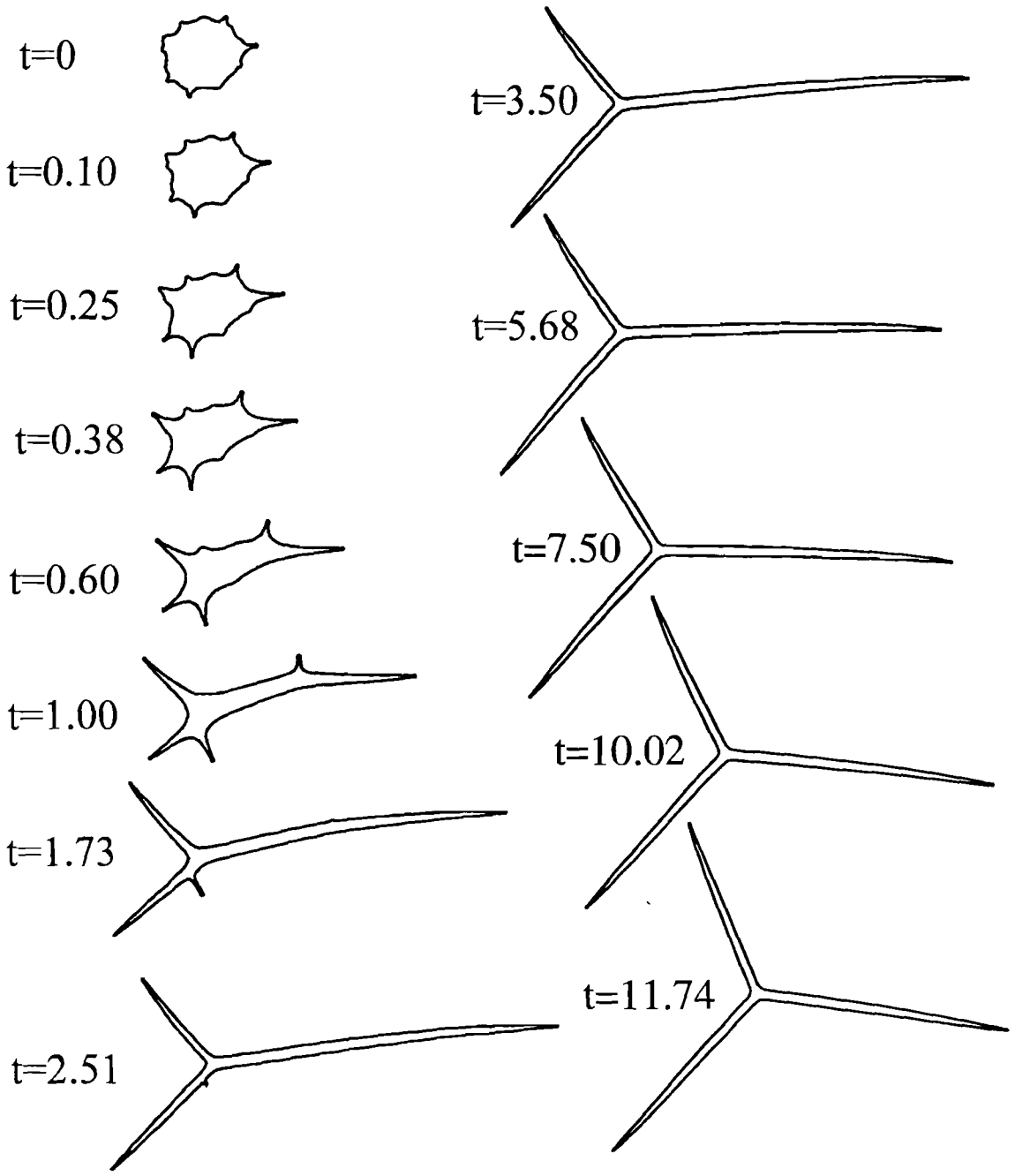
Bm=200, μ=25, N=350
t=0
t=0.10
t=0.25
t=0.38
t=0.60
t=1.00
t=1.73
t=2.51
t=3.50
t=5.68
t=7.50
t=10.02
t=11.74

Figure 1b

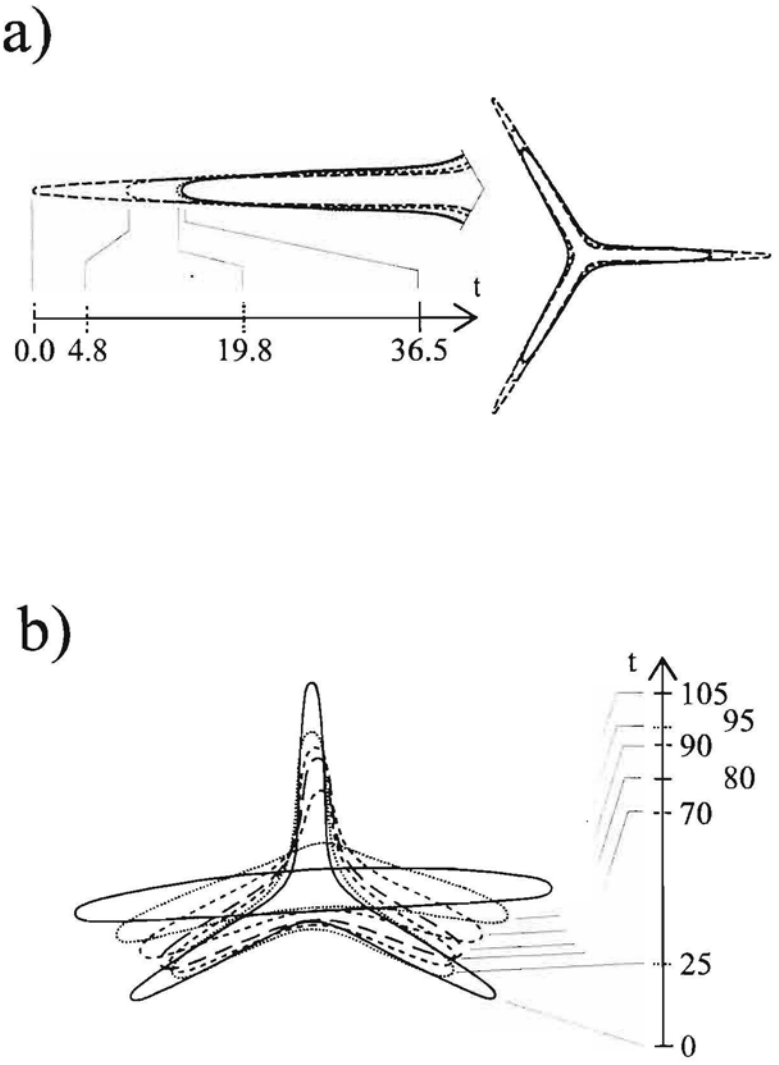

Figure 2

Conclusions

1. The small perturbation linear analysis gives the number of lobes of the most unstable mode in dependence on magnetic field strength. In the case of the potential flow in 2D the number of lobes is proportional to the square of the magnetic field strength, in the case of pure creeping flow it is directly proportional to the magnetic field. The last relation is proved by the results of a numeric simulation.

2. The threshold value in respect to 2-lobe perturbation (4.4) for the magnetic Bond number Bm turns out to be the absolute threshold in respect to any perturbation, what is proved by BEM simulation (see Fig.2.7). If Bm is smaller than this absolute threshold value, a droplet holds circular shape.

3. It is found that in 2D there are only two stable shapes: 2-spike shape and 3-spike one. The 3-spike shape exists like metastable state, since 2-spike shape has less energy. The decrease of a magnetic field below the turning point or, by a sufficiently high perturbation the transition to 2-spike shape takes place. Evidently there exists no in 2D metastable shapes with more than three spikes in a high-frequency rotating magnetic field under assumptions used in the present work.

4. There is no the stable 4-spike shape found by numerical simulations. Evidently a shape with four and more spikes is unstable in respect to splitting of the "body", where spikes comes together.

Chapter 5

Magnetic fluid droplet in low-frequency rotating magnetic fields

The behaviour of a ferrofluid droplet in low frequency magnetic field [5*,63*] have a similar character to one of the motion of bounded spheres in [9,57,101,102]. The essential difference obviously is that in the case of a droplet there is a fluid flow inside the droplet and the surface tension effects are quite different from the bound which exist between pair of magnetic holes (microspheres in ferrofluid) in [57,101,102] or between pair of magnetic particles in [9].

In the low-frequency range the rotating field is given as

$$\begin{cases} H_{0X} = H_0 \cos \omega t, \\ H_{0Y} = H_0 \sin \omega t, \end{cases} \qquad (5.1)$$

and the magnetic term in the surface forces formula (1.26) becomes essentially time-dependent.

Thus the BEM method is used in such a way that at first the marker points, which describe the boundary, are redistributed according to the actual local curvature of the boundary contour. To prevent the too dense accumulation of marker points in some local places and rarefaction of them in others, the limits of lover and higher allowable curvatures for marker point distribution are given as input data for a computer code. To solve time dependent free moving boundary problem, in every discrete time instant the magnetic field is calculated according to (2.12) and (2.15) by the Gaussian elimination method. Obtained magnetic field components are implemented in (1.26) to calculate a surface force, needed by (2.33) and (2.34). Once the velocity field at the boundary is calculated, the position of the interface is

advanced by Euler scheme. There are two mechanisms to control time step, initial value of which is given by default. The first mechanism controls the shift of every marker point so that it does not exceed the *a priori* given limit, and time step is adjusted to satisfy this requirement. The second mechanism controls the time step in such a way that the shift of every marker point exceeds no 20% of distance to the nearest neighbour. The calculations performed at $\lambda \neq 1$ have shown that present method, described in Chapter 2, works up to $\lambda=10$, but this limiting value already is critical to perturbation of the droplet shape at tips for a rotational motion, what obviously is a numerical artefact.

The numerical simulation via BEM indicate two scenarios [5*] of the droplet's behaviour in dependence on a value of the magnetic Bond number $Bm=(H_0)^2R/\sigma$. These scenarios are based on the fact that the magnetic torque, acting to the droplet in a magnetic field has some maximal value, which for fixed shape is frequency independent. The friction torque, which is present due to the viscous stresses in creeping flow around the droplet are proportional, in contrary, to the angular velocity of the droplet's rotation. In high-frequency rotating field, droplet could stay elongated only if the magnetic Bond number has high enough value. Therefor there are two scenarios [5*,63*]:

1. "Low-field" behaviour:

If the magnetic Bond number is less than the critical value Bm_{cr}, the droplet can not stay elongated in the high-frequency rotating magnetic field; the extension of a droplet in stationary configurations is diminishing with the increase of the rotating field frequency, and the maximal phase lag value $\pi/4$ is reached at infinite frequency. The rotation of the droplet's shape in this case is not identical to the quasi-solid rotation of the droplet. This shape movement is caused by rather intrinsic flow inside the droplet, which is more like the travelling wave propagation on the surface of fluid.

2. "High-field" behaviour:

For the magnetic Bond numbers larger than the critical one the maximal phase lag ($\approx\pi/4$) is reached already at a finite critical frequency Ω_{CR}. If the field

frequency Ω_H exceeds Ω_{CR}, the phase lag between the field and the droplet increases more and more, exceeds the value $\pi/2$, and the droplet moves toward the field. Thus beyond the critical frequency the motion of the droplet starts to be "jerky": the rotations alternates with stops and backward motions [5*].

The BEM simulation have proved that the shape of a droplet in the case of steady motion is near to the elliptic one if the ratio of viscosities $\lambda=\eta_{in}/\eta_{ex}=1$. The two different sets of equations of motion are derived in [5*,63*] and the sufficient agreement with BEM simulation is found (see Fig.2 in [5*] and Fig.2 in [63*]). On the basis of these equations the stability of the steady motion of a ferrofluid droplet in subcritical frequency range is explained in [5*]. To illustrate the "high-field" behaviour, in Fig.5.1 the time-averaged frequency $\overline{\Omega}$ of the droplet rotation is plotted versus magnetic field frequency Ω_H. The first part of the figure ($\Omega_H<\Omega_{CR}$) shows the steady motion, when the droplet follows the rotation of a magnetic field. The shapes of a droplet and the orientation of the magnetic field vector indicate how the phase lag between the droplet orientation and the magnetic field direction increases and the elongation of a droplet decreases as Ω_H approaches the critical frequency Ω_{CR}. Beyond the critical frequency ($\Omega_H>\Omega_{CR}$) the motion of a droplet becomes "jerky", what is illustrated by the trajectories of the droplet's tip. Increasing a field frequency Ω_H, the oscillations of a droplet tip becomes more often but the oscillation amplitude decreases.

What is the difference between the two sets of equations of motion [5*,63*]? The first what should be mentioned is that the equations of motion in [5*] are obtained in more approximate way than ones in [63*]. Nevertheless even such a phenomenological approach have yielded rather good agreement.

The configuration of the elliptic droplet is described by its large semi-axis a and the phase lag ϑ of the large semi-axis with respect to the field direction (see Fig.1a in [5*]). The First set is obtained by separation of the motion of the elliptical 2D droplet in two processes [5*], as it is described below:

$$\dot{a} = \frac{a^2}{\pi(\lambda + p)}\left[\frac{(\mu-1)^2}{16}\mathrm{Bm}\, a\left(\frac{h_a^2}{\left(a^2+\mu\right)^2} - \frac{h_a^2}{\left(a^2\mu+1\right)^2}\right) - \frac{\Phi(a)}{a^4-1}\right], \qquad (5.2)$$

$$\dot{\varphi} = h_a h_b \frac{Bm}{8\pi} \frac{(\mu-1)^2 a^2 (a^4-1)}{(a^2+\mu)(a^2\mu+1)(a^4+1)}, \qquad (5.3)$$

Here $h_a = \cos\vartheta$, $h_b = \sin\vartheta$, ϑ being the phase lag between the instantaneous direction of a field and the orientation of the major semi-axis of an elliptical shape of a droplet. The definition of term $\Phi(a)$ is given in [5*,63*] (both papers are included in the present chapter).

The first process is an extension-contraction motion caused by the surface tension and the action of a magnetic field. The change rate of the total energy in this process is balanced by an energy dissipation in the viscous flow inside and outside the droplet. The energy dissipation inside the droplet is approximated by the homogeneous extension-contraction motion, the energy dissipation outside is assumed to be proportional to the one inside the droplet up to phenomenological parameter p divided by the ratio of viscosities λ. Thus from the energy balance [5*] the equation (5.2) is obtained. To describe the second process, namely the droplet rotation, the balance of the viscous and magnetic torques is considered. The friction torque of viscous forces is determinated by a creeping flow around rotating rigid elliptic cylinder [5*, 59], and it has to be balanced by a magnetic torque [5*] arriving at (5.3).

To derive the Second set

$$\dot{a} = \frac{2a^4}{\pi(a^4+1+2\lambda a^2)} \times \left[\frac{(\mu-1)^2}{16} Bm\, a \left(\frac{h_a^2}{(a^2+\mu)^2} - \frac{h_a^2}{(a^2\mu+1)^2}\right) - \frac{\Phi(a)}{a^4-1}\right], \qquad (5.4)$$

$$\dot{\varphi} = h_a h_b \frac{Bm}{8\pi} \frac{(\mu-1)^2 a^2}{(a^2+\mu)(a^2\mu+1)} \frac{2a^2 \frac{a^4+1}{a^4-1} + \lambda(a^4-1)}{2a^2 + \lambda(a^4+1)}. \qquad (5.5)$$

the virial moment technique [25,42,41] is used to satisfy the dynamic boundary conditions integrally [63*]. Fluid flow outside the droplet is treated exactly, applying the 2D analogue of the Jeffrey solution [59], but inside is described in approximation of constant velocity gradients. The main approximation is made integrally satisfying the dynamic boundary conditions by virial moment technique. What is the difference between the boundary conditions, which are satisfied integrally and exactly? The

exactly satisfied boundary conditions should introduce some perturbation from an elliptic shape of the droplet obtained by integrally satisfied boundary conditions. Thus the other essential assumption about an elliptic shape of a droplet is related to the approximation of the dynamic boundary conditions, which is used for both sets of equations. Numerical simulation of droplet motion is carried out applying Runge-Kutta 4th order algorithm for both First and Second sets.

The comparison of both sets displays that the equation (5.3) in the First set is to obtain from (5.5) tending λ to infinity. It is quite natural result since the equation (5.3) is obtained from rigid ellipse rotation. Substitution of the phenomenological parameter p in (5.2) with the following expression

$$p = \frac{a^4 + 1}{2a^2} = \frac{a^2}{2} + O\left(\left(\frac{1}{a}\right)^2\right) \qquad (5.6)$$

arrives at equation (5.5). The conclusion could be drawn that the First set of equations is some simplification of the Second set in the case of very viscous droplet.

The answer to the question, how good is the approximation of the shape of a droplet by an ellipse, could be obtained by a BEM simulation. In the case of λ=1, the juxtaposition of a BEM simulation with results of the First and the Second sets of equations of motion are given in Fig.5.2. The comparison of all three series of shapes shows that:

1. The agreement between the "Second set" and BEM simulation is very good up to t=6.07, when the perturbations from an elliptic shape develops for a droplet, as it is displayed by a BEM simulation.
2. The shape of a droplet obtained by the "First set" is not sufficiently good at t=6.07, the difference is already present at t=4.41, because it is not possible to account for a shear flow inside a droplet by the equations of the First set.
3. After t=8.39 the shape of a free droplet is different in comparison with an elliptic one and hence both sets of equations of motion are inadequate to describe such a motion.

Thus, it is proved that equations of motion could be used with good accuracy only if the shape of the droplet is close to an elliptic one. Other detail to discuss is the

range of λ, the ratio of viscosities, for which requirement about near elliptic shape is fulfilled. Even in Fig.5.2 at t=4.41 the free droplet (BEM simulation) exhibits the tendency to bending. A more explicit phenomenon is shown in Fig.5.3 where the shapes of the droplet in the case of a periodic rotation at the ratio of viscosities λ=5 are presented. Here magnetic field characteristics Bm=105, μ=5 are chosen to have a moderate elongation of a droplet. The field rotation frequency Ω_H=0.8 is slightly larger than critical frequency, thus the time interval during which the droplet unsuccessfully tries to follow the field as well as the backward motion is longer than for higher frequencies. The time-averaged frequency of a droplet's rotation is $\overline{\Omega} = 0.28$. It means that the droplet is exposed a time long enough to the perpendicular magnetic field. The behaviour of the droplet during time intervals t=13..15 and t=19.5..22 displays bending instability in the magnetic field which is orientated approximately perpendicular to its major dimension. How bending instability appears here? At time moment $t \approx 12$, for example, magnetic field is near to perpendicular direction and by the shear stresses both tips of the droplet is already slightly "twisted". Obviously droplet is unstable with respect to the bending instability in the perpendicular field and if some initial perturbation is present, the time interval Δt=3 is sufficient to cause such a large effect as it appears from t=11.78 to t=15.00. The next question is what is the role of the λ value in this instability? In Fig.5.4 the similar results for λ=1 are shown, leaving others parameters unchanged. The comparison with Fig.5.3 proves that at the smaller viscosity of the droplet, the shear flow inside it plays more important role. Thus, rather intrinsic transitions at $t \approx 9$ and $t \approx 16$ take place. The nature of these transitions is not yet well studied and it could be the subject of further research but nevertheless, it is obvious that the more viscous droplet of Fig.5.3 exhibits tendency to bend instead of changing shape by the way of a shear flow, because the bending flow requires less energy dissipation inside the viscous droplet. Another phenomena in Fig.5.4 which causes interest is the transition to steady motion with constant phase lag and constant elongation (b/a=3.88) at the end of simulation (t=30..42). This last difference in the behaviour of a droplet at λ=1 and λ=5 is evidently the same what is mentioned in [5*]: moderate values of λ causes stabilisation of droplet configurations if the phase lag ϑ is slightly greater than the critical value $\pi/4$, but an increase of λ causes the loss of stability. In present case it

means that for λ=5 droplet can not follow a field rotation. At λ=1 the transition of a droplet finishes with the steady motion of it. The droplet follows the field rotation with a constant phase lag (see Fig.5.4).

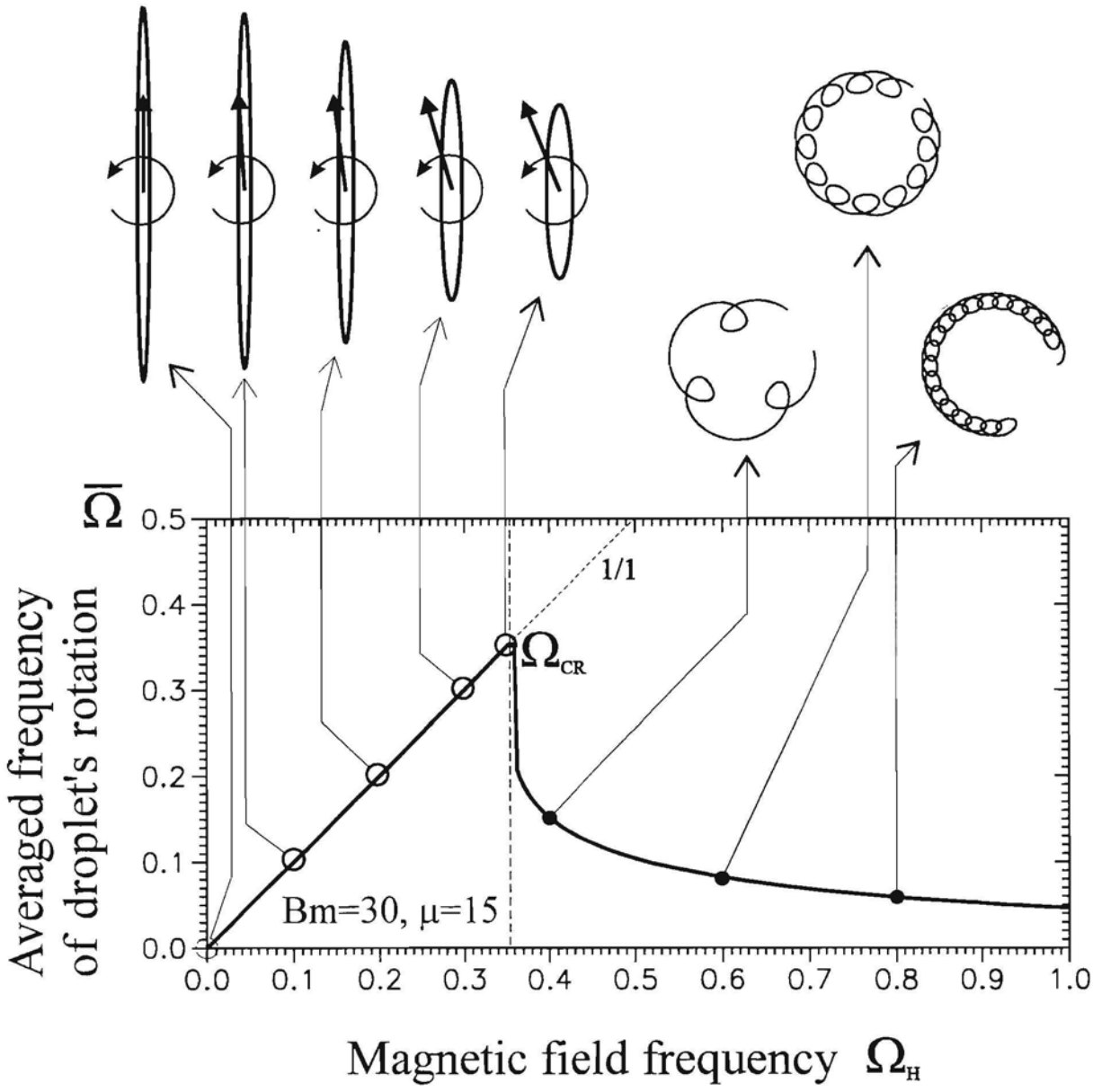

Figure 5.1. Droplet rotation: the time-averaged frequency of a droplet's rotation versus the frequency of a magnetic field

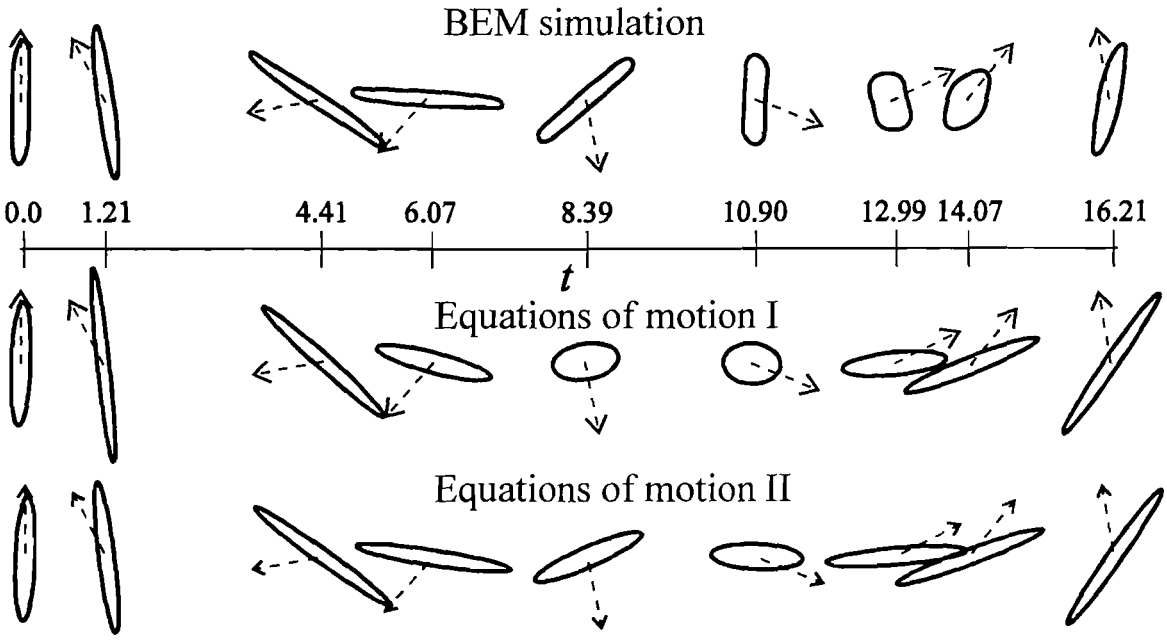

Figure 5.2. Juxtaposition of a BEM simulation with simulation by two kinds of equations of motion

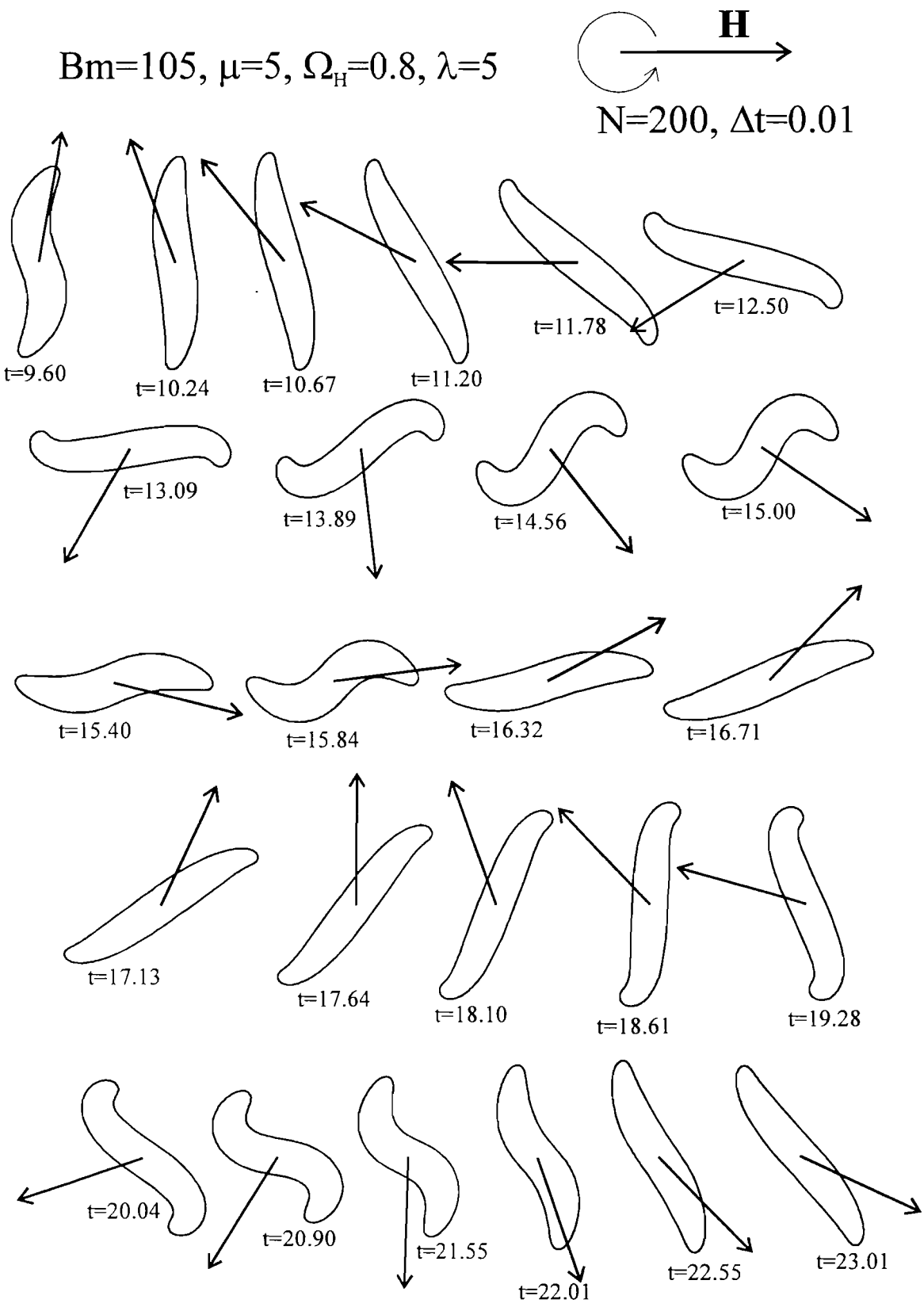

Figure 5.3. Rotation shapes of a viscous droplet: the bending instability in the "perpendicular field"

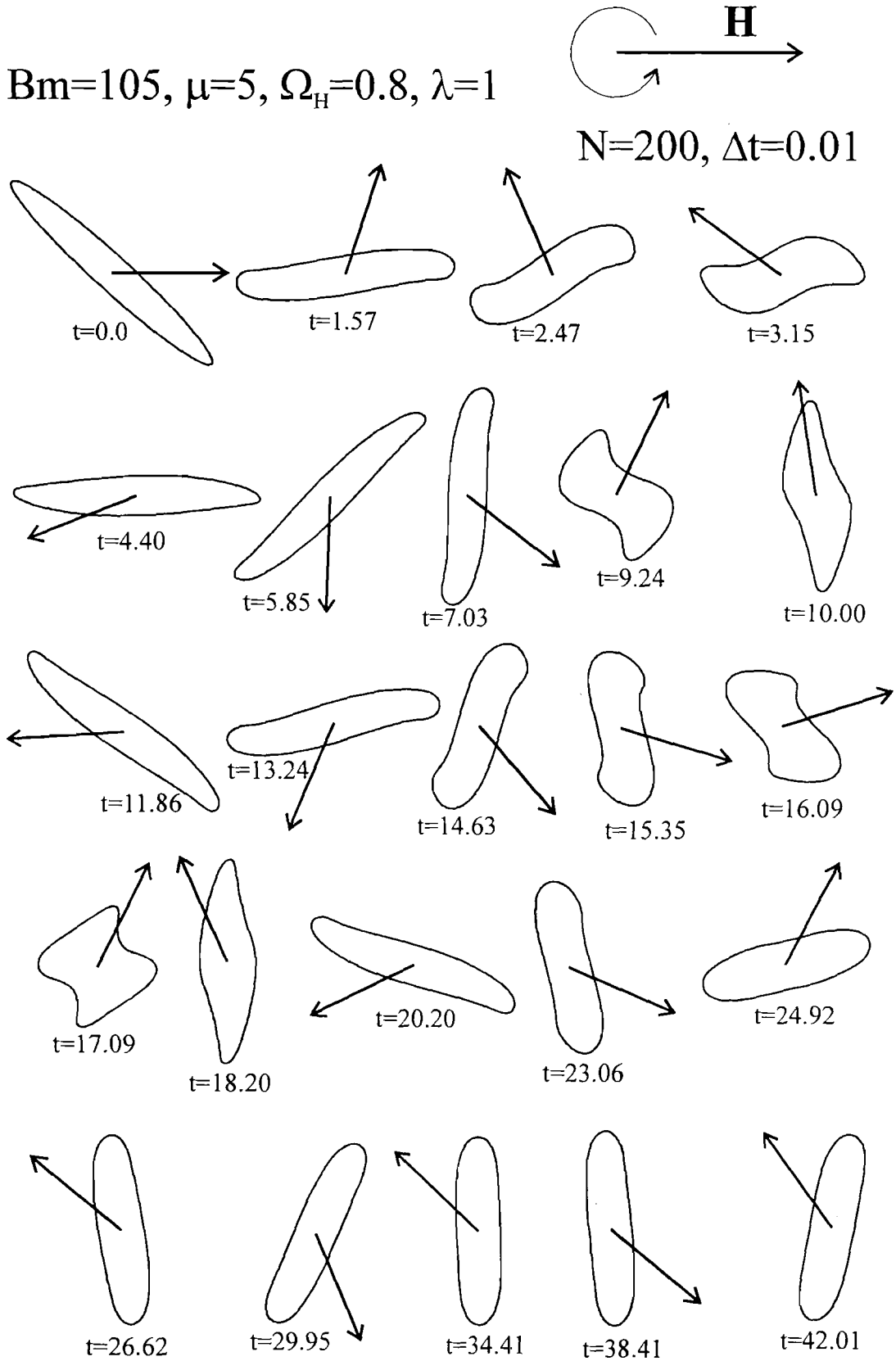

Figure 5.4. Transition to steady state

Included papers:

1.

J.C.Bacri, A.Cēbers, S.Lācis, R.Perzynski

Dynamics of the magnetic fluid droplet in rotating field

Journal of Magnetism and Magnetic Materials, 1995, Vol.149, 143-147

2.

S.Lācis

The equations of motion of the 2D elliptic magnetic fluid droplet in rotating field

Magnitnaya Gidrodinamika, 1996, (accepted to publish)

ELSEVIER

Journal of Magnetism and Magnetic Materials 149 (1995) 143–147

Journal of magnetism and magnetic materials

Dynamics of a magnetic fluid droplet in a rotating field

J.C. Bacri [a,*], A. Cebers [b], S. Lacis [b], R. Perzynski [a]

[a] *Lab. AOMC (Assoc. CNRS), Université P.M. Curie, 4 place Jussieu, 75252 Paris Cedex 05, France*

[b] *Latvian Academy of Sciences, Institute of Physics, Salaspils-1, LV-2169, Latvia*

Abstract

The response of a magnetic fluid microdrop to a rotating magnetic field is studied numerically in 2D by the boundary element method (BEM). On increasing field frequency, the motion of the droplet goes through a transition from a state where the droplet follows the magnetic field with a constant phase lag to a state where the phase lag increases in a series of kinks when the field frequency passes the critical one. The equations of the droplet motion are derived analytically and good agreement with the BEM is obtained.

It is well known that for a rigid magnetic dipole there is a critical angular velocity of the rotating field below which the rotation of particle and field are synchronized [1]. Similar phenomena are observed for a bound pair of soft magnetic particles [2,3]. The interplay between magnetic and viscous forces leads to various modes of motion, which in Refs. [2,3] are classified as (1) steady-state rotations; (2) 'jerky' (rotations with stops and backward motions); and (3) localized oscillations. Transitions between these modes are well described by a single non-linear equation and depend on the frequency and amplitude of the rotating field, the fluid viscosity and the magnetic susceptibility. It is found both experimentally and numerically [3] that for a pair of free spheres phase locking takes place in an elliptical polarized field $\bar{\Omega}/\Omega_H = 1/2, 1/4$, etc., where $\bar{\Omega}$ is the average angular frequency of the pair-rotation and Ω_H is the angular frequency of the magnetic field rotation. The magnetic fluid (MF) microdroplet in the rotating magnetic field includes a wide variety of very complex phenomena in the high-frequency range [4]. In the low-frequency range, an elongated droplet rotates with magnetic field frequency, with the surface tension playing an equivalent role to that of the soft binding in a pair of magnetic spheres.

The scope of the present paper is the behaviour of the MF droplet in the intermediate frequency range of a rotating magnetic field, studied by a numerical simulation. In the two-dimensional (2D) case, we apply the boundary integral equation technique (BEM: the boundary element method) considered previously in Refs. [5,6]. We assume that the magnetic permeability is constant (μ = const), and that gravity and inertia forces are negligible due to the very small size of the droplet. Hence the effective surface forces have only the following normal component:

$$f_s^n = \sigma/R_L - (\mu - 1)(\mu H_n^2 + H_t^2)/(8\pi). \tag{1}$$

Here σ is the surface tension, R_L is the local curvature radius, and μ is the magnetic permeability of the MF. Both the normal and tangential components H_n, H_t of the magnetic field strength on the boundary are found as solutions of the corresponding boundary integral equations [5]:

$$H_n|_{l'} = \frac{2H_{0x}}{(\mu+1)}\frac{\partial x}{\partial n} + \frac{2H_{0Y}}{(\mu+1)}\frac{\partial y}{\partial n} + \frac{1}{\pi}\frac{(\mu-1)}{(\mu+1)} \times \oint_L H_n(l')|_{l'} K(\boldsymbol{r}, \boldsymbol{r}')\frac{\mathrm{d}l'}{\sqrt{x_l^2 + y_l^2}}. \tag{2}$$

$$H_t|_{l'} = \frac{2H_{0x}}{(\mu+1)}\frac{\partial x}{\partial l} + \frac{2H_{0Y}}{(\mu+1)}\frac{\partial y}{\partial l} - \frac{1}{\pi}\frac{(\mu-1)}{(\mu+1)} \times \oint_L H_t(l')|_{l'} K(\boldsymbol{r}, \boldsymbol{r}')\frac{\mathrm{d}l'}{\sqrt{x_l^2 + y_l^2}}, \tag{3}$$

$$K(\boldsymbol{r}, \boldsymbol{r}') = \frac{x_l(y'-y) - y_l(x'-x)}{(y'-y)^2 + (x'-x)^2}.$$

Calculated field components are used for effective surface forces (1). The surface motion is calculated using the potential theory of viscous flow, described in Refs. [7,8].

* Corresponding author. Email: jcbac@ccr.jussieu.fr; fax: +33-1-44273854. Affiliation: Université Paris VII.

SSDI 0304-8853(95)00357-6

The corresponding boundary integral equation for the velocity v of the fluid on the boundary of the droplet in 2D is

$$v_i(x) = -\frac{1}{2\pi(\eta_{ex}+\eta_{in})}\oint_L n_j f_s^n G_{ij}(x, x')\,dl' + \frac{\eta_{ex}-\eta_{in}}{4\pi(\eta_{ex}+\eta_{in})} \times \oint_L v_j(x') n_k(x') f_s^n T_{ijk}(x, x')\,dl', \quad (4)$$

where

$$G_{ij}(x, x') = -\delta_{ij}\ln|\hat{x}| + \frac{\hat{x}_i\hat{x}_j}{|\hat{x}|^2},$$

$$T_{ijk}(x, x') = -4\frac{\hat{x}_i\hat{x}_j\hat{x}_k}{|\hat{x}|^4}, \qquad \hat{x} = x' - x.$$

η stands for viscosity, the subscripts 'in' denotes the MF droplet and 'ex' the surrounding fluid. In the present paper only the results obtained by BEM for the case of equal viscosities ($\eta_{in} = \eta_{ex}$), are presented. In this case Eq. (4) simplifies to

$$v_i(x) = -\frac{1}{2\pi(\eta_{ex}+\eta_{in})}\oint_L n_j f_s^n G_{ij}(x, x')\,dl'. \quad (5)$$

The boundary contour is approximated by a finite number of marker points connected together by interpolating cubic spline functions. As in Ref. [6], the distance of marker points separation is proportional to the local radius of curvature within limits which prevent the absence of points at places on the contour with small curvature. This non-equidistant distribution of marker points gives a better accuracy at droplet tips where the contour curvature is larger.

The approximation technique for Eqs. (2), (3), (5), described in detail in Refs. [5,9], is based on linear interpolation of the corresponding unknowns (H_n, H_t, v_i) between marker points along the droplet contour and application of the Galerkin method. The singularities are subtracted and integrated analytically. The first and second derivatives along the boundary contour (x_l, x_{ll}, y_l, y_{ll}) are calculated by differentiating the corresponding cubic spline functions. For a rotating field we have $H_{0X} = H_0 \cos \Omega_H t$, $H_{0Y} = H_0 \sin \Omega_H t$. The sets of linear algebraic equations, obtained for Eqs. (2), (3) are solved using Gaussian elimination The approximation of (5) leads to a sum. In each time step, magnetic field components are calculated and applied for the surface movement velocity calculation. Once the velocity has been calculated, the position of the interface is advanced using an explicit Euler method. After each time step the droplet dimensions are rescaled to improve the volume conservation.

Further in this paper, a dimensionless form for physical parameters and geometric dimensions of droplet is used. The external field strength H_0, the surface tension σ, the external fluid viscosity η_{ex} and the unperturbed droplet (i.e. circle) radius R are chosen as characteristic values. Physical processes are characterized by the magnetic Bond number $B_m = H_0^2 R/\sigma$, the surface energy of a circular 2D droplet per unit length of a cylinder $E_c = 2\pi R\sigma$, the characteristic time interval for droplet motion $\tau = \eta_{ex} R/\sigma$

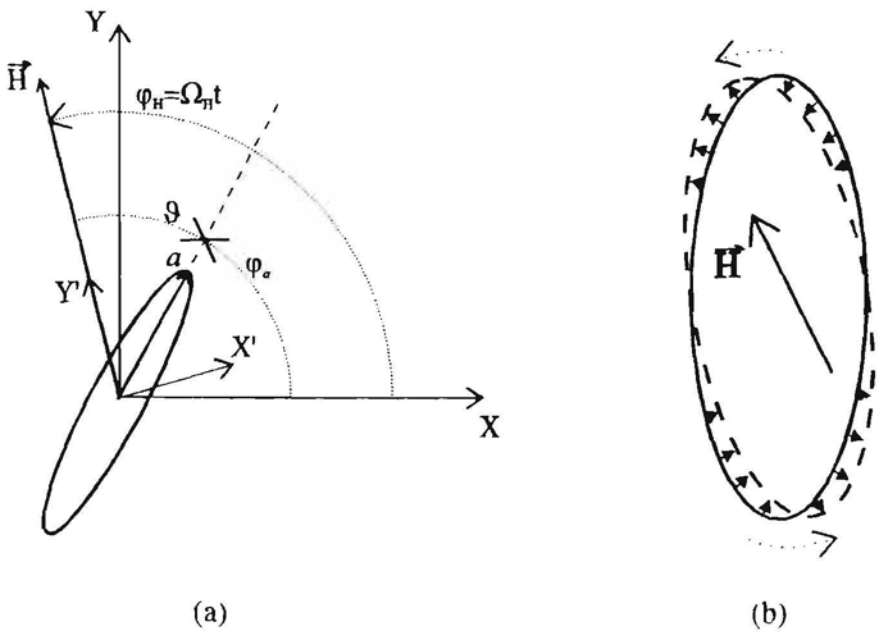

Fig. 1. (a) The orientation of a droplet with respect to the magnetic field and laboratory coordinates. (b) The wave-like perturbation propagation.

and the ratio of viscosities $\lambda = \eta_{in}/\eta_{ex}$. So we have dimensionless coordinates $\tilde{x} = x/R$, $\tilde{y} = y/R$, a dimensionless velocity $\tilde{v} = v\tau/R$, a dimensionless magnetic field $\boldsymbol{H} = \boldsymbol{H}/H_0$, a dimensionless frequency of field rotation $\tilde{\Omega} = \Omega\tau$ and a dimensionless time $\tilde{t} = t/\tau$. All the further formulae are written in a dimensionless form dropping the tilde; in special cases the dimensional form is denoted by a circumflex (^).

The behaviour of the MF droplet in a rotating magnetic field can be understood on the basis of a simple model, derived under the assumption of an elliptical shape of the 2D droplet. The configuration of the elliptical droplet is described by its large semi-axis $a = \hat{a}/R$ and the phase lag ϑ of the large semi-axis with respect to the field direction (see Fig. 1(a)). Let us separate the motion of the elliptical 2D droplet into two processes. The first is an extension–contraction motion caused by the surface tension and the magnetic field, acting on the droplet in a direction determinated by the phase lag ϑ. The total energy (magnetic plus surface contributions) of the elliptic 2D droplet [9] is, with respect to the field direction (in a dimensionless form),

$$E_t = \frac{2a\mathrm{E}(e)}{\pi} - \frac{\mu - 1}{16\pi} B_m \left(\frac{a^2 + 1}{a^2 + \mu} \cos^2\vartheta + \frac{a^2 + 1}{a^2\mu + 1} \sin^2\vartheta \right), \tag{6}$$

where

$$\mathrm{E}(e) = \int_0^{2\pi} \sqrt{1 - (e \sin x)^2}\, \mathrm{d}x$$

is the complete elliptic integral of the first kind. $e^2 = 1 - b^2/a^2$.

In this process, the total energy changes are balanced by an energy dissipation in the viscous flow inside and outside the droplet:

$$\dot{E} = \dot{E}_{in} + \dot{E}_{ex} = \frac{\mathrm{d}E_t}{\mathrm{d}t} = \dot{a}\frac{\mathrm{d}E_t}{\mathrm{d}a}. \tag{7}$$

The energy dissipation inside the droplet is approximated as an homogeneous extension–contraction motion ($v_{x'} = x'\dot{a}/a$, $v_{y'} = -y'\dot{a}/a$, see Fig. 1(a) for x', y'). It gives

$$\dot{E}_{in} = -2\lambda(\dot{a}/a)^2. \tag{8}$$

For the energy dissipation outside the droplet the following approximation is used:

$$\dot{E}_{ex} = -2p(\dot{a}/a)^2, \tag{9}$$

where p is some phenomenological parameter of the model.

Collecting Eqs. (6)–(9) together, we obtain the droplet motion equation for large semi-axis a:

$$\dot{a} = \frac{a^2}{\pi(\lambda + p)} \left[\frac{(\mu - 1)^2}{16} B_m a \left(\frac{\cos^2\vartheta}{(a^2 + \mu)^2} - \frac{\sin^2\vartheta}{(\mu a^2 + 1)^2} \right) - \frac{\Phi(a)}{a^4 - 1} \right], \tag{10}$$

$$\Phi(a) = \left((a^4 + 1)\mathrm{E}(e) - 2\mathrm{K}(e) \right),$$

where

$$\mathrm{K}(e) = \int_0^{2\pi} 1/\sqrt{1 - (e \sin x)^2}\, \mathrm{d}x$$

is the complete elliptic integral of the second kind.

The second process is the droplet rotation, characterized by the balance of the viscous and magnetic torques ($\hat{N}_f + \hat{N}_m = 0$). The viscous forces are determinated by a creeping flow around the rotating elliptic cylinder, which could be derived using the method described for a general ellipsoid in Ref. [10], modifying this method for the case of 2D. The obtained viscous torque (the dimensional z-component, per unit length of a cylinder) is

$$\hat{N}_f = -2\pi\hat{\eta}_{ex}\hat{\Omega}(\hat{a}^2 + \hat{b}^2). \tag{11}$$

It has to be balanced by a magnetic torque

$$\hat{N}_m = \int_S \hat{\boldsymbol{M}}\, \mathrm{d}\hat{S} \times \hat{\boldsymbol{H}} = H_0^2 \frac{\sin 2\vartheta}{8} \hat{a}\hat{b} \frac{(\mu - 1)^2(\hat{a}^2 - \hat{b}^2)}{(\hat{a} + \mu\hat{b})(\hat{a}\mu + \hat{b})}. \tag{12}$$

The angular frequency of an ellipse rotation in laboratory coordinates is (see Fig. 1(a) for the definitions of φ_a, φ_H)

$$\Omega = \dot{\varphi}_a = \dot{\varphi}_H - \dot{\vartheta} = \Omega_H - \dot{\vartheta}. \tag{13}$$

Collecting together Eqs. (11)–(13) we obtain the dimensionless droplet motion equation for the phase lag ϑ:

$$\dot{\vartheta} = \Omega_H - \Omega_{cr} \sin 2\vartheta, \tag{14}$$

where

$$\Omega_{cr} = \frac{B_m}{16\pi} \frac{(\mu - 1)^2 a^2 (a^4 - 1)}{(a^2 + \mu)(a^2\mu + 1)(a^4 + 1)}.$$

At low magnetic field rotation frequencies Ω_H, the MF droplet rotates uniformly with a frequency equal to that of the field. Steady-state rotations are studied using both the BEM and the simple model, and the results for $\lambda = 1$ are shown in Fig. 2 in coordinates (x', y') which rotate together with the magnetic field so that the y'-axis is pointed in the field direction (see Fig. 1(a)). A typical number of marker points for BEM calculations is $N = 200$. For the simple model simulations, the value $p = 1$ is used. The solid curve in Fig. 2 represents the positions of the elliptic droplet tips for a continuously varying frequency Ω_H. The end of the large semi-axis with coordinates $x'_a = a \sin\vartheta$,

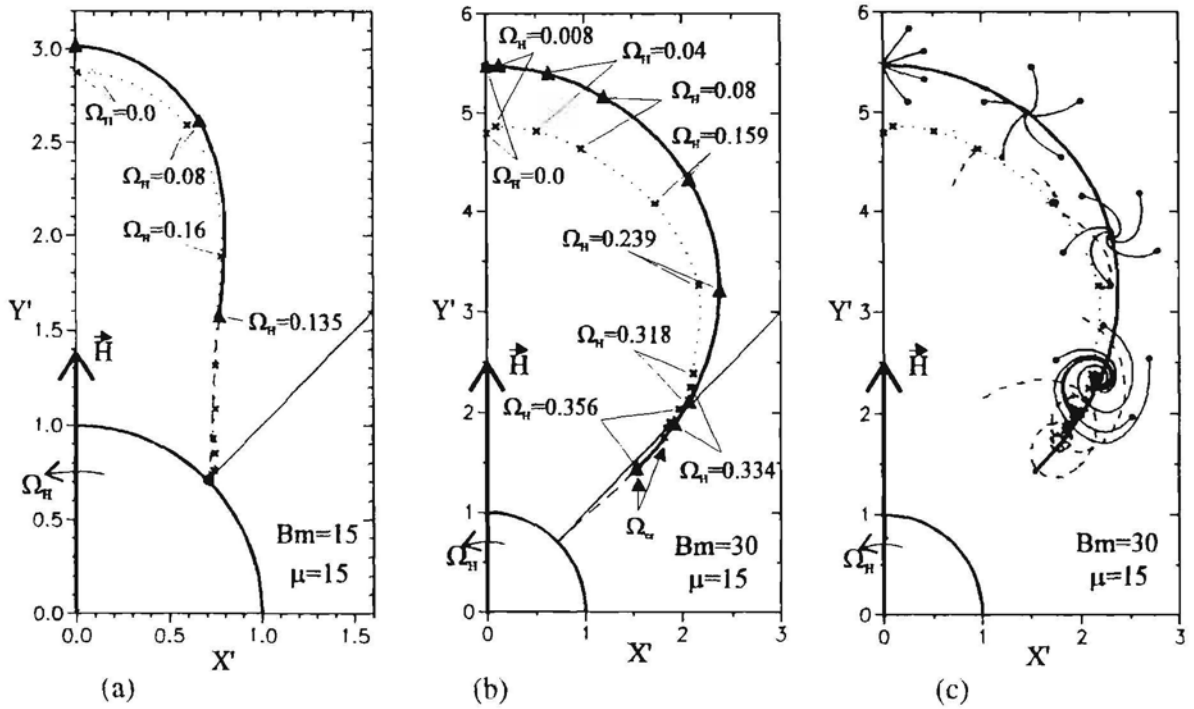

Fig. 2. (a),(b) Steady-state configurations of a MF droplet in a rotating field. (c) Paths leading to the steady state. Results for different field rotation frequencies. Thick solid lines and triangles: simple motion model; dotted lines and crosses: BEM; dashed line in (a), (b): unstable simple model configurations. In (c) thin solid lines are simple model paths to steady state, initial state is given by solid circles; dashed lines are paths calculated by BEM.

$y'_a = a \cos \vartheta$ is taken as the tip. In Fig. 2(a),(b) the solid curve is continued by a dashed one, which corresponds to the unstable simple model configurations. Triangles show the stable configurations at definite frequencies Ω_H. The steady-state configurations obtained by the BEM at definite frequencies Ω_H are shown by crosses, the pointed curve represents the interpolation of these results for a continuously varying frequency Ω_H. In the case of the BEM the most extended point from the centre of the droplet is taken as the tip of the droplet, and the phase lag is calculated for this point. The comparison between the BEM calculations and the simple motion equations calculation shows a fairly good agreement. Discrepancies could be explained by two causes. The first is that the shape of a droplet in BEM calculations (see also Fig. 3) has more rounded tips, and hence the droplet has a smaller extension. The second is that the simple model does not account for the wave-like perturbation propagation on the free

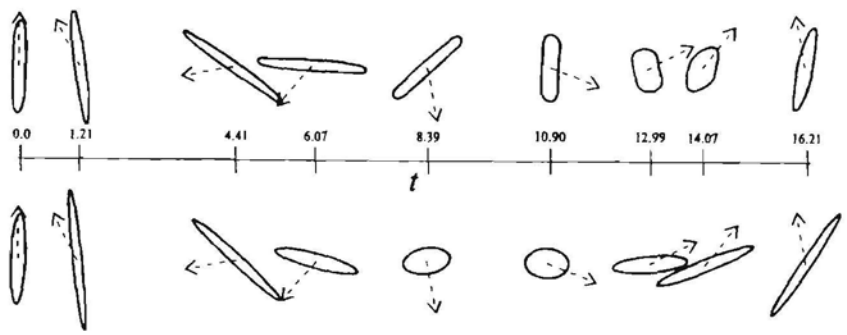

Fig. 3. Series of droplet shapes at fixed time moments for transient motion in laboratory coordinates. The upper series is for the BEM, the lower for the simple model simulation. Dashed arrows represent the field direction; the length of arrow is $3R$.

surface, caused by asymmetric stresses (see Fig. 1(b)). At low values of the elliptic extension ($a < 2$) these stresses cause a motion of the droplet surface which dominates over the pure rotational motion. Thus the simple model simulation shows the lack of stable configurations (Fig. 2(a)) for large field rotation frequencies when a is small.

Two different types of steady-state behaviour are observed (see Fig. 2(a),(b)) depending on the magnetic field strength. These two types are separated by the critical value of the magnetic Bond number, which turns out to be the threshold value of the instability of a 2D droplet in a high-frequency rotating field with respect to the elliptical deformations [9]: $B_{m_{cr}} = 6\pi(\mu+1)^3/(\mu-1)^3$. If the magnetic Bond number is less than the critical one ($B_{m_{cr}} = 28.14$, $\mu = 15$), the extension of the droplet in stationary configurations is diminishing with increase of the rotating field frequency, and the maximal phase lag value $\pi/4$ is reached at infinite frequency as it is shown in Fig. 2(a). For the magnetic Bond numbers larger than the critical one the maximal phase lag ($\approx \pi/4$) is reached already at a finite critical frequency Ω_{cr} (Fig. 2(b)). Phase portraits of the system are presented in Fig. 2(c), they are in accordance with the BEM simulation. As one can see, the dynamics of the droplet in the subcritical range of angular frequencies ($\Omega_H < \Omega_{cr}$) is characterized by the existence of a stable focus, whatever are the initial conditions. In the case of anticlockwise field rotation, the tip of the droplet near the focus rotates clockwise in coordinates (x', y'). The imaginary part of the perturbation decrement when Ω_{cr} is approached is increasing in comparison with the real part, thus causing the rise of the droplet tip rotation around the focus.

In Fig. 3 a transient droplet rotation is shown by a series of droplet shapes and corresponding field orientations. One can see that there is a fair agreement between the simple model and the BEM for large droplet extensions and some discrepancies for small ones. If $B_m > B_{m_{cr}}$ then for large field rotation frequencies ($\Omega_H > \Omega_{cr}$) the motion of the droplet turns out to be jerky and just similarly to the case of the two bound spheres [2,3] it can be characterized as rotation with stops and backward motions. The jerky rotation of the droplet could be described by average angular frequency $\bar{\Omega}$. Fixing the value of a ($\lambda \gg 1$, or $\Omega_H \gg \Omega_{cr}$), the integration of the droplet motion equations gives [3]

$$\bar{\Omega} = \Omega_H - \sqrt{\Omega_H^2 - \Omega_{cr}^2}\,. \qquad (15)$$

The value of a could be obtained from the non-linear equation (10) by $\dot{a} = 0$. The results of simple model simulation are shown in Fig. 4 for two different magnetic Bond number values ($B_m = 30$, $B_m = 50$). As one can see, the critical frequency increases with the increase of B_m. Another important conclusion could be drawn about the dependence of the critical frequency on λ: finite values of λ cause stabilization of droplet configurations if the phase

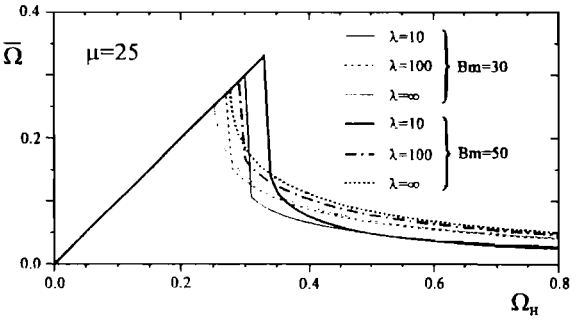

Fig. 4. Plot of the average angular frequency of the droplet rotation versus the field rotation frequency. $\lambda = \infty$ corresponds to the analytical solution for fixed a.

lag ϑ is slightly greater than the critical value $\pi/4$. Increasing λ (the viscosity of the droplet), the critical frequency decreases and tends to its analytical value Ω_{cr} (14). This effect could be explained by the small perturbations from the steady-state configuration a_0, ϑ_0. Denoting the right part functions in Eqs. (10), (14) by $g(a, \vartheta)$, respectively, $h(a, \vartheta)$, the perturbation amplitude depends on time as $\exp((g_a + h_\vartheta)t/2)$, where $g_a = \partial g/\partial a$, $h_\vartheta = \partial h/\partial\vartheta$ at a_0, ϑ_0. Beyond $\pi/4$, $h_\vartheta > 0$, thus the stability criterion is $g_a < -h_\vartheta$. From Eq. (10) it follows that $g_a \propto 1/(\lambda + p)$, hence obviously an increase of λ causes the loss of stability.

Test simulations show that in the case of an elliptic polarized rotating magnetic field, phase locking is found like in Ref. [3].

Acknowledgements: This work was supported by 'Le Réseau Formation Recherche No. 90R0933 du Ministère de l'Enseignement Superieur et de la Recherche' of France. Two of the authors (A.C. and S.L.) are thankful to the International Science Foundation for financial support through long-term grant LBG000.

References

[1] R.E. Rosensweig Ferrohydrodynamics (Cambridge University Press, Cambridge, 1985).
[2] G. Helgessen, P. Pieranski and A.T. Skjeltorp, Phys. Rev. Lett. 64 (1990) 1425.
[3] A.T. Skjeltorp and G. Helgessen, Physica A 176 (1991) 37.
[4] J.C. Bacri, A.O. Cebers and R. Perzynski, Phys. Rev. Lett. 72 (1994) 2705.
[5] A. Cebers, Magnitnaya Gidrodinamika N4 (1986) 3 (in Russian).
[6] J.D. Sherwood, J. Fluid Mech. 188 (1988) 133.
[7] O.A. Ladyzhenskaya, The Mathematical Theory of Viscous Incompressible Flow (Gordon and Breach, New York, 1969).
[8] C. Pozrikidis, Boundary Integral and Singularity Methods for Linearized Viscous Flow (Cambridge University Press, Cambridge, 1992).
[9] J.C. Bacri, A. Cēbers, S. Lācis and R. Perzynski, Magnitaya Gidrodinamika, to appear.
[10] G.F. Jeffrey, Proc. R. Soc. A102 (1922) 161.

The equations of motion of the 2D elliptic magnetic fluid droplet in rotating field

S.Lācis

Latvia University, Fac. Phys. Math., Raina boul. 19, Riga, LV-1586, Latvia;
Latvian Academy of Sciences, Institute of Physics, Salaspils-1, LV-2169, Latvia

Abstract: Equations of motion for 2D magnetic fluid droplet in low-frequency rotating field are derived under the assumption of its elliptic shape. Fluid flow outside the droplet is treated exactly, but inside is described in approximation of constant velocity gradients. Dynamic boundary conditions are satisfied integrally by virial moment technique. Numerical simulation of droplet motion is carried out applying Runge-Kutta 4th order algorithm. Juxtaposing with the numerical simulation results of the droplet motion in low-frequency rotating field by boundary integral equation technique good accordance is confirmed.

It is well-known that for rigid magnetic dipole there is a critical angular velocity of the rotating field below which the rotation of particle and field are synchronized [1]. Similar phenomena are observed for a bound pair of soft magnetic particles [2,3]. The behavior of the magnetic fluid (MF) microdroplet in the rotating magnetic field includes a wide variety of very complex phenomena in the high-frequency range [4].

The scope of the present paper is to derive simple equations of motion for 2D MF droplet under assumption of its elliptic shape. Simple equations describing the behavior of 2D elliptic droplet in rotating field are considered previously in [7] and by comparison with the numerical simulation data it has been found that near the critical frequency of the locking of the field and droplet rotation quite large discrepancies exist. Here a new set of equations is proposed taking into account shear flow inside and outside the droplet. For that exact solution of 2D Stokes equations for the velocity distribution outside the droplet with homogeneous deformation rate is found. As result much better agreement with the numerical simulation data on basis of boundary integral equations method (BEM) is found.

A small size of microdroplet and relatively small characteristic velocities of flow allows to neglect inertia and gravity terms, concentrating on surface tension and magnetic forces on the surface of the droplet. Hence the dynamics of a free surface of a droplet can be described in the framework of the creeping flow. Elliptic incompressible MF droplet is completely determined by the length of its large semiaxis a and the angle φ of its orientation with respect to X_{lab}-axis of the laboratory frame (see Fig.1). Arbitrary viscosities of fluids inside and outside the droplet are considered.

Governing equations for a fluid flow inside the droplet under the assumptions, mentioned above, are:

$$-\frac{\partial}{\partial x_i}\left(p^{in}-\frac{\mu-1}{8\pi}\mathrm{H}^2\right)+\frac{\partial \sigma_{ik}^{in}}{\partial x_k}=0, \qquad (1)$$

$$\operatorname{div} \mathrm{v}=0, \qquad (2)$$

where p is pressure and σ_{ik} is viscous stress tensor:

$$\sigma_{ik} = \eta\left(\frac{\partial v_k}{\partial x_i} + \frac{\partial v_k}{\partial x_i}\right). \tag{3}$$

Here v is a velocity of a fluid and η its viscosity. Here and further superscript 'ex' stays for the domain outside the droplet and 'in' for the domain inside it.

To derive equations of motion, the virial technique [5] is applied. For that equation (1) is multiplied by x_j and integrated over domain S^{in} (see Fig.1). Obtained virial moments are:

$$V_{ij} = -\oint_L n_i x_j \left(p^{in} - \frac{\mu-1}{8\pi}\mathrm{H}^2\right)dl + \delta_{ij}\int_{S^{in}}\left(p^{in} - \frac{\mu-1}{8\pi}\mathrm{H}^2\right)dS + \oint_L n_k x_j \sigma_{ik}^{in} dl - \int_{S^{in}} \sigma_{ij}^{in} dS = 0 \tag{4}$$

The boundary conditions on a droplet surface are

$$\mathrm{v}^{in} = \mathrm{v}^{ex}, \quad \sigma_{\tau n}^{in} = \sigma_{\tau n}^{ex},$$
$$-p^{in} + \sigma_{nn}^{in} = -p^{ex} + \sigma_{nn}^{ex} + 2\pi(\mathrm{Mn})^2 - \sigma/R_C \tag{5}$$

where subscript 'n' denotes normal component but subscript τ tangential one, R_C: local contour curvature radius, σ: surface tension. n is an external normal. Accounting due to the continuity of tangential stresses for

$$n_i\left(\sigma_{nn}^{in} - \sigma_{nn}^{ex}\right) = n_k\left(\sigma_{ik}^{in} - \sigma_{ik}^{ex}\right) \tag{6}$$

one can obtain

$$n_i\left(p^{ex} - p^{in} + \frac{\mu-1}{8\pi}\mathrm{H}^2\right) + n_k\left(\sigma_{ik}^{in} - \sigma_{ik}^{ex}\right) =$$
$$n_i\left(-\sigma_{nn}^{in} + \sigma_{nn}^{ex} + 2\pi(\mathrm{Mn})^2 - \sigma\,\mathrm{div}\,\mathrm{n} + \frac{\mu-1}{8\pi}\mathrm{H}^2\right) + n_k\left(\sigma_{ik}^{in} - \sigma_{ik}^{ex}\right) = \tag{7}$$
$$n_i\left(2\pi(\mathrm{Mn})^2 - \sigma\,\mathrm{div}\,\mathrm{n} + \frac{\mu-1}{8\pi}\mathrm{H}^2\right).$$

Applying boundary conditions to expression (4) the virial moment transforms to

$$V_{ij} = -\oint_L x_j n_i p^{ex} dl + \oint_L x_j n_i\left(2\pi(\mathrm{Mn})^2 + \frac{\mu-1}{8\pi}\mathrm{H}^2\right)dl - \sigma\oint_L x_j n_i\,\mathrm{div}\,\mathrm{n}dl + \oint_L x_j n_k \sigma_{ik}^{ex} dl + \delta_{ij}\int_{S^{in}}\left(p^{in} - \frac{\mu-1}{8\pi}\mathrm{H}^2\right)dS - \eta^{in}\oint_L\left(n_j v_i + n_i v_j\right)dl \tag{8}$$

To conserve elliptic shape of the droplet a flow inside the droplet is approximated by constant gradients γ_{ik} of velocity field

$$v_i = \gamma_{ik} x_k, \tag{9}$$

what leads to constant pressure inside the droplet:

$$p^{in} = p_0^{in}. \tag{10}$$

A magnetic field inside elliptic cylinder with constant magnetic permeability μ is constant:

$$\mathrm{H}^2 = H_a^2 + H_b^2 = H_{0a}^2\left(\frac{a+b}{a+\mu b}\right)^2 + H_{0b}^2\left(\frac{a+b}{\mu a+b}\right)^2, \tag{11}$$

Here H_x, H_b are magnetic field intensity components in instant directions of axes *a,b* of the ellipse (see Fig.1).

For the calculation of the virial moment external stresses on the boundary of droplet are needed. A creeping flow outside the droplet is treated exactly [6], using harmonic functions $\Omega(x,y)$, $\Phi(x,y)$:

$$\Omega(x,y)=\int_{\rho}^{\infty}F'(\xi)\left(\frac{x^2}{a^2+\xi}+\frac{y^2}{b^2+\xi}\right)d\xi+F(\xi),\quad \Phi(x,y)=x\,y\int_{\rho}^{\infty}R^3(\xi)d\xi,$$
$$F'(\xi)=R(\xi)=1\Big/\sqrt{(a^2+\xi)(b^2+\xi)},\qquad \Delta\Omega=0,\ \Delta\Phi=0 \tag{12}$$

Here ρ is a positive root of the equation $\frac{x^2}{a^2+\rho}+\frac{y^2}{b^2+\rho}=1$. Flow velocity and pressure can be described in terms of harmonic functions $\Omega(x,y)$, $\Phi(x,y)$ (subscripts x,y of harmonic functions denote partial derivatives):

$$\begin{aligned}
v_x^{ex} &= T\Phi_x - S\Phi_y + A_{11}\left(x\Omega_{xx}-\Omega_x\right)+A_{12}\left(x\Omega_{xy}-\Omega_y\right)+\\
&\quad A_{21}y\Omega_{xx}+A_{22}y\Omega_{xy}\\
v_y^{ex} &= T\Phi_y + S\Phi_x + A_{11}x\Omega_{xy}+A_{12}x\Omega_{yy}+\\
&\quad A_{21}\left(y\Omega_{xy}-\Omega_x\right)+A_{22}\left(y\Omega_{yy}-\Omega_y\right)\\
p^{ex} &= p_0^{ex}+2\eta^{ex}\left(A_{11}\Omega_{xx}+\left(A_{12}+A_{21}\right)\Omega_{xy}+A_{22}\Omega_{yy}\right)
\end{aligned} \tag{13}$$

Values of constant coefficients T, S, A_{ij} are associated with definite flow. The values of derivatives of harmonic functions on the droplet surface in the elliptic coordinates

$$\begin{cases} x = c\cosh\alpha\cos\beta \\ y = c\sinh\alpha\sin\beta \end{cases} \tag{14}$$

are

$$\Phi_{x,0}=-\frac{2}{(a+b)h_0^2}\sin\beta\left(2\cos^2\beta-\frac{a}{a+b}\right)$$

$$\Phi_{y,0}=-\frac{2}{(a+b)h_0^2}\cos\beta\left(2\sin^2\beta-\frac{b}{a+b}\right)$$

$$\Omega_{x,0}=\frac{4\cos\beta}{a+b},\quad \Omega_{y,0}=\frac{4\sin\beta}{a+b},\quad \Omega_{xy,0}=-\frac{4}{h_0^2}\sin\beta\cos\beta,$$

$$\Omega_{xx,0}=\frac{4}{h_0^2}\left(\frac{a}{a+b}-\cos^2\beta\right),\quad \Omega_{yy,0}=\frac{4}{h_0^2}\left(\frac{b}{a+b}-\sin^2\beta\right),$$

$$\Omega_{xxx,0}=-\Omega_{xyy,0}=\frac{4b}{h_0^6}\cos\beta\left(-3a^2+\cos^2\beta\left(3a^2+b^2\right)\right)$$

$$\Omega_{xxy,0}=\frac{4a}{h_0^6}\sin\beta\left(-a^2+\cos^2\beta\left(a^2+3b^2\right)\right)$$

$$\Phi_{xx,0}=-\sin\beta\cos\beta\left(3a^2-\cos^2\beta\left(5a^2+b^2\right)+\cos^4\beta\left(2a^2-2b^2\right)\right)\Big/h_0^6,$$

$$\Phi_{xy,0}=-2\Big(a^3(2a+b)-\cos^2\beta\,3a(a+b)\left(2a^2+ab+b^2\right)+$$
$$\cos^4\beta\,6a^2(a+b)^2-\cos^6\beta\,2(a+b)^3(a-b)\Big)\Big/\left(h_0^6(a+b)^2\right)$$

here

$$h_0^2 = a^2 - (a^2 - b^2)\cos^2\beta,$$

subscript 0 denotes function value on the surface (ξ=0).

Velocity of external flow, given by (13), on the surface of a droplet is equal to velocity of a flow inside the droplet

$$\begin{aligned} v_x &= \gamma_{xx} a\cos\beta + \gamma_{xy} b\sin\beta \\ v_y &= \gamma_{yx} a\cos\beta + \gamma_{yy} b\sin\beta \end{aligned} \qquad (15)$$

In order to express values of characteristic coefficients of external flow (13) by velocity gradients γ_{ij} inside the droplet both sides of the equation $v^{in} = v^{ex}$ from boundary conditions (5) are multiplied by h_0^2 and the obtained equation is treated like Fourier series. This procedure gives the following values:

$$\begin{aligned} T &= \frac{ab(a+b)}{4}(\gamma_{xy} + \gamma_{yx}) & S &= \frac{(a+b)^2(a^2+b^2)\gamma_{yy}}{4}, \\ A_{11} &= -\frac{(a+b)^2\gamma_{yy}}{8}, & A_{21} &= -\frac{a(b\gamma_{xy} + (2a+b)\gamma_{yx})}{8}, \\ A_{12} &= -\frac{b((a+2b)\gamma_{xy} + a\gamma_{yx})}{8}, & A_{22} &= \frac{(a+b)^2\gamma_{yy}}{8}. \end{aligned} \qquad (16)$$

From incompressibility $\mathrm{div}\, v = 0$ it follows that $\gamma_{xx} = -\gamma_{yy}$. Viscous stresses (3) outside the droplet are

$$\begin{aligned} &\sigma_{xx}^{ex} = -\sigma_{yy}^{ex} = \\ &2\eta^{ex}(T\Phi_{xx} - S\Phi_{xy} + A_{11}x\Omega_{xxx} + A_{12}x\Omega_{xxy} + A_{21}y\Omega_{xxx} + A_{22}y\Omega_{xxy} \\ &\sigma_{xy}^{ex} = \sigma_{yx}^{ex} = \\ &2\eta^{ex}(T\Phi_{xy} + S\Phi_{xx} + A_{11}x\Omega_{xxy} + A_{12}x\Omega_{xyy} + A_{21}y\Omega_{xxy} + A_{22}y\Omega_{xyy} \end{aligned} \qquad (17)$$

Evaluation of integrals in (8) gives the following values for three necessary combinations of virial moments:

$$\begin{aligned} V_{xx} - V_{yy} &= -\mathrm{Bm}\frac{(\mu-1)^2}{16}\hat{a}^2\left(\frac{H_{0a}^2}{H_0^2}\frac{1}{(\hat{a}^2+\mu)^2} - \frac{H_{0b}^2}{H_0^2}\frac{1}{(\hat{a}^2\mu+1)^2}\right) - \\ &\quad \hat{a}\frac{\Phi(\hat{a})}{\hat{a}^4-1} - \pi\tau_b\gamma_{xx}\left(\frac{\hat{a}^4+1}{2\hat{a}^2} + \lambda\right) = 0 \\ V_{xy} - V_{yx} &= -\mathrm{Bm}\frac{(\mu-1)^2}{8}\frac{\hat{a}^4-1}{(\hat{a}^2+\mu)(\hat{a}^2\mu+1)}\frac{H_{0a}H_{0b}}{H_0^2} + \pi\tau_b\frac{\hat{a}^4\gamma_{yx} - \gamma_{xy}}{\hat{a}^2} = 0 \\ V_{xy} + V_{yx} &= \mathrm{Bm}\frac{(\mu-1)^2}{8}\frac{\hat{a}^4+1}{(\hat{a}^2+\mu)(\hat{a}^2\mu+1)}\frac{H_{0a}H_{0b}}{H_0^2} - \\ &\quad \pi\tau_b\left(\frac{\hat{a}^4\gamma_{yx} + \gamma_{xy}}{\hat{a}^2} + \lambda(\gamma_{xy} + \gamma_{yx})\right) = 0 \end{aligned} \qquad (18)$$

Here

$$\Phi(a) = ((\hat{a}^4+1)\mathrm{E}(e) - 2\mathrm{K}(e)) \quad \lambda = \eta_{in}/\eta_{ex}, \quad \hat{a} = a/R,$$

where $E(e)=\int_0^{\pi/2}\sqrt{1-(e\sin x)^2}\,dx$ and $K(e)=\int_0^{\pi/2}1/\sqrt{1-(e\sin x)^2}\,dx$ are the complete elliptic integrals of first, resp., second kind, $e^2=1-a^2/b^2$, η_{in}, η_{ex}: viscosities of fluid inside, resp., outside the droplet, $R=\sqrt{ab}$: a radius of a circular drop shape. A time scaling unit is $\tau_b = R\eta_{ex}/\sigma$, $\mathrm{Bm} = H_0^2 R/\sigma$: magnetic Bond number.

The large semi-axis a of an ellipse and the angle φ of its orientation (see Fig.1) are chosen as system variables to characterize the state of an elliptic droplet. The relation between rate of change of a,φ and velocity gradients γ_{ij} is established by considering the evolution of an elliptic droplet during the time interval dt. In a dimensionless form

$$\dot{\hat{a}} = \hat{a}\gamma_{xx}, \quad \dot{\varphi} = \frac{\gamma_{xy}+\hat{a}^4\gamma_{yx}}{\hat{a}^4-1}. \tag{19}$$

Expressing γ_{ij} from (18) and inserting in (19) one obtains the following motion equations:

$$\dot{\hat{a}} = \frac{2\hat{a}^4}{\pi\left(\hat{a}^4+1+2\lambda\hat{a}^2\right)}\times$$
$$\left[\frac{(\mu-1)^2}{16}\mathrm{Bm}\,\hat{a}\left(\frac{H_{0a}^2}{H_0^2}\frac{1}{\left(\hat{a}^2+\mu\right)^2}-\frac{H_{0b}^2}{H_0^2}\frac{1}{\left(\hat{a}^2\mu+1\right)^2}\right)-\frac{\Phi(\hat{a})}{\hat{a}^4-1}\right] \tag{20}$$

$$\dot{\varphi} = \frac{H_{0a}H_{0b}}{H_0^2}\frac{\mathrm{Bm}}{8\pi}\frac{(\mu-1)^2\hat{a}^2}{\left(\hat{a}^2+\mu\right)\left(\hat{a}^2\mu+1\right)}\frac{2\hat{a}^2\dfrac{\hat{a}^4+1}{\hat{a}^4-1}+\lambda\left(\hat{a}^4-1\right)}{2\hat{a}^2+\lambda\left(\hat{a}^4+1\right)} \tag{21}$$

Results of numerical simulation, applying Runge-Kutta 4th order algorithm are shown on Fig.2. The main difference of results comparing with [7] is the following: if a magnetic Bond number (Bm=15, Fig.2a) is below the critical value then critical field frequency is equal to infinity like it is obtained by BEM simulations [7]. It means that by field frequency tending to infinity droplet still follows the field and the reason of it is that droplet extension diminishes and a shape of the droplet tends to unpertubed one. This phenomenon is not observed using equations of motion, described in [7]. If magnetic Bond number (Bm=30, Fig.2b) is beyond the critical value then critical frequency exists exceeding which droplet can not follow the field because friction forces on an extended droplet in a surrounding fluid are too large. Other evidence of better agreement of the present motion equations with 2D BEM simulation [7] is smaller difference between stable states calculated by both method (BEM and the equations of motion derived here). Main improvement is achieved due to better representation of the extensional motion of a droplet and due to accounting for rotational motion caused by a shear flow inside the droplet. Results prove that the present equations of motion could be used to simulate droplet behavior in a magnetic field with sufficient accuracy. It is interesting to note in Fig.2b that unstable focuses beyond critical frequency exist.

This work was supported by "Le Réseau Formation Recherche n°90R0933 du Ministère de l'Enseignement Superieur et de la Recherche" of France and by International Science Foundation in terms of long-time grant LBG000. Author is grateful to Dr.J.C.Bacri, Dr.A.Cēbers and Dr.R.Perzynski for helpful discussions.

References

[1] *Rosensweig R.E.* Ferrohydrodynamics - Cambridge University Press - 1985.
[2] *Helgessen G., Pieranski P., Skjeltorp A.T.* // Phys.Rev.Lett. - 1990. - Vol.64, N12 - P.1425
[3] *Skjeltorp A.T., Helgessen G.* // Physica A, 1991, v.176, p.37
[4] *Bacri J.C., Cebers A.O., Perzynski R.* Behaviour of a magnetic fluid microdrop in a rotating magnetic field // Phys.Rev.Lett. - 1994. - Vol.72, N17 - PP.2705-2708
[5] *Cebers A.* // Magnitnaya Gidrodinamika (in Russ) - 1985. - N1 - pp.25-34
[6] *Jeffrey G.F.* // Proc. Roy. Soc. - 1922. - A102 - PP.161-179
[7] *Bacri J.C., Cēbers A., Lācis S., Perzynski R.* // Abstracts of 7th ICMF -Bhavnagar - 1995. - PP.187-188

Captions

Figure 1
An elliptic 2D droplet in laboratory coordinates. Axis X,Y rotates synchronously with magnetic field.

Figure 2
Stationary positions of the droplet tip for different field frequencies. Bm=15 : magnetic field value below critical one, Bm=30 : magnetic field beyond critical value.

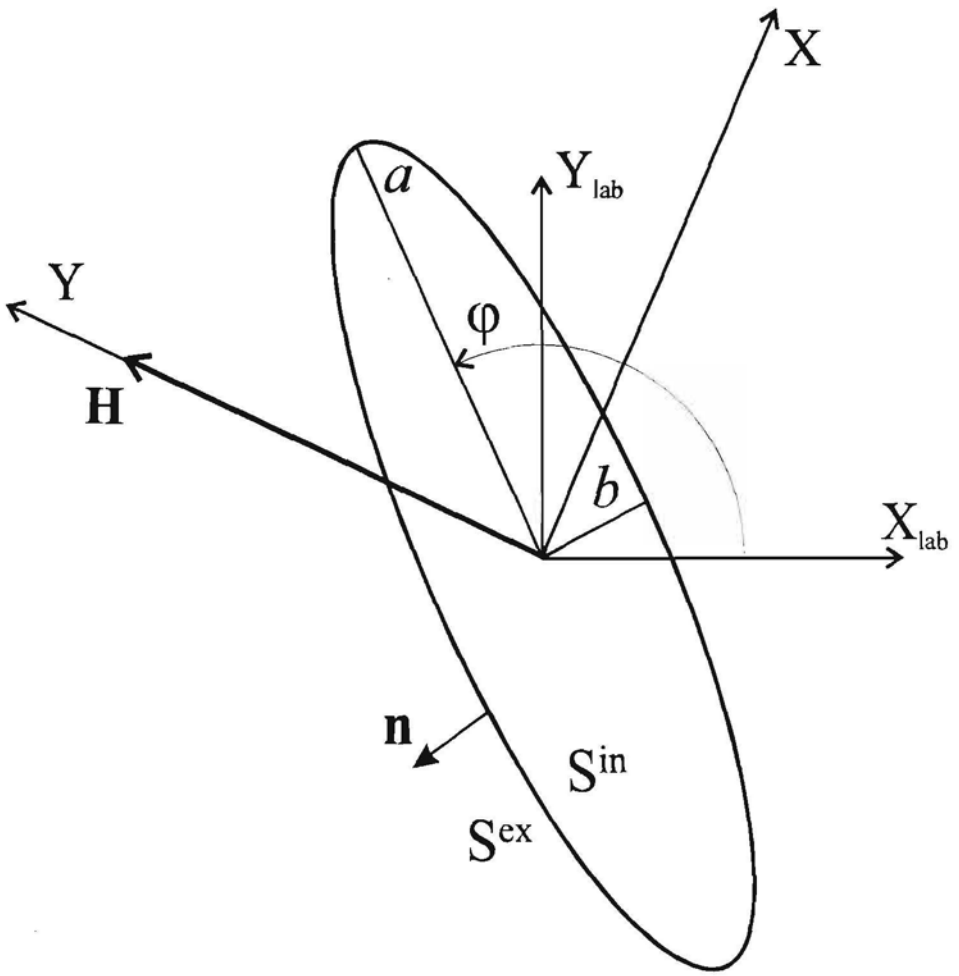

Figure 1

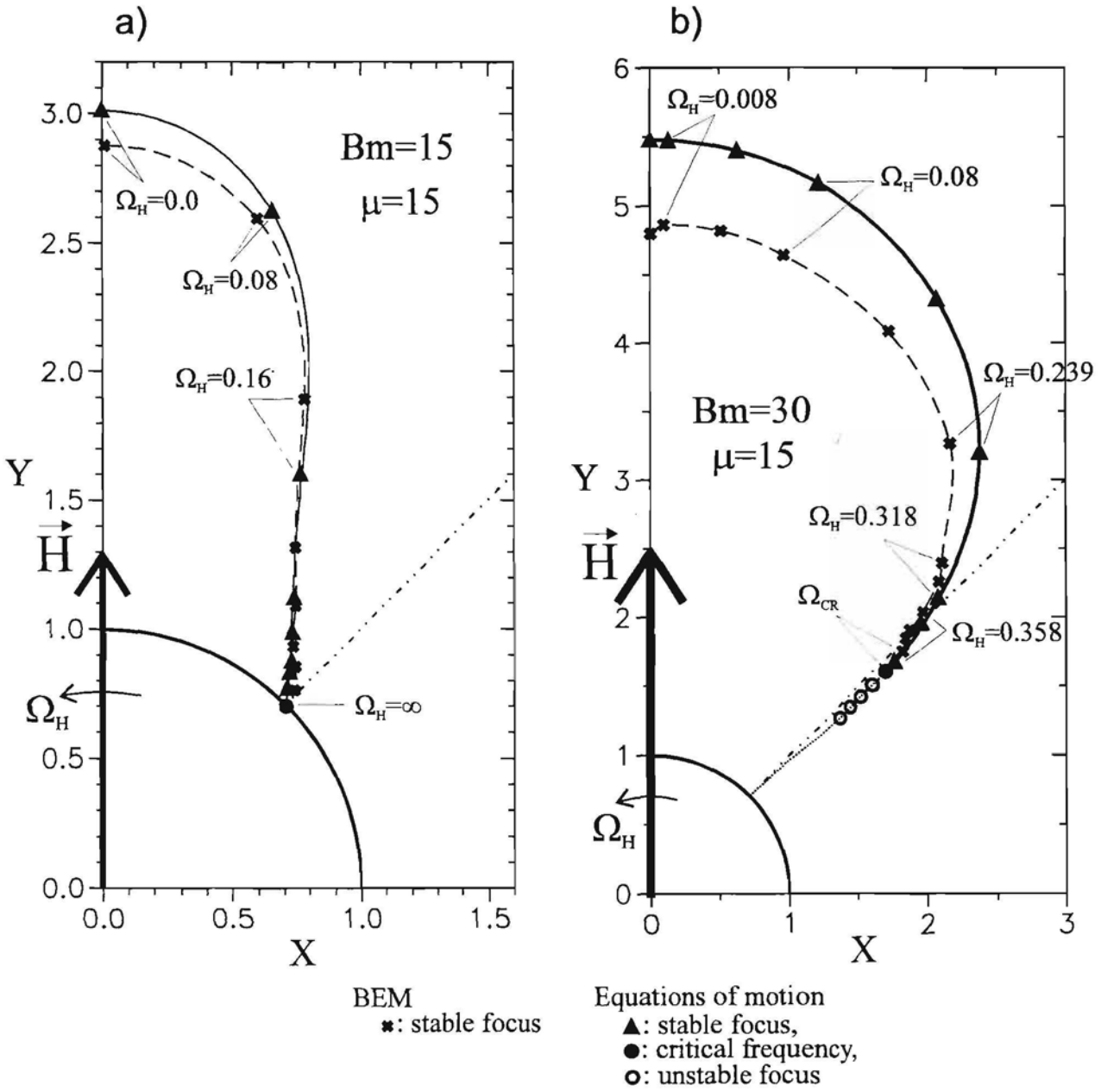
a)
Bm=15
μ=15
Ω_H=0.0
Ω_H=0.08
Ω_H=0.16
Ω_H=∞
Y
X
H
Ω_H
BEM
✱: stable focus
b)
Bm=30
μ=15
Ω_H=0.008
Ω_H=0.08
Ω_H=0.239
Ω_H=0.318
Ω_CR
Ω_H=0.358
Y
X
H
Ω_H
Equations of motion
▲: stable focus,
●: critical frequency,
o: unstable focus

Figure 2

Conclusions

1. In low-frequency magnetic fields a ferrofluid droplet exhibits two kinds of a behaviour in dependence on the applied magnetic field strength. The critical Bond number which separates these two kinds of behaviour turns out to be approximately the same as the threshold value with respect to 2-lobe perturbation in a high-frequency field.

2. At lower values of the viscosity of the droplet the critical frequency with respect to an ability to follow a rotation of a magnetic field is slightly higher than for a rigid droplet. The configurations of a droplet with the phase lag ϑ larger than $\pi/4$ are unstable for large values of λ, but moderate values of λ cause the stabilising effect: there exist steady states with ϑ slightly larger than $\pi/4$ (Ω_H slightly smaller than Ω_{CR}).

3. The motion of 2D droplet could be described by a simple set of equations of motion, given in the present chapter under the name "the Second" set. The use of this set is limited by assumption of an elliptic shape of a droplet, what means that it is adapted for moderate ratios of viscosities $\lambda \approx 1$ and the accuracy is better if higher values of the magnetic Bond number are considered, since at low values the flow can not be described by constant velocity gradients with a high accuracy. Beyond these limits the equations could be still used to predict the common properties of the behaviour of a droplet.

4. A 2D viscous droplet ($\lambda \geq 5$) exhibits a bending instability in the magnetic field oriented perpendicular to the major dimension of a droplet. The significant bending effect is observed in the case when droplet is exposed long enough to such a field, i.e. if the field frequency slightly exceeds the critical one with respect to the ability to follow the field. More detailed studies of this effect are highly desirable.

Chapter 6

Droplet in low-frequency elliptically polarised field: mode locking and Devil's staircase

As it is shown in Chapter 5, the "jerky" motion of a ferrofluid droplet beyond the critical frequency in a rotating field exhibits a "smooth" dependence on field frequency Ω_H in the case of "high-field" (see Chapter 5) behaviour, if the polarisation of a rotating field is circular and $\Omega_H > \Omega_{CR}$. By the "smooth" dependence on Ω_H it is understood that time-averaged angular frequency $\overline{\Omega}$ of a droplet rotation decreases strongly as Ω_H increases (see Fig.5.1). The consequence of that "smoothness" is the following: in a rotating field with circular polarisation there is no frequency locking between Ω_H and $\overline{\Omega}$. This observation is quite natural since there is just one frequency, namely the frequency of droplet oscillations $\Omega_D = \Omega_H - \overline{\Omega}$, which is present in such rotation (see the trajectories in Fig.5.1). The frequency $\overline{\Omega}$ have mostly mathematical sense in this case. The field frequency Ω_H excites rotation of droplet, the oscillations appears by change of the phase lag ϑ which depends not only on Ω_H, but also on the friction torque. The physical situation changes if the inertia effects are taken into account: in such a case there is a frequency of a shape oscillations and hence an eventual frequency locking may take place. In the case of microdroplets inertia plays no role and all oscillations are damped during a fraction of a self-oscillation period due to the viscous dissipation of the energy.

The frequency locking is the common phenomenon in systems with two frequencies. The ferrofluid droplet behaviour could obtain a second frequency by an

elliptically polarised field: it contains the pure rotational component, which is an origin of the frequency $\Omega_D=\Omega_H-\overline{\Omega}$, and the pure linearly oscillating component, which has the frequency Ω_H [6*]. The characteristic property of the system like a ferrofluid droplet is that the response to the oscillating field has frequency $2\Omega_H$. Thus, the ferrofluid droplet in the elliptically polarised field possesses the necessary requirement for a mode locking. The subject of the present chapter is to describe mode locking for a ferrofluid droplet. Similar phenomena were already observed in [57,101,102] for a pair of bounded non-magnetic spheres in a magnetic fluid (this system is called "magnetic holes"). There mode locking ranges are found experimentally and well described by a single nonlinear equation.

In fact, the mode locking is not a rare phenomenon, it appears in many systems, where at least two competing frequencies are present [16,80]. The simplest example is the one observed in the 17th century by Christian Huyghens: two clocks hanging back to back on the wall tend to synchronise their motion [16]. The two frequencies may arise dynamically within the system itself or through the coupling of an oscillator to external periodic force. There is usually some parameter, varying which the system passes through regimes that are phase locked and regimes that are not. When systems are phase locked the ratio between their frequencies is a rational number. The width of the phase-locked intervals depends on the strength of a coupling. A typical example of mode locking intervals is so called Devil's staircase [16,80]. The Devil's staircase appears not only in dynamical systems, but also in long-range spatially periodic solid structures.

Here only some examples, where a phase-locking takes place, are mentioned. Thus key physiological systems, such as the cardiovascular, respiratory, neuromuscular, and hormonal systems, display intrinsic oscillatory behaviour [53]. These systems interact with another and the outside environment. Moreover, there are innumerable feedback loops acting to maintain physiological variables within normal limits. Another example is the driven van der Pole oscillator [82]. It is one of the most intensively studied systems in nonlinear dynamics. Van der Pole oscillator is described by an equation, which in the 1920s was introduced as a model for a simple vacuum tube oscillator circuit [80]. The well-known example is also the Belousov-

Zabotinsky reaction. It is a complex chemical reaction with oscillatory character [80,16]. The Rayleigh-Bénard hydrodynamic convection systems exhibit similar properties [60].

Most of information about main properties could be obtained analysing very simple dynamical systems, called circle maps [3,80], which are mappings in terms of an angular variable θ_n on the form

$$\theta_{n+1} = \theta_n + \Omega - K\,g(\theta_n). \qquad (6.1)$$

The circle map is a discrete analogue of a differential equation

$$\dot{\theta} = \Omega - K\,g(\theta_n\ , \qquad (6.2)$$

written in the form

$$d\theta = (\Omega - K\,g(\theta_n))dt. \qquad (6.4)$$

Here K and Ω are constants and g is a periodic function, θ and θ_n are not the same due to the different scaling. The winding number is defined as

$$W = \lim_{n\to\infty} \frac{\theta_n - \theta_0}{n}, \qquad (6.5)$$

and it is studied in dependence on Ω for different values of K. The comparison of (6.5) with (6.3) shows that W is the ratio between time-averaged angular frequency of the system (parameter $\bar{\dot{\theta}}$) and the driving frequency Ω.

If K>0, than mode-locking takes place and results in a diagram W versus Ω, which owns the name "the devil's staircase" due to its fractal properties [80], see Fig.3 in [6*]. The function W versus Ω at K=1 is called a complete devil's staircase, because all the range of Ω completely covered by mode-locking intervals without any overlapping. Consequently, at K<1, W versus Ω is an incomplete devil's staircase. In the present case mode-locking means, that W is equal to a rational number in some frequency range. In the case of an incomplete devil's staircase between mode-locking intervals exist values of Ω, at which the W is irrational.

An irrational value of W indicates a quasiperiodic motion, which basically can be thought of as a mixture of periodic motions of several different incommensurable fundamental frequencies [80]

The phase-locked oscillations are easy to find by numerical methods, since mode-locking means that small perturbations, caused by numerical errors, lead to the same mode and same winding number W. The quasiperiodic oscillation in present case is not possible to detect by numerical methods, because it will be approximated by the nearest phase-locked oscillation mode.

An interesting property of the devil's staircase is that mode-locking intervals correspond to a structure, called the Farey tree [74] as it is shown in [6*]. The dependence of mode-locking on the control parameter K usually is illustrated by the plot of mode-locking domains in phase diagram K versus Ω. The mode-locking domains in such diagram are shown by so-called Arnold's tongues (see Fig.9 in [6*]). The structure of the Arnold's tongue is sketched in Fig.6.1 [26]. The domain of the definite mode locking consists of the entire region between lines OA_L, OA_R. Below the critical line K=1 the W is unique, above the critical line there are three important lines: first the hyperbole-like curve with tip at D where a period doubling takes place and the point D correspond to the lowest value of K for that. The period doubling in this case does not change the value of the winding number, because the orbit changes from P/Q to 2P/2Q, as it is illustrated by an example from the behaviour of ferrofluid droplet in Fig.6.2. In this trajectory plot two doublets of period doubling are present. It is typical, that above that hyperbola-like curve there is a complicate set of period doublings. Second there are in Fig.6.1 two lines g_L and g_R, corresponding to the neighbour tongues. Between these two lines the winding number W is still unique, but overlapping with the neighbour tongue, for example, between OA_L and g_L, leads to the effect that in this region it is possible to find a whole interval of winding numbers.

The period doubling scenarios and transition to a chaos are extremely interesting phenomena, studies of them could explain the behaviour of a ferrofluid droplet in the "X-region" in Fig.9 [6*]. Until now mostly the properties of the mode-locking domain for subcritical values of control parameter is considered and summarised in [6*]. As last, in Fig.6.3 and Fig.6.4 the one example of a motion, which could be chaotic, is shown by the states at time moment, which correspond to the magnetic field orientation along X-axis. Thus, these pictures correspond to the all time moments $t_j=\pi \cdot j/\Omega_H$. Both figures are obtained performing calculation of time-averaged

frequency of a droplet rotation. As result for every point in the diagram some value of W is obtained. All together more than 100 different values are detected, in both figures only the six mostly met are shown, the initial states of the rest are shown by dots. Are they all really different? It is not sure, because if there is quasiperiodic motion, or motion which is near quasiperiodic, even during rather long time intervals, essentially different average frequencies could be observed. Here 2000 field periods are taken for averaging of every point. The parameters Bm=50; m=15, l=5, Ω_H=0.35, g=0.3 already correspond to the X-region in [6*]. It is obvious that even in the zoomed area (see Fig.6.4) there is no some concentration of one mode. Further research of this phenomenon implementing calculation of Lyapunov exponents [1] should give sure answer about the character of the behaviour of a ferrofluid droplet in an elliptic field if parameters match the X-region.

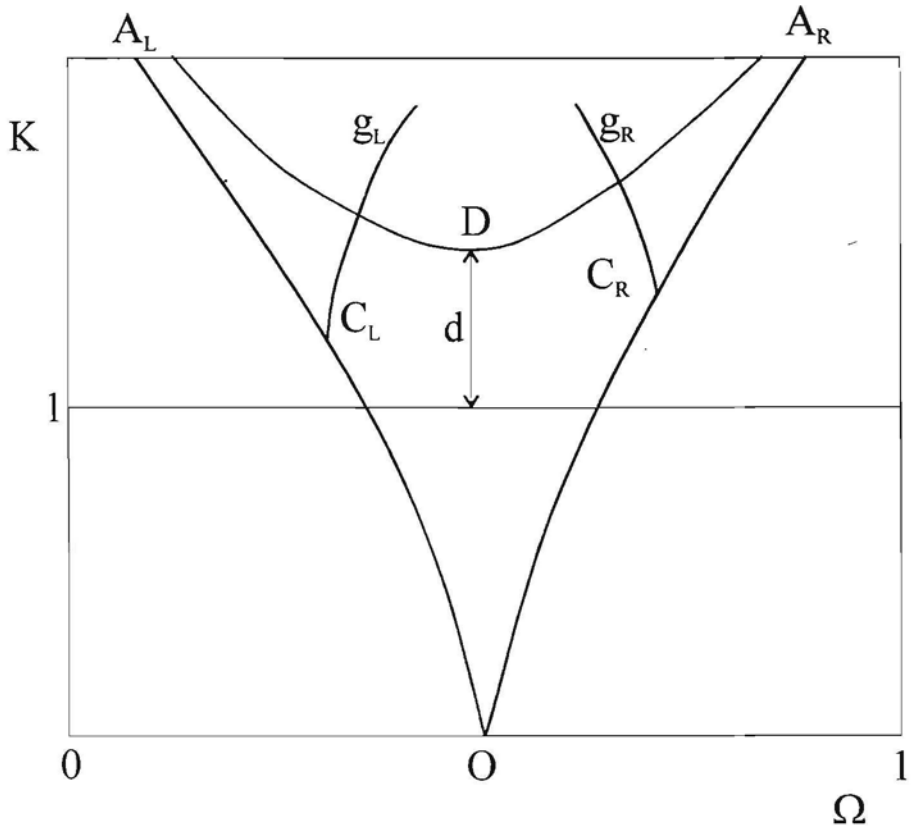

Figure 6.1. Anatomy of an Arnold tongue as explained in the text

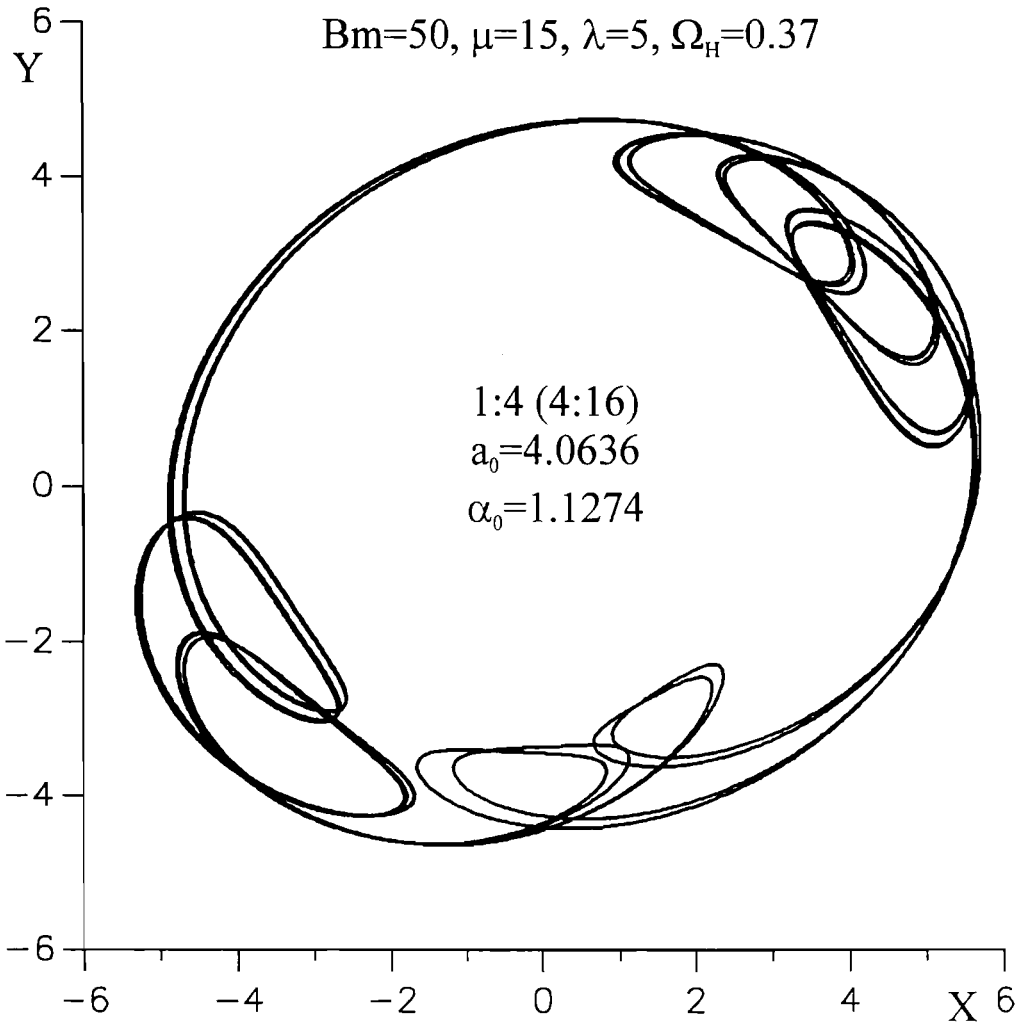

Figure 6.2. The second period doubling:
a doublet of doubled trajectories

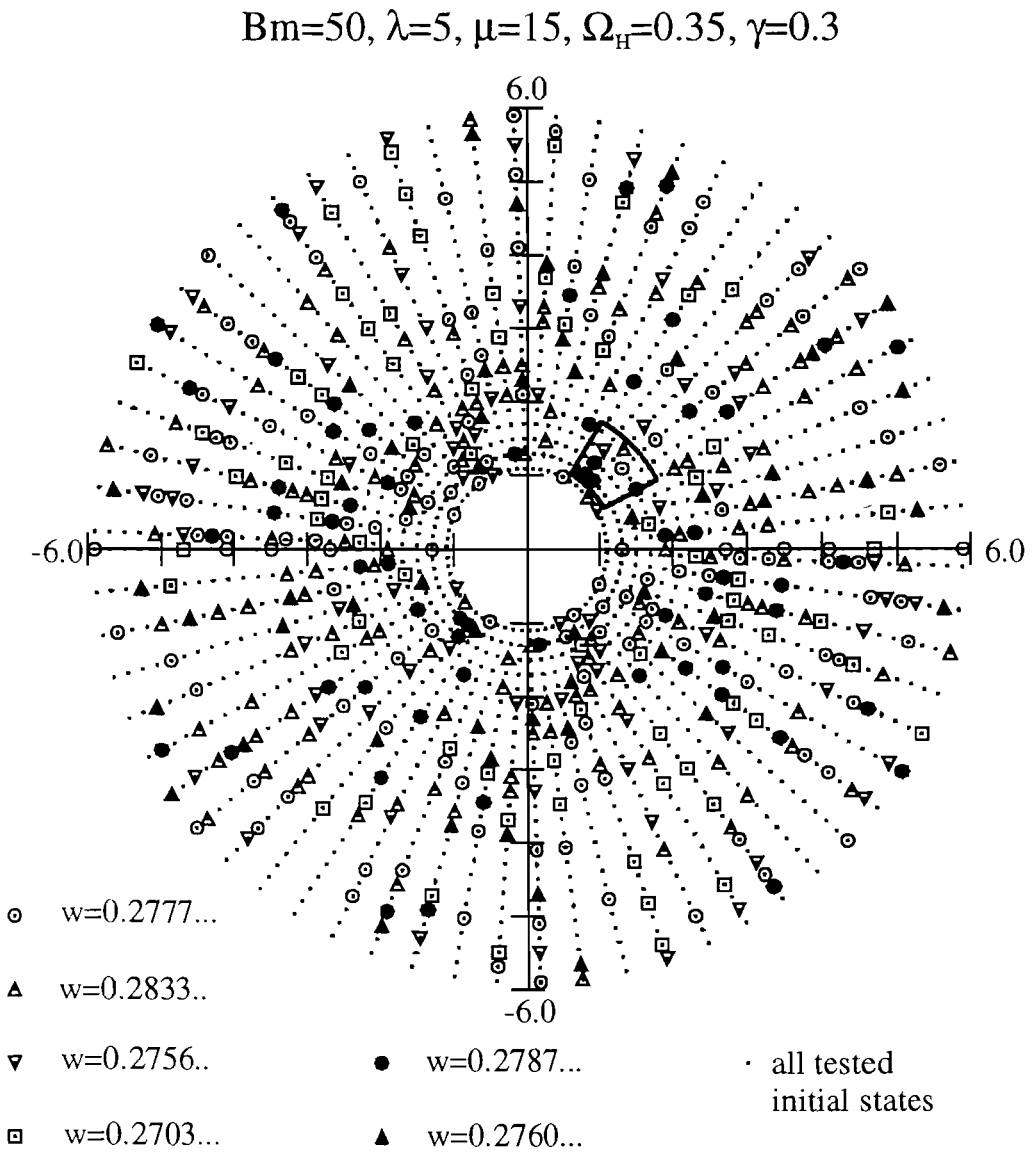

Figure 6.3. Map of the modes obtained from different initial states in the laboratory coordinates

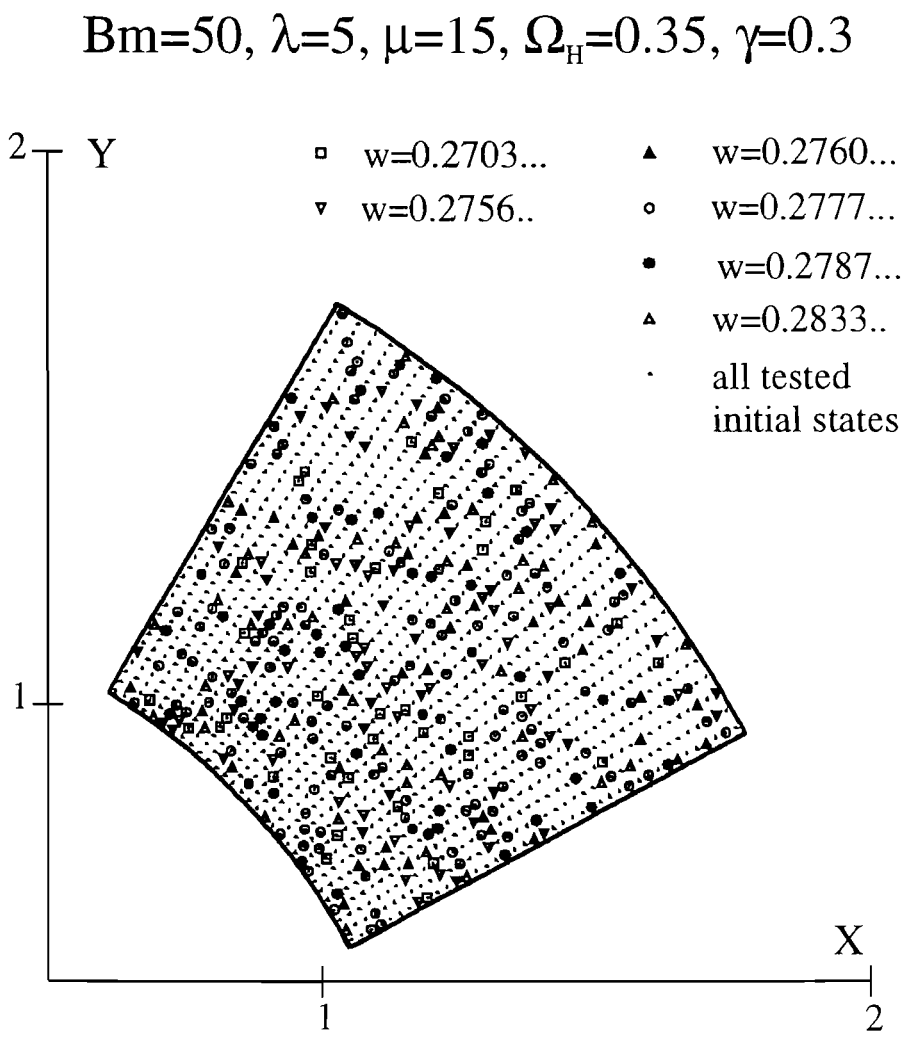

Figure 6.4. The zoomed area of the modes obtained from different initial states in the laboratory coordinates

Included paper

J.C.Bacri, A.Cēbers, S.Lācis, R.Perzynski

Mode locking and devil's staircase for 2D ferrofluid droplet in elliptically polarized rotating magnetic field

Physica D (submitted)

J.C.Bacri, A.Cēbers, S.Lācis, R.Perzynski

Mode locking and devil's staircase for 2D ferrofluid droplet in elliptically polarized rotating magnetic field

Abstract. - Numerical studies reveal that dynamics of the magnetic fluid droplet under the action of elliptically polarized rotating magnetic field can be quite complicate including transition to chaotic behavior. On the basis of the equations of motion derived by virial method devil's staircase and its Farey tree structure for the time-averaged angular velocity of the droplet in dependence on the angular velocity of elliptically polarized field has been found. Considering mode locking (Arnold tongues) in dependence on magnetic Bond number multiple basins of the attraction in different regions of the parameter space have been established. By numerical simulations their fractal properties are illustrated. Existence of the period doublings and transition to chaotic behavior is also predicted.

A system with non-zero magnetic dipole moment in rotating magnetic field tends to follow the field rotation, until at some critical frequency friction torque can no more be balanced by magnetic torque [1]: "break-off" takes place and a rotation of the droplet becomes "jerky". Similar phenomena are observed for a bound pair of non-magnetic particles in a magnetic fluid [2,3]. The interplay between magnetic and viscous forces leads to various modes of motion, classified as 1) steady-state rotations; 2) rotations with stops and backward motions; and 3) localized oscillations. Transitions between these modes are well described by a single nonlinear equation and depend on the frequency and amplitude of the rotating field, the fluid viscosity and the magnetic susceptibility. It is both experimentally and numerically found out

[3] that for a pair of free spheres phase locking takes place in the elliptical polarized field: $\overline{\Omega}/\Omega_H = 1/2,\ 1/4$, etc., where $\overline{\Omega}$ is the average angular frequency of the pair rotation, and Ω_H is the angular frequency of the magnetic field rotation. Recent studies of a pair of rigid ferrofluid drops in a rotating magnetic field [4] display the existence of a plateau for the frequency of a pair rotation at high-frequency range. The chaotic motion of a compass [5] and a permanent magnet rotor [6] is already studied in oscillating field accounting for inertia of a system since energy dissipation rate is quite small in these two cases. The behavior of the magnetic fluid (MF) microdroplet in the rotating magnetic field includes a wide variety of very complex phenomena in the high-frequency range [7]. In low-frequency range the shape of droplet is close to a general ellipsoid [7,8], but nevertheless the behavior even at low frequencies could be rather complex, since a droplet has more degrees of freedom than rigid magnetic dipole placed in a rotating field. One very important characteristic of such a system is the extraordinary high rate of the energy dissipation due to the small size of droplets, hence the inertia play no role.

In [9] we have studied numerically the response of a magnetic fluid microdrop to a rotating magnetic field in 2D by the boundary element method (BEM). In the low-frequency range, an elongated droplet rotates with magnetic field frequency. Increasing field frequency, the motion of the droplet goes through a transition from a state where the droplet follows the magnetic field with a constant phase lag to a state where the phase lag increases in a series of kinks when the field frequency passes the critical one. The equations of the droplet motion were derived analytically and good agreement with BEM was obtained.

Two different types of steady-state behaviors were observed depending on the magnetic field strength. These two types are separated by the critical value of the magnetic Bond number, which turns out to be the threshold value of the instability of a 2D droplet in a high-frequency rotating field with respect to the elliptical deformations [10]:

$$Bm_{cr} = 6\pi(\mu+1)^3/(\mu-1)^3. \qquad (1)$$

At μ=15 we have Bm_{cr}=28.14.

1. **"Low-field" behavior:** If the magnetic Bond number is less than the critical one ($Bm_{cr} = 28.14,\ \mu = 15$), the extension of droplet in stationary configurations is

diminishing with the increase of the rotating field frequency, and the maximal phase lag value $\pi/4$ is reached at infinite frequency.

2. **"High-field" behavior:** For the magnetic Bond numbers larger than the critical one the maximal phase lag ($\approx \pi/4$) is reached already at a finite critical frequency Ω_{cr}.

It was shown in [9] by linear small perturbations analysis of differential equations for a motion near the stable point that finite value of viscosity inside the droplet causes stabilizing effect to the ability of droplet to follow the magnetic field rotation. It results in time-averaged frequency jump from field frequency Ω_H to some smaller value just after critical frequency Ω_{cr} in the case of the "high-field" behavior. Increasing ratio of viscosities $\lambda=\eta^{in}/\eta^{ex}$ the critical frequency Ω_{cr} slightly decreases and tends to its analytical value Ω_{cr0} (see relation (14) further in the text).

Test simulations have shown [9] that in the case of elliptic polarized rotating magnetic field phase locking takes place like in [3]. The phase locking and Devil's staircase in the phase plane $\overline{\Omega}/\Omega_H$ versus Ω_H is the subject of our present studies reported here.

For these studies improved (to compare with [9]) equations of motion, derived in [11] are used. The new set of equations describes a 2D magnetic fluid droplet in low-frequency rotating field under the assumption of elliptic shape and accounts for shear flow inside the droplet. 2D Stokes flow outside the droplet is treated exactly, but inside is described in approximation of constant velocity gradients. Dynamic boundary conditions are satisfied integrally by virial moment technique. Arbitrary viscosities of fluids inside and outside the droplet are considered. A small size of microdroplet and relatively small characteristic velocities of flow allows to neglect inertia and gravity terms, concentrating on surface tension and magnetic forces on the surface of the droplet. Hence the dynamics of a free surface of a droplet can be described in the framework of the creeping flow.

Elliptic incompressible MF droplet is completely determined by the length of its large semi-axis a and the angle φ of its orientation with respect to X_{lab}-axis of the laboratory frame (see Fig.1). To conserve elliptic shape of the droplet a flow inside the droplet is approximated by constant gradients γ_{ik} of velocity field

$$v_i = \gamma_{ik} x_k . \qquad (2)$$

Thus the equations of motion [11] in non-dimensional form are

$$\dot{a} = \frac{2a^4}{\pi\left(a^4+1+2\lambda a^2\right)} \times$$
$$\left[\frac{(\mu-1)^2}{16}\,\mathrm{Bm}\,a\left(\frac{H_{0a}^2}{H_0^2}\frac{1}{\left(a^2+\mu\right)^2}-\frac{H_{0b}^2}{H_0^2}\frac{1}{\left(a^2\mu+1\right)^2}\right)-\frac{\Phi(a)}{a^4-1}\right] \qquad (3)$$

$$\dot{\varphi} = \frac{H_{0a}H_{0b}}{H_0^2}\frac{\mathrm{Bm}}{8\pi}\frac{(\mu-1)^2a^2}{\left(a^2+\mu\right)\left(a^2\mu+1\right)}\frac{2a^2\dfrac{a^4+1}{a^4-1}+\lambda\left(a^4-1\right)}{2a^2+\lambda\left(a^4+1\right)} \qquad (4)$$

Here

$$\Phi(a)=\left((a^4+1)\,\mathrm{E}(e)-2\,\mathrm{K}(e)\right) \quad \lambda=\eta_{in}/\eta_{ex}, \quad a=a_{\dim}/R,$$

where $E(e)=\int_0^{\pi/2}\sqrt{1-\left(e\sin x\right)^2}\,dx$ and $\mathrm{K}(e)=\int_0^{\pi/2}1\Big/\sqrt{1-\left(e\sin x\right)^2}\,dx$ are the complete elliptic integrals of first, resp., second kind, $e^2=1-b^2/a^2$, μ: magnetic permeability, η_{in}, η_{ex}: viscosities of fluid inside, resp., outside the droplet.

A radius of a circular drop $R=\sqrt{ab}$ and a time scaling unit $\tau_h = R\eta_{ex}/\sigma$ are used to obtain non-dimensional form of equations, the interplay of magnetic forces and a surface tension is characterized by magnetic Bond number $\mathrm{Bm} = H_0^2 R/\sigma$.

Main improvement is achieved due to better representation of the extensional motion of a droplet and due to accounting for rotational motion caused by a shear flow inside the droplet. Results prove that the present equations of motion could be used to simulate droplet behavior in a magnetic field with sufficient accuracy.

In the case of elliptic field polarization, instant external magnetic field components are given by the following relations:

$$H_X(t)=H_{0X}\cos\left(\Omega_H t\right), \qquad (5)$$
$$H_Y(t)=H_{0Y}\sin\left(\Omega_H t\right).$$

We introduce parameter γ to control magnetic field ellipticity, assuming $H_{0X}\geq H_{0Y}$:

$$H_{0X}=H_0\sqrt{1+\gamma}, \qquad (6)$$
$$H_{0Y}=H_0\sqrt{1-\gamma},$$
$$\gamma=\frac{H_{0X}^2-H_{0Y}^2}{H_{0X}^2+H_{0Y}^2}. \qquad (7)$$

Advantage of such a definition is that mean square value for external field is fixed by choice of H_0 whatever is the value of γ, keeping constant effective magnetic Bond number Bm = $H_0^2 R/\sigma$:

$$\overline{H^2} = \overline{\left(H_{0X}\cos(\Omega_H t)\right)^2 + \left(H_{0Y}\sin(\Omega_H t)\right)^2} = \frac{1}{2}\left(H_{0X}^2 + H_{0Y}^2\right) = H_0^2. \qquad (8)$$

Hence elliptically polarized field is given by its "average" intensity H_0 and ellipticity parameter γ. For the physical interpretation of elliptical field polarization we can divide the field in the pure rotational field $\mathbf{H}_{rot}$, the components are

$$\begin{cases} H_{X,rot}(t) = H_0\sqrt{1-\gamma}\cos(\Omega_H t) \\ H_{Y,rot}(t) = H_0\sqrt{1-\gamma}\sin(\Omega_H t) \end{cases}$$

and a non-dimensional amplitude is $h_{rot} = \sqrt{1-\gamma}$, and the pure linear-oscillating field $\mathbf{H}_{osc}$, the components are

$$\begin{cases} H_{X,rot}(t) = H_0\left(\sqrt{1+\gamma} - \sqrt{1-\gamma}\right)\cos(\Omega_H t) \\ H_{Y,rot}(t) = 0 \end{cases}$$

and the non-dimensional amplitude is $h_{osc} = \sqrt{1+\gamma} - \sqrt{1-\gamma}$. Increasing g from 0 to 1, the rotational field amplitude h_{rot} tends to 0, but the oscillating field amplitude h_{osc}, in contrary, increases from 0 to $\sqrt{2}$.

The instant projections of external field intensity to directions of both axes of elliptic droplet H_{0a}, H_{0b}, implemented in equations (3), (4), are derived as

$$H_{0a}(t) = H_X(t)\cos\varphi + H_Y(t)\sin\varphi, \qquad (9)$$
$$H_{0b}(t) = -H_X(t)\sin\varphi + H_Y(t)\cos\varphi.$$

Here φ is the angle between the major semi-axis of a droplet and X-axis of the laboratory coordinates. Let us introduce non-dimensional field components in directions of semi-axes of the elliptic droplet $h_a = H_{0a}/H_0$ and $h_b = H_{0b}/H_0$. Then

$$h_a^2 = \left[1 + \cos 2\varphi_H \cos 2\varphi + \gamma\left(\cos 2\varphi_H + \cos 2\varphi\right) + \sqrt{1-\gamma^2}\sin 2\varphi_H \sin 2\varphi\right]/2, \qquad (10)$$

$$h_b^2 = \left[1 - \cos 2\varphi_H \cos 2\varphi + \gamma\left(\cos 2\varphi_H - \cos 2\varphi\right) - \sqrt{1-\gamma^2}\sin 2\varphi_H \sin 2\varphi\right]/2, \qquad (11)$$

$$h_a h_b = \left[-\cos 2\varphi_H \sin 2\varphi - \gamma \sin 2\varphi + \sqrt{1-\gamma^2}\sin 2\varphi_H \cos 2\varphi\right]/2. \qquad (12)$$

Here $\varphi_H = \Omega_H t$. In the case of circular field polarization (γ=0) we have

$$h_a^2\big|_{\gamma=0} = \left[1+\cos 2\varphi_H \cos 2\varphi + \sin 2\varphi_H \sin 2\varphi\right]/2 = \cos^2(\varphi_H - \varphi),$$

$$h_b^2\big|_{\gamma=0} = \left[1-\cos 2\varphi_H \cos 2\varphi - \sin 2\varphi_H \sin 2\varphi\right]/2 = \sin^2(\varphi_H - \varphi),$$

$$h_a h_b\big|_{\gamma=0} = \left[-\cos 2\varphi_H \sin 2\varphi + \sin 2\varphi_H \cos 2\varphi\right]/2 = \sin 2(\varphi_H - \varphi)/2.$$

Hence the rigid droplet limit $\lambda\to\infty$ in the case of circular field polarization is analogous to bound pair of soft magnetic particles [2]:

$$\dot{\varphi} = \Omega_{cr} \sin 2(\varphi_H - \varphi), \qquad (13)$$

$$\Omega_{cr} = \frac{\mathrm{Bm}}{16\pi} \frac{(\mu-1)^2 a^2 (a^4-1)}{(a^2+\mu)(a^2\mu+1)(a^4+1)}. \qquad (14)$$

Time-averaged frequency $\overline{\Omega}$ of a droplet rotation is defined as

$$\overline{\Omega} = \lim_{T\to\infty} \frac{1}{T} \int_0^T \dot{\varphi} dt. \qquad (15)$$

An analytical integration for (13) gives the following expression for time-averaged frequency:

$$\overline{\Omega} = \Omega_H - \sqrt{\Omega_H^2 - \Omega_{cr}^2}. \qquad (16)$$

N.B.: the value of a is fixed, what corresponds either to "rigid droplet" approximation $\lambda>>1$ or "high-frequency" approximation $\Omega_H>>\Omega_{cr}$. Tending Ω_H/Ω_{cr} to infinity we arrive at approximation for "very high" frequencies:

$$\overline{\Omega} \approx \frac{\Omega_{cr}^2}{2\Omega_H}. \qquad (17)$$

In [4] it is reported that after a jerky regime, the frequency of the pair rotation reaches a plateau independent of Ω_H. Hence in really high frequencies ($\Omega_H/\Omega_{cr}>>10$) present approximations could be to rough to describe the behavior of the droplet, account for effects like internal rotation could be necessary.

The elongation of a droplet depends on the intensity of applied magnetic field, i.e. major semi-axis a could be obtained from equation (4) at constraint $\dot{a} = 0$:

$$\frac{(\mu-1)^2}{32} \mathrm{Bm}\, a \left(\frac{1}{(a^2+\mu)^2} - \frac{1}{(a^2\mu+1)^2} \right) = \frac{\Phi(a)}{a^4-1}. \qquad (18)$$

Curves of a versus Bm are plotted in Fig.2. Curves for different μ values certificate that influence of magnetic permeability to droplet extension could be very strong. In dependence on magnetic permeability the instability in respect to elliptic shape

perturbation beyond the magnetic field threshold has either the first order ($\mu<10.71$) or the second order ($\mu>10.71$) transition properties [10].

Let us now discuss rigid droplet limit $\lambda\to\infty$ in the case of elliptic field polarization. Equation (4) transforms to

$$\dot{\varphi} = \Omega_{cr}\left[-\cos 2\varphi_H \sin 2\varphi - \gamma \sin 2\varphi + \sqrt{1-\gamma^2}\sin 2\varphi_H \cos 2\varphi\right] . \qquad (19)$$

Though multiplier Ω_{cr} is constant in the approximation of rigid droplet, analytical integration of equation (19) in order to obtain $\overline{\Omega}$ is not possible due to strong nonlinearity. Hence 4th order Runge-Kutta algorithm is applied to solve the system of equations of motion (3),(4). Time-averaged frequency $\overline{\Omega}$ is obtained in the following way: at first numerical algorithm is run some transition time T_t in order to obtain from initial perturbations free state, afterwards this state is taken as initial one for numerical algorithm. After N field revolutions winding number [12]

$$w_N = \frac{1}{2\pi N}\int_{T_t}^{T_t+2\pi N/\Omega_H} \dot{\varphi}\, dt = \frac{\varphi_H - \varphi_0}{2\pi N} \qquad (20)$$

is found. Increasing N, averaged frequency $\overline{\Omega} = w_N\Omega_H$ could be found with arbitrary accuracy, of course, truncation errors as well as accuracy of Runge-Kutta algorithm should be taken into account. In Fig.3a the winding number $w_N = \overline{\Omega}/\Omega_H$ is plotted versus field frequency Ω_H, Bm=50, μ=15, λ=5, γ=0.15. The solid curve shows the winding number w obtained increasing field frequency, the dashed one: decreasing it. There is two new phenomena introduced by elliptic field polarization: mode locking in certain frequency ranges and overlapping of modes. The first two rather wide mode self-locking steps $w_{1/1}$ and $w_{1/2}$ correspond to the frequency range in which circular field has stabilization of droplet rotation with field frequency due to finite value of λ. The overlapping of both modes results in mode hysteresis: increasing field frequency there is jump in phase plane from mode $w_{1/1}$ directly to mode $w_{1/2}$ passing over non-existent modes with winding numbers between 1 and 0.5. Increasing further field frequency, sequentially mode-locking $w_{1/3}$, $w_{1/4}$, $w_{1/5}$ take place. Here and further ratios like p/q with integer p,q are used to denote frequency ratios $w_{p/q} = \overline{\Omega}/\Omega_H = p/q$. Such a mode locking structure is called Devil's staircase [12,13]. Here we have degenerated Devil's staircase since overlapping take place and winding numbers between modes 1/1 and 1/2 are not present. The classical Devil's

staircase is fractal structure, where sequentially all ratios from Farey tree [12] are present. Obviously degeneration could be eliminated, diminishing stabilization of droplet's rotation with field frequency, i.e. increasing λ.

Another self-locking modes overlapping takes place for the field frequencies in range about Ω_H=0.372..0.376 where exist modes $w_{1/2}$ for the increase of a frequency and sequence of modes without detected mode-locking steps for the decrease of a frequency. According to Devil's staircase properties, in this last case mode-locking intervals for frequency could exist, just the width of them are to small to detect by frequency step $\Delta\Omega_H$=0.0005.

In Fig.03b the frequency range Ω_H=[0.372..0.385] is plotted magnified to compare with the Fig.3a. The left part of the plot is degenerated due to overlapping of modes already mentioned above. The noisy character of the lower curve corresponding to the increase of a field at frequencies about 0.374 could be caused either by not a sufficiently long averaging time or by the presence of competing modes situated close each another in the phase space. For frequencies larger than Ω_H=0.377 the character of the curve changes to the classical devil staircase [13], the winding numbers for mode-locking intervals correspond very well to the construction of Farey tree [12,13] as it is shown in Fig.3b above the plot of the winding number versus field frequency. One can see quite well the self-similarity of the devil's staircase in that frequency range.

The equation of motion (3),(4) show that the solution of them depends on five parameters: Bm, μ, λ, γ, Ω_H. Here we do not discuss influence of magnetic permeability μ on the solution, but it should be pointed out that μ can not be eliminated from equations of motion by including it in magnetic Bond number since there are two terms like $(a^2+\mu$ and $(a^2\mu+1$, containing both a and μ. In the present paper we focus on the case μ=15 which corresponds to an intermediate value of μ, since special effects, caused by different choice of μ are not yet observed.

The influence of Bm

In [9] it is already shown that behavior of ferrofluid droplet in circular rotating magnetic field depends on Bond number Bm in such a way that two different scenarios exist (already described above):

1. "low-field" behavior,

2. "high-field" behavior.

Similar properties are inherit in the case of the elliptic field polarization. In Fig.4 mode-locking domains are plotted in phase plain Bm versus Ω_H. One can clearly see the field threshold, below which only one mode $w_{1/1}$ (droplet follows the field) corresponding to scenario 1. exist. Beyond the field (magnetic Bond number) threshold mode-locking domains for different modes appear. Width of them do not change essentially, increasing Bm, slope of boundaries is nearly constant.

We can point out main sequence of mode locking: $w_{1/q}$, where q is an integer. According to Farey tree law between two modes with winding numbers p1/q1 and p2/q2 there is an other mode $(p_1+p_2)/(q_1+q_2)$. In present case it works good just for second sequence, obtained from the main one, for example (1+1)/(2+3) gives 3/5. In general every next sequence becomes more and more narrow and hence harder to detect. If the width of the mode-locking plateau becomes smaller than a frequency step for numerical algorithm, then we "do not see" that mode-locking at all. For the frequency range from mode $w_{1/3}$ till infinity and Bm larger than 40 the behavior of a mode-locking seems to be more less regular: mode-locking domain boundaries are parallel with fixed slope, increasing q, a mode-locking $w_{1/q}$ frequency-width decreases. For lower frequencies rather wide overlapping domain take place for modes $w_{1/1}$ and $w_{1/2}$. Between modes $w_{1/2}$ and $w_{2/5}$ we have observed frequency interval with oscillations close to quasiperiodic ones (see further in text for definition of quasiperiodicity), so for these modes overlapping exists no.

More complex behavior is for Bm just after the threshold till values about 34 and for field frequencies Ω_H between 0.32 and 0.36. This part of phase space is plotted in "zoomed" area. Due to finite numerical methods, mode-locking domains $w_{4/5}$ and $w_{3/4}$ perhaps are not well detected. More accurate are plotted domains for locking with winding numbers $w_{1/1}$, $w_{1/2}$, $w_{2/3}$ and $w_{3/5}$. Here for the point (Ω_H=0.335, Bm=30.5) of the phase space an overlapping for four modes take place. It is illustrated by trajectories of the droplet's tip in the laboratory coordinates in Fig.5. Trajectories show rather stable motion without any transitions. The "choice" of the mode, in which a droplet self-locks, depends from initial conditions. To illustrate it in Fig.6 bassins of attraction [14] are plotted. This map represents laboratory coordinates at initial (t=0) moment, at which a magnetic field has only positive X-component according to (5).

There are 4 bassins of attraction (domains of initial conditions) leading to mode $w_{1/2}$, separated by the mode $w_{3/5}$ on the diagram. Domains of initial conditions for mode 1/1 are concentrated near the corresponding Poincare sections at time moments $t_n=n*\pi/\Omega_H$. Interesting is the structure of the spiral tails of those domains, it, as well as initial points for mode $w_{2/3}$ exhibit fractal like properties, proved by the "zoom" of the present picture, shown in Fig.7. In both diagrams mode $w_{1/1}$ is shown by empty circles, $w_{1/2}$: by crosses, $w_{2/3}$: by filled circles, and mode $w_{3/5}$ by small "-" characters. Main conclusion, which is drawn from both figures, is that the mode could be very sensitive to the choice of initial conditions, from which it evolves. If the hole map of initial conditions has fractal structure it should lead to a chaotic motion, since every small perturbation leads to the transition to a different mode, and thus, to the loss of the information about initial conditions. In the present case, periodical solutions for equations of motion show that initial conditions which initiate periodical motion without any perturbation, are placed in non-fractal regions of map, hence here just the sensitivity for a transition to some definite mode for the certain ranges of initial conditions is present.

Another quite important question is how the threshold for magnetic field behaves if frequency is fixed but the ellipticity parameter γ of the field polarization is increased from zero. Fig.8 shows that increasing γ, the changes of the threshold value are near negligible. It proves the choice of magnetic Bond number: it characterizes the field threshold. Two curves in the Fig.8 stays for the increase of Bond number (solid curve) and decrease of Bond number (dashed curve), shift between them displays the presence of a hysteresis with a magnitude which corresponds quite well to the hysteresis magnitude in the case of magnetic permeability like $\mu=15$ [10]. If γ reaches some limiting value, a droplet is locked by the oscillating component of the field and the rotating component is too weak to cause droplet rotation. A tip of a droplet provides located oscillations without any rotation.

The influence of γ

In Fig.8 the influence of γ is observed by mode-locking to $w_{0/1}$, i.e., the mode of localized oscillations without rotation of the droplet. The critical value of γ is about $\gamma=0.3..0.4$ (Bm=30..140). That corresponds to the amplitude of pure rotating field

h_{rot}=0.84..0.77 and the amplitude of pure oscillating one h_{osc}=0.30..0.55. So the limit of γ for rotation of a droplet increases rising the value of Bm. It displays that increasing Bm, the rise of the magnetic torque turn out to be more significant than the rise of the friction torque and the thus a droplet can perform full revolutions up to slightly higher limit of γ (see Fig.8).

The traditional representation for the mode-locking phenomena in dependence on nonlinear coupling control parameter is so-called Arnold's tongue diagram [13,15]. In Fig.9a the mode locking domains are plotted in the phase plane of the field ellipticity parameter γ versus the field frequency Ω_H for Bm=50, μ=15, λ=5. Two modes $w_{1/1}$ and $w_{0/1}$ predominates in the frequency range Ω_H without any overlapping. The space between them is filled with Arnold's tongues for other modes at γ<0.275, the behavior of a droplet for γ>0.275 is the subject of our studies to be published elsewhere. The boundaries of the domains $w_{1/1}$ and $w_{0/1}$ are rather smooth, except the single step with some slope for the mode $w_{1/1}$ at γ about 0.275. This value, γ=0.275, turns out to be near the critical γ, beyond which motion of a droplet becomes chaotic and Arnold's tongues loses their structure. In Fig.9b the region below γ=0.3 is plotted in more details for the same values of passive parameters (Bm=50, μ=15, λ=5). Here "Region X" is that one, results about which we shall publish elsewhere, flat top boundaries of tongues are not very realistic, detailed studies of them are related to the "Region X" subject. In the Fig.9b one can see quite well the two sequences of mode-locking: the main sequence as 1/q and the second one as 2/(2q+1), q: integer. Beyond $w_{1/10}$ the structure of tongues becomes too dense to show it, intervals "..." are used to substitute $w_{1/q}$ and $w_{2/(2q+1)}$, q>10. The unique property of the present system is overlapping for mode $w_{1/2}$: even at $\gamma \to 0$ complete overlapping takes place for modes $w_{1/1}$ and $w_{1/2}$. The mode-locking domain $w_{2/3}$ at γ about 0.27 and Ω_H about 0.35 looks curious but in fact that strange placement of it obviously should be explained by common properties of Arnold's tongues in the case of the supercritical regime. Throughout the work the value γ=0.15 is used in the cases, when g is a "passive" parameter (i.e., it is constant). This value, γ=0.15, is regarded as a moderate value for the field ellipticity control parameter.

The influence of λ

By increase of λ the ratio of viscosities are changed. Here we discuss almost the case λ=5, what could be called the case of moderate viscosity of a ferrofluid, if we compare with [7], where λ≈100. 2D simulation using the boundary element method shows [16] that in the case of an arbitrary shape (without the constraint of the elliptic shape) ferrofluid droplet displays bending instability for λ>>1 and even for λ=5. The results of present studies nevertheless could be applied because for λ=5 bending just slightly eliminates effective extension of a droplet and thus causes a minor decrease of a friction coefficient. General properties for droplet rotation still stay the same.

In the Fig.10 Arnold's tongues are plotted in the phase plane λ (log-scale) versus Ω_H. The values of passive parameters are Bm=50, μ=15, γ=0.15. The overlapping of modes $w_{1/1}$ and $w_{1/2}$ is common phenomena up to λ=115, for larger values of λ modes do not overlap. Overlapping for modes $w_{1/2}$ and $w_{1/3}$ is present just up to λ≈1.5. In general, increase of λ makes mode-locking width smaller and thus tends to eliminate overlapping. Nevertheless at λ=100 the width of the mode $w_{1/2}$ is still quite commensurable with distances between this mode and neighbor ones, whether $w_{1/1}$ or $w_{1/3}$. he second property of λ is the shift of mode-locking frequencies into the direction of a larger frequency, if λ increases.

The character of that how the mode-locking width depends on λ follows from general mechanism of mode-locking for ferrofluid droplet in the elliptically polarized magnetic field. The ellipticity of the field polarization, in fact, is the key-parameter for mode-locking phenomena in for the present problem. Since inertia plays no any role for oscillations of the droplet due to the small size of it, there must be two oscillatory motions to have mode-locking. One oscillation frequency quite naturally is maintained by rotational component of the magnetic field $\mathbf{H}_{rot}$. Other one is introduced into the motion of the droplet by pure oscillatory field $\mathbf{H}_{osc}$. The sketch of the mechanism of mode locking in present case is as follows. The $\mathbf{H}_{rot}$ causes whether the steady rotation of a droplet or the non-steady but periodic rotation with oscillations if the field frequency exceeds the critical one [9]. In the last case the frequency of droplet rotation is less than that of the field. The pure linear oscillations of a magnetic field causes oscillations of the droplet with frequency $2\Omega_H$ in X-axis direction. The amplitudes of both oscillations strongly depend on λ: increasing λ,

amplitudes diminishes. In the limit $\lambda \to \infty$ (rigid droplet) the elongation of the droplet is fixed (constant) and just the phase lag between the magnetic field and the droplet could oscillate according to (19). For a system without inertia the self-resonance is absent and two "external" frequencies are needed to realize the mode-locking. Hence the rigid droplet and the droplet in a magnetic field with the circular polarization definitely do not have mode-locking. The "soft" droplet in the field following regime, naturally, has the simplest mode-locking $w_{1/1}$. After the exceeding of the critical frequency the break-off for the droplet takes place and it rotates with some lower frequency than the magnetic field (see approximation (16)). This is "the clock" which may, or may not, lock to the another "clock" of pure linear oscillations.

Conclusions

The ferrofluid droplet in elliptically polarized field exhibits Devil's staircase like mode-locking to the magnetic field rotation frequency. In the limit of the circular field polarization the mode-locking disappears. In the case of linear field polarization pulsing oscillations of a droplet takes place. The difference from traditional Devil's staircases is overlapping at very small values of control parameter. Thus the interesting mode-locking system for dissipative system without inertia is found and described. The transition to the chaos will be described elsewhere.

REFERENCES

[1] R.E.Rosensweig. Ferrohydrodynamics. Cambridge University Press, 1985

[2] G.Helgessen, P.Pieranski, A.T.Skjeltorp Phys.Rev.Lett., 1990, v.64, N12, p.1425

[3] A.T.Skjeltorp, G.Helgessen, Physica A, 1991, v.176, p.37

[4] J.C.Bacri, C.Drame, B.Kashevsky, S.Neveu, R.Perzynski, C.Redon - Motion of a pair of rigid ferrofluid drops in a rotating magnetic field - Progr.Colloid.Sci.(1995) 98, pp124-127

[5] V.Croquette, C. Poitou - Cascade of period doubling bifurcations and large stochasticity in the motions of a compass - J.Physique Lettres 42 (1981) pp L537 - L539

[6] F.C.Moon, J.Cusumano, P.J.Holmes - Evidence for homoclinic orbits as a precursor to chaos in a magnetic pendulum - Physica 24D (1987) pp 383-390

[7] J.C.Bacri, A.O.Cēbers, R.Perzynski Behaviour of a magnetic fluid microdrop in a rotating magnetic field, Phys.Rev.Lett. - 1994. - Vol.72, N17 - PP.2705-2708

[8] A.Cēbers, S.Lācis Magnetic fluid free surface instabilities in high frequency rotating magnetic fields. - Brazilian Journal of Physics,1995,Vol.25, N2 ,pp.101-111

[9] J.C.Bacri, A.Cēbers, S.Lācis, R.Perzynski Dynamics of the magnetic fluid droplet in rotating field -Journal of Magnetism and Magnetic Materials 149 (1995) 143-147

[10] J.C.Bacri, A.Cēbers, S.Lācis, R.Perzynski On the shape calculation of the magnetic fluid droplet in rotating magnetic field - Magnitnaja Gidrodinamika (to be published)

[11] S.Lācis Equation of motion of 2D elliptic magnetic fluid droplet in a rotating magnetic field - Magnitnaja Gidrodinamika (to be published, full text)

[12] F.C.Moon Chaotic and fractal dynamics : an introduction for applied scientists and engineers, New York : Wiley, 1992, 508p

[13] P.Bak The Devil's staircase Physics Today, 1986, Vol.39, N12, pp38-45

[14] E.Ott Chaos in dynamical systems New York: Cambridge University Press, 1993, 385p

[15] V.I.Arnold Geometrical methods in the theory of ordinary differential equations New York:Springer-Verlag, 1983, 334p

[16] J.C.Bacri, A.Cēbers, S.Lācis, R.Perzynski - (to be published)

FIGURE CAPTIONS

FIG.1 - Sketch of the droplet in laboratory coordinates

FIG.2 - Droplet extension in time-averaged high-frequency rotating magnetic field

FIG.3a - Winding number w versus magnetic field frequency Ω_H. Bm=50, μ=15, λ=5. Field ellipticity parameter γ=0.15. The solid line corresponds to increase of a frequency, dashed one: decrease of it.

FIG.3b - Zoom from the FIG.3a. Winding number w versus magnetic field frequency Ω_H. Bm=50, μ=15, λ=5. Field ellipticity parameter γ=0.15. The solid line corresponds to increase of a frequency, dashed one: decrease of it. Farey tree branches for construction of observed mode-locking intervals are shown above the plot.

FIG.4 - Mode-locking domains (Arnold tongues) in phase plane Bm versus Ω_H. γ=0.15, μ=15, λ=5.

FIG.5 - Four different modes for the point (Ω_H=0.335, Bm=30.5) of phase plane. μ=15, λ=5, γ=0.15.

FIG.6 - Map of initial conditions for four different modes of Fig.5.

FIG.7 - Zoomed area from FIG.06.

FIG.8 - Magnetic field threshold versus the ellipticity parameter γ of the field polarization.

FIG.9a - Arnold's tongues diagram in the phase plane the field ellipticity control parameter γ versus the field frequency Ω_H. Mode locking domains for $w_{1/1}$ and $w_{0/1}$.

FIG.9b - Arnold's tongues diagram in the phase plane the field ellipticity control parameter γ versus the field frequency Ω_H. Mode locking domains for intermediate γ values.

FIG.10 - The width of mode locking in dependence on droplet viscosity, Arnold's tongues in phase plane λ versus field frequency Ω_H.

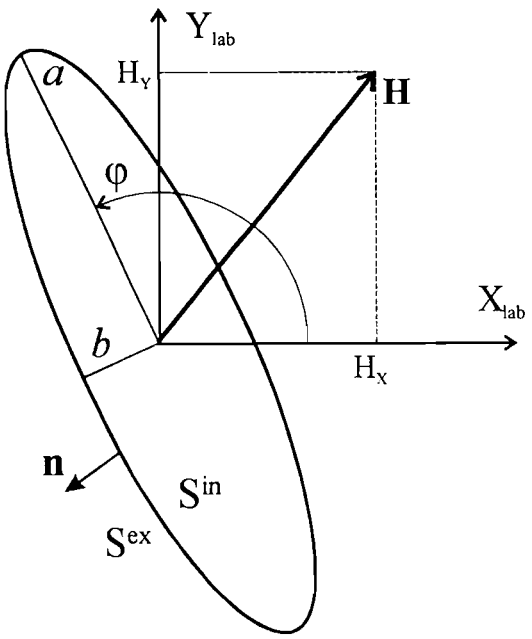

Fig.1

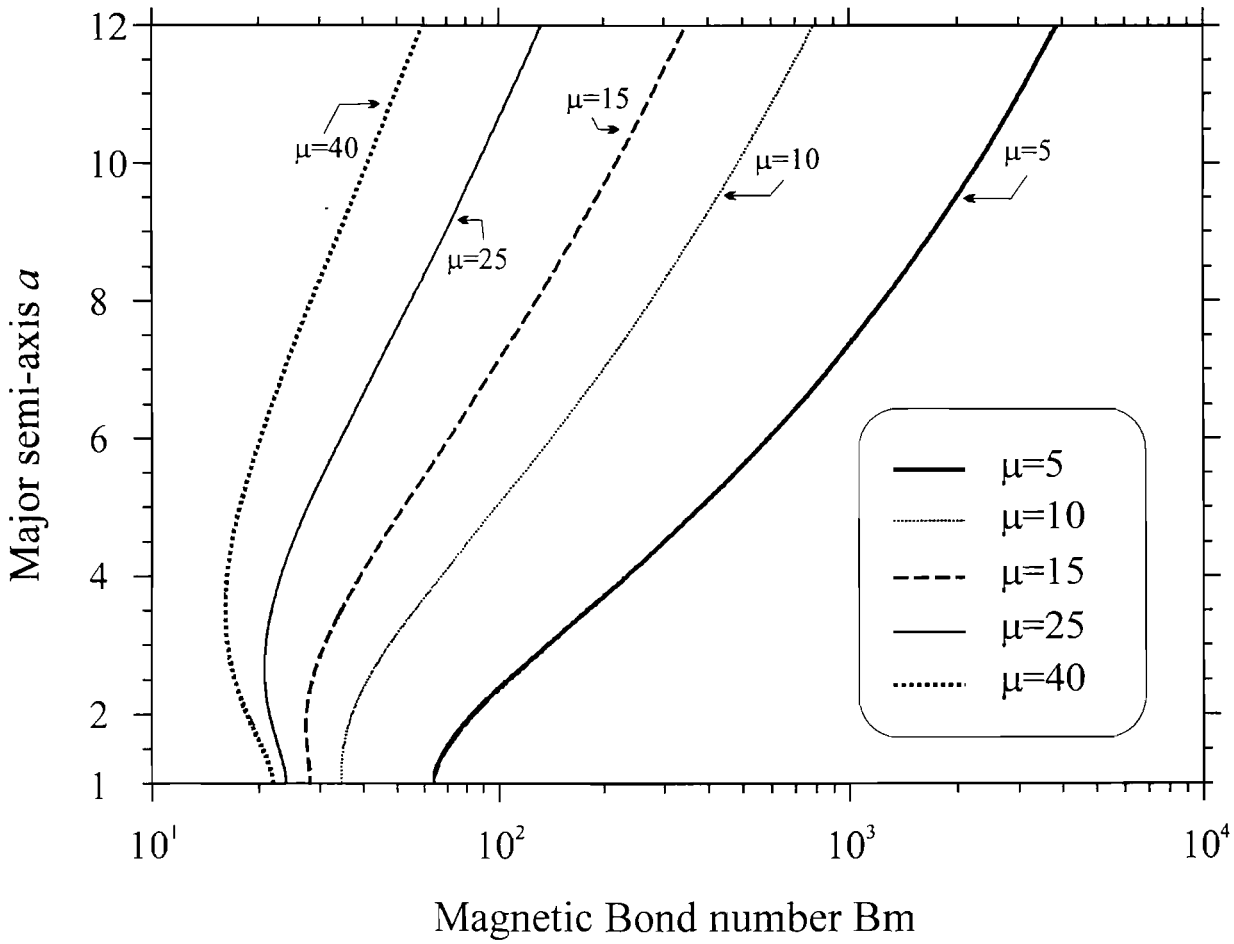
12
10
8
6
4
2
1
Major semi-axis a
μ=40
μ=25
μ=15
μ=10
μ=5
μ=5
μ=10
μ=15
μ=25
μ=40
10^1
10^2
10^3
10^4
Magnetic Bond number Bm

Fig.2

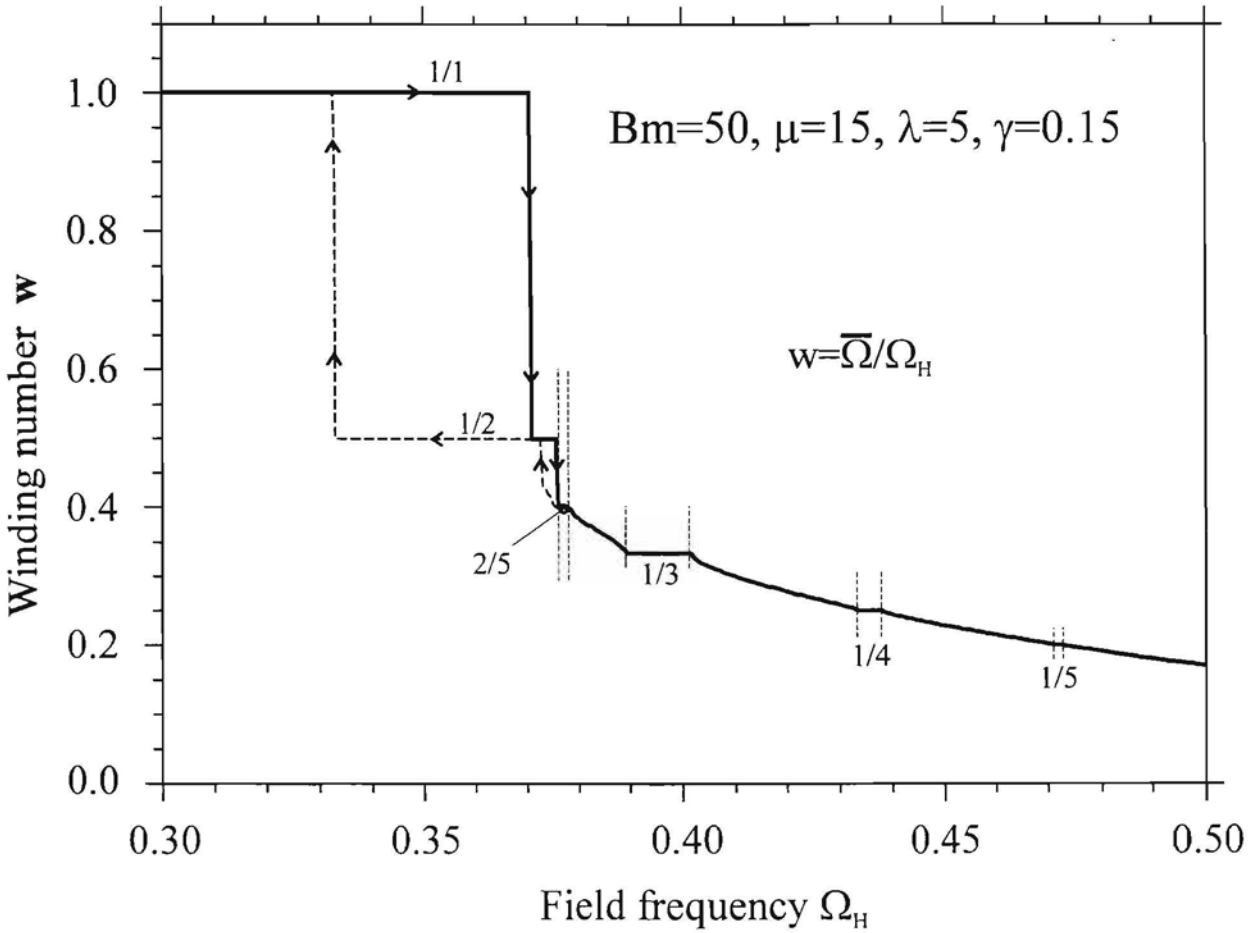
Bm=50, μ=15, λ=5, γ=0.15
w=Ω̄/Ω_H
1/1
1/2
2/5
1/3
1/4
1/5
Winding number w
Field frequency Ω_H
1.0
0.8
0.6
0.4
0.2
0.0
0.30
0.35
0.40
0.45
0.50

Fig.3a

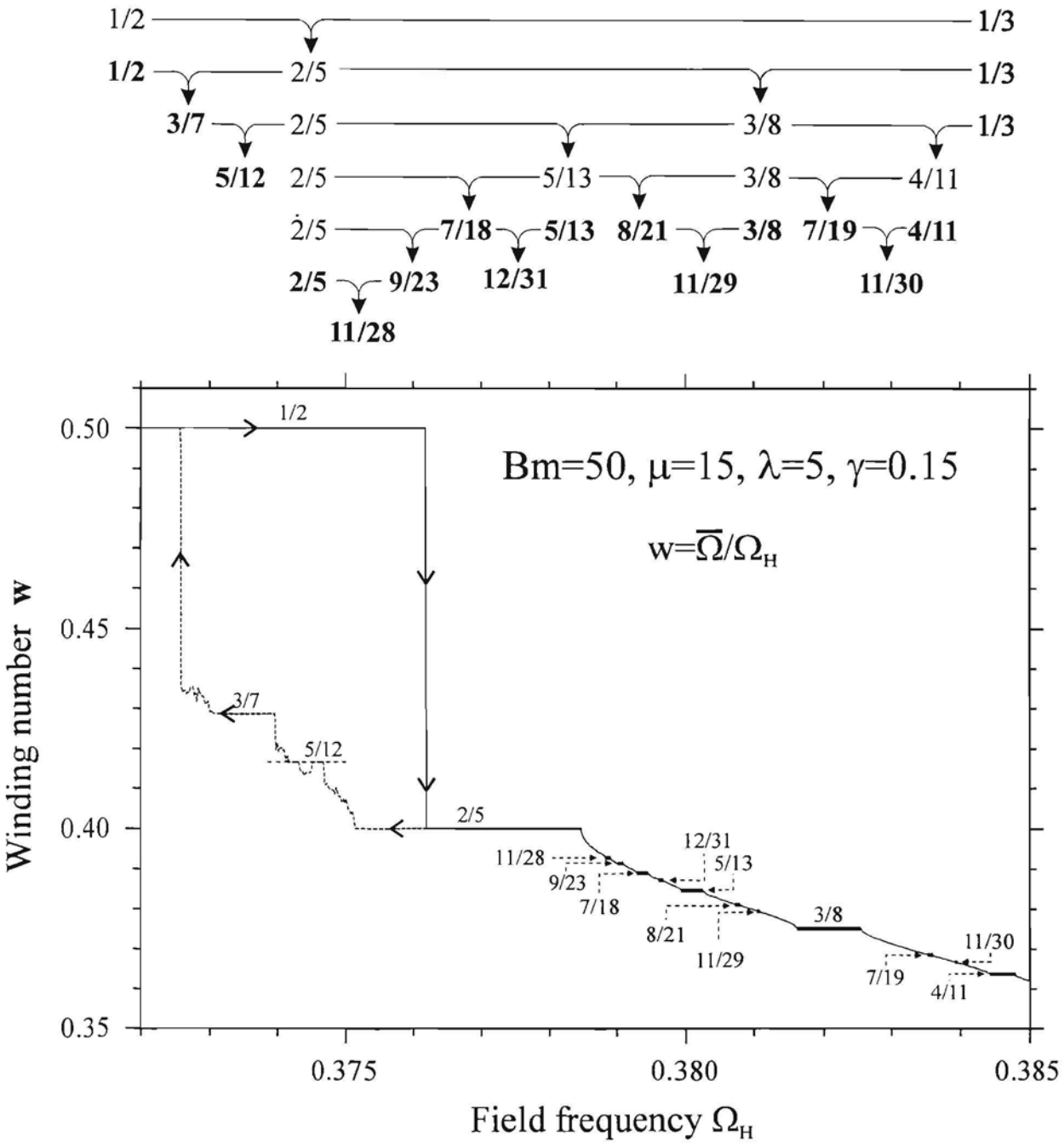
1/2
1/3
1/2
2/5
1/3
3/7
2/5
3/8
1/3
5/12
2/5
5/13
3/8
4/11
2/5
7/18
5/13
8/21
3/8
7/19
4/11
2/5
9/23
12/31
11/29
11/30
11/28
Bm=50, μ=15, λ=5, γ=0.15
w=Ω̄/Ω_H
Winding number w
0.50
0.45
0.40
0.35
0.375
0.380
0.385
Field frequency Ω_H
1/2
3/7
5/12
2/5
11/28
9/23
7/18
12/31
5/13
8/21
11/29
3/8
7/19
11/30
4/11

Fig.3b

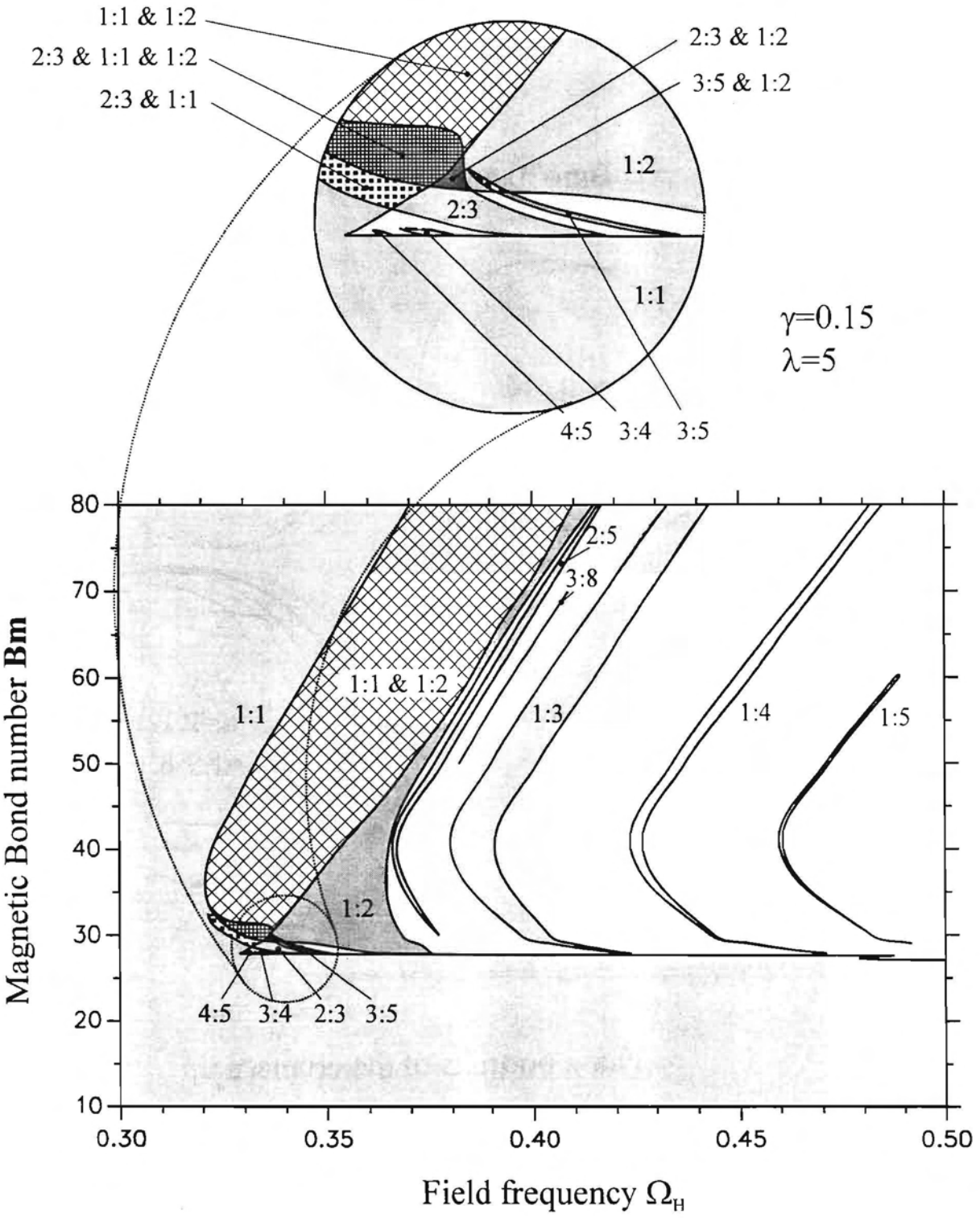
1:1 & 1:2
2:3 & 1:1 & 1:2
2:3 & 1:1
2:3 & 1:2
3:5 & 1:2
1:2
2:3
1:1
4:5
3:4
3:5
γ=0.15
λ=5
Magnetic Bond number Bm
Field frequency Ω_H
80
70
60
50
40
30
20
10
0.30
0.35
0.40
0.45
0.50
2:5
3:8
1:1 & 1:2
1:1
1:3
1:4
1:5
1:2
4:5
3:4
2:3
3:5

Fig.4

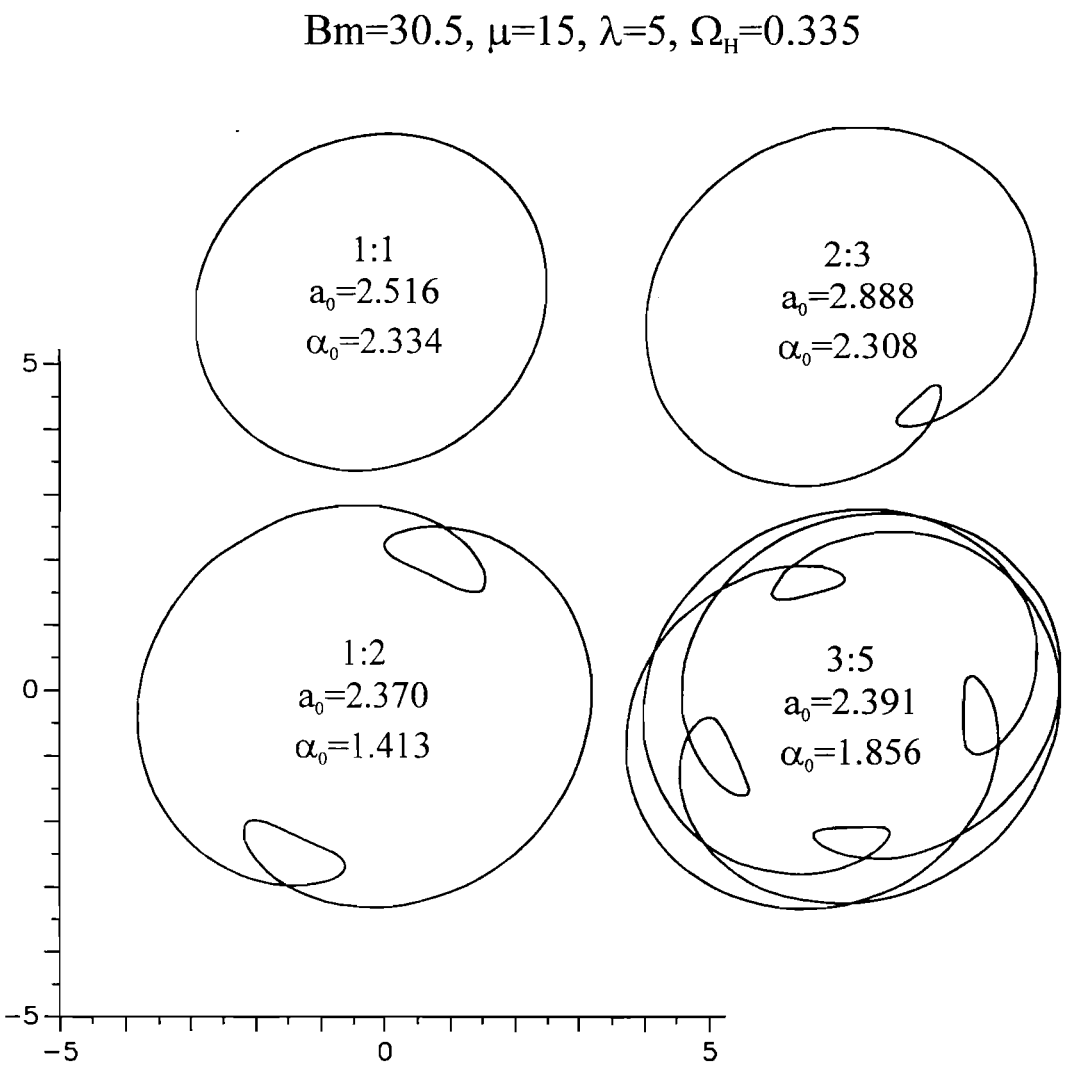

Phase portraits of the droplet's tip

Fig.5

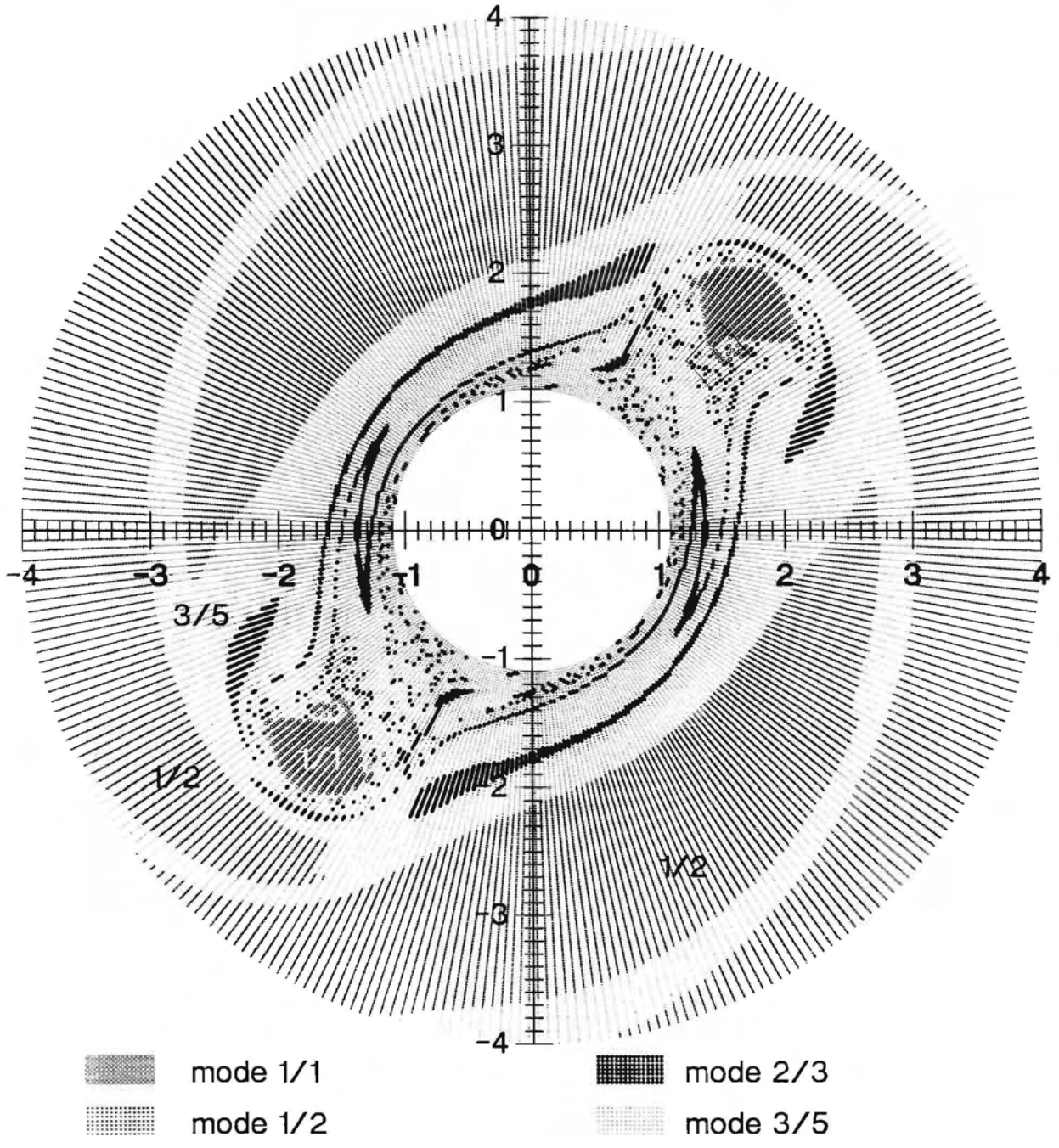

Map of initial conditions, leading to different modes

Fig.6

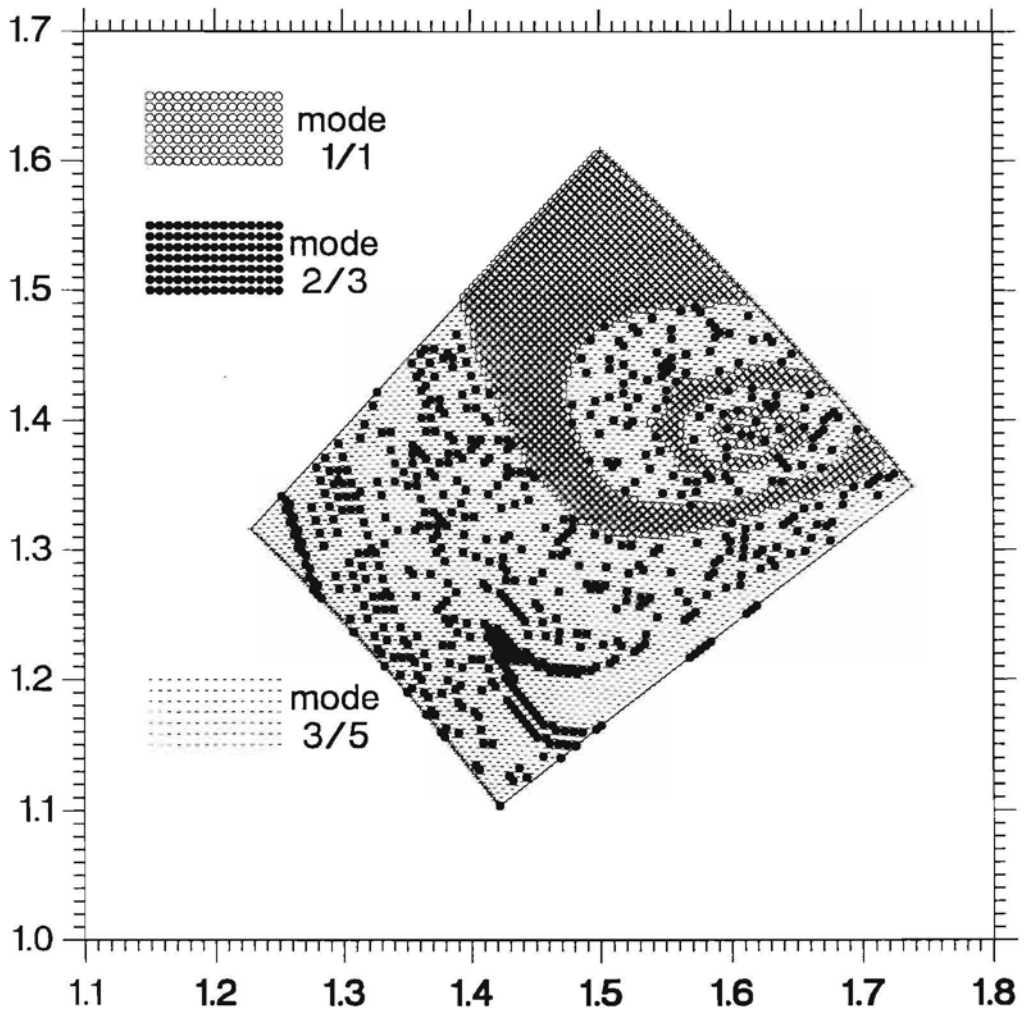

Zoomed are from the map of initial states
for different modes of locking

Fig.7

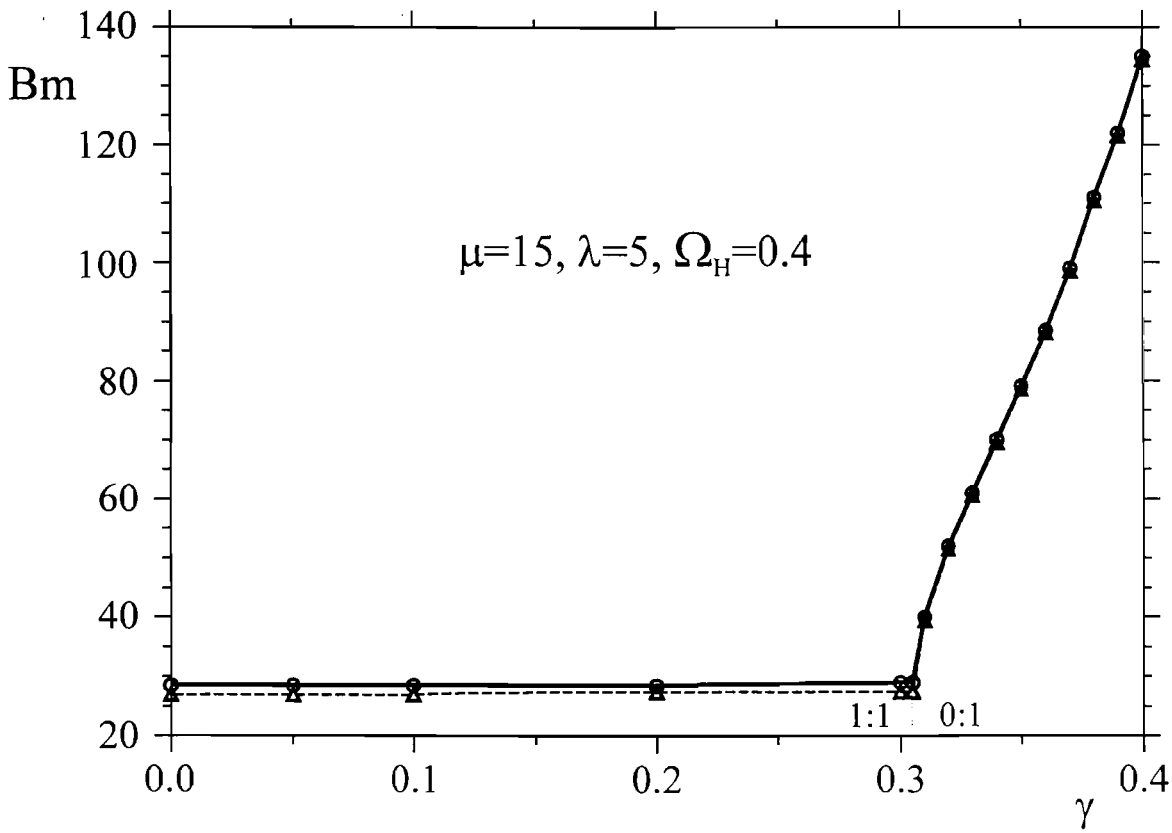

Fig.8

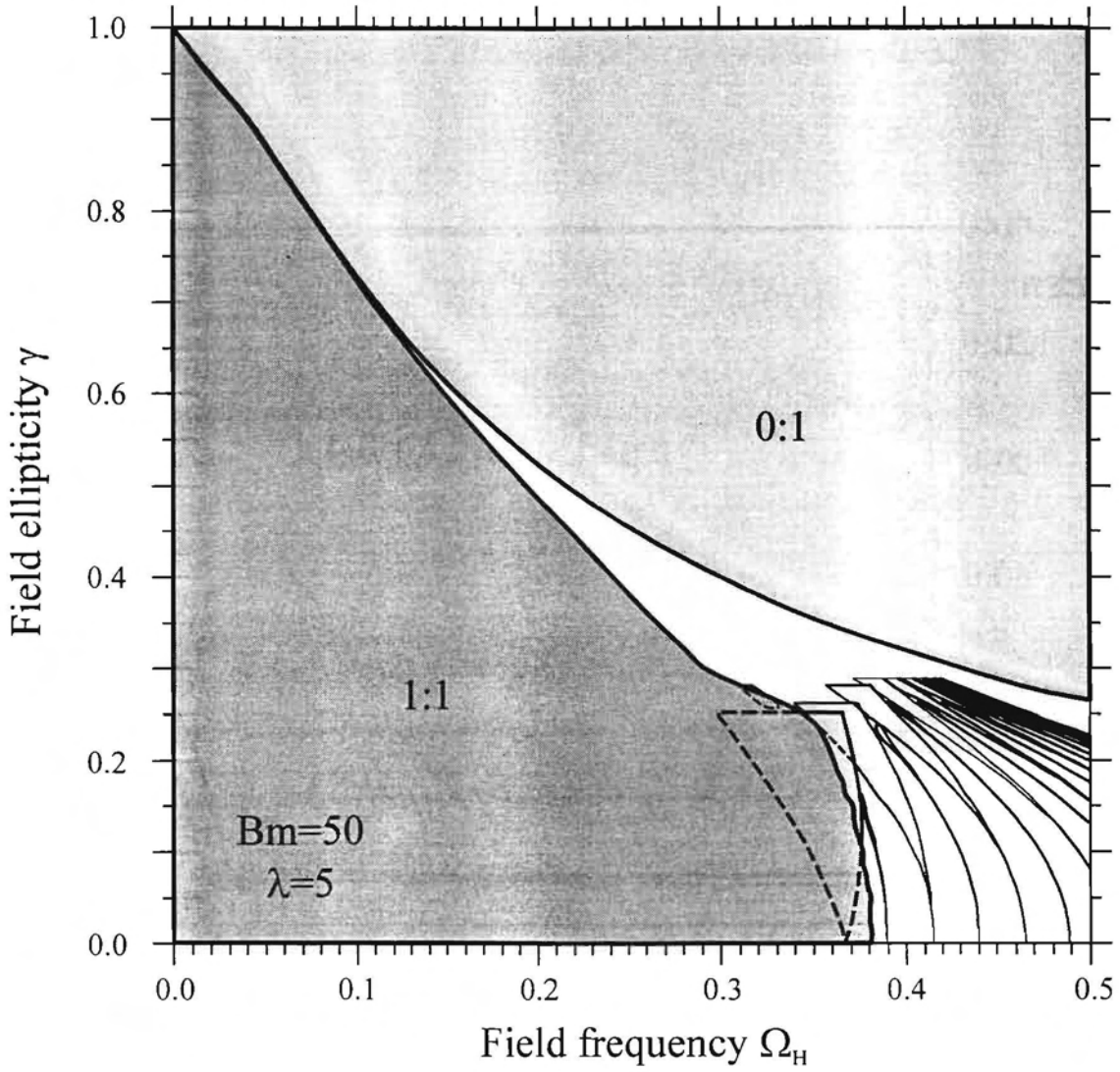
1.0
0.8
0.6
0.4
0.2
0.0
Field ellipticity γ
0.0
0.1
0.2
0.3
0.4
0.5
Field frequency Ω_H
0:1
1:1
Bm=50
λ=5

Fig9a

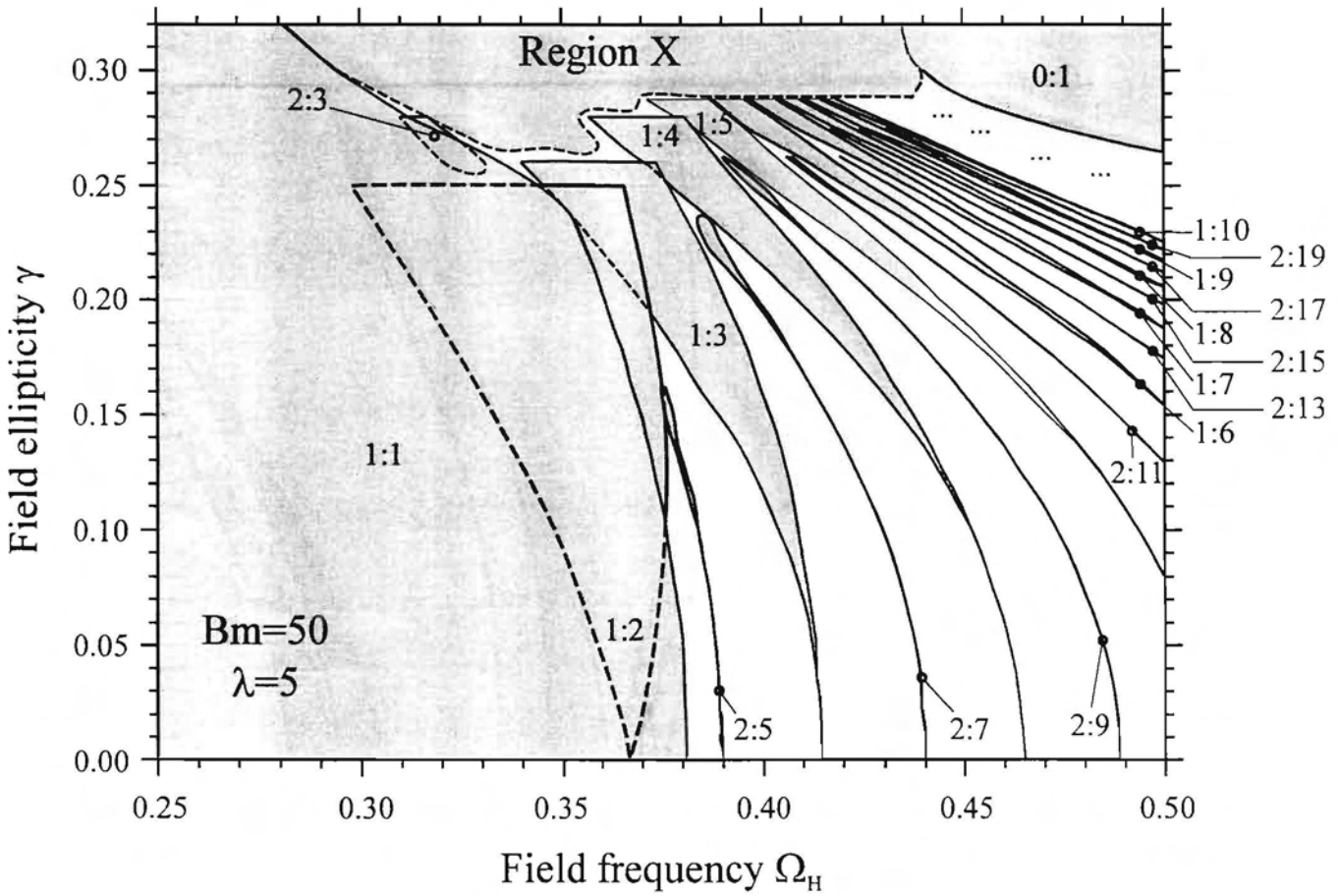
Region X
0:1
2:3
1:4
1:5
1:10
2:19
1:9
2:17
1:8
2:15
1:7
2:13
1:6
2:11
1:3
1:1
1:2
Bm=50
λ=5
2:5
2:7
2:9
Field ellipticity γ
Field frequency Ω_H
0.00
0.05
0.10
0.15
0.20
0.25
0.30
0.25
0.30
0.35
0.40
0.45
0.50

Fig.9b

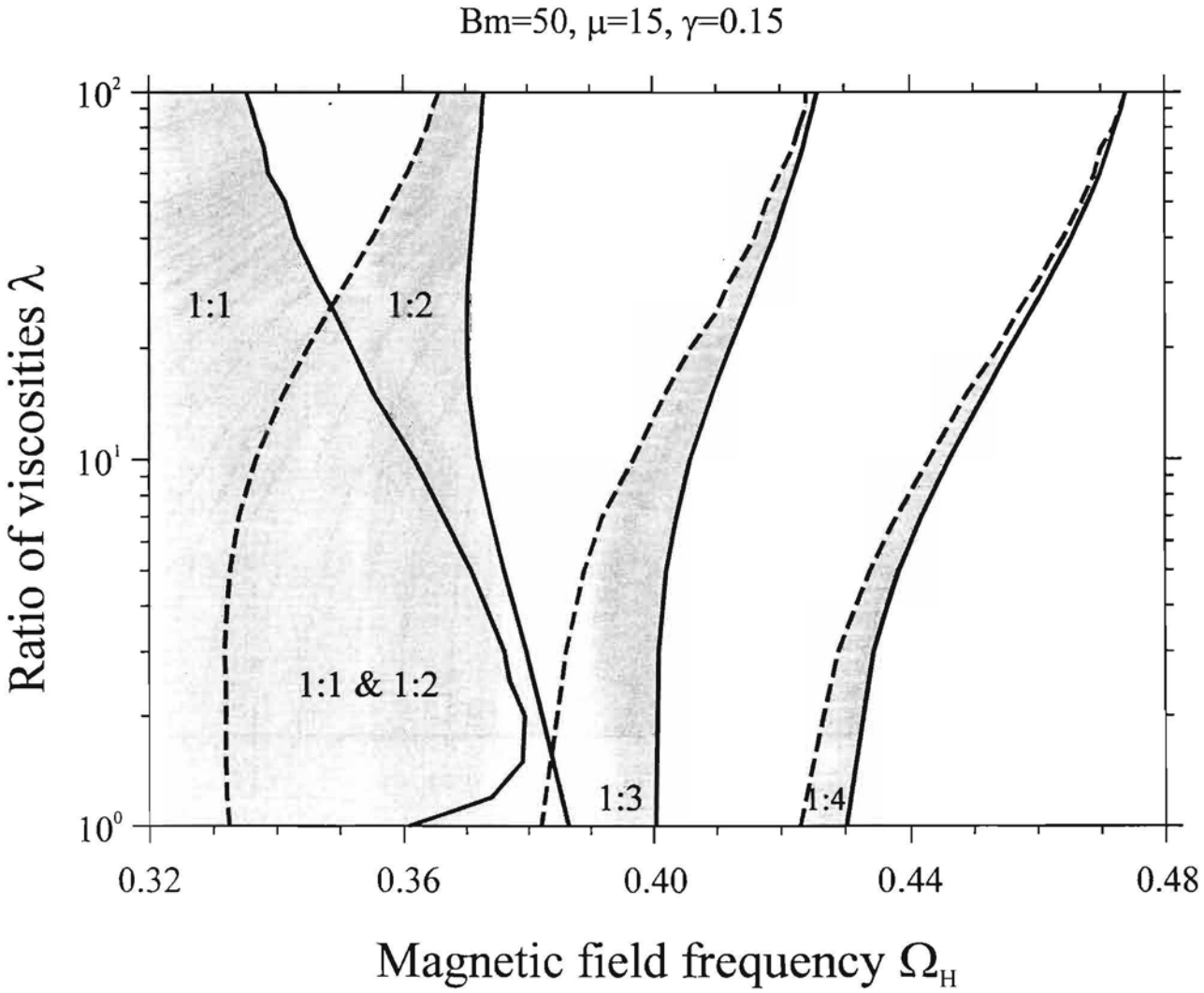
Bm=50, μ=15, γ=0.15
Ratio of viscosities λ
Magnetic field frequency Ω_H
10^2
10^1
10^0
0.32
0.36
0.40
0.44
0.48
1:1
1:2
1:1 & 1:2
1:3
1:4

Fig.10

Conclusions

Here the behaviour of the 2D ferrofluid droplet in an elliptically polarised magnetic field is studied by analysis of the equations of motion. These equations are the set of two first-order nonlinear ordinary differential equations. It is the difference from traditional approach to mode-locking studies, where mostly "difference" equations like circle maps are analysed. The ferrofluid droplet in elliptically polarised field exhibits Devil's staircase like mode-locking to the magnetic field rotation frequency. It is proved that the sequences of mode-locking obey the Farey tree law. In the limit of the circular field polarisation the mode-locking disappears. In the case of linear field polarisation pulsing oscillations of a droplet takes place. The influence of parameters, such as a magnetic Bond number, a ratio of viscosities as well as an ellipticity parameter γ for field polarisation, on the character of mode-locking is studied in great detail.

The difference from traditional Devil's staircase is overlapping at very small values of control parameter. The mode-locking disappears only in the limit of the circular field polarisation. Thus the interesting mode-locking system for dissipative system without inertia is found and described. The transition to the chaos is the extremely interesting topic, studies of which should be continued to explain the behaviour of a droplet at large value of a control parameter. The simulation by model equations have already displayed the period doubling scenario and the transition to chaotic dynamics.

General Conclusions

In the present thesis work, the 2D droplet behaviour in rotating magnetic fields is studied, assuming linear magnetisation of a ferrofluid and creeping flow inside the droplet and outside it. To perform this task, different algorithms and corresponding computer codes are developed, tested and applied. Particularly, the computer codes are developed, using the boundary element method (BEM), for the following purposes:

- to solve the magnetic field problem in the case of time-averaged magnetic energy at given magnetic Bond number and at given shape of a 2D droplet in a high frequency rotating field and to find the shape with the minimal total energy from the given set of shapes;
- to solve the unsteady coupled creeping flow and magnetic field problem in the case of time-averaged magnetic surface forces for a 2D droplet in a high frequency rotating field;
- to solve the unsteady coupled creeping flow and magnetic field problem accounting for instantaneous magnetic surface forces for a 2D droplet placed in a low frequency rotating field.

The BEM is based on the boundary integral equation technique, which is a powerful tool to solve the free moving boundary problem for a ferrofluid droplet in an external magnetic field in terms of surface values for both velocity and magnetic field. In present work the local curvature dependent, non-equidistant marker point distribution is applied to solve the magnetic field problem which is very sensitive to boundary contours with sharp tips. In the Chapter 2 a special technique is proposed to solve the magnetic field problem in new variables. These variables depend only on shape of a droplet and its magnetic permeability in the case of the linear magnetisation. It is shown that the magnetic field problem could be reduced either to a problem of magnetic surface charges or to a problem of equivalent surface currents,

called indirect magnetic field problem formulations. The direct formulation of the magnetic field problem in terms of tangential and normal field components, with respect to the boundary contour, provides solution with less approximation error. The principal difference of the indirect magnetic field problem formulation from the direct one is that the indirect formulation allows to obtain by a simple integration the one of two field components when another one is already found.

Beside that, analytical investigations are carried out to get simplified equations of motion which match numerical simulation data obtained by BEM and allow more thoroughly investigation of the droplet behaviour that could include even transition to chaotic dynamics. On the basis of the equations of motion the set of computer codes is developed implementing Runge-Kutta fourth order method to simulate the droplet rotation and to perform time averaging of it. This method is able to describe phenomena of simple periodic rotations, quasiperiodic rotations, rotation with a mode-locking, and chaotic motion of a droplet. The special technique is used to study multiple basins of attraction to different phase locking modes.

In general the motion of a droplet in rotating field could be classified in two cases with respect to the field frequency: the case of a high-frequency field and the case of a low-frequency field. In the present work the term high-frequency field is used with respect to the field frequency at which the characteristical relaxation time of droplet is much larger than the rotation period of a field.

It is found by the energy approach that:

1. There exists a magnetic field threshold with respect to any perturbation from circular shape in 2D in the high-frequency rotating magnetic field. The increase of a magnetic Bond number beyond the threshold value causes evolution of spikes on the surface, which become sharper at further growth.
2. A 2D numerical analysis of MF droplets with different numbers of spikes shows that the equilibrium shape with two-spikes corresponds to the lowest energy and thus the transition from 2-spike shape to the shape with larger amount of spikes does not take place if only energetical arguments are involved.

The small perturbation analysis and the direct BEM simulation of a 2D droplet in the high-frequency rotating magnetic field prove that:

1. In the high-frequency rotating magnetic field a field threshold exists with respect to any perturbation from circular shape. If Bm is smaller than this absolute threshold value, a droplet holds circular shape. Increasing the magnetic Bond number beyond the "absolute threshold", the most unstable mode develops. The small perturbation linear analysis gives the number of lobes for the most unstable mode in dependence on magnetic field strength. In the case of pure creeping flow in 2D the number of lobes is directly proportional to the magnetic field. This relation is proved by BEM simulation.
2. It is found that in 2D a 3-spike shape is metastable, but a 2-spike shape has the absolute minimum of energy. The transition to a 2-spike shape from a 3-spike one takes place either if a magnetic field strength is decreased below the turning point or by a sufficiently high shape perturbation. Evidently in 2D there exists no metastable shapes with more than three spikes in a high-frequency rotating magnetic field under assumptions used in the present work. The simulations of a 4-spike shape display splitting instability for the "body" of a droplet, where spikes come together. So it could be concluded that the symmetric shapes with 4 and more spikes, obtained by the energy approach, correspond to saddle points in a phase space and thus they are unstable.

It is found by the BEM simulation and the numerical solution of the equations of motion that in the low-frequency rotating magnetic field the droplet exhibits the following properties:

1. There are two kinds of a behaviour for a 2D ferrofluid droplet in dependence on the applied magnetic field strength in low-frequency magnetic fields, called the "high-field behaviour" and the "low-field behaviour". The critical Bond number which separates these two kinds of behaviour turns out to be approximately the same as the threshold value with respect to 2-lobe perturbation in a high-frequency field. If the magnetic Bond number is larger than critical one, a droplet even at high frequencies, where it can not follow the field, stays elongated. If the magnetic

Bond number is smaller than critical one, a droplet elongation diminishes to a circle as the frequency tends to infinity.

2. At lower values of the viscosity of a droplet the critical frequency with respect to an ability to follow a rotation of a magnetic field is slightly higher than for a droplet with large viscosity in comparison with the fluid outside the droplet.
3. Analytical model is derived, which allows to describe the motion of a 2D droplet by a set of non-linear equations of motion, if the droplet shape is near the elliptic one.
4. A 2D viscous droplet ($\lambda \geq 5$) exhibits a bending instability if the magnetic field oriented perpendicular to the major dimension of a droplet. The significant bending effect is observed if the droplet is exposed a time long enough to such a field, i.e. if the field frequency slightly exceeds the critical one with respect to the ability to follow the field.

In the case of an elliptically polarised rotating field, the droplet exhibits rather complex motion, properties of which strongly depend on the ellipticity of the field. By equations of motion it is proved that Devil's staircase like mode-locking to the magnetic field rotation frequency takes place. In the limit of the circular field polarisation the mode-locking disappears. The outstanding property of the present mode-locking is that the remarkable overlapping of mode-locking intervals is present even at very small values of control parameter. The simulation by model equations have displayed the period doubling scenario and the transition to chaotic dynamics.

The bending of the viscous droplet in a rotating field and the transition to the chaos for a droplet rotation in an elliptically polarised rotating magnetic field are put in evidence for the first time. The further research in these two directions is highly desirable.

In short, present studies has proved that many phenomena, observed in real 3D experiments concerning ferrofluid droplet behaviour, could be explained on the basis of 2D model, accounting only for the linear magnetisation of a ferrofluid and the constant surface tension on the interface between a droplet and an external fluid. Some effects are caused by the 2D geometry but, nevertheless, the obtained results could be

implemented to explain the behaviour of so called "liquid bridges" between two plates, having approximately the two-dimensional geometry. For a more precise agreement between experiments and numerical simulation results, the 3D simulation algorithms, which are more computer-time expensive, are supposed to be elaborated during the further research.

References

[1] H.D.I.Abarbanel, R.Brown, M.B.Kennel - Lyapunov exponents in chaotic systems: their importance and their evolution using observed data, Int.Journ.Mod.Phys.B, 1991, Vol.5, N9, p.1347-1375

[2] V.I.Arkhipenko, Y.D.Barkov, V.G.Bashtovoi - Shape of a drop of magnetized fluid in a homogeneous magnetic field, Magnetohydrodynamics, 1978, V14, p373 (Magnitnaya gidrodinamika. (in Russ) 1978, N3, pp.131-134)

[3] V.I.Arnold - Small Denominators, I: Mappings to the Circumference Into-Itself: AMS Transl.Series 2, 1965, Vol.46, p216

[4] J.-C.Bacri, A.Cebers, R.Perzynski - Behaviour of a magnetic fluid microdrop in a rotating magnetic field, Physical Review Letters, 1994, Vol.72, N17, pp.2705-2708

[5*] J.C.Bacri, A.Cēbers, S.Lācis, R.Perzynski - Dynamics of the magnetic fluid droplet in rotating field, J.Magn.Magn.Mater. 1995, Vol.149, pp.143-147: *) **included in the Chapter 5**

[6*] J.C.Bacri, A.Cēbers, S.Lācis, R.Perzynski - Mode locking and devil's staircase for 2D ferrofluid droplet in elliptically polarized rotating magnetic field. Physica D (submitted), *) **included in the Chapter 6**

[7*] J.C.Bacri, A.Cēbers, S.Lācis, R.Perzynski - Shapes of 2D magnetic fluid droplets in a rotating magnetic field, Magnitnaya Gidrodinamika, 1995, N3 (accepted to publish) *) **included in the Chapter 3**

[8*] J.C.Bacri, A.Cēbers, S.Lācis, R.Perzynski - Numerical simulation of the transient stages of 2D magnetic fluid droplet in high-frequency rotating magnetic fields, Magnitnaya Gidrodinamika, 1996 (accepted to publish) *) **included in the Chapter 4**

[9] J.C.Bacri, C.Drame, B.Kashevsky, S.Neveu, R.Perzynski, C.Redon - Motion of a pair of rigid ferrofluid drops in a rotating magnetic field - Progr.Colloid.Sci., 1995, Vol.98, pp.124-127

[10] J.-C.Bacri, R.Perzynski, D.Salin, A.O.Cebers - Instabilities of a ferrofluid droplet in an alternating and rotating magnetic fields, Math.Res.Soc.Symp.Proc., 1992, Vol.248, pp.241-246

[11] J.-C.Bacri, D.Salin - Instability of ferrofluid magnetic drops under magnetic field, J.Physique Lettres, 1982, Vol.43, pp.L649-654

[12] J.-C.Bacri, D.Salin - Dynamics of the shape transition of a magnetic ferrofluid drop, J.Physique Lettres, 1983, Vol.44, pp.L415-420

[13] J.-C.Bacri, D.Salin - First-order transition in the instability of a magnetic fluid interface, J.Physique Lettres, 1982, Vol.43, pp.L649-654

[14] J.-C.Bacri, D.Salin, R.Massart - Study of the deformation of ferrofluid droplets in a magnetic field, J.Physique Lettres, 1982, Vol.43, pp.L179-184

[15] R.L.Baily - Lesser known applications of ferrofluids. J.Magnetism Magnetic Mater., 1983, Vol.39, N1/2, pp.178-182

[16] P.Bak The Devil's staircase Physics Today, 1986, Vol.39, N12, pp.38-45

[17] O.A.Basaran, F.K.Wohlhuter - Effect of nonlinear polarization on shapes and stability of pendant and sessile drops in an electric (magnetic) field, J.Fluid Mech., 1992, Vol.244, pp.1-16

[18] G.K. Batchelor - An Introduction to Fluid Dynamics, New York: Cambridge University Press, 1970, 615p

[19] B.Berkovsky, V.Bashtovoi - Instabilities of magnetic fluids leading to a rupture of continuity, IEEE Trans.Magnetics, 1980, Vol.16, N2, pp.288-297

[20] B.Berkovsky, V.Bashtovoi, E.Mikhalevich, S.Pogirnitskaya, A.Reks - A shape of a drop (bubble) of a magnetic fluid between parallel planes, in: 7th International Conference on Magnetic Fluids - Bhavnagar, India 9-14 Jan. 1995, pp.126-127

[21] B.M.Berkovsky, V.I.Kalikmanov - Topoligical instability of magnetic fluids, J.Physique Lettres, 1985, Vol.46, N11, pp.L483-491

[22] B.M.Berkovskii, V.F.Medvedev, M.S.Krakov - Magnetic fluids: engineering applications, Oxford; New York: Oxford University Press, 1993, 243p

[23] E.Blūms, R.P.Kerno, G.E.Kroņkalns, M.M.Maiorov - Application of magnetic liquids for cooling of moving-coil loudspeakers (in Russ), in: Hydromechanics and thermophysics of magnetic liquids, Salaspils, 1980, pp.237-242

[24] E.Blūms, Yu.A.Mikhailov, P.J.Ozols - Heat and Mass Transfer in Magnetic Field (in Russ), Zinatne, Riga, 1980, 355p

[25] E.Blūms, M.M.Maiorov, A.Cēbers - Magnetic Liquids (in Russ), Zinatne, Riga, 1989, 386p

[26] T.Bohr, G.Gunaratne - Scaling for supercritical circle-maps: numerical investigation of the onset of bistability and period doubling, Phys.Letters, 1985, Vol.113A, N2, pp.55-60

[27] A.G.Boudouvis, J.L.Puchalla, L.E.Scriven - Magnetohydrostatic equilibria of ferrofluid drops in external magnetic fields. Chem. Eng. Comm. 1988, v.67, pp.129-144

[28] A.G.Boudouvis, J.L.Puchalla, L.E.Scriven, R.E.Rosensweig - Normal field instability and patterns in pools of ferrofluid, J.Magn.Magn.Mater. 1987, Vol.65, N2/3, pp.307-310

[29] A.G.Boudouvis, L.E.Scriven - Sensitivity analysis of hysteresis in deformation of ferrofluid drops. J.Magn.Magn.Mater. 1993, v.122, pp.254-258

[30] C.A. Brebbia - Topics in Boundary Element Research - New York, Springer-Verlag, Vol.1 1984 256p, Vol.2 1985 260p, Vol.3 1987 296p, Vol.4 1987 172p, Vol.5 1989 181p, Vol.6 1989 234p, Vol.7 1990 208p

[31] V.Cabuil, Yu.L.Raikher, J.-C.Bacri, R.Perzynski - Colloidal stability of magnetic fluids, in: Magnetic fluids and applications, Handbook, UNESCO, Engineering and technology division

[32] A.Cēbers - Virial method for investigation of static and dynamic of magnetizable fluid droplets, Magnitnaya Gidrodinamika (in Russ) , 1985, N1, pp.25-34

[33] A.O.Cēbers - Numerical simulation of dynamics of a magnetic fluid droplet in static and rotating magnetic fields. Magnitnaya gidrodinamika. 1986, No 4, pp3-10

[34] A.Cēbers, I.Driķis - A numerical study of the evolution of quasi-two-dimensional magnetic fluid shape, Magnitnaya Gidrodinamika - 1996 (to be published)

[35] A.Cēbers, S.Lācis - Magnetic fluid free surface instabilities in high frequency rotating magnetic fields. - Brazilian Journal of Physics, 1995, Vol.25, N2 ,pp.101-111

[36] A.O.Cēbers, M.M.Maiorov - Magnetostatic instability in flat layers of magnetizable fluid, Magnitnaya Gidrodinamika (in Russ) - 1980, N1, pp.27-35

[37] A.O.Cēbers, M.M.Maiorov - Comblike instability in thin layers of magnetic fluid, Magnitnaya Gidrodinamika (in Russ) - 1980, N2, pp.22-26

[38] A.O.Cēbers, M.M.Maiorov - The structure of the boundary between a bubble and a magnetic fluid in a magnetic field, Magnitnaya Gidrodinamika (in Russ) - 1980, N3, pp.15-20

[39] A.O.Cēbers, A.A.Zemītis - Modelling MHD surface instability via numerical experiment, Magnitnaya Gidrodinamika (in Russ) - 1983, N4, pp.15-26

[40] S.Chandrasekhar - The stability of a rotating liquid drop, Proc.Roy.Soc., 1965, Vol.286, N1404, pp.1-26

[41] S.Chandrasekhar - Hydrodynamic and hydromagnetic stability, New York: Dover Publications, 1981, 652p.

[42] S.Chandrasekhar - Ellipsoidal figures of equilibrium, New York: Dover Publications, 1987, 254p.

[43] M.D.Cowley, R.E.Rosensweig - The interfacial stability of a ferromagnetic fluid, J.Fluid Mech., 1967, Vol.30, N4, pp.671-688

[44] C.De Boor - A practical guide to splines, Springer-Verlag, 1978

[45] D.G.Dritschel - Contour surgery : a topological reconnection scheme for extended integrations using contour dynamics - Journal of Computational Physics, 1988, Vol.77, pp.240-266

[46] V.I.Drozdova, T.V.Skrobotova, V.V.Chekanov - Experimantal study of the hydrostatics characterizing the interphase boundary in a ferrofluid,

Magnetohydrodynamics, 1979, V15, p12 (Magnitnaya gidrodinamika. (in Russ) 1979, N1, pp.16-18)

[47] H.Fay, J.M.Quets - Density separation of solids in ferrofluids with magnetic grids. Separation Sci.Technol., 1980, Vol.15, N3, pp.339-369

[48] R.Finn - Equilibrium Capillary Surfaces, New York:Springer-Verlag, 1986, 245p

[49] C.Flament, S.Lācis, J.-C.Bacri, A.Cēbers, S.Neveu, R.Perzynski - Measurements of ferrofluid surface tension in confined geometry, Phys.Review E (to be published)

[50] J.Frenkel - The kinetic theory of liquids, New York : Dover 1955

[51] A.Gailītis - Shape of the ferromagnetic fluid surface instability (in Russ), Magnitnaya Gidrodinamika, 1969, N1, pp.68-70

[52] A.Gailītis - Formation of the hexagonal pattern on the surface of a ferromagnetic fluid in applied magnetic field, J.Fluid Mech., 1977, Vol.82, N3, pp.401-413

[53] L.Glass - Simple mathematical models for complex dynamics in physiological systems, in: Directions in Chaos, v.2, ed. Hao Bai-lin, Singapore: World Scientific, 1988, 384p

[54] E.Guyon, J.P.Hulin, L.Petit - Hydrodynamique physique, Paris: Edition du CNRS, 1991, 506p

[55] J.Happer, H.Brenner - Low Reynolds Number Hydrodynamics, Englwood Cliffs, N.J., Prentice-Hall, 1965, 553p

[56] D.B.Hathaway - Use of ferrofluid in moving-coil loudspeakers. dB-Sound Eng.Mag. 1979, Vol.13, N2, pp.42-44

[57] G.Helgessen, P.Pieranski, A.T.Skjeltorp - Nonlinear phenomena in systems of magnetic holes, Phys.Rev.Lett., 1990, v.64, N12, p.1425

[58] D.P.Jackson,R.E.Goldstein,A.O.Cebers - Hydrodynamics of fingering instabilities in dipolar fluids, Phys.Rev.E 50, 1994, pp.298-307

[59] Jeffrey G.F. - The motion of ellipsoidal particles immersed in a viscous fluid, Proc. Roy. Soc. 1922, A102, pp.161-179

[60] M.H.Jensen - Multifractals in convection and aggregation, in : Random Fluctuations and Pattern Growth: Expariments and Models, ed. H.E.Stanley, N.Ostrowsky, Boston: Kluwer Academic Publishers, 1988, 355p

[61] O.D. Kellog - Foundations of potential theory Berlin, New York : Springer-Verlag, 1967, 384p

[62] Ye.A.Kuznetsov, M.D.Spektor - About existance of hexagonal pattern on the surface of the fluid dielectric in external field (in Russ), JETP, 1976, Vol.71, N1, pp.262-271

[63*] S.Lācis - The equations of motion of the 2D elliptic magnetic fluid droplet in rotating field, Magnitnaya Gidrodinamika, 1996, (accepted to publish) *) **submitted to the Chapter 5**

[64] A.O.Ladyzhenskaya - The mathematical theory of viscous incompressible flow, New York, Gordon and Breach, 1969, 224p

[65] L.D.Landau, E.M.Lifshitz - Electrodynamics of continuous media, Oxford, New York: Pergamon Press, 1960, 417p

[66] L.D.Landau, E.M.Lifshitz - Fluid mechanics, Oxford, New York: Pergamon Press, 1959, 536p

[67] S.A.Langer, R.E.Goldstein, D.P.Jackson - Dynamics of labyrinthine pattern formation in magnetic fluids, Phys.Rev.A, 1992, Vol.46, N8, pp.4894-4904

[68] H.Li, T.C.Hasley, A.Lobkovsky - Singular shape of a drop in an electric or magnetic field, Europhysics Letters, 1994, Vol27, pp.575-580

[69] L.Lichtenstein - Über einige Existenzprobleme der Hydrodynamik, Math.Z., 28, 1928, pp.387-415,725

[70] H.A.Lorentz - Ein allgemeiner Satz, die bewegung einer reibender Fluessigkeit betreffen, nebst einigen anwendungen Desselben, Abhand.Theor.Phys. (Leiptzig), 1907, Vol.1, pp.23-42

[71] G.I. Marchuk - Methods of numerical mathematics - New York : Springer-Verlag, 1975, 316p

[72] S.Maruno, K.Yubakani, S.Soga - Plain paper recording process using magnetic fluids. J.Magnetism Magnetic Mater., 1983, Vol.39, N1/2, pp.187-189

[73] R.Massart - Preparation of aqueous magnetic liquids in alkaline and acidic media, I.E.E.E. Trans.Magn. 1981, Vol.MAG-17, N2, pp.1247-1248

[74] F.C.Moon - Chaotic and fractal dynamics : an introduction for applied scientists and engineers, New York : Wiley, 1992, 508p

[75] Y.Morimoto, M.Akimoto, Y.Yotsumoto - Dispersion state protein-stabilized magnetic emulsion. Chem.Pharm.Bull., 1982, Vol.30, N8, pp.3024-3027

[76] R.Moskowitz - Dynamic sealing with magnetic fluids, ASLE Trans., 1975, Vol.18, N2, pp.135-143

[77] J.L.Neuringen, R.E.Rosensweig - Ferrohydrodynamics, Phys.Fluids., 1964, Vol.7, N12, pp.1927-1937

[78] R.S.Newbower - A new technique for circulatory measurements employing magnetic fluid tracers, in Proc. 1972 Biomedical Symp., 1972, San Diego.

[79] F.K.G.Odqvist - Über die rangwertaufgaben der Hydrodynamik zäher Flüssigkeiten, Math.Z., 1930, Vol.32, pp.329-375

[80] E.Ott - Chaos in dynamical systems, Cambridge University Press, New York, 1993, 385p.

[81] S.S.Papell - Low viscosity magnetic fluid obtained by the colloidal suspension of magnetic particles. U.S. Patent 3 215 572. 1965

[82] U.Parlitz, W.Lauterborn - Period-doubling cascades and devil's staircases of the driven van der Pol oscillator, Phys.Rev.A, 1987, Vol.36, N3, pp.1428-1433

[83] P.A.Petit, M.A.de Albuquerque, V.Cabuil, P.Molho - Evolution of the domain-like pattern in a film of ferrofluid in normal fields, J.Magn.Magn.Mater. 1992, Vol.113, pp.127-131

[84] J.Pļaviņš, M.Lauva - Study of colloidal magnetite-binding erythrocites: Prospects for cell separation, J.Magnetism Magnetic Mater., 1993, Vol.122, pp.349-353

[85] C. Pozrikidis - Boundary integral and singularity methods for linearized viscous flow - New York : Cambridge University Press, 1992, 259p

[86] A.F.Pshenitchnikov, I.Yu.Shurubov - Isvestiya Akad. Nauk. SSR Ser. Phys., 1987, Vol.51, p1081

[87] K.Raj, B.Moskowitz, R.Casiari - Advances in ferrofluid technology, J.Mag.Mag.Mat. 1995, Vol.149, pp.174-180

[88] C.E.Rosenkilde - Stability of axisymmetric figures of equilibrium of a rotating charged liquid drop, Journal of mathematical physics, Vol.8, N1, (1967), pp. 98-118

[89] C.E.Rosenkilde - Stability of axisymmetric figures of equilibrium of a rotating charged liquid drop, Proc.Roy.Soc.A, 1969, Vol.312, pp. 473-494

[90] R.E.Rosensweig - Fluid dynamics and science of magnetic liquids. In advances in electronics and electron physics, 1979, Vol.48, L.Marton, Ed. Academic Press, New York, pp. 103-199

[91] R.E.Rosensweig - Ferrohydrodynamics, New York : Cambridge University Press, 1985, 344p

[92] R.E.Rosensweig, M.Zahn, R.Shumovich - Labyrinthine instability in magnetic and dielectric fluids, J.Magn.Magn.Mater. 1983, Vol.39, N1/2, pp.127-132

[93] A.H. Schatz, V. Thomee, W.L. Wendland - Mathematical Theory of Finite and Boundary Element Methods - Boston : Birkhauser, 1990, 276p

[94] P.C.Scholten - How magnetic can a magnetic fluid be? J.Mag.Mag.Mat., 1988, Vol.39, N1/2, pp.99-106

[95] P.C.Scholten - Some material problems in magnetic fluids, Chem.Eng.Comm., 1988, Vol.67, pp.331-340

[96] O.E.Sero-Guillaume, D.Zouaoui, D.Bernardin, J.P.Brancher - The shape of a magnetic liquid drop, J.Fluid Mech., 1992, Vol.241, pp.215-232

[97] J.D.Sherwood - Breakup of fluid droplets in electric and magnetic fields, J.Fluid Mech., 1988, Vol.188, pp.133-146

[98] J.Shimoiizaka, K.Nakatsuka, T.Fujita, A.Kounosu - Sink-float separators using permanent magnets and water based magnetic fluid. IEEE Trans. Magnetics, 1980, Vol.MAG-16, N2, pp.368-371

[99] M.I.Shliomis - Magnetic fluids, Uspehi fiziceskih nauk (in Russ), 1974, Vol.112, N3, pp.427-458

[100] M.I.Shliomis, T.P.Lyubimova, D.V.Lyubimov - Ferrohydrodynamics: an essay on the progress of ideas, Chem.Eng.Comm., 1988, Vol.67, pp.275-290

[101] A.T.Skjeltorp - Physical modelling using microparticles, in: Complex Fluids, Ed. Luis Garido, New York : Springer-Verlag, 1992, 413p

[102] A.T.Skjeltorp, G.Helgessen - Condensation and ordering of colloidal spheres disperse in a ferrofluid, Physica A, 1991, Vol.176, p.37

Table of figures